Institut national de la recherche scientifique

université de BORDEAUX

Thèse en cotutelle présentée pour obtenir le grade de

Docteur de
l'Institut national de la recherche scientifique
et de l'Université de Bordeaux

INRS-ÉMT

Programme : Sciences de l'énergie et des matériaux

École doctorale SPI

Spécialité : Lasers, matière et nanosciences

par **Simon Vallières**

.....

Towards Reliable, Intense and High Repetition-Rate Laser-Driven Ion Beamlines

.....

Sous la direction de Patrizio Antici et d'Emmanuel d'Humières

Soutenue le 3 décembre 2020

Membres du jury :

M. François Légaré	Professeur	INRS-ÉMT	Président du jury
Mme Magdalena Bazalova-Carter	Professeure adj.	Univ. de Victoria	Rapporteure
Mme Tammy Ma	Chargée de recherche	LLNL-NIF	Rapporteure
M. Victor Malka	Professeur	Institut Weizmann	Examinateur externe
M. Patrizio Antici	Professeur	INRS-ÉMT	Directeur de thèse
M. Emmanuel d'Humières	Professeur	Univ. de Bordeaux	Directeur de thèse

© Simon Vallières 2020

For a better tomorrow to humankind.

"Love what you do and do what you love. Don't
listen to anyone else who tells you not to do it."

— Ray Bradbury

Résumé

Les accélérateurs de particules attirent beaucoup d'attention en raison de leur nombreuses applications dans des domaines allant des sciences fondamentales, à la médecine jusqu'aux applications industrielles. Ces travaux de doctorat se situent au premier plan du développement des sources d'ions générées par laser, afin de les rendre plus compétitives face aux accélérateurs conventionnels. Pour ce faire, les sources d'ions obtenues par laser doivent être compactes, efficaces par rapport aux coûts, fiables, intenses et opérées à des taux de répétition élevés. L'effort général de ces travaux de doctorat vise à pousser leur performance sur trois fronts, soit l'alignement précis des cibles, l'amélioration des cibles à l'aide de nanostructures ainsi que le développement de détecteurs de particules efficients. Cette quête d'efficacité accrue a requis des travaux autant numériques, par l'utilisation de calcul de haute performance, qu'expérimentaux, par le montage d'une ligne d'accélération d'ions de pointe sur les installations de l'Advanced Laser Light Source (ALLS) 100 TW ainsi qu'en effectuant plusieurs campagnes expérimentales à l'étranger.

Les travaux visent d'abord à augmenter la fiabilité des faisceaux d'ions par le positionnement précis des cibles solides utilisées en accélération d'ions par laser. Pour ce faire, un interféromètre de positionnement des cibles (Target Positioning Interferometer, TPI), atteignant une précision d'alignement sous-micrométrique, a été développé. Le design novateur du TPI est un interféromètre de Michelson modifié dans lequel nous avons introduit une lentille convergente asphérique dans le bras de la cible, afin de le transformer en un système de positionnement absolu ayant un unique point d'inambiguïté dans l'espace. La fine capacité d'alignement du TPI est atteinte également avec l'aide d'un algorithme numérique d'analyse des franges d'interférences qui maximise l'extraction de signaux à grand rapport signal-sur-bruit, effectuée dans une fenêtre de temps optimisée.

La deuxième partie des travaux concerne le rehaussement du mécanisme d'accélération, permettant de générer de plus grandes quantités d'ions à des plus hautes énergies cinétiques, menant à des faisceaux d'ions plus intenses. Les cibles solides typiquement utilisées sont des feuilles métalliques minces, limitant l'efficacité de conversion d'énergie du laser aux ions à quelques pourcents tout au plus. Une façon d'augmenter cette efficacité de conversion est en nanostructurant la surface des cibles afin d'emprisonner l'onde incidente, augmentant ainsi le transfert d'énergie aux ions. Nous avons démontré, de façon théorique et expérimentale, qu'un ajustement optimal des paramètres géométriques des nanostructures, en particulier avec des nanosphères et des nanofils, mène à une augmentation du nombre d'ions et de leur énergies cinétiques de plusieurs fois les valeurs obtenues avec le même pulse laser incident sur une cible plane faite du même matériau.

Dans la dernière partie, les travaux sont orientés sur le développement de détecteurs de particules efficients afin d'être implémentés sur les lignes d'accélération d'ions à haut taux de répétition. Une calibration en nombre absolu des nouveaux films radiochromiques EBT-XD a

d'abord été effectuée. Il a été observé que les EBT-XD offrent une plus grande plage de mesure de dose ainsi qu'un seuil minimum d'énergie de détection plus élevé que leur homologue EBT3, étant donc mieux adaptés pour les lignes d'ions plus intenses. Nous avons également mesuré une sévère inhibition de la réponse des EBT-XD lorsque le pic de Bragg de la particule mesurée tombe directement dans la couche active des films, causant des erreurs importantes dans l'estimation du nombre de particules. Finalement, nous avons implémenté, sur la ligne d'accélération d'ions d'ALLS 100 TW, un système de détecteurs de particules calibrés en croisés incluant un spectromètre à parabole Thomson (TP) ainsi que deux en temps de vol.

Abstract

Particle accelerators attract a lot of attention in the scientific and non-scientific community as a result of their wide applicability in fields ranging from fundamental sciences, medicine to industrial applications. This doctoral work stands at the forefront of laser-based ion accelerators, and pushes forward their development to make them more competitive ion sources compared to conventional particle accelerators. For achieving higher competitiveness, laser-driven ion sources must be compact, cost-effective, reliable, intense and operated at high repetition-rates, which all together yield ion beam characteristics that cannot be realistically matched by any other kind of ion accelerator. To do so, the general effort of this doctoral work tackled three different aspects of laser-based ion acceleration, namely precise target alignment, improved targetry using nanostructures and the development of efficient particle diagnostics. The endeavor required to perform equivalent amounts of numerical work, through simulations using High-Performance Computing, as well as experimental work, by implementing a cutting-edge ion beamline at the Advanced Laser Light Source (ALLS) 100 TW facility and to carry out several experimental campaigns abroad.

The first part of the work aims at improving the reliability of ion beams through the precise positioning of solid targets used in laser-driven ion acceleration. For this purpose, a Target Positioning Interferometer (TPI) that reaches subwavelength positioning precision was developed. The TPI's novel design is a modified Michelson interferometer that incorporates an aspherical converging lens in the target arm to transform it from a relative to an absolute positioning device, having a single unambiguity point in space. The high positioning accuracy is also achieved by a numerical fringe analysis algorithm that maximizes the extraction of signals with high signal-to-noise ratio, in an optimized timeframe. The development of a fast algorithm is crucial to make the TPI a viable solution for its implementation in a laser-based ion accelerator.

The second part of the work is focused on enhancing the acceleration mechanism to generate higher ion numbers and kinetic energies, leading to more intense ion bunches. The solid targets used are typically flat metallic targets which allow for less than 10% of laser energy absorption, thereby limiting the laser-to-ion conversion efficiency to a few percent. A way to increase this conversion efficiency is by using target surface nanostructuration to trap the incoming laser pulse, ultimately leading to a greater energy transfer to the ions. I have shown, both theoretically and experimentally, that a careful optimization of a nanostructure's geometrical parameters, in particular for nanospheres and nanowires, leads to multiple-fold enhancements of ion numbers and kinetic energies, compared to the use of the same laser pulse incident on flat targets of the same material.

The final part of the work is dedicated to the development of efficient particle diagnostics suitable for being implemented on high repetition-rate laser-based ion beamlines. I first performed the absolute number calibration of the new EBT-XD type of radiochromic films (RCF). The EBT-XD exhibit larger dose detection range and higher minimum energy threshold compared to their EBT3 counterpart, hence more suitable for intense ion beamlines. A severe response quenching was remarked when the Bragg peak of the measured particle falls directly within the active layer of the RCF, causing significant particle number misestimation errors. Finally, I have developed a Thomson Parabola (TP) and Time-of-Flight cross-calibrated set of particle diagnostics that were incorporated on the ALLS 100 TW ion beamline. The TP spectrometer uses a microchannel plate (MCP) detector that was calibrated from single proton impacts to reconstruct the response function of the MCP detection system.

Remerciements

I would first like to acknowledge the Jury members of this thesis, Tammy Ma, Magdalena Bazalova-Carter, Victor Malka and François Légaré, for carefully reading the manuscript and actively participating to a rigorous evaluation.

Il m'est absolument indispensable de remercier chaleureusement mes deux directeurs de thèse, Patrizio Antici et Emmanuel d'Humières. Quel tandem vous faites, des compétences et personnalités si différentes, mais ô combien complémentaires. Vous avez été des piliers de mon apprentissage, de ma façon de travailler et de voir les choses aujourd'hui. Je pense sincèrement que cela va au-delà de m'avoir appris les rouages de la recherche scientifique, vous m'avez également appris, chacun à votre façon, comment devenir une meilleure personne et je vous en remercie. Patrizio, quelle aventure nous avons parcourue ensemble depuis notre petite rencontre conviviale dans une salle du centre UCS. J'ose croire que tous les deux ce jour-là nous n'avions aucune idée à quel genre de personne nous avions affaire l'un en face de l'autre. J'ai découvert une personne avec un esprit vif, qui en mène pas mal large avec tes implications partout dans le monde. En fait, je n'ai jamais compris comment tu faisais et ça m'a toujours impressionné. Tu m'as également amené à un autre niveau de travail acharné, surtout lors des manips. Tu m'as montré que le vrai travail commence lorsque ton setup marche, peu importe combien d'énergie humaine ça prendra pour que ça marche. Manu, merci d'avoir accepté d'être ma porte d'entrée à Bordeaux. Établir cette cotutelle a été, sans l'ombre d'un doute, une des meilleures décisions que j'ai prises dans ma vie. Je dois admettre qu'à chaque fois que j'ai un échange avec toi, que ce soit pour la science ou non, j'en sors grandi et gonflé à bloc. Ton enthousiasme indestructible envers la physique, ta constante bonne humeur, rien ne semble t'effrayer et j'ai beaucoup appris de ça. Tu m'as toujours impressionné par la finesse de tes commentaires sur mes travaux, alors que je te bombardais de trucs durant nos courtes rencontres. Merci, sincèrement.

Mes études à l'INRS m'ont permis de rencontrer des gens formidables, qui ont eu une influence considérable sur mon parcours. Sur cette note, je dois remercier en tout premier lieu Stéphane Payeur. En v'la un autre éternel enthousiaste qui n'a pas froid aux yeux. Je n'ai sincèrement jamais rencontré quelqu'un d'aussi à l'aise avec des setups expérimentaux aussi compliqués. Je suis choyé d'avoir pu bénéficier de tes précieux conseils et la qualité des travaux de cette thèse n'aurait jamais atteint ce niveau sans ton inestimable support. Ensuite, mes remerciements les plus chaleureux vont à Léonard Pelletier, Joël Maltais et Guy Lebrun. Vous avez été des ressources techniques absolument indispensables, je n'ose même pas penser de quoi auraient eu l'air mes montages sans votre contribution. Vous êtes l'essence même du bon roulement de la recherche et trop peu de gens le comprennent vraiment. Merci à Sylvain Fourmaux pour m'avoir épaulé au labo et pour les nombreuses discussions parfois très techniques. Tu as un

savoir qui vaut de l'or et je me considère privilégié que tu aies voulu le partager avec moi. Un gros merci également à Antoine Laramé et Philippe Lassonde, pour les précieux conseils et les nombreuses pièces que je vous ai emprunté, parfois à plus long terme que prévu.

Thanks to the iPAT-LAB members, for the different scientific endeavors undertaken together. The first set of thanks goes to the Italian brigade, Marianna Barberio, Massimiliano Sciciò and Simona Veltri. I was really proud to say that I was the only Québécois in an Italian group when it was the case, what a treat that was to learn the rudiments of the Italian language. Massi, I will forever remember that moment in the LULI campaign, when we were so exhausted after 3 weeks of excessive work that English suddenly disappeared as the main conversing language, and we both fiercely swore after our setup problems in our respective mother tongues... But, we understood the other person so clearly thereafter. Then, I must sincerely acknowledge Pilar Puyuelo-Valdés, whom I owe several ones when I had, for instance, technical problems with my broken cellphone during some passages in Bordeaux. Thanks also for being such a great lab partner, I will remember for a long time the great duo we were making to mount that entire setup on ALLS, it was way worth all the headaches. Finally, thanks to a special friend made unexpectedly, Martina Salvadori. Teamworking with you was an enormous pleasure, we went through so many experimental storms together, and each time it felt like it could never fail because we knew we had the other person as mutual support.

Je dois également remercier les gens du CELIA. Merci à Xavier Ribeyre, pour les nombreuses discussions intéressantes à ton bureau ou à la machine à café. J'espère toujours être autant fasciné par la physique que toi plus tard, tu es vraiment un passionné, quelqu'un de très agréable et j'ai beaucoup de respect pour toi. Merci à Sam Beaulieu, qui m'a si chaleureusement montré comment ça se passe à Bordeaux : les meilleurs spots, quels coins habiter, le choix judicieux de s'acheter un vélo, et bien d'autres. Merci pour les nombreux conseils, tu es une personne d'un humanisme exceptionnel. Après, merci aux potes du B12 : Juju, quel hurluberlu ce mec, ta détermination à ne pas comprendre mes expressions québécoises m'a fait bien rire. Merci à Jojo le paquebot, Julien et Erwan, notre cohésion en tant que compatriotes de bureau était sensass, je m'en rappellerai longtemps. Merci également à mes autres potes du CELIA : Gabriele, Pedro, Alessandro, Stéphane, Léo, Quentin, Paul et Paul, vous avez rendu mon expérience au CELIA plus qu'agréable. Un merci particulier à Dimitri et Guilhem, étrangement c'était comme si ça faisait 15 ans que l'on se connaissait quand on s'est rencontré, déjà des vieux amis.

Un énorme merci également aux gens de l'accélérateur de l'Université de Montréal, avec qui j'ai pu mener à bien de nombreuses expériences : Louis Godbout, François Schiettekatte, Martin Chicoine, Sjoerd Roorda et Hugo Bouchard. Même si le Tandem Van de Graaff n'est plus très jeune, c'est impressionnant à quel point il est encore utile. Mes expériences passées avec

vous (4) ne constituent pas moins du tiers de cette thèse. Merci vraiment pour votre accueil toujours chaleureux dans les installations.

A set of thanks goes to my international friends made at JUAS: Markus, Alexander, Micol, Hélène, Nicolas, Rakesh, Marie and Alexandre. I never expected to participate to an accelerator school during this thesis, I expected even less to go out of it with a precious group of new European friends like you guys. Special thanks go to my mobile home partners, Jonas and Thomas, our (really tasty) dinners discussing particle acceleration and life in general were quite memorable. Jonas, I thought the Viking era was ended, but you proved me the exact opposite. You are a true Viking of science, and I hope we can exchange further in Denmark or Québec someday.

Ensuite, un gros merci à mes vieux chums, Phil, Christo et Lil. Votre amitié inconditionnelle me fait un énorme bien à l'âme, merci de réussir à me changer les idées aussi bien que vous le faites. Évidemment, merci aux Ehrenboys : Melik, Guy, Franky, Tony, Hamza, Pinto, Chuck, Jacob, Duke, Xave, John et Ford. Vous êtes des malades et je me considère extrêmement choyé d'avoir des chums aussi précieux que vous. Je pense que bien des gens rêvent d'une telle cohésion de groupe et vous êtes tous des personnes plus fascinantes les unes que les autres. Merci également aux chums de McGill : Mik, Marc, Gab, Fern et, plus récemment, Tanner, c'est toujours agréable de partager des moments avec vous.

Finalement, mes remerciements ultimes vont à ma famille, Julie, Joannie, Martin, Sophie et Luc, ainsi qu'à leur conjointes et conjoints. Vous avez su m'encourager dans les moments les plus difficiles, je vous en suis éternellement reconnaissant. Un merci particulier à ma mère, Suzanne, qui me supporte de près dans mes aventures scientifiques depuis le tout début, tout jeune. Merci sincèrement de m'avoir laissé autant de liberté dans mes choix, ainsi que de m'avoir toujours aidé à devenir la meilleure version de moi-même.

Merci, Thanks, Grazie, Gracias, Tak, Danke.

Table of Contents

List of Figures

Préface

0.1 Sources de rayonnements

Les rayonnements sont omniprésents, nous y sommes exposés partout, à tout moment. Les rayonnements sont des particules voyageant avec une certaine énergie qui collisionnent et interagissent avec la matière, causant des dommages ou non. Il existe deux grandes classes de rayonnements, *non-ionisants* et *ionisants*. D'une part, les rayonnements *non-ionisants* ne peuvent pas ioniser la matière puisque que leur énergie cinétique est inférieure au potentiel d'ionisation des atomes et des molécules avec lesquels ils interagissent, les rendant incapables d'éjecter un électron d'une orbitale et de perturber la structure de la matière. En général, les rayonnements non-ionisants réfèrent aux ondes électromagnétiques telles que les ondes radio, les micro-ondes, les rayonnements infrarouges, la lumière visible jusqu'au rayonnement dans le proche ultraviolet (*i.e.* les photons non-ionisants). Ils sont utilisés dans des technologies comme la radio AM/FM, les fours à micro-ondes, le Wi-Fi, le Bluetooth, les systèmes de géo-localisations (GPS), les stations de télévision, les téléphones cellulaires, les ouvre-portes de garage, *etc*. D'autre part, les rayonnements *ionisants* ont la capacité d'éjecter un électron d'une orbitale d'un atome puisque leur énergie cinétique dépasse le potentiel d'ionisation de l'absorbeur, causant par le fait même un déséquilibre de charge et perturbe son environnement. Nous sommes constamment frappés par des rayonnements ionisants : le rayonnement de fond naturel provenant du sol (en particulier par le Radon gazeux), les rayons cosmiques qui traversent l'atmosphère, les isotopes radioactifs dans la nourriture que l'on ingère (par exemple la teneur élevée en potassium-40 dans les bananes ou le carbone-14 dans les viandes et légumes), l'eau que l'on boit, l'air que l'on respire et les sources produites par les humains (les tomodensitomètres, les radiographies, la production de radioisotopes, les centrales nucléaires, les

détecteurs de fumée, les signes de *sortie*, *etc*.). Bien comprendre la nature ainsi qu'utiliser correctement les rayonnements ont révolutionné l'humanité depuis un peu plus de 100 ans déjà et devrait également continuer d'être au sommet des intérêts de l'humain pour au moins les quelques centaines d'années à venir.

Types de rayonnements ionisants

Les rayonnements ionisants peuvent être subdivisés en deux parties dépendamment de leur mode d'interaction, étant soit *directement* (particules chargées) ou *indirectement* (particules neutres) ionisants. Les rayonnements *directement* ionisants (électrons, pions, protons, particules alpha ou les ions lourds par exemple) déposent leur énergie par des interactions de Coulomb entre eux et un électron d'une ortbiale d'un atome de la matière. Les rayonnements *indirectement* ionisants, quant à eux, déposent leur énergie par un processus à deux étapes, d'abord en étant absorbés par un atome, ce qui provoque l'éjection d'une particule chargée par l'interaction, suivi par un dépôt d'énergie de cette particule chargée dans la matière. Un sommaire de la classification des types de rayonnements ionisants est présenté à la Figure 0.1.

Déposition d'énergie dans la matière par les rayonnements ionisants

Dépendamment de la nature de la particule, les rayonnements ionisants déposent leur énergie dans la matière par des processus variés. Il en résulte une multitude d'interactions différentes, donc également de profils de dépôt de dose, lors de leur propagation dans la matière. Un résumé des principaux profils de dépôt de dose pour les rayons X, les électrons, les neutrons et les ions lourds est présenté à la Figure 0.2. Les photons de haute énergie (rayons X) sont d'une importance particulière et sont présentés à la Figure 0.2.a, pour des énergies allant du keV (rayons X mous) au MeV (rayons X durs). Il est d'abord important de noter que les photons sont des particules sans masse et donc ne déposent pas de dose directement, mais sont plutôt atténués, c'est-à-dire absorbés avec une certaine probabilité en fonction de la profondeur. Cette caractéristique les rend très pénétrants dans la matière, particulièrement pour les hautes énergies (MeV). Autrement dit, il existe toujours une probabilité non-nulle de trouver un photon à une profondeur infinie dans un matériau. C'est une des raisons pour lesquelles les photons avec des énergies dans les MeV sont utilisés en radiothérapie pour traiter les tumeurs situées profondément dans le corps, comme dans la prostate ou les poumons par exemple.

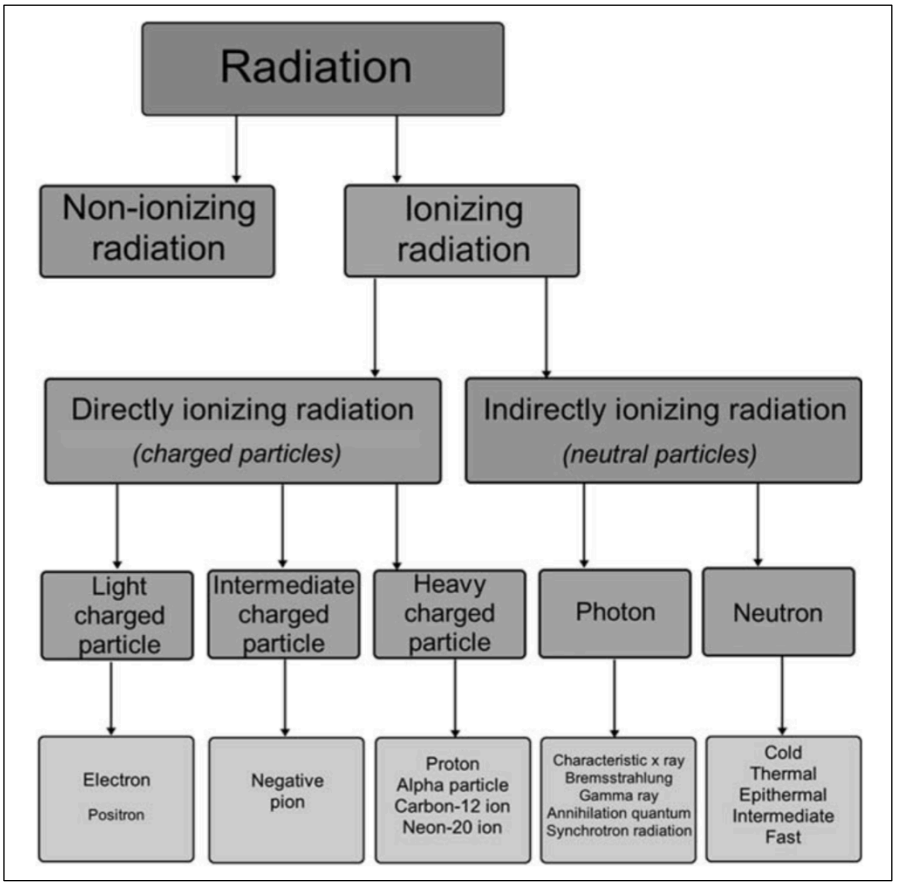

FIGURE 0.1: Classification des types de rayonnements ionisants. Cette figure est extraite et adaptée de E. B. Podgoršak, "Radiation Physics for Medical Physicists", 2^{e} édition, *Springer*, (2010).

Cette particularité les différencie aux photons d'énergie de l'ordre du keV, ces derniers étant plutôt utilisés pour traiter les cancers de la peau, puisque la très grande majorité de leur atténuation a lieu dans les tissus situés en surface. Comme on peut le voir sur la Figure 0.2.c, les neutrons sont également très pénétrants puisqu'ils interagissent très peu avec la matière, dû au fait qu'ils ne déposent pas leur énergie par des interactions de coulombiennes comme les particules massiques chargées. Concernant les particules chargées légères, il est possible de voir sur la Figure 0.2.b qu'elles ont un profil de dose peu profond, ce qui est particulièrement intéressant pour sonder ou irradier la matière en surface. Cependant, elles effectuent une très grande quantité d'évènements de diffusion, en raison de leur faible masse, produisant des dépôts de dose aux marges très diffuses. Finalement, contrairement aux particules chargées légères, les particules chargées lourdes dévient très peu de leur orientation initiale (faible diffusion menant à une trajectoire plus rectilinéaire) lors de leur propagation dans la matière, en raison de leur plus grande masse. Leur profil de déposition de dose contient ce qui est

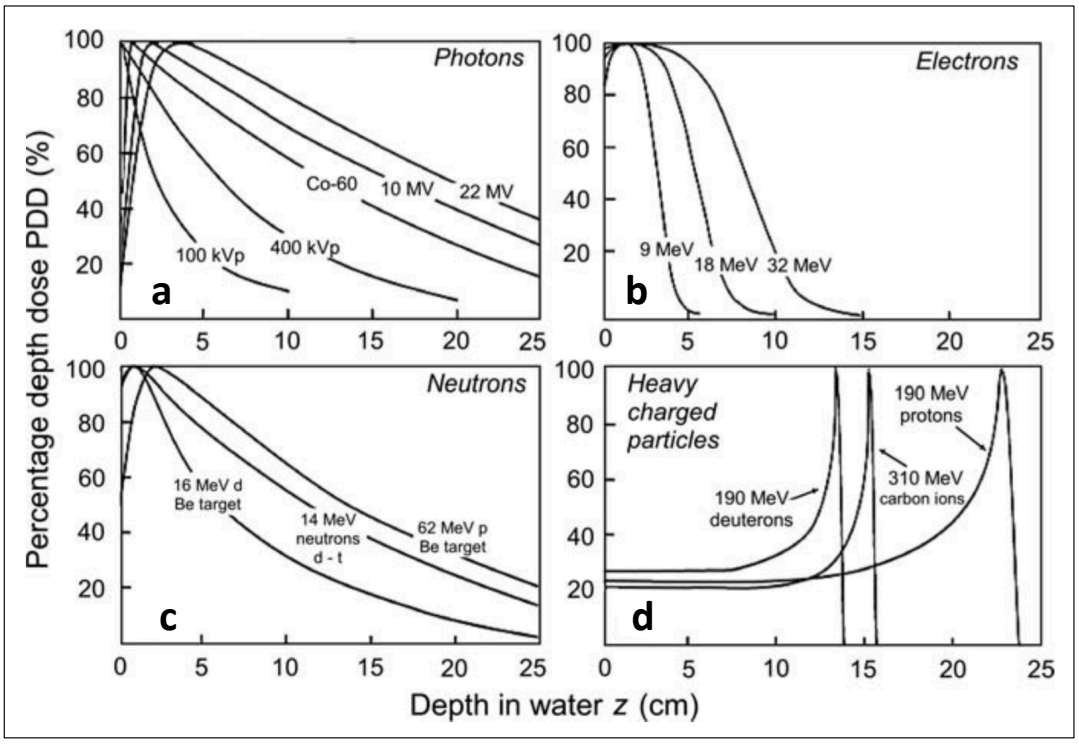

FIGURE 0.2: Principaux profils de déposition de dose en fonction de la profondeur pour différents types de rayonnements ionisants comme (a) les rayons X (b) les électrons, (c) les neutrons et (d) les ions lourds. Cette figure est extraite et adaptée de E. B. Podgoršak, "Radiation Physics for Medical Physicists", 2^{e} édition, *Springer*, (2010).

communément appelé un *pic de Bragg* (voir Figure 0.2.d), c'est-à-dire un taux de déposition d'énergie très abrupte ayant lieu sur une très courte distance, suivi d'une zone de dose nulle après le pic, puisque la particule est complètement arrêtée. Il en est de même pour les particules chargées légères, cependant celles-ci génèrent beaucoup plus de rayons X secondaires produits par *Bremsstrahlung* (littéralement *rayonnement de freinage* en Allemand) lors de leur dépôt d'énergie, produisant ainsi une «queue de dose» non-négligeable sur de grandes profondeurs due à la caractéristique très pénétrante des photons de haute énergie. Cette caractéristique particulière, qu'est le pic de Bragg, a engendré une industrie de plusieurs milliards de dollars à travers le monde appelée *thérapie par hadrons*, le type le plus largement commercialisé étant la proton-thérapie. L'hadronthérapie consiste à effectuer de la radiothérapie de tumeurs avec des ions, en bénéficiant du pic de Bragg en irradiant fortement une tumeur placée à une profondeur qui correspond à la position du pic. Cela résulte en une très forte déposition d'énergie dans la tumeur en épargnant mieux les tissus sains environnants comparativement à la radiothérapie conventionnelle avec des faisceaux de rayons X.

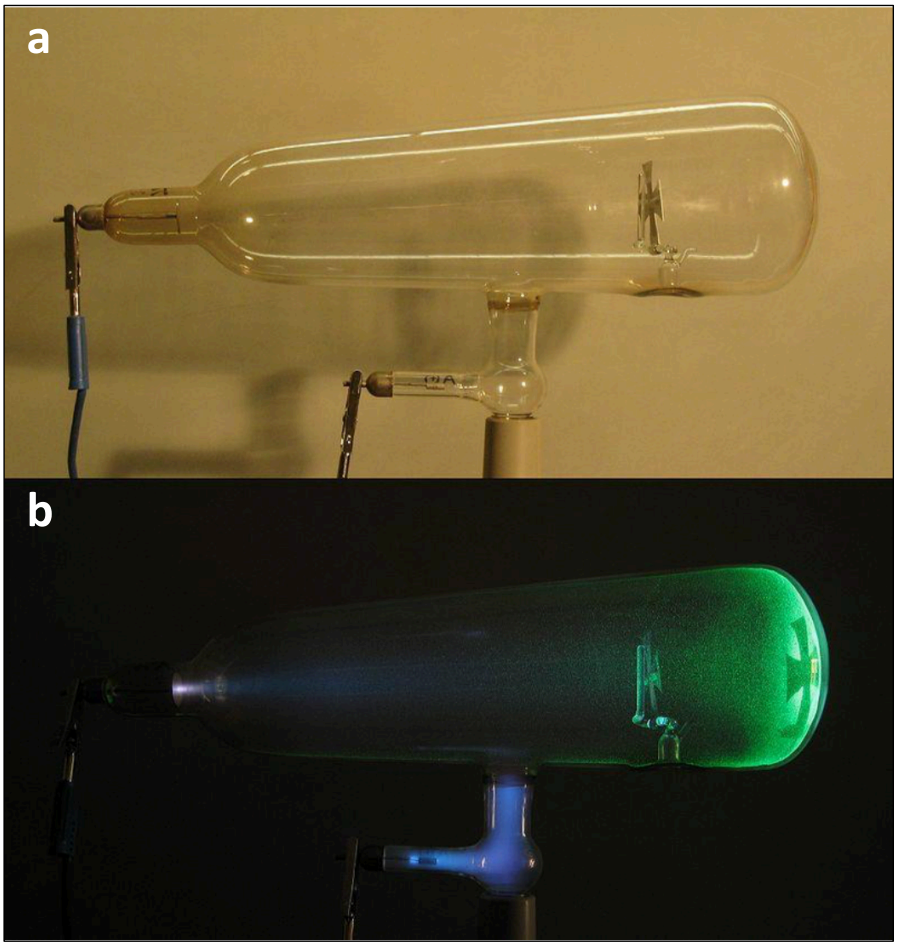

FIGURE 0.3: Tube de Crookes : un faisceau d'électrons accélérés sous vide partiel par une haute tension statique. (a) Hors tension (b) Sous-haute tension. Cette figure est extraite et adaptée de P. Lebrun, "Particle accelerators, instruments of discovery in physics", Lecture, *Joint Universities Accelerator School*, (2018).

Les accélérateurs de particules comme source de rayonnements ionisants

Pour tous les types de rayonnements ionisants susmentionnés, la source de ces rayonnements implique d'accélérer des particules à un certain point pour générer la source elle-même, ce qui a engendré et soutenu le développement d'accélérateurs de particules au fil des ans. Ce grand périple vers l'accélération de particules a débuté avec l'invention du tube de Crookes par William Crookes en 1869, dont un exemple est montré à la Figure 0.3. En appliquant une forte tension électrique entre une anode et une cathode placées sous vide, cela génère ce qui était appelé des «rayons cathodiques» (c'est-à-dire un faisceau d'électrons accélérés, phénomène

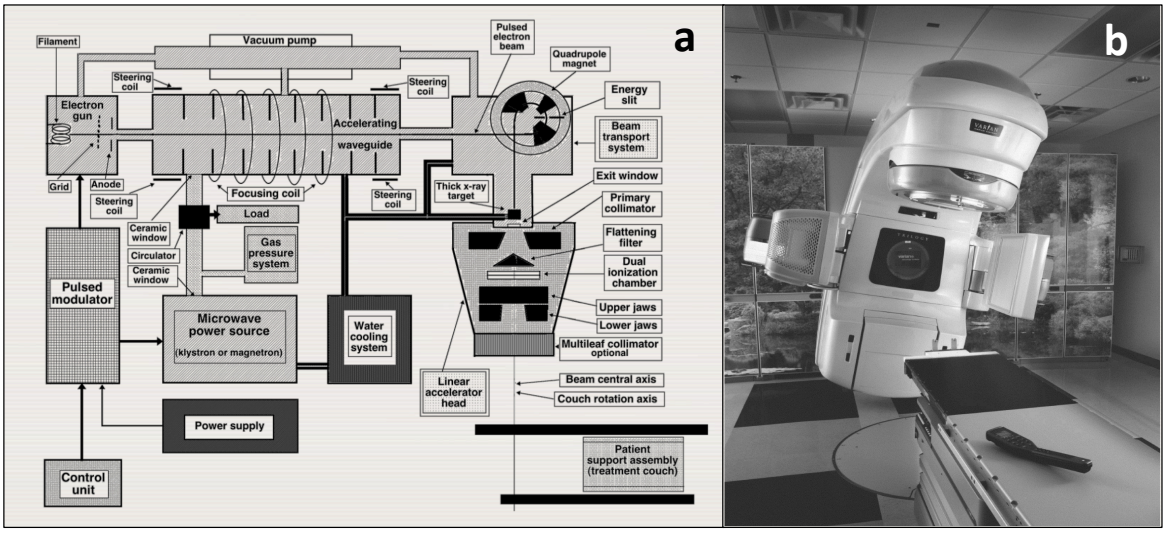

FIGURE 0.4: Accélérateur linéaire (linac) médical utilisé pour l'irradiation de tumeurs en radiothérapie. (a) Diagramme schématique d'un linac médical. (b) Linac médical de la compagnie *Varian Medical Systems*. Cette figure est extraite et adaptée de E. B. Podgoršak, "Radiation Oncology Physics: A Handbook for Teachers and Students", Lecture, *IAEA*, (2006).

FIGURE 0.5: Vue aérienne du Grand Collisionneur de Hadrons (LHC) au CERN à Genève en Suisse. Crédit photo: CERN, extraite de https://phys.org/news/2019-01-cern-vision-next-generation-particle-collider.html.

inconnu à l'époque), utilisés pour imager l'ombre d'un objet placé devant un écran phosphorescent. Le même type de tube a été utilisé ensuite par Wilhelm C. Röntgen pour la découverte des rayons X en 1895. Dès lors, une série d'étapes cruciales pour notre compréhension de la Nature a eu lieu en impliquant des accélérateurs de particules telles que la découverte de l'électron (Joseph J. Thomson, 1897), la découverte du proton (Ernest Rutherford, 1919), l'invention de la cavité accélératrice à base de radiofréquences (Rolf Wideröe, 1928), la découverte du neutron (James Chadwick, 1932), le premier bris d'un noyau atomique (John D. Cockcroft and Ernest T. S. Walton, 1932), pour n'en nommer que quelques-uns. De nos jours, les accélérateurs de particules ont excessivement évolué et sont devenus des dispositifs très sophistiqués utilisés partout dans le monde. Ceux-ci vont d'un format commercial très compact comme les accélérateurs linéaires (linacs) médicaux servant au traitement des tumeurs en radiothérapie (voir Figure 0.4) à des machines énormes telles que le Large Hadron Collider (LHC, voir Figure 0.5) qui nous permettent d'étudier les propriétés fondamentales de la Nature. Voici une liste non-exhaustive des applications des accélérateurs de particules regroupées dans différents domaines.

- Médical : radiothérapie, imagerie médicale, production de radioisotope.
- Industriel : implantation d'ions, analyse par faisceaux d'ions, traitement de matériaux, stérilisation.
- Securité : contrôle du fret, banc d'essai hydrodynamique.
- Sources de lumière synchrotron et lasers à électrons libres : biologie, médecine, science des matériaux.
- Diffusion de neutrons : science de matériaux.
- Énergie de fusion: chauffage par faisceaux d'ions, fusion inertielle par ions lourds, science des matériaux.
- Énergie de fission : brûlage de déchets thermonucléaires, amplificateur de carburant au thorium.
- Énergie par bio-carburant : production de bio-carburant.
- Environnement : traitement des eaux, traitements des gaz/fumée.
- Patrimoine culturel : analyse/datation non-destructive d'oeuvres d'art et d'artéfacts.

0.2 Les lasers de haute puissance crête

L'invention du laser par Theodore H. Maiman en 1960 avec un cristal de rubis, basée sur les travaux théoriques de Charles H. Townes et Arthur L. Schawlow, a révolutionné le monde moderne que l'on connait aujourd'hui. Les lasers sont omniprésents dans notre vie de tous les jours, s'étalant en taille de simples diodes-laser au laser le plus énergétique au monde situé au National Ignition Facility (NIF) à Livermore, CA aux États-Unis. Entre ces deux extrêmes, il existe une panoplie de domaines d'applications tels que l'usinage industriel, les télécommunications, la microscopie, la spectroscopie, la science des matériaux, l'astronomie, le domaine militaire, la chirurgie, pour n'en nommer que quelques-uns. Ces applications ont été possibles au fil du temps grâce à l'escalade continuelle des intensités laser par le biais de plusieurs innovations techniques telles que la *commutation-Q*, le *blocage de modes* et finalement par ce qui est considéré comme la deuxième révolution dans le domaine des lasers, la technique d'amplification par dérive de fréquences (CPA), développée par Gérard Mourou et Donna Strickland en 1985 (prix Nobel de physique 2018). Cette montée des intensités laser est présentée à la Figure 0.6. L'avènement de la technique CPA, et par le fait même des lasers de classe TW (10^{12} W), a ouvert de nouveaux horizons dans plusieurs champs d'applications comme la chirurgie de l'oeil par exemple, tout en permettant d'atteindre des intensités suffisamment élevées pour arracher les électrons de valence et de coeur de atomes et des molécules ($I_0 \sim 10^{15} - 10^{17}$ W/cm^2), ainsi que d'ouvrir une nouvelle classe de problèmes inexplorés en physique de l'optique relativiste ($I_0 > 10^{18}$ W/cm^2). Pris indépendamment, les photons visibles et infrarouges utilisés dans la plupart des lasers sont considérés comme des rayonnements non-ionisants. Cependant, lorsque l'on focalise un faisceau laser à une intensité suffisamment élevée, des phénomènes d'absorption photons multiples peuvent avoir lieu, permettant du même coup des évènements d'ionisation avec des photons dans le visible-infrarouge. En augmentant davantage l'intensité laser, le champ électrique de l'onde électromagnétique devient si fort qu'il perturbe le champ de Coulomb autour d'un noyau atomique, permettant ainsi d'éjecter des électrons par ionisation tunnel ou en s'échappant directement si le champ électrique est suffisamment intense. Aujourd'hui avec l'arrivée des lasers de classe PW (10^{15} W), nous sommes à l'aube d'ouvrir une nouvelle frontière en physique dans le champ de recherche de l'optique ultra-relativiste, un domaine qui permettra l'étude de phénomènes d'électrodynamique quantique (QED) en champs forts. Ces phénomènes constituent une classe d'évènements prédits par la théorie

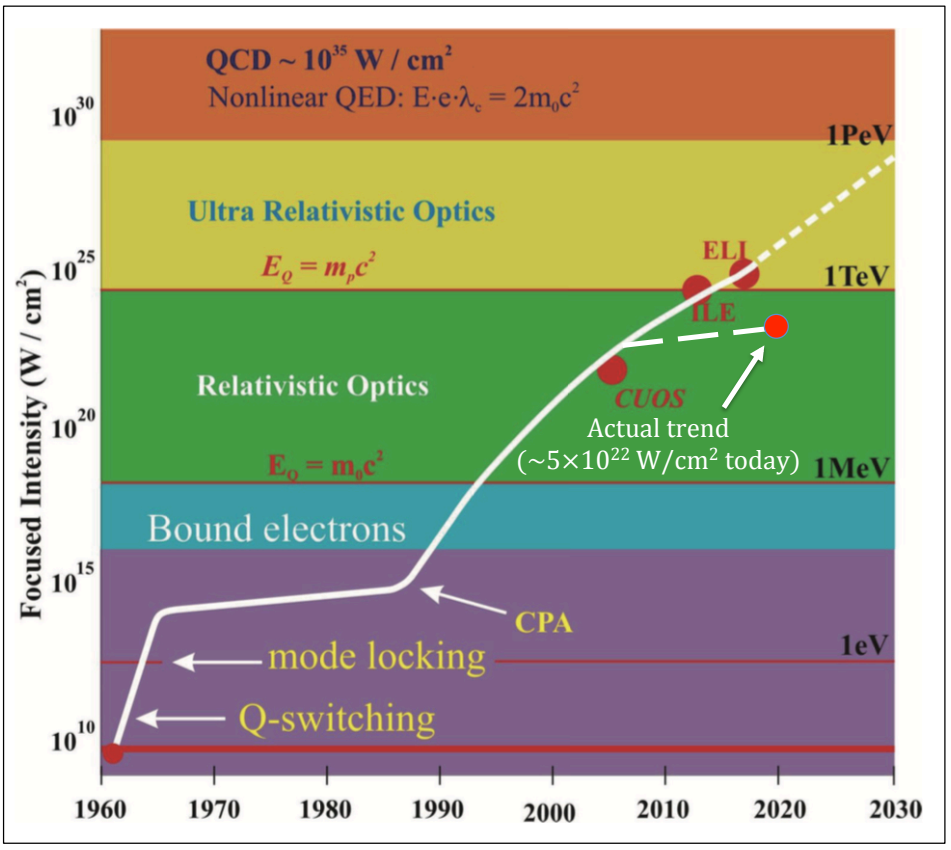

FIGURE 0.6: La montée des intensités laser depuis son invention en 1960. Cette figure est extraite et adaptée de G. A. Mourou, T. Tajima & S. V. Bulanov, "Optics in the relativistic regime", *Rev. Mod. Phys.*, vol. 78, 309-371 (2006).

quantique des champs (QFT), mais qui n'ont jamais été mesurés expérimentalement à ce jour, notamment en raison des ultra-hautes intensités requises ($I_0 > 10^{23}$ W/cm^2) pour activer ce genre de phénomènes.

0.3 Rayonnements ionisants générés par laser

Lorsque l'intensité du laser est supérieure au seuil relativiste des électrons ($I_0 > 10^{18}$ W/cm^2 pour une longueur d'onde de 1 micron), les atomes sont très facilement ionisés par le champ électromagnétique, mais les électrons effectuent également des trajectoires inhabituelles puisqu'ils oscillent dans le champ laser à des vitesses s'approchant de la vitesse de la lumière, rendant les effets relativistes très importants. Cela permet l'activation de nouveaux processus d'absorption dans les cibles solides et gazeuses. La forte séparation de charge induite par les laser intenses à impulsion très courte (fs-ps), conjointement avec les champs électriques très

élevés que peuvent supporter les plasmas, rend possible l'accélération de particules par laser. En effet, les accélérateurs conventionnels sont limités à des champs électriques de l'ordre de 100 MV/m tout au plus, afin d'éviter le claquage de la cavité accélératrice. Cependant, les plasmas peuvent supporter des champs électriques de l'ordre du TV/m, c'est-à-dire au moins quatre ordres de grandeur plus élevés, ce qui permet d'atteindre des énergies équivalentes ou supérieures à celles obtenues avec des accélérateurs conventionnels dans un format très compact, réduisant ainsi les coûts de fabrication. L'idée originale fut amenée par Toshiki Tajima et John M. Dawson en 1979, à un moment opportun par rapport à l'avènement de la technique CPA six ans plus tard. La conjonction de ces deux évènements engendrera par la suite le développement des accélérateurs d'électrons et d'ions par laser.

Accélération d'électrons et sources de rayons X

L'accélération d'électrons par laser peut se faire selon différents mécanismes d'accélération, le plus connu étant l'accélération par onde de sillage laser (Laser Wakefield Acceleration, LWFA). Ce mécanisme d'accélération a lieu lorsqu'un laser est focalisé à haute-intensité ($I_0 > 10^{18}$ W/cm^2) dans un gaz, ce qui cause une très forte séparation de charges suite au passage de l'impulsion laser et induit une onde plasma dans son sillage. Les champs électriques générés dans le sillage sont typiquement de l'ordre du GV/m jusqu'au TV/m. Si un paquet d'électrons entre dans l'onde plasma avec la bonne vitesse de phase, le paquet d'électrons se voit accéléré par le champ électrique orienté dans la direction de propagation du laser, d'une façon tout à fait équivalente à un surfeur qui glisse sur une vague en la prenant avec la bonne vitesse et au bon moment. Cela implique donc deux conditions nécessaires pour l'accélération de particules. Tout d'abord, il doit y avoir une composante du champ électrique dans la direction de propagation et ensuite, la vitesse de phase doit s'accorder avec celle de l'onde accélératrice pour l'obtention d'un transfert d'énergie optimal. De nos jours, les expériences typiques d'accélération d'électrons accélèrent des paquets d'électrons (nC) jusqu'à plusieurs GeV d'énergie avec une cellule gazeuse de l'ordre du centimètre. De toute évidence, cela réduit fortement la taille des accélérateurs d'électrons comparativement aux accélérateurs conventionnels requérant fréquemment plusieurs dizaines (voire des centaines) de mètres de longueurs pour atteindre des énergies équivalentes.

Le passage d'un pulse laser très court et de haute-intensité dans un gaz pousse les électrons hors de sa trajectoire sous l'action de la force pondéromotrice (discutée plus amplement dans

ce dissertation), laissant ainsi dans son sillage un canal d'ions positifs. Les électrons hautement relativistes, accélérés par une onde plasma à plusieurs centaines de MeV jusqu'au GeV, sont alors attirés en retour par le champ électrique provenant du canal d'ions positifs et oscillent autour de celui-ci tout en voyageant dans la direction de propagation du laser. Ces changements abruptes de direction durant les oscillations génèrent l'émission d'un faisceau de rayons X, tel que le requiert les équations de Maxwell, communément appelé rayonnement *betatron*. Ce faisceau de rayons X a une durée très courte (allant de quelques dizaines à quelques centaines de femtosecondes) tout en étant hautement cohérent spatialement et très directionnel, ce qui en fait une source int'eressante pour une variété d'applications comparativement aux sources de rayons X conventionnelles. Les qualités intrinsèques du faisceau de rayonnement betatron généré par laser compétitionnent avec celles des sources de lumière synchrotron, qui sont des accélérateurs circulaires de plusieurs centaines de mètres de circonférence, alors qu'une source de rayonnement betatron générée par laser requiert seulement quelques mètres d'espace, la rendant ainsi beaucoup moins coûteuse à produire.

Accélération d'ions et sources de neutrons

L'accélération d'ions par laser a lieu lorsque l'on focalise un faisceau laser de haute intensité ($I_0 > 10^{18}$ W/cm^2) sur une cible, produisant alors une très importante séparation de charges qui établit un fort champ électrique accélérateur dans le plasma généré par laser. D'autres mécanismes d'accélération impliquent également de pousser directement les ions par le biais du très fort champ électrique de l'onde laser elle-même. L'accélération d'ions par laser s'effectue typiquement à l'aide de deux types de cible d'interaction distinctes : les jets de gaz et les cibles solides. Le plus grand avantage des jets de gaz est dû au rafraîchissement continuel de la cible avec un flux de gaz approprié, permettant la possibilité d'obtenir des interactions laser-matière de haute-intensité opérant à des taux de répétition de plusieurs dizaines de Hz (voir kHz), générant ainsi des flux de particules très élevés. Le désavantage majeur des cibles gazeuses concerne les plus faibles énergies cinétiques des ions accélérés, comparativement à l'utilisation de cibles solides. En effet, les cibles solides peuvent maintenir des gradients de densité plus abruptes permettant d'obtenir des champs accélérateurs très élevés en raison de la plus forte séparation de charges induite par l'interaction laser-matière avec la cible. Cette dernière étant complètement évaporée localement des suites de l'interaction, la nécessité d'un système efficace de rafraîchissement des cibles solides est inévitable, amenant de grands défis

techniques pour obtenir un taux de rafraîchissement des cibles atteignant le taux de répétition du laser. Au moment d'écrire ces lignes, le record des énergies cinétiques atteintes en accélération d'ions par laser est autour de 100 MeV par nucléon. Quatre types de mécanismes sont reconnus pour accélérer efficacement les ions avec impulsions laser de haute intensité et de courte durée : «Target-Normal Sheath Acceleration» (TNSA), «Radiation Pressure Acceleration» (RPA), «Collisionless Shock Acceleration» (CSA) et les explosions coulombiennes. Les trois premiers schémas d'accélération seront discutés plus amplement dans ce dissertation. Le plus connu et le plus consolidé d'entre-eux est assurément le mécanisme TNSA, qui sera au centre des travaux de cette thèse.

Lorsqu'un faisceau d'ions irradie cible, composée de fluorure de lithium (LiF) par exemple, il est possible d'induire une réaction nucléaire de laquelle résulte l'émission d'un neutron, permettant alors d'obtenir une source de neutrons par laser. Plus précisément, la réaction ^{7}Li(p,n)^{7}Be est d'un intérêt particulier par sa section efficace élevée (c'est-à-dire une forte probabilité d'interaction) lors de l'utilisation d'un faisceau de protons de quelques dizaines de MeV, tel qu'obtenu de façon routinière par l'accélération de protons par laser avec des cibles solides en régime TNSA. Ce schéma spécifique de génération de neutrons par laser se nomme système «pitcher-catcher». Cette technique de génération de neutrons promet d'atteindre des records de brillance avec les nouvelles installations laser de très haute puissance en construction au moment présent (le laser Apollon ou les piliers ELI par exemple), obtenus en produisant de très haut flux de neutrons dans une impulsion excessivement courte (sous la nanoseconde).

0.4 Objectifs de la thèse

Tel que mentionné précédemment, ces travaux de thèse s'inscrivent dans le contexte de l'accélération d'ions par laser avec des cibles solides par le mécanisme TNSA. Ils ont été effectués dans un contexte de cotutelle Québec-France, et comprennent une partie expérimentale ainsi qu'une partie numérique pour l'optimisation des sources d'ions générés par laser. Les travaux principaux incluent cinq articles révisés par les pairs qui sont publiés ou acceptés dans des journaux scientifiques, dont je suis le premier auteur. Ils sont séparés en trois thèmes, chacun d'eux constituant un Chapitre de cette thèse : l'optimisation de l'alignement

des cibles solides (Chapitre 3, un article), le développement de détecteurs de particules efficients (Chapitre 4, deux articles) ainsi que l'amplification des interactions entre le laser et la cible (Chapitre 5, deux articles)

Développement d'un instrument d'alignement des cibles à précision sous-micrométrique

Le développement de sources de particules par laser ayant pris son essor à la fin de la décennie de 1990, beaucoup d'avancées expérimentales ont été effectuées depuis les trente dernières années. Cette essor a eu lieu à la suite de l'avènement des lasers de classe TW, rendus possibles par la technique du CPA. L'obtention d'un point focal très intense et d'une très grande qualité est, certes, le premier jalon à atteindre pour accélérer des particules par laser. Cependant, beaucoup de travail reste néanmoins à être accompli en particulier pour le rafraichissement des cibles d'interaction, autant solides que gazeuses. En effet, bien que ces dernières semblent être conceptuellement plus avantageuses pour le haut taux de répétition, plusieurs avancées sont à venir quant au développement des buses produisant des flux de gaz supersoniques permettant d'atteindre des densités gazeuses se rapprochant de la densité critique du laser (densité au-dessus de laquelle le laser ne peut plus se propager), de même que pour les gaz cryogéniques qui posent plusieurs défis d'ingénierie. Qui plus est, les énergies cinétiques des ions obtenus avec des cibles gazeuses sont typiquement plus basses que celles obtenues par des cibles solides minces, nécessitant alors des installations laser de plus grande envergure. Cela est également combiné à des fluences d'ions par tir plus basses en partie dues à la plus grande divergence des faisceaux. Concernant les cibles solides, certaines avancées restent à être accomplies concernant l'automatisation du rafraichissement des cibles, afin d'atteindre optimalement la fréquence de répétition du laser. Le simple fait d'augmenter la rapidité de rafraichissement d'une cible se fait au détriment de la précision du positionnement, ce qui réduit la répétabilité tir-à-tir de la source d'ions en raison de la courte longueur de Rayleigh du laser obtenue en forte focalisation. Le défi est donc d'implanter un système multi-cibles limitant le compromis entre la précision et la répétabilité, tout en offrant une fréquence de rafraichissement des cibles équivalente à la fréquence de répétition du laser. Ce défi fera l'objet du Chapitre 3 de cette thèse, visant d'abord à implémenter un interféromètre à haute précision pour le positionnement des cibles solides, puis en optimiser sa rapidité d'exécution et son automatisation.

Faits saillants du Chapitre 3 : Un interféromètre à haute précision pour le positionnement des cibles solides (appelé TPI ci-après) a été développé. Des mesures expérimentales ont démontré que le TPI peut effectuer un positionnement avec une incertitude jusqu'à 350 nm (2σ), en utilisant une lentille avec une ouverture numérique de 0.2. Ce résultat est également soutenu par des simulations numériques basées sur l'optique gaussienne, fournissant des lois d'échelle pour l'utilisation du TPI dans différentes conditions. D'autres étapes pour améliorer le système comprendront l'adaptation du TPI pour des cibles solides hautement absorbantes utilisées dans des expériences d'accélération d'ions par laser, telles que des cibles métalliques nanostructurées avec des nanofils ou des nanosphères. La nanostructuration de surface déforme intrinsèquement le front d'onde incident, ce qui à son tour produit une mesure très bruitée. La sensibilité du système doit donc être réglée suffisamment haute pour qu'il soit encore possible de positionner correctement la cible au point focal du laser, tout en faisant un compromis avec une plus grande incertitude. Lorsqu'il sera incorporé avec succès dans l'accélérateur, le TPI permettra d'augmenter la fiabilité des interactions laser-matière, fournissant ainsi des spectres de protons reproductibles. Enfin, bien que la précision du TPI soit plus que suffisante pour nos besoins, il serait tout de même possible d'augmenter encore sa précision de mesure en utilisant un objectif avec une ouverture numérique plus élevée, en faisant la moyenne sur plusieurs images, ainsi qu'en combinant avec des mesures interférométriques conventionnelles.

Implémentation de détecteurs de particules rapides et efficaces pour le haut taux de répétition

Le second grand défi qu'amènent les sources d'ions générées par laser est relié à la détection rapide et efficace des flux de particules produits, afin de diagnostiquer correctement le faisceau en temps réel. Étant donné la nature pulsée de l'interaction, les faisceaux de particules produits se propagent sous forme d'un regroupement de charges d'une durée variant entre quelques picosecondes à la source à quelques nanosecondes après quelques mètres de propagation. Ainsi, un très grand nombre de particules frappent presque simultanément le détecteur, ce qui peut induire de la saturation et de l'accumulation de charges, donc un diagnostic erroné du faisceau incident. Pour pallier à ce problème, les détecteurs plutôt analogiques comme les plaques photographiques, les films radiochromiques et les CR-39 ont longtemps été les détecteurs de référence dans le domaine, également en raison de leur résistance à la forte pollution électromagnétique engendrée lors de l'interaction laser-matière. De toute évidence, le désavantage

des détecteurs analogiques de ce type est leur incompatibilité avec le haut taux de répétition, nécessitant une remise à l'air de la chambre où ils se trouvent afin d'en numériser les données. Cela est suivi du renouvellement du détecteur dans la chambre pour ensuite effectuer un remise à vide et ce, pour chaque tir. La nécessité d'installer des diagnostics de particules permettant de numériser les données sans remise à l'air semble donc évidente, en plus de devoir offrir une bonne résistance à la pollution électromagnétique causée par l'interaction, d'avoir un niveau de saturation relativement élevé permettant de soutenir des flux de particules intenses et de permettre un haut taux de répétition. L'implémentation de ce type de diagnostics sur la ligne d'accélération d'ions avec le Advanced Laser Light Source (ALLS) 100 TW constituera le Chapitre 4 de cette thèse.

Faits saillants du Chapitre 4 : La première étude de ce Chapitre présente l'étalonnage expérimental de films radiochromiques EBT-XD avec des faisceaux de protons, pour les énergies cinétiques $\mathcal{E}_{K,0} = 4$, 7 et 10 MeV, effectué sur l'accélérateur 2×6 MV Tandem Van de Graaff de l'Université de Montréal. Une forte similarité a été observée entre les courbes d'étalonnage de 7 et 10 MeV, ainsi qu'une excellente correspondance avec l'étalonnage présent dans la littérature pour des protons de 148.2 MeV (<5% de différence de dose). Cependant, il est observé que la courbe détalonnage pour les protons de 4 MeV présente un effet d'inhibition sévère de sa réponse, dû à un pouvoir d'arrêt plus élevé à l'intérieur de la couche active. Les différences de dose entre les courbes de 4 MeV et 10 MeV atteignent jusqu'à 50%, d'où une dépendance en énergie non-négligeable des films. Pour pallier à ce problème, un modèle semi-empirique a été développé permettant de linéariser la dépendance en énergie. Il n'est pas recommandé d'utiliser ce modèle en-dessous de 3.6 MeV en raison de la forte non-linéarité causée par le pic de Bragg entrant dans la couche active. Cependant, la très bonne correspondance entre les courbes de 10 MeV et les autres étalonnages de la littérature (jusqu'à 148.2 MeV) suggère qu'il est possible d'utiliser les courbes de 10 MeV sans forte discordance dans l'évaluation de la dose.

La seconde étude du Chapitre présente la configuration la plus récente de la ligne d'accélération d'ions par laser sur ALLS 100 TW, utilisant des spectromètres à paraboles Thomson (TP) et en temps de vol (TOF) étalonnés en croisé pour le diagnostic des particules. La galette de microcanaux (MCP) utilisée comme détecteur dans le spectromètre à TP a été étalonnée en intensité, sur l'accélérateur 2×6 MV Tandem Van de Graaff de l'Université de Montréal, en utilisant des impacts de proton unique afin de mesurer la réponse du détecteur, permettant

ainsi de déterminer et comparer les nombres de particules observés dans la TP pour les protons et les ions de carbone. Les données expérimentales de la réponse ont été obtenues en effectuant une analyse par grappes de pixels des impacts de protons sur la MCP. Un modèle semi-empirique a été ajusté aux données afin d'en extrapoler l'étalonnage à des énergies cinétiques plus élevées ainsi qu'à d'autres espèces d'ions. Deux lignes TOF utilisant des détecteurs en diamant, placées à +6° et -9° par rapport à l'axe normal à la cible, ont été utilisées pour déterminer les intégrales de champs liées aux dispersions électriques et magnétiques du spectromètre à TP. Les deux lignes TOF permettent de vérifier l'alignement du faisceau d'ions à chaque tir ainsi que de caractériser la divergence du faisceau. Les diagnostics de particules utilisés sont compatibles avec le développement d'un système de rafraîchissement des cibles à taux de répétition élevé, contrairement à l'utilisation de films radiochromiques ou de plaques d'imagerie, constituant ainsi une étape cruciale dans l'automatisation de la ligne d'accélération d'ions prévue.

Amplification des interactions laser-matière relativistes avec des cibles nanostructurées

Le troisième grand défi que posent les sources d'ions générées par laser est relié à l'optimisation du transfert d'énergie du laser aux ions. En effet, l'obtention d'une très haute intensité laser supérieure au seuil relativiste des électrons (10^{18} W/cm^2) est essentielle pour activer les bons mécanismes d'accélération. Le positionnement répétable d'une cible au centre du point focal du laser est tout aussi indispensable. Cependant, il peut être difficile de justifier tous ces investissements si le transfert d'énergie du laser aux ions est inférieur à 1%, rendant le processus très inefficace. D'une part, les cibles gazeuses conventionnelles ont des densités électroniques sous-denses ($n_e \sim 10^{18} - 10^{20}$ cm^{-3}), c'est-à-dire inférieures à la densité critique d'un laser à 800 nm ($n_c \sim 10^{21}$ cm^{-3}), ce qui rend la cible plutôt transparente au passage du laser et donc non-optimale en termes de transfert d'énergie. Le défi dans cette situation est alors d'augmenter la densité de la cible gazeuse près de la densité critique dans le plan focal du laser afin de maximiser l'absorption d'énergie par les électrons, se traduisant ultimement par des énergies cinétiques plus élevées des ions et également par des flux de particules plus importants. Les tentatives les plus prometteuses dans cette avenue sont les jets de gaz supersoniques et les gaz cryogéniques. D'autre part, les cibles solides typiquement utilisées pour l'accélération d'ions sont des cibles métalliques ayant des densités électroniques sur-denses

($n_e \sim 10^{23}$ cm^{-3}), c'est-à-dire supérieures à la densité critique d'un laser à 800 nm, les rendant ainsi plutôt réfléchissantes au laser, comme on peut le voir directement à l'oeil nu avec les métaux. Ces derniers ont, en très grande majorité et en l'absence de pré-plasma, des coefficients de réflexion d'au moins 95% à 800 nm, ce qui impose déjà une borne supérieure de 5% au transfert d'énergie du laser aux particules chargées dans un cas idéal. En pratique, une partie de ce 5% est transmis au travers de la cible, une partie est conservée par les électrons qui accélèrent les ions, puis l'énergie est également distribuée sur plusieurs espèce d'ions, ce qui réduit typiquement le taux de conversion d'énergie du laser aux protons autour de 1% ou moins. L'objectif à atteindre dans cette situation est de profiter de cette haute réflectivité des métaux pour emprisonner l'onde électromagnétique dans une série de réflexions permettant de maximiser les interactions laser-matière, et donc d'augmenter le transfert d'énergie du laser aux électrons, puis de façon subséquente aux ions. Ce problème est donc purement géométrique, se faisant à l'aide de nanostructures métalliques de tailles comparables à la longueur d'onde du laser, et fera l'objet du Chapitre 5 de cette thèse.

Faits saillants du Chapitre 5 : La première étude du Chapitre a permis de démontrer que des cibles nanostructurées avec des nanoparticules (NP) métalliques ultra-petites permettent d'améliorer l'absorption d'énergie du laser, ainsi que d'augmenter l'énergie cinétique et le nombre de protons générés. De plus, nous avons étudié l'effet de la distance g entre les NP, montrant que ce paramètre a un effet d'amélioration plus important sur l'énergie maximale des protons que le diamètre des NP. Cette conclusion diffère des autres résultats publiés dans la littérature, où l'utilisation de NP de 10 nm devrait être d'une importance négligeable pour l'amélioration des faisceaux de protons. Nous montrons que les NP ultra-petites fournissent une amélioration significative de l'énergie des protons, en particulier en raison de ce fort effet d'espacement entre les NP.

La seconde étude du Chapitre est la première à présenter une étude systématique de l'amélioration des faisceaux de protons générés par laser apportée par les cibles avec nanofils, en fonction des paramètres géométriques pertinents (diamètre, espacement et longueur). L'étude démontre l'influence des nanofils sur les caractéristiques des spectres de protons (énergie maximale, température et nombre total) dans le régime TNSA, fournissant ainsi une compréhension plus générale de l'amélioration des faisceaux de protons générés par laser avec des cibles nanostructurées. Les résultats expérimentaux montrent des facteurs d'augmentation élevés pour les caractéristiques des spectres, en accord avec les simulations. Une optimisation

de la géométrie a également été réalisée par le biais de simulations PIC permettant de définir les meilleurs paramètres pour les caractéristiques du laser LLC, à Lund en Suède, où les expériences ont été effectuées. Une valeur d'espacement plus grande de $g = 800$ nm entre les nanofils devrait fournir des facteurs de rehaussement encore plus élevés selon nos simulations et fera l'objet d'une étude subséquente.

0.5 Contexte de cotutelle Québec-France

Cette thèse s'inscrit dans un contexte de cotutelle entre le Québec et la France. D'une part, une section de cette thèse s'effectue au centre Énergie, Matériaux et Télécommunications de l'Institut national de la recherche scientifique (INRS-ÉMT) à Varennes, près de Montréal au Québec, sous la direction de Prof. Patrizio Antici. Le groupe de Prof. Antici compte typiquement 3-4 étudiants au doctorat, également en cotutelle, ainsi que de nombreux partenariats internationaux. Cette partie nord-américaine de la thèse sert de plateforme expérimentale pour le montage et le développement d'un système d'accélération d'ions par laser sur les installations du laser ALLS 100 TW de l'INRS-ÉMT. La très grande majorité des travaux expérimentaux ont été effectués en étroite collaboration avec de nombreux acteurs-clés : Stéphane Payeur (agent de recherche), Sylvain Fourmaux (associé de recherche), Joël Maltais (technicien laser), Léonard Pelletier (technicien hors-du-commun et magicien), Guy Lebrun (ingénieur), Pilar Puyuelo-Valdés (doctorante en cotutelle avec UBordeaux), Martina Salvadori (doctorante en cotutelle avec URome) et Charles Bienvenue (stagiaire de 1er cycle pendant deux étés). Concernant les campagnes expérimentales effectuées à l'extérieur de l'INRS, il est indispensable de mentionner l'étroite collaboration avec Prof. Julien Fuchs (directeur de recherche au CNRS à l'École Polytechnique de l'Université Paris-Saclay), Marianna Barberio (professeure associée à l'INRS), Massimiliano Scisciò (doctorant en cotutelle avec URome) et Simona Veltri (doctorante en cotutelle avec UCalabria). Il est également primordial de mentionner le support théorique et expérimental des gens de l'accélérateur de particules de l'Université de Montréal (UMontréal), où tout un pan d'expériences ont été effectuées au fil des ans : Louis Godbout (technicien et opérateur du Tandem), François Schiettekatte (professeur à UMontréal), Martin Chicoine (agent de recherche à UMontréal), Sjoerd Roorda (professeur à UMontréal) et Hugo Bouchard (physicien médical au CHUM et professeur à UMontréal).

L'autre partie de cette thèse se déroule au Centre Lasers Intenses et Application (CELIA) de l'Université de Bordeaux en France, sous la direction de Prof. Emmanuel d'Humières. Le groupe de Prof. d'Humières compte environ une dizaine d'étudiants français et internationaux, s'insèrant dans un regroupement de chercheurs appelé Interaction, Fusion par Confinement Inertiel et Astrophysique (IFCIA) du CELIA. Cette partie à l'étranger a pour but premier de développer et peaufiner des simulations Particle-In-Cell avec le code PICLS 2D, un code co-développé par Prof. d'Humières. Le fait d'être présent au CELIA a fait avancer à très grande vitesse mon apprentissage des codes PIC et du développement de mes propres simulations avec des nanostructures, ce qui aurait autrement nécessité beaucoup plus de temps s'il y avait eu seulement des interactions à distance avec Prof. d'Humières. Mon passage au CELIA m'a également fait bénéficier d'une vision élargie de la recherche, laquelle fait maintenant partie intégrante de mon expertise. Il est essentiel de mentionner que les travaux de simulations de cette thèse ont été effectués avec plusieurs collaborateurs essentiels : Xavier Ribeyre (chercheur CEA), Quentin Moreno (doctorant au CELIA), Léo Esnault (doctorant au CELIA), Dimitri Khaghani (chercheur postdoctoral au CELIA) et Bertrand Martinez (doctorant au CEA-DAM).

Preface

0.1 Radiation sources

Radiations are ubiquitous, we are exposed to them everywhere, all the time. They consist of particles traveling with a certain energy that collide and interact with matter, causing damage or not. There are two major classes of radiation, namely *non-ionizing* radiations and *ionizing* radiations. On the one hand, *non-ionizing* radiation cannot ionize matter since its kinetic energy is lower than the ionization potential of the atom it is interacting with, hence making it incapable of ejecting an orbital electron and disturbing the structure of matter. Non-ionizing radiation usually refer to all electromagnetic waves such as radio waves, microwaves, infrared photons, visible light and up to near ultraviolet radiation (*i.e.* non-ionizing photons). They encompass technologies such as AM/FM radio, microwave ovens, Wi-Fi, Bluetooth, Global Positioning Systems, television stations, cellphones, garage-door openers, *etc*. On the other hand, *ionizing* radiations have the capability to knock out an orbital electron from an atom because their energy exceeds the ionization potential of the absorber, causing a charge imbalance and perturbing its environment. We are impacted by ionizing radiations everywhere: natural background radiation from the soil (in particular from Radon gas), cosmic rays traversing the atmosphere, radioactive isotopes from the food we eat (high potassium-40 content in bananas or carbon-14 in meats or vegetables for instance), the water we drink, the air we breath and man-made sources (CT scans, radiographies, radioisotope production, nuclear power plants, smoke detectors, exit signs, *etc*.). Understanding the nature of ionizing radiations, as well as their proper use, has revolutionized humankind for more than a hundred years now, and will continue to be one of the top concerns of humans for at least the few hundred years to come.

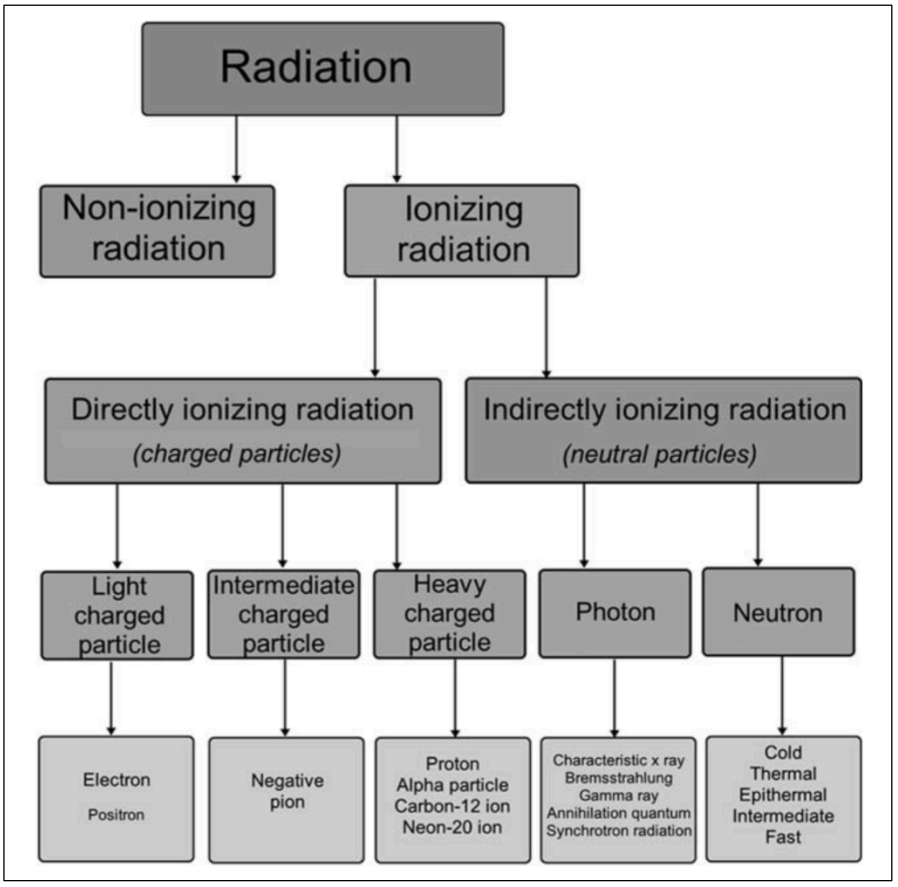

FIGURE 0.1: Classification of ionizing radiation sources. This figure is extracted and adapted from E. B. Podgoršak, "Radiation Physics for Medical Physicists", 2nd edition, *Springer*, (2010).

Types of ionizing radiation

Ionizing radiations can be divided in two sub-parts depending on their mode of interaction, being either *directly* (charged particles) or *indirectly* (neutral particles) ionizing. *Directly* ionizing radiations (electrons, pions, protons, alpha particles or heavy ions for instance) deposit their energy directly through Coulomb interactions between them and the orbital electron from an atom in matter. *Indirectly* ionizing radiations (photons and neutrons) rather deposit their energy in a two-step process, firstly being absorbed by an atom which ejects a charged particle from the interaction, and secondly by an energy deposition of the ejected charged particle in matter. A summary of the classification of ionizing radiation is shown in Figure 0.1.

Energy deposition of ionizing radiation in matter

Depending on the nature of the particle, ionizing radiations deposit energy in matter through various processes. This results in a plethora of different interactions and therefore a wide range of energy deposition characteristics as the particles traverse the matter. To properly protect ourselves and correctly use ionizing radiations, it is necessary to understand the depth-dose deposition profiles of the most common ionizing radiation particles, and their variation with energy. A summary of depth-dose profiles for X-ray photons, electrons, neutrons and heavy ions is shown in Figure 0.2. Of particular importance are the keV-MeV ranged photons presented 0.2.a, for which the dose deposition profiles are shown for energies ranging from keV (soft X-rays) to MeV (hard X-rays). It is first important to note that photons are massless, and therefore do not deposit dose directly but are attenuated (*i.e.* interact with an associated probability with penetration depth). This characteristic makes them very penetrating, especially at high energies (MeV-ranged). Said differently, there is always a non-zero probability of finding a photon at an infinite depth in a material. This is one of the reasons why MeV photons are used in radiotherapy for treating deep-seated tumors located in prostates or lungs for example, as opposed to keV photons that are used to treat skin cancers because most of their attenuation occurs on surface tissues. Neutrons are also very penetrating (see Figure 0.2.c) particles since they do not interact through Coulomb interactions, and thus barely interact with matter. Light charged particles like electrons or positrons (Figure 0.2.b) have a very shallow deposition profile, but undergo also a lot of scattering events due to their small mass and hence produce a diffused dose deposition. Finally, heavy charged particles do not deviate very much from their initial direction (small amount of scattering leading to a more rectilinear trajectory) when propagating in matter, due to their greater mass. Their dose deposition profile undergoes the so-called "Bragg peak" (see Figure 0.2.d), *i.e.* a very steep energy deposition rate occurring within a short distance, followed by zero dose after the peak since the particle is completely stopped. This also occurs for light charged particles, however their peak gets blurred out from the large amount of scattering events they undergo. Additionally, light charged particles generate a copious amount of secondary X-rays through *Bremsstrahlung* (literally "braking radiation" in German) when depositing energy, which provokes a non-negligible "dose tail" at large depths due to strong penetrating power of high-energy photons. This interesting Bragg peak characteristic has triggered a multi-billion dollar industry throughout the world called

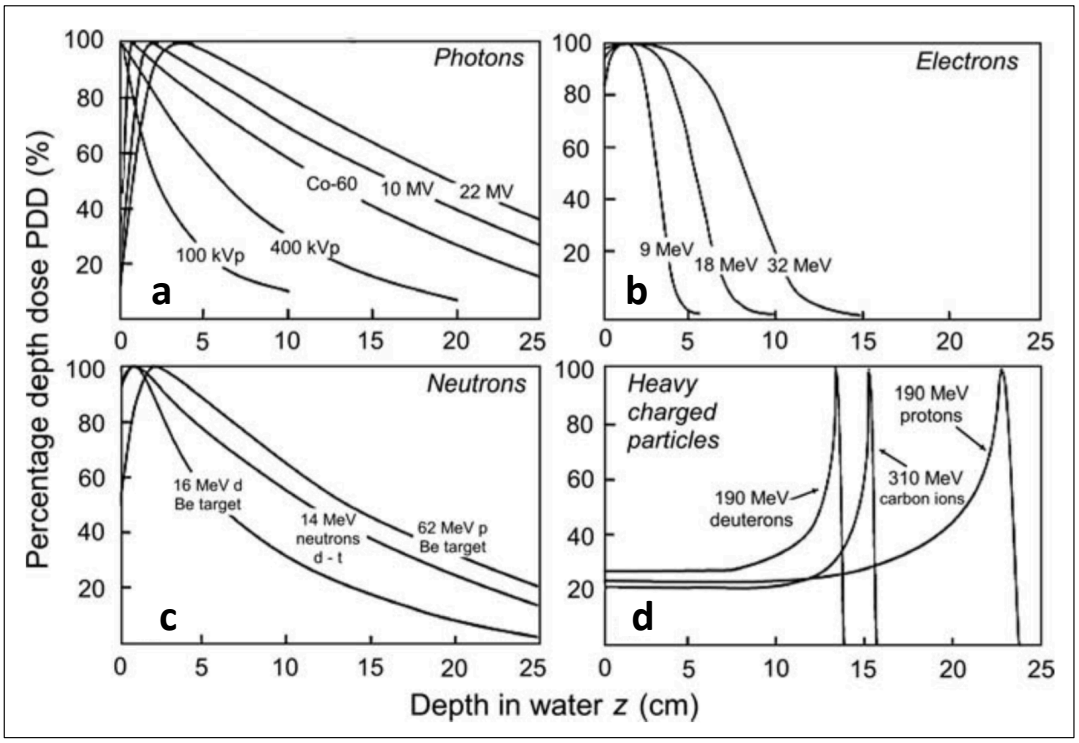

FIGURE 0.2: Energy deposition profiles with penetration depth for different types of ionizing radiation such as (a) keV-MeV ranged photons, (b) electrons, (c) neutrons and (d) heavy ions. This figure is extracted and adapted from E. B. Podgoršak, "Radiation Physics for Medical Physicists", 2nd edition, *Springer*, (2010).

hadrontherapy, the most heavily commercialized being proton-therapy. It consists of performing radiotherapy on tumors with ion beams in order to benefit from the spread-out Bragg peak and strongly irradiate a tumor placed at a depth that corresponds to the position of the peak, which results in a high energy deposition inside the tumor combined with high sparing of healthy tissues compared to the conventional radiotherapy with X-ray beams.

Particle accelerators as particle sources

For any of the aforementioned types of ionizing radiations, the radiation sources involve the acceleration of particles at a certain point to generate the source itself, which has triggered and sustained the development of particle accelerators. This journey of particle acceleration for ionizing radiation sources has started with the invention of the Crookes tube (see Figure 0.3) by William Crookes in 1869. By putting a high voltage between an anode and a cathode placed under vacuum, this resulted in the so-called cathode rays (*i.e.* a beam of accelerated

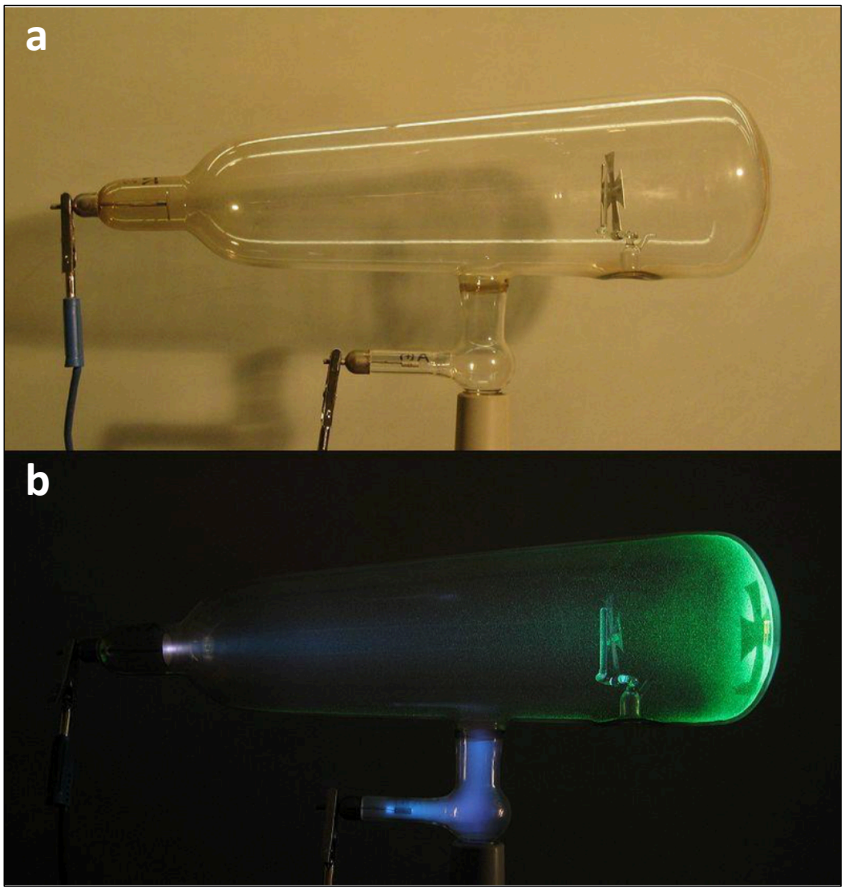

FIGURE 0.3: Crookes tube: a beam of accelerated electrons under partial vacuum by a high static voltage. (a) Voltage off. (b) Voltage on. This figure is extracted and adapted from P. Lebrun, "Particle accelerators, instruments of discovery in physics", Lecture, *Joint Universities Accelerator School*, (2018).

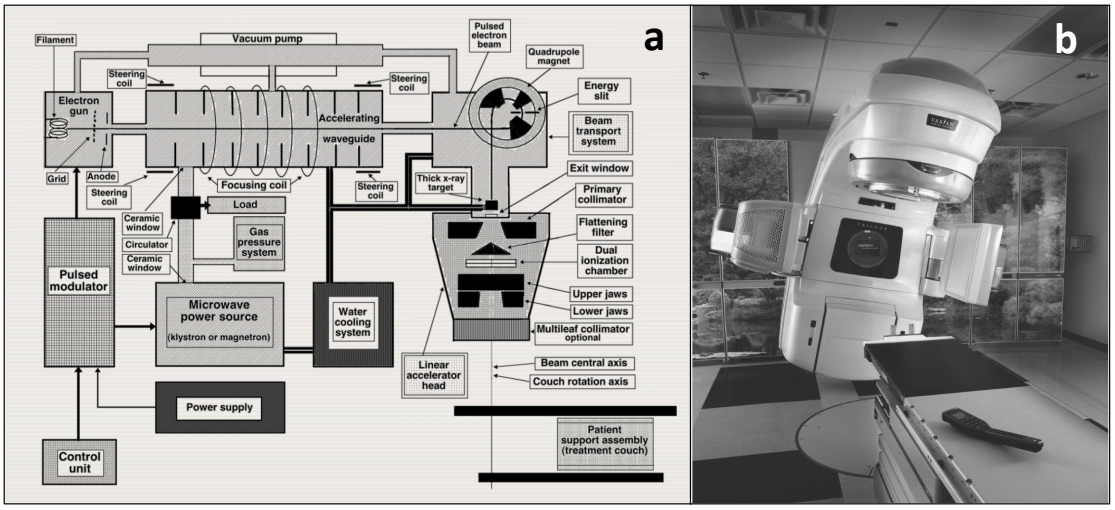

FIGURE 0.4: Medical linear accelerator used for the irradiation of tumors in radiotherapy. (a) Schematic diagram of a linac. (b) Medical linac from *Varian Medical Systems*. This figure is extracted and adapted from E. B. Podgoršak, "Radiation Oncology Physics: A Handbook for Teachers and Students", Lecture, *IAEA*, (2006).

FIGURE 0.5: Aerial view of the Large Hadron Collider (LHC) at CERN in Geneva, Switzerland. Photo credit: CERN, taken from https://phys.org/news/2019-01-cern-vision-next-generation-particle-collider.html.

electrons, unknown at the time) that were used for imaging the shadow of an object located before a phosphorescent screen. The same kind of tube was used by Wilhelm C. Röntgen in 1895 for the discovery of X-rays. Since then, so many important milestones regarding our understanding of nature happened involving particle accelerators, namely the discovery of the electron (Joseph J. Thomson, 1897), the discovery of the proton (Ernest Rutherford, 1919), the invention of the radiofrequency-based accelerating cavity (Rolf Wideröe, 1928), the discovery of the neutron (James Chadwick, 1932), the first breaking of an atomic nucleus (John D. Cockcroft and Ernest Thomas Sinton Walton, 1932), to name a few. Nowadays, particle accelerators evolved tremendously and have become very sophisticated devices which are used everywhere in the world, ranging from very compact and commercialized devices like medical Linear Accelerators (linacs) for the treatment of tumors in radiotherapy (see Figure 0.4) to enormous machines to study the fundamental properties of nature such as the Large Hadron Collider (see Figure 0.5). A non-exhaustive list of particle accelerator applications in different fields is presented below.

- Medical: radiotherapy, medical imaging, radioisotope production.
- Industrial: ion implantation, ion beam analysis, material processing, sterilization.
- Security: X-ray cargo screening, hydrodynamic testing.
- Synchrotron Light Sources and Free Electron Lasers: biology, medicine, materials science.
- Neutron scattering: materials science.
- Fusion energy: ion beam heating, heavy ion inertial fusion, materials studies.
- Fission energy: waste burner, thorium fuel amplifier.
- Bio-fuel energy: bio-fuel production.
- Environment: water treatment, flue gas treatment.
- Cultural Heritage: non-destructive analysis/dating of works of art and artifacts.

0.2 High peak-power lasers

The invention of the laser by Theodore H. Maiman in 1960 using a ruby crystal, based on the theoretical work of Charles H. Townes and Arthur L. Schawlow, has revolutionized the modern world we live in today. Lasers are also everywhere in our day-to-day lives, ranging in size from laser diodes to the most energetic laser in the world at the National Ignition Facility (NIF) in Livermore, CA in the United States. In between, there exists an extremely wide variety of applications such as industrial machining, telecommunications, microscopy, spectroscopy, materials science, astronomy, military-based applications, surgery, to name a few. These applications were enabled in time by the continuous escalation of laser intensities through important technical milestones like *Q-switching*, *Mode-locking* and finally by the second revolution in the laser field, the *Chirped Pulse Amplification* (CPA) technique developed by Gérard Mourou and Donna Strickland in 1985 (Nobel Prize in Physics 2018). The rise of laser intensities since 1960 is shown in Figure 0.6. The advent of the CPA technique and TW-class (10^{12} W) lasers unlocked new horizons in several applications such as eye laser surgery, but also allowed to reach intensities high enough to strip out tightly bound electrons ($I_0 \sim 10^{15} - 10^{17}$ W/cm^2) from the attraction of atomic nuclei and further opened a new class of unexplored physics problems in the field of "relativistic optics" ($I_0 > 10^{18}$ W/cm^2). Taken independently, visible and infrared

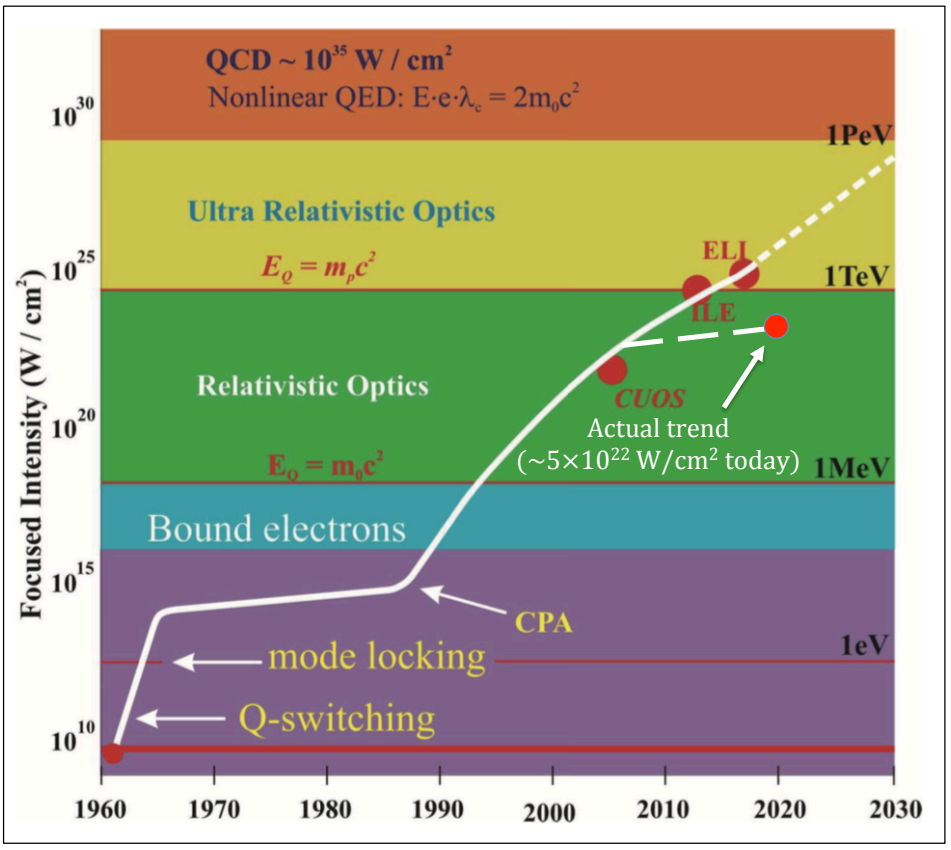

FIGURE 0.6: The climb of laser intensities since its invention in 1960. This figure is extracted and adapted from G. A. Mourou, T. Tajima & S. V. Bulanov, "Optics in the relativistic regime", *Rev. Mod. Phys.*, vol. 78, 309-371 (2006).

photons used by lasers are considered as non-ionizing radiations. However, when focusing laser beams at sufficiently high intensities, multiphoton absorptions can occur which enables ionization events from visible-infrared photons. Further increasing the intensity, the electric field of the electromagnetic wave can become so elevated that it strongly bends the Coulomb potential around an atomic nucleus, which allows the ejection of electrons through tunnel ionization or through direct escape if the electric field is high enough. Today with the advent of PW-class (10^{15} W) lasers, a new frontier in physics called "ultra-relativistic optics" is on the verge of being open, which would allow the study of high-field Quantum ElectroDynamics (QED) phenomena. They constitute a class of processes that are predicted by the Quantum Field Theory (QFT) but are not yet measured experimentally, due to the ultra-high intensities ($I_0 > 10^{23}$ W/cm^2) required to trigger these events.

0.3 Laser-driven ionizing radiation sources

Above the electron relativistic intensity threshold ($I_0 > 10^{18}$ W/cm^2 for a wavelength of 1 micron), atoms are not only easily ionized by the strong electromagnetic field, but electrons perform unusual trajectories since they oscillate in the field at velocities near the speed of light, which triggers relativistic effects. This enables a whole new series of absorption processes in gases and solid targets. The strong charge separation induced by high-intensity short-pulsed lasers, along with the very intense electric fields that plasmas can sustain, open the field of laser-driven particle acceleration. Indeed, conventional particle accelerators are limited to electric fields on the order of 100 MV/m at most in vacuum in order to avoid the electrical breakdown of the accelerating cavity. However, plasmas can sustain fields in the TV/m range, *i.e.* at least four orders of magnitude higher, which allows equivalent energies or higher than conventional accelerators to be produced in a very compact scheme, which substantially lowers the fabrication costs at the same time. The original idea was initially brought up by Toshiki Tajima and John M. Dawson in 1979, at a timely moment with regards to the advent of the CPA technique which would occur six years after. These two events further triggered the development of laser-based electron and ion acceleration.

Electron acceleration and X-ray sources

Laser-driven electron acceleration occurs in different experimental schemes, the most well-known being Laser Wakefield Acceleration (LWFA). This type of acceleration occurs when focusing a high-intensity laser ($I_0 > 10^{18}$ W/cm^2) in a gas, which causes a strong charge separation after its passage and induces a plasma wave in the pulse's wake. The electric fields generated in the wake are typically on the order of the GV/m and up to the TV/m. If an electron bunch gets trapped in a plasma wave with the right phase velocity, the bunch gets accelerated by the electric field in the forward direction with respect to the propagation direction of the laser, just like a surfer gets accelerated by sliding a water wave at the right moment. This places two necessary conditions for particle acceleration. First, there must be an electric field component along the propagation direction, and secondly the phase velocity must match the one of the accelerating field for an optimal energy transfer. Typical laser-driven electron acceleration experiments nowadays accelerate electrons bunches (nC) to several GeV in energy with

a cm-long gas cell. This obviously dramatically reduces the size of electron accelerators compared to conventional accelerators that required tens of meters of length to reach an equivalent kinetic energy.

The passage of a high-intensity short-duration laser pulse in a gas cell pushes the electrons out of its trajectory through the ponderomotive force (discussed further in this dissertation) and thus leaves a positive ion channel in its trail. The highly-relativistic accelerated electrons (several hundreds of MeV to GeV) are thus attracted by the electric field of this positive ion channel that produce a restoring force, and oscillate around it while moving in the forward direction. These abrupt direction changes during the oscillations generate the emission of a beam of X-ray photons, as dictated by Maxwell's equations, commonly referred to as "betatron" radiation. The resulting X-ray beam is very short in duration (tens to hundreds of femtoseconds), exhibits high spatial coherence and low directional, which makes it a very interesting source compared to the conventional ones for a variety of applications. The intrinsic qualities of the betatron beam compete with those of synchrotron light sources which are circular accelerators of several hundred meters of circumference, whereas a laser-driven betatron source is several meters long, hence being much less costly.

Ion acceleration and neutron sources

Laser-driven ion acceleration occurs when focusing a high-intensity ($I_0 > 10^{18}$ W/cm^2) laser pulse onto a target, thereby producing a strong charge separation that leads to the establishment of a very high accelerating electric field in the generated plasma. Other acceleration mechanisms imply to directly push the ions with the high electric field of the laser pulse itself. Laser-driven ion acceleration is typically performed using two distinct target types, namely gas jets or solid targets. The most attractive advantage of gas jets is regarding the continuous target replacement with an appropriate gas flow, which brings the possibility to have high-intensity laser-matter interactions running at tens of Hz, thereby generating high particle fluxes. The downside of gas jets is the typically lower ion kinetic energies produced when compared to solid targets. Indeed, solid targets can maintain sharper density gradients that can lead to higher accelerating fields due to the stronger charge separation induced by the laser impinging on the target. With the solid target being blown away (*i.e.* evaporated) after the interaction, the target needs to be refreshed after each laser shot, however there are many

technical challenges to overcome for obtaining a replacement rate as high as the repetition rate of the laser. At the present time, the record kinetic energies for ion acceleration is around 100 MeV per nucleon. Four acceleration schemes are known to produce efficient ion acceleration with high-intensity short-pulse lasers: Target-Normal Sheath Acceleration (TNSA), Radiation Pressure Acceleration (RPA), Collisionless Shock Acceleration (CSA) and Coulomb Explosions. The first three of these acceleration schemes will be discussed further in this dissertation. The most widely known and investigated is the TNSA mechanism using solid targets, which will be the mechanism at the focus of this thesis.

When irradiating a secondary target, made with lithium fluoride (LiF) for instance, with a laser-driven ion beam (protons being particularly effective), it is possible to induce a nuclear reaction which results in the emission of a neutron, thereby producing a laser-driven neutron source. More precisely, the ^{7}Li(p,n)^{7}Be reaction is of particular interest due to its high cross-section (*i.e.* high interaction probability) when using protons of a few tens of MeV, as routinely obtained by laser-driven proton acceleration with solid target using the TNSA mechanism. This specific laser-driven neutron beam generation scheme is called the "pitcher-catcher system", and is promising to reach record neutron brightnesses in upcoming high-power laser facilities being built at the present time (Apollon laser or ELI pillars for instance), due to the high flux generated during a short duration (sub-ns) of the neutron beam.

0.4 Thesis objectives

This thesis work stands in the context of laser-driven ion acceleration with solid targets using the TNSA mechanism. It is performed in a Québec-France cotutelle context and encompasses experimental as well as numerical work for the optimization of laser-driven ion beamlines. The doctoral work comprises five peer-reviewed articles published or accepted in scientific journals, for which I am the first author. The studies are separated in three themes: solid target alignment optimization (Chapter 3, one article), efficient particle diagnostics (Chapter 4, two articles) and enhanced relativistic laser-matter interactions (Chapter 5, two articles). Each theme constitutes a Chapter of the thesis with their context further described below.

Development of a target alignement interferometer with submicrometric precision

Laser-driven particles sources underwent substantial progress since the end of the 90's, and many experimental advances have been done since the last 30 years with the advent of the TW class of lasers, essentially made possible by the CPA technique. Obtaining a very intense focal spot of high quality is indeed the first step towards laser-driven particle acceleration, nevertheless a lot of work still needs to be done regarding the continuous replacement of targets used for the interaction, both for solid and gaseous targets. Even though gas jets appear to be conceptually more promising to satisfy the high-repetition rate targetry, several breakthroughs are still to come concerning the development of nozzles that provide supersonic gas flows which increase the gas density near the critical density of the laser (density over which the laser cannot propagate anymore), as well as for the use of cryogenic gases which bring many engineering challenges. Moreover, the kinetic energies of ions obtained with gas jets are typically lower than those obtained with thin solid foils, thus requiring larger laser facilities to compensate, combined with lower ion fluences partly due to the larger divergence of ion beams obtained with gas jets. Regarding solid targets, several advances are being investigated regarding the automation of target replacement, with the aim to optimally reach the repetition rate of the laser. However, increasing the rate of target replacement comes with the downside of reducing the precision of target positioning, which in turn decreases the shot-to-shot repeatability of the ion source, due to the short Rayleigh length of the laser obtained when using tight focusing. The challenge here is to implement a target alignment system that limits the compromise between precision and repeatability, while still offering a target replacement rate equivalent to the repetition rate of the laser. This goal will be the subject of Chapter 3 of this thesis, first aiming to implement high-precision interferometer for solid target positioning and then to optimize its execution speed and automation.

Design and implementation of efficient particle diagnostics

The third great challenge brought up by laser-driven ion sources is in regard to their efficient detection in a high repetition-rate scheme, so as to correctly probe the ion beams in real time. Due to the pulsed nature of the interaction, laser-driven particle beams travel through space as charge bunches with a duration varying from a few picoseconds at the source to several nanoseconds after a few meters of propagation. Hence, a high number of particles are hitting

the detector almost simultaneously which can induce signal saturation, charge accumulation and therefore an erroneous diagnostic of the incoming beam. To overcome this problem, analog detectors such as Image Plates (IPs), RadioChromic Films (RCFs) and CR-39 have been the reference detectors in the domain for a long time, also due to their resistance to the strong electromagnetic pollution produced by the laser-matter interaction. The major disadvantage of this kind of analog detectors is their incompatibility with high-repetition rate setups, requiring a venting of the vacuum chamber they are located to digitize their data, followed by a replacement of the detector and a re-pumping of the chamber, this entire process repeated at every shot. The necessity of installing particle detectors that directly digitize data upon acquisition without venting the chamber is therefore obvious, moreover the used detectors need to offer a good resistance to the electromagnetic pollution caused by the interaction, exhibiting a high signal saturation level to sustain the high particles fluxes as well as permitting a high-repetition rate readout. The implementation of this type of diagnostic on the ALLS 100 TW ion acceleration beamline will constitute the Chapter 4 of this thesis.

Enhancing relativistic laser-matter interactions with nanostructured solid targets

The second grand challenge that are facing laser-driven ion sources is related to the optimization of the energy transfer from the laser to the ions. Indeed, obtaining a very high laser intensity that is superior to the electron relativistic threshold (10^{18} W/cm^2) is essential to trigger the right acceleration mechanisms, along with the proper target positioning at the center of the focal spot, however it can be difficult to justify all these investments if the energy transfer from the laser to the ions is less than 1%, making the process very inefficient. On the one hand, conventional gas targets have underdense electronic densities ($n_e \sim 10^{18} - 10^{20}$ cm^{-3}), more precisely being lower than the critical density of a laser operating at 800 nm ($n_c \sim 10^{21}$ cm^{-3}), making the target more transparent to the passage of the laser and thus being less optimal in terms of energy transfer. The challenge in this situation is to increase the density of gas jets near the critical density in the focal plane to maximize the energy absorption from electrons, providing in turn greater kinetic energies to the accelerated ions, as well as higher particle fluxes. The most promising avenues in this direction are supersonic gas jets and cryogenic gases. On the other hand, typical solid targets used for laser-driven ion acceleration are metallic targets with over-dense electronic densities ($n_e \sim 10^{23}$ cm^{-3}), *i.e.* higher than the critical density of a 800 nm laser, making them more reflective with respect to the laser as it is possible to notice

with the naked eye. Metals have, for the great majority of them and assuming the absence of a preplasma at the target front, reflection coefficients of at least 95% at 800 nm, thereby imposing an upper bound of 5% to the energy transfer to charged particles in an ideal case. In practice, part of this 5% is transmitted through the target, another part of it is conserved by the electrons that accelerate the ions in their wake, plus the energy is distributed over several ion species, which in sum typically reduces the laser-to-proton conversion efficiency to 1% or less. The challenge here is to benefit from the high reflectivity of metals to trap the incoming electromagnetic wave in a series of reflections to maximize the laser-matter interactions, leading to a greater energy transfer to the electrons and then subsequently to the ions. Hence, this goal is purely geometrical and is achieved by using metallic nanostructures of comparable size to the laser wavelength, being the subject of Chapter 5 of this thesis.

0.5 Québec-France cotutelle context

This thesis is done in a dual PhD context (also called cotutelle) between Québec and France. On the one hand, part of the thesis work is performed at the Énergie, Matériaux et Télécommunication center of the Institut National de la Recherche Scientifique (INRS-EMT) in Varennes, close to Montréal in Québec, under the supervision of Prof. Patrizio Antici. The research group of Prof. Antici typically comprises 3-4 PhD students also in cotutelle, along with numerous international partnerships and collaborations. This north american section of the thesis is dedicated to the design, mounting and development of a laser-driven ion acceleration beamline on the Advanced Laser Light Source (ALLS) 100 TW from INRS-EMT. The great majority of the experimental work was performed in strong collaboration with several key-actors: Stéphane Payeur (Research Officer), Sylvain Fourmaux (Research Associate), Joël Maltais (Laser Technician), Léonard Pelletier (Outstanding Technician and Wizard), Guy Lebrun (Engineer), Pilar Puyuelo-Valdés (PhD student in cotutelle with UBordeaux), Martina Salvadori (PhD student in cotutelle with URome) and Charles Bienvenue (undergraduate research intern for two summers). Concerning the experimental campaigns performed outside of INRS-EMT, it is important to mention the narrow collaborations with Prof. Julien Fuchs (CNRS research director at École Polytechnique from Paris-Saclay University), Marianna Barberio (associate professor at INRS), Massimiliano Scisciò (PhD student in cotutelle with URome) and Simona Veltri (PhD

student in cotutelle with UCalabria). It is as well essential to note the theoretical and experimental support from the people at the Tandem particle accelerator from Université de Montréal (UMontréal), where a series of experiments have been performed throughout the years: Louis Godbout (technician and Tandem operator), François Schiettekatte (Professor at UMontréal), Martin Chicoine (Research Officer), Sjoerd Roorda (Professor at UMontréal) and Hugo Bouchard (Medical Physicist at CHUM and Professor at UMontréal).

On the other hand, a section of this thesis is done at the Centre Lasers Intenses et Application (CELIA) from University of Bordeaux in France, under the supervision of Prof. Emmanuel d'Humières. The research group of Prof. d'Humières comprises about 10 French or international students, and is part of larger regroupment of researchers within CELIA called Interaction, Inertinal Confinement Fusion and Astrophysics (IFCIA). The purpose of this thesis section done oversea is to develop and refine Particle-In-Cell simulations with the code PICLS 2D, which is co-developed by Prof. d'Humières. Being in person at the CELIA allowed to boost the efficiency of this entire thesis section, which would have required much more time if there would have been only distanced interactions through emails, phone calls or videoconference with Prof. d'Humières. My time spent at CELIA also made me benefit from a widen and more international vision of scientific research, which is now an integral part of my research experience. It is essential to mention that these simulation works were performed in strong collaboration with the following researchers: Xavier Ribeyre (CEA Researcher), Quentin Moreno (PhD student), Léo Esnault (PhD student), Dimitri Khaghani (Postdoctoral Researcher) and Bertrand Martinez (PhD student at CEA-DAM).

Disclaimer: The English version of the Preface does not contain the highlights of the Chapters since they can be found in details within each independent study of this dissertation.

Chapter 1

Context of Particle Acceleration

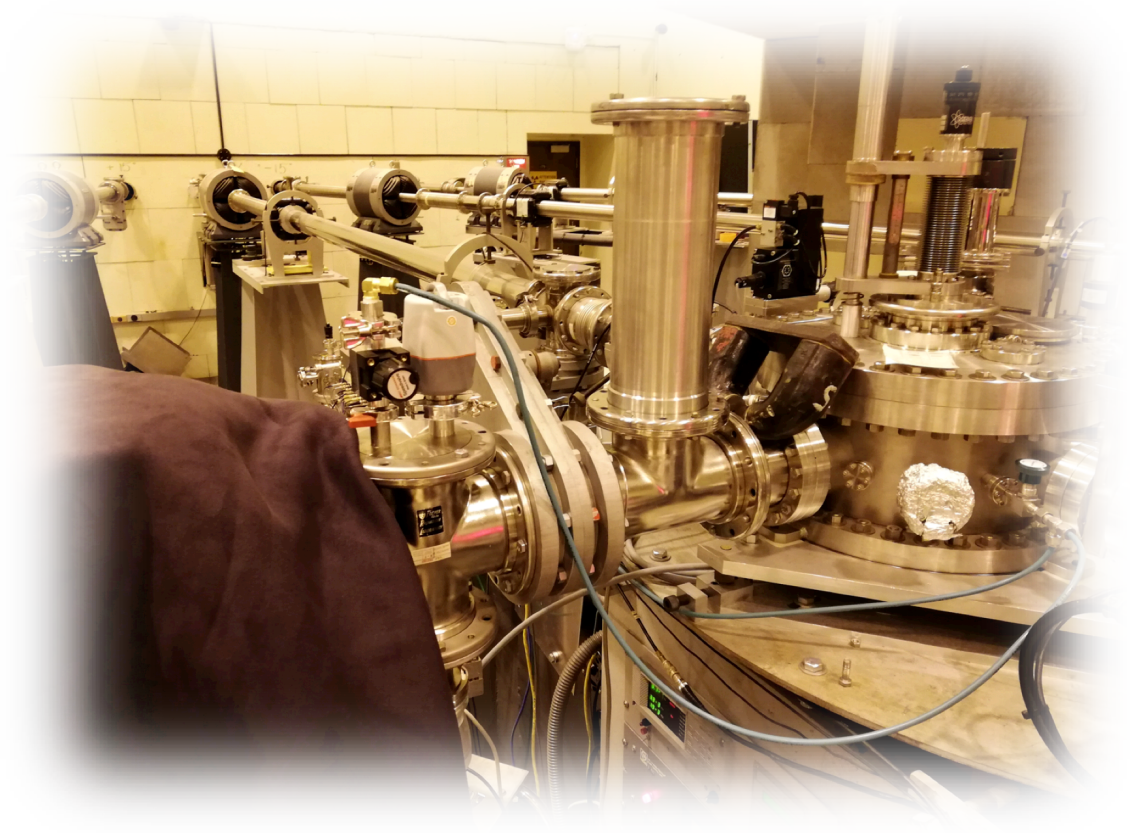

Rutherford Backscattering Spectroscopy on a Tandem Van de Graaff accelerator.

Chapter Content

Science is dedicated at understanding the fundamental processes and building blocks of our Universe. To understand these processes, one requires to construct a model, formulate sound hypotheses based on the model and verify their truthfulness by testing them. The answer to the test will help to infer conclusions and further refine the model, these steps being repeated until the model is complete. Testing an hypothesis through an experiment requires to probe a process, the latter requiring an exchange of energy or information to interrogate a system. This methodology of science has led, over time, to tremendous amounts of discoveries that changed our perception of Nature. In physics, these discoveries often concerned the fundamental particles of the Universe. The different processes to be probed for hypothesis testing are triggered by different amounts of energy, being transported by these fundamental particles. Hence, it was necessary to generate sources of particles with various energy levels to obtain answers to these questions. To vary the energy of particles, as will be shown in the next section, requires

that they experience an acceleration. The goal of this Chapter is to provide the main context for the development of particle accelerators over time, helping to properly position the advent of laser-based particle acceleration today. The first section of this Chapter covers the most essential concepts behind particle acceleration and electromagnetic fields. The main accelerator types relevant to this doctoral work are then reviewed in chronological order, namely the Tandem Van de Graaff, Linear Accelerators, Cyclotrons and Synchrotrons. The last section finally covers the advent of laser-driven particle accelerators, in particular regarding electron and ion acceleration.

1.1 Particle acceleration and electromagnetic fields

The total relativistic energy $\mathcal{E}$ of a free (*i.e.* without potential energy U) particle is defined by the following relationship, first introduced by Paul Dirac in 1928:

$$\mathcal{E} = \sqrt{(pc)^2 + (m_0c^2)^2} = \gamma m_0 c^2 = \mathcal{E}_\mathrm{K} + m_0 c^2 \tag{1.1}$$

where p is the particle momentum, m_0 is the rest mass, $\mathcal{E}_\mathrm{K}$ is its kinetic energy, c is the speed of light, and γ is the relativistic Lorentz factor defined by:

$$\gamma = \frac{1}{\sqrt{1-\beta^2}} \tag{1.2}$$

with $\beta = v/c$ being the particle's normalized velocity. The momentum is in turn defined as:

$$p = \gamma m_0 v = \gamma \beta m_0 c \tag{1.3}$$

Hence, to vary the energy of a particle, it is necessary to change the amplitude of its momentum, and this is done by applying a force $\boldsymbol{F} = \langle F_x, F_y, F_z \rangle$ as we are instructed by Newton's second law expressed in vectorial terms:

$$\boldsymbol{F} = \frac{d\boldsymbol{p}}{dt} = \frac{d[\gamma(\boldsymbol{v}) m_0 \boldsymbol{v}]}{dt} = \frac{\gamma^3(\boldsymbol{v}) m_0}{c^2}(\boldsymbol{v}\cdot\boldsymbol{a})\boldsymbol{v} + \gamma(\boldsymbol{v}) m_0 \boldsymbol{a} \tag{1.4}$$

with $\boldsymbol{a} = d\boldsymbol{v}/dt$ being the acceleration and where we define the notation of a vector norm as $p = |\boldsymbol{p}| = \sqrt{\boldsymbol{p}\cdot\boldsymbol{p}}$. From equations (1.1) and (1.4), we see that increasing the energy of a particle requires to apply a force to accelerate it. In the case of charged particles, this is done through

their interaction with electric $\boldsymbol{E}$ and magnetic $\boldsymbol{B}$ (or electromagnetic, EM) fields, as described by the Lorentz force:

$$\boldsymbol{F} = q(\boldsymbol{E} + \boldsymbol{v} \times \boldsymbol{B}) \tag{1.5}$$

where q is the particle charge. The generation of electromagnetic fields is governed by Maxwell's equation, expressed here in vacuum:

$$\boldsymbol{\nabla} \cdot \boldsymbol{E} = \frac{\rho}{\varepsilon_0} \tag{1.6}$$

$$\boldsymbol{\nabla} \cdot \boldsymbol{B} = 0 \tag{1.7}$$

$$\boldsymbol{\nabla} \times \boldsymbol{E} = -\frac{\partial \boldsymbol{B}}{\partial t} \tag{1.8}$$

$$\boldsymbol{\nabla} \times \boldsymbol{B} = \mu_0 \left(\boldsymbol{J} + \varepsilon_0 \frac{\partial \boldsymbol{E}}{\partial t} \right) \tag{1.9}$$

with ρ being the charge density (per unit volume), ε_0 the vacuum permittivity, $\boldsymbol{J}$ the current density (per unit surface) and μ_0 is the vacuum permeability. Since energy is proportional to potentials, and forces are proportional to the gradient of potentials, it is often convenient to express the fields $\boldsymbol{E}$ and $\boldsymbol{B}$ in terms of potential gradients. Defining $\boldsymbol{B} = \boldsymbol{\nabla} \times \boldsymbol{A}$, where $\boldsymbol{A}$ is the vector potential, implies that the electric field should be expressed as $\boldsymbol{E} = -\boldsymbol{\nabla}\Phi - \frac{\partial \boldsymbol{A}}{\partial t}$ through equation (1.8) (Faraday's law), with Φ being the scalar electric potential. It is possible to show in a straightforward way that Maxwell's equations imply an oscillatory behavior of Φ and $\boldsymbol{A}$ (*i.e.* also of $\boldsymbol{E}$ and $\boldsymbol{B}$) through wave equations. By using the Lorenz gauge:

$$\boldsymbol{\nabla} \cdot \boldsymbol{A} + \varepsilon_0 \mu_0 \frac{\partial \Phi}{\partial t} = 0 \tag{1.10}$$

we can insert equation (1.10) into the first Maxwell equation (1.6), leading to:

$$\boldsymbol{\nabla} \cdot \left(-\boldsymbol{\nabla}\Phi - \frac{\partial \boldsymbol{A}}{\partial t} \right) = -\boldsymbol{\nabla} \cdot (\boldsymbol{\nabla}\Phi) - \frac{\partial}{\partial t} (\boldsymbol{\nabla} \cdot \boldsymbol{A}) = -\boldsymbol{\nabla}^2\Phi + \frac{\partial}{\partial t} \left(\varepsilon_0 \mu_0 \frac{\partial \Phi}{\partial t} \right)$$

$$\therefore \qquad \boldsymbol{\nabla}^2\Phi - \frac{1}{c^2} \frac{\partial^2 \Phi}{\partial t^2} = -\frac{\rho}{\varepsilon_0} \tag{1.11}$$

which is the well-known wave equation for Φ with the charge density ρ as the source term. Similarly, using the definition of the potentials in equation (1.9) (Ampère's law) again in the

Lorenz gauge leads to:

$$\boldsymbol{\nabla} \times (\boldsymbol{\nabla} \times \boldsymbol{A}) = \mu_0 \boldsymbol{J} + \varepsilon_0 \mu_0 \frac{\partial}{\partial t} \left(-\boldsymbol{\nabla}\Phi - \frac{\partial \boldsymbol{A}}{\partial t} \right)$$

$$\boldsymbol{\nabla} (\boldsymbol{\nabla} \cdot \boldsymbol{A}) - \boldsymbol{\nabla}^2 \boldsymbol{A} = \mu_0 \boldsymbol{J} - \varepsilon_0 \mu_0 \boldsymbol{\nabla} \left(\frac{\partial \Phi}{\partial t} \right) - \varepsilon_0 \mu_0 \frac{\partial^2 \boldsymbol{A}}{\partial t^2}$$

$$\boldsymbol{\nabla} \left(\boldsymbol{\nabla} \cdot \boldsymbol{A} + \varepsilon_0 \mu_0 \frac{\partial \Phi}{\partial t} \right) - \boldsymbol{\nabla}^2 \boldsymbol{A} + \frac{1}{c^2} \frac{\partial^2 \boldsymbol{A}}{\partial t^2} = \mu_0 \boldsymbol{J}$$

$$\therefore \qquad \boldsymbol{\nabla}^2 \boldsymbol{A} - \frac{1}{c^2} \frac{\partial^2 \boldsymbol{A}}{\partial t^2} = -\mu_0 \boldsymbol{J} \tag{1.12}$$

which is the wave equation for $\boldsymbol{A}$ with the current density $\boldsymbol{J}$ as the source term. This derivation of wave equations shows that charged particles acquire energy by being accelerated with EM waves, which themselves are generated from charge and current distributions. These concepts are at the basis behind the construction of particle accelerators. Even though they were first invented to further extend our scientific knowledge on the fundamental components of Nature, particle accelerators serve a much larger purpose in the modern society, and have found their place in a myriad of applications that are discussed further in this manuscript.

1.2 Conventional particle accelerators

1.2.1 Tandem Van de Graaff

The invention of the Crookes tube in 1869 by William Crookes for generating "cathode rays" (*i.e.* accelerated electron beam in vacuum, electron was unknown at the time) has triggered an ascent towards numerous discoveries about the fundamental properties of nature. One of the earliest and most groundbreaking, the discovery of X-rays by Wilhelm C. Röntgen in 1895, has led to the first application of accelerators for society with the famous radiograph of his wife's hand. Again using the same concept of the Crookes tube followed the discovery of the electron by Joseph J. Thomson in 1897 and the discovery of the proton by Ernest Rutherford in 1919, completely changing our perception of the atom. Since then, the quest for building larger accelerators yielding higher kinetic energies had become obvious to further study the fundamental properties of matter. Robert J. Van de Graaff presented his concept of a 1.5 MV electrostatic generator in 1931 [1] while being a researcher at Princeton University. This was

followed by the first breaking of an atomic nucleus using 125 keV accelerated protons by J. D. Cockcroft & E. T. S. Walton in 1932 with their electrostatic voltage multiplier [2]. The year after, Robert J. Van de Graaff and his group presented the concept of a 10 MV electrostatic accelerator [3], and succeeded in producing a 7 MV machine at MIT. In his accelerator concept, electrical charges are transported mechanically by an insulating conveyor belt and collected at a terminal electrode, typically a very large metallic sphere. Charged particles can therefore be accelerated in one step to tens of MeV (depending on the ion charge) by this electrostatic high-voltage source. The concept was further developed through time, now being used under vacuum for ion transport and with the tank containing the conveyor belt being immersed in SF_6 gas to raise the electrical breakdown limit. The concept was also expanded into a "tandem" acceleration, for which negatively charged particles are first accelerated by the potential before passing through a stripping foil or gas where they loose electrons and become positively charged, thus getting repelled by the high-voltage and are accelerated a second time by the same potential, thereby doubling the produced ion energies. Nevertheless, the electrical breakdown limit is still reached at 25.5 MV today at the Oak Ridge National Laboratory, where the Tandem Van de Graaff accelerator with the highest potential is located. A schematic diagram of a Tandem Van de Graaff accelerator is presented in Figure 1.1.a. In Figures 1.1.b-c are shown pictures of the 2×6 MV EN-1 Tandem Van de Graaff accelerator from Université de Montréal (UMontréal), where several experiments have been conducted during the course of this thesis work. This accelerator is actually the first Tandem accelerator prototype in the world, which was initially installed at Chalk River Laboratories in 1954, and then transferred to UMontréal in 1966. A new source and charge system were installed in 2002. The facility allows for monoenergetic ion acceleration (typically protons, helium and carbon ions) with kinetic energies ranging between 1-12 MeV per charge state, with an energy selector of a few keV of bandwidth. The ion beam is continuous with currents ranging from a few nanoamperes (nA) to microamperes (μA), and is measured at different instances along the beamline using relative charge collectors and Faraday cups calibrated in absolute terms. The vergence of the beam can be adjusted using a series of quadrupoles, and the transverse beamsize can range from a few centimeters to a few microns. The facility comprises seven beamlines (see Figure 1.1.b) available for setting experiments, for which the beam can be easily steered to one or the other. Here is a list of different techniques used and developed at the accelerator:

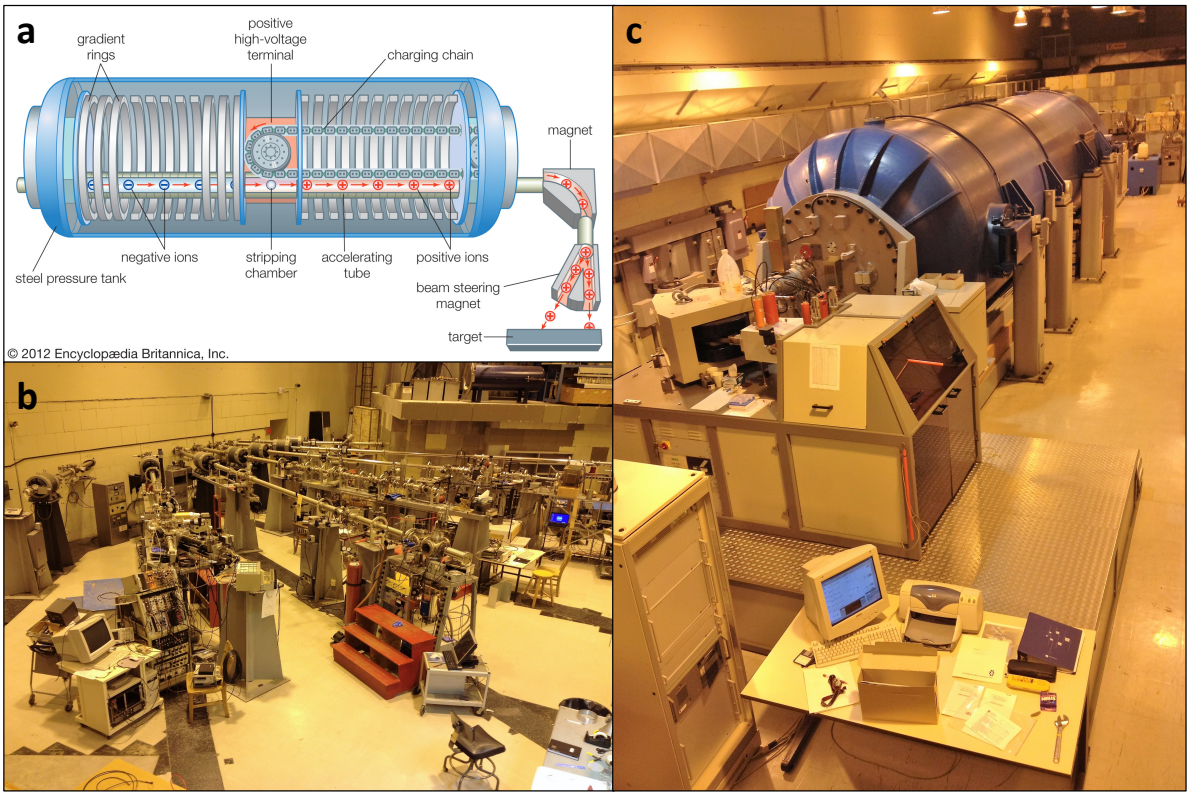

FIGURE 1.1: (a) Schematic diagram of a Tandem Van de Graaff accelerator. (b)-(c) Tandem Van de Graaff accelerator from UMontréal. (b) Available beamlines for use. (c) Tandem EN-1 accelerator. This figure is reproduced with permission from the ion beam lab of UMontréal.

1. Ion implantation
2. Rutherford Backscattering Spectroscopy (RBS)
3. Time-of-flight Elastic Recoil Detection (TOF-ERD)
4. Resonant Nuclear Reactions Analysis (RNRA)
5. Medium Energy Ion Scattering (MEIS)
6. Proton-Induced X-ray emission (PIXE)

1.2.2 Linear accelerators

1.2.2.1 Basic principles of the accelerating cavity

In the quest for obtaining higher energy particle beams to study the fundamental properties of matter, the Norwegian Rolf Wideröe published his doctoral dissertation [4] in 1928, presenting the concept of a linear particle accelerator that uses a radiofrequency (RF) generator.

This would be the birth of the RF-based linear accelerator (linac), revolutionizing accelerator physics thereafter. Following this event, substantial progress in RF sources would occur during World War II for the development of radar technologies. The after-war years were then very flourishing for the development of the RF linac, and Luis Walter Alvarez presented in 1953 the first practically usable RF linac embedded in a resonating cavity [5], which would constitute the bases of modern linac technologies. The experimental demonstration would use a 4 MeV proton beam exiting a Van de Graaff electrostatic accelerator, which would be inserted in an RF linac enclosed in a metallic cavity for further acceleration up to 32 MeV. The accelerating cavity included metallic drift tubes to shield the particle beam from the decelerating electric field (*i.e.* the field oriented in the negative direction with respect to the forward longitudinal axis), and was called the Drift Tube Linac (DTL). Linac technologies underwent tremendous progress since then, ranging from the relatively compact medical linacs used for X-ray beam production in cancer radiotherapy, to the enormous 3-km long linacs such as the one located at the Stanford Linear Accelerator Center (SLAC) in California, United States, as shown in Figure 1.2.a. A simplified schematic diagram of an accelerating cavity is also shown in Figure 1.2.b. Assuming that the electric field inside the cavity (*i.e.* in a bounded medium) has separable solutions from space and time (*i.e.* stationary state), it is possible to express the solution of the wave equation for the electric field as shown by equation (1.13).

$$\boldsymbol{E}(x,y,z,t) = \boldsymbol{E}(x,y,z) \cdot e^{-i\omega t} \tag{1.13}$$

In equation (1.13), $\boldsymbol{E}(x,y,z)$ is the the electric field that is only a function of space which is tailored by the cavity geometry, and ω is the angular frequency of the time-varying field $E(t) = e^{-i\omega t}$. We are interested in the acceleration along the longitudinal axis a_z, as given by the Lorentz force shown in equation (1.14):

$$a_z = \frac{d^2z}{dt^2} = \frac{q}{m}\left(E_z + \frac{dz}{dt} \times \boldsymbol{B}\right) \tag{1.14}$$

In equation (1.14), only the electric field along the longitudinal axis E_z provides an energy gain through acceleration, whereas any magnetic field $\boldsymbol{B}$ is used for focusing or bending the beam since it does not accelerate particles but deviates their trajectory due to the cross product. We can then evaluate the average electric field on-axis (*i.e.* $x = y = 0$) in the direction of the beam propagation z at a given moment of time when $E(t)$ is maximum in a cavity of length L, as

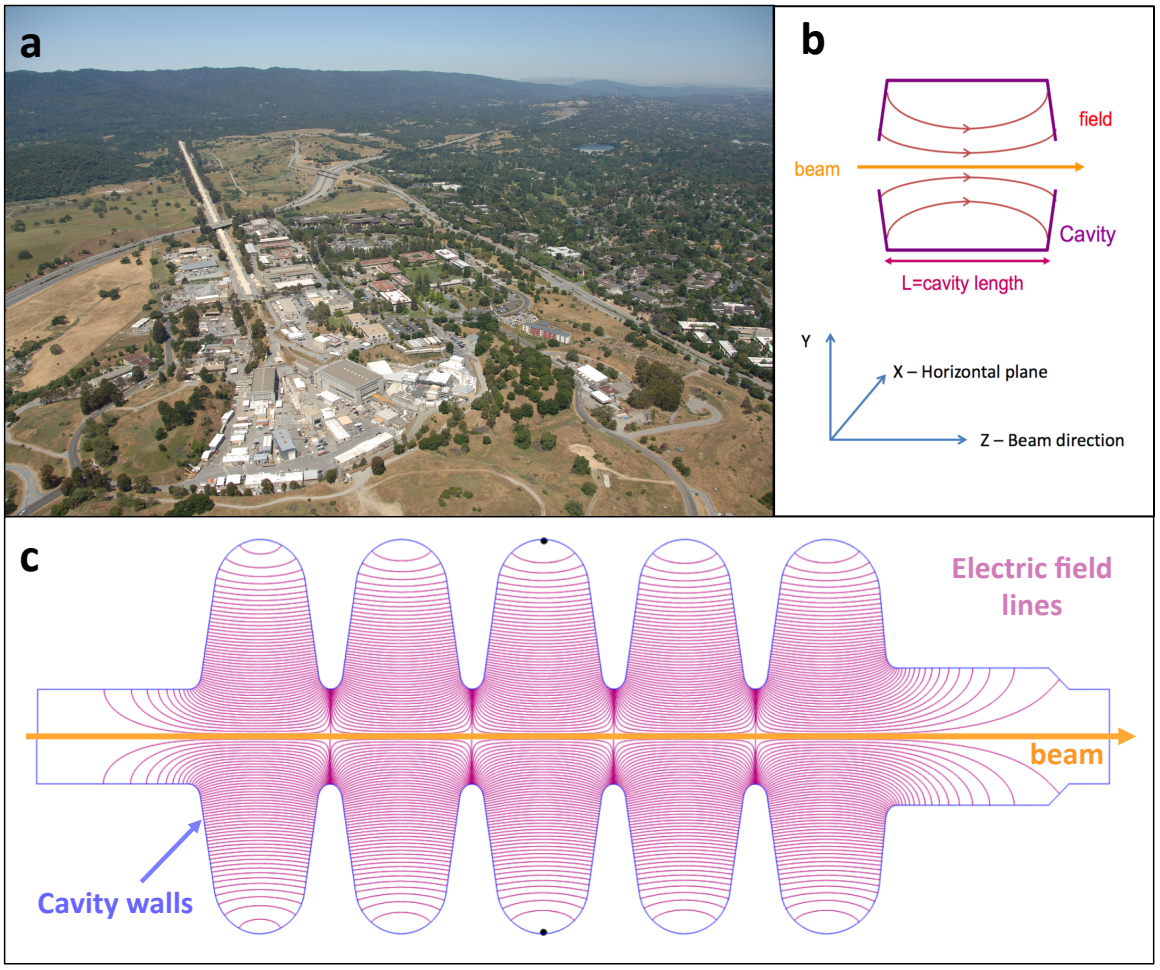

FIGURE 1.2: (a) SLAC aerial view. Photo credit: SLAC. (b) Schematic principle of an accelerating cavity unit. (c) Linear sequence of accelerating cavities providing longitudinal acceleration to a charged particle beam in incremental steps. The accelerating electric field is provided by an RF source that fills the entire cavity with an EM wave.

expressed by equation (1.15):

$$\overline{E}_0 = \frac{1}{L}\int_0^L E_z(0,0,z)\mathrm{d}z \tag{1.15}$$

In equation (1.15), $\overline{E}_0$ is a measure of the effective electric field available for acceleration. This value depends of the cavity's geometry, resonating modes and frequencies. The accelerating cavity can either be used as a traveling wave (TW) cavity into which an RF wave is inserted in the system and extracted at the end, or can be used as a standing wave (SW) cavity for which the RF energy is reflected back in the $-z$ direction when it reaches the end of the structure and establishes a standing wave oscillation within the cavity by a superposition with the forward-directed wave. For a traveling wave cavity, the time needed for the electromagnetic energy to

fill the cavity is evaluated as:

$$t_{\mathrm{F,\,TW}} = \int_0^L \frac{\mathrm{d}z}{v_{\mathrm{g}}(z)} \tag{1.16}$$

In equation (1.16), $t_{\mathrm{F,\,TW}}$ is called the filling time and $v_{\mathrm{g}}(z)$ is the group velocity of the wave. For the standing wave configuration, the filling time definition is slightly different since the cavity is already filled *a priori* by a standing wave, and therefore is evaluated as the time taken for the electromagnetic energy to be dissipated by $1/e$ in the cavity walls. This filling value is obtained as twice the ratio of the stored energy U_{cav} with the power dissipated in the walls P_{wall}, as expressed by equation (1.17).

$$t_{\mathrm{F,\,SW}} = \frac{2U_{\mathrm{cav}}}{P_{\mathrm{wall}}} \tag{1.17}$$

Once the cavity is filled with electromagnetic energy, we can evaluate the energy gain ΔW of a particle of charge q that enters a cavity on-axis with phase ϕ by:

$$\Delta W = \int_0^L qE_z(0,0,z)e^{-i(\omega t+\phi)}\mathrm{d}z \tag{1.18}$$

Assuming a constant velocity of the particle crossing the cavity as an approximation, it is possible to relate the on-axis position by:

$$z = vt = \beta ct \qquad \Longrightarrow \qquad t = \frac{z}{\beta c}$$

We can then further evaluate an important parameter called the transit time factor T, which is defined as the ratio of the energy gained in the time-varying RF electric field to the average field, as shown by the following equation (1.19):

$$T = \frac{\int_{-\frac{L}{2}}^{\frac{L}{2}} E_z(z)e^{-i\left(\frac{\omega z}{\beta c}\right)}\mathrm{d}z}{\int_{-\frac{L}{2}}^{\frac{L}{2}} E_z(z)\mathrm{d}z} = \frac{\int_{-\frac{L}{2}}^{\frac{L}{2}} E_z(z)e^{-i\left(\frac{\omega z}{\beta c}\right)}\mathrm{d}z}{\overline{E}_0 L} \tag{1.19}$$

The numerator of equation (1.19) is in fact the Fourier transform of the on-axis electric field distribution windowed in the range $\left[-\frac{L}{2}, \frac{L}{2}\right]$. The transit time factor is a dimensionless quantity that measures the energy gain reduction caused by the sinusoidal time variation of the field in the gap. Since it is expressed as a normalized quantity, it does not depend on the amplitude

of the electric field, nor on the position z since it is integrated over all z assuming a periodic cavity shape. It is bound to values in the range $[-1, 1]$, and characterizes the effectiveness of the longitudinal acceleration for a normalized particle velocity β passing through a cavity of length L. This allows to express the energy gain per gap ΔW of equation (1.18) by the following simplified equation (1.20):

$$\Delta W = q\overline{E}_0 LT\cos(\phi) \tag{1.20}$$

Hence, it is necessary to adapt the cavity's shape such that it maximizes the transit time factor to optimize the energy transfer of the RF wave to the particle traveling at a given velocity. This is why typically the cavity gap L increases as the particle velocity increases to maximize the interaction of the forward-oriented electric field with the particle kinematics through synchronicity. An important quantity that evaluates the level of RF energy concentration in the useful region (*i.e.* if the structure is optimized) is called the shunt impedance Z, and is calculated as the ratio of the squared average electric field $\overline{E}_0^2$ to the power per unit of length that is dissipated on the surface of the walls $\frac{dP_{\text{wall}}}{dL}$ as shown by the following equation (1.21):

$$Z = \frac{\overline{E}_0^2}{\frac{dP_{\text{wall}}}{dL}} \tag{1.21}$$

However, to properly design the cavity, it is more practical to evaluate the effective shunt impedance ZT^2, which measures if the structure is adapted to the velocity of the particle to be accelerated at a given position. This is shown through equation (1.22):

$$ZT^2 = \frac{(\overline{E}_0 T)^2}{\frac{dP_{\text{wall}}}{dL}} \tag{1.22}$$

This is a more useful quantity to evaluate in order to maximize the energy gain of the particle per unit power dissipation. Indeed, a superior limit exists for the maximal electric field reachable in a cavity before the electrical breakdown occurs. Nowadays, accelerating electric fields generated from modern RF sources reach peak values on the order of 100 MV/m in the GHz frequency range. Hence, the maximum kinetic energy obtained with linacs depends essentially on the full length of the structure. For example, the about 1 m-long cavity structure for a medical linac accelerates electrons up to 22 MeV, whereas accelerated electrons at SLAC (3 km-long) can reach 50 GeV. Particularly for electrons, one of the great advantages of linacs is the absence of energy loss through synchrotron radiation, since the charged particles travel almost straight ahead and therefore have low radiative energy losses compared to synchrotron light sources,

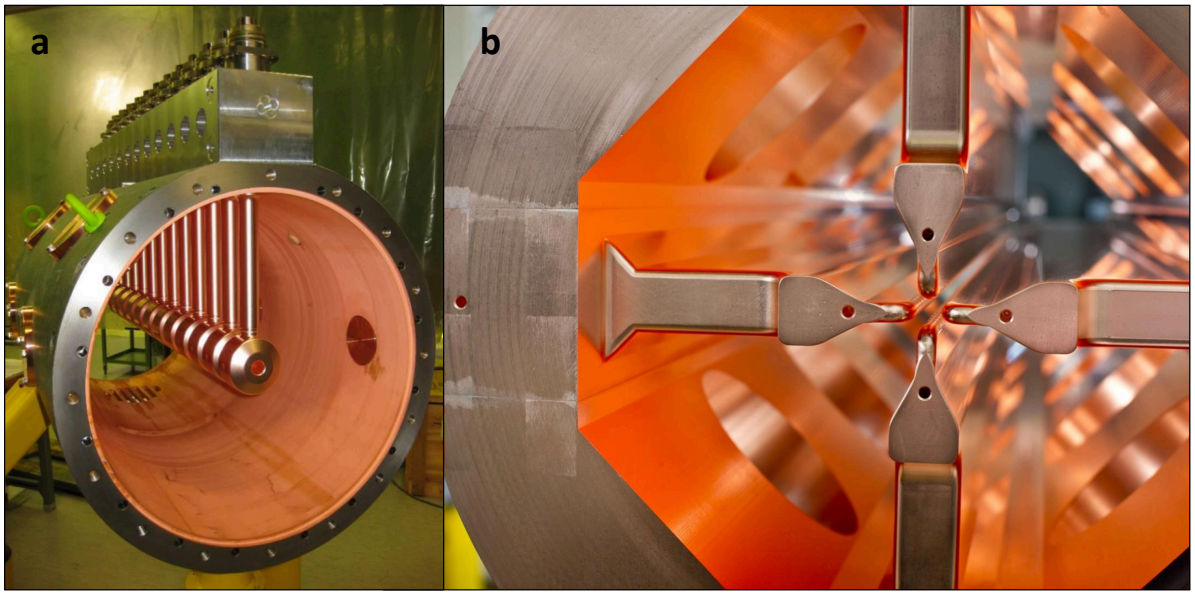

FIGURE 1.3: (a) Drift Tube Linac (DTL) cavity. (b) RadioFrequency Quadrupole (RFQ) cavity. These figures are extracted and adapted from [6].

which are discussed further in this dissertation (see section 1.2.4.1). Aside from the cavity length L and the full length of the structure, the cavity shape is the most important part for an optimized energy transfer. There exist different types of effective structures for acceleration, the most basic one being the Drift Tube Linac (DTL), as shown in Figure 1.3.a. It essentially consists of a cylindrical structure with drift tubes placed at the precise positions where the electric field is decelerating the particles. This is done to screen the undesired electric field portion for the particles. More complex cavity types are now used, such as the RadioFrequency Quadrupole (RFQ) cavity which consists of an electric quadrupole with a continuous longitudinal oscillation, as is shown in Figure 1.3.b. In particular, the RFQ is the only structure that allows simultaneously for transverse focusing, longitudinal bunching and acceleration with a continuous beam of particles, however being most effective for low β values below 0.1. Hence, the type of structure to adopt depends on the type of particle to accelerate (mass and charge) and the desired application (beam current required, kinetic energy, pulsed or continuous beam, *etc.*).

1.2.2.2 X-Ray Free Electron Lasers

Electron linacs are also used to drive one of the brightest type of X-ray light source existing to this day, such as the Linac Coherent Light Source (LCLS) located at the end of the 3

km-long SLAC accelerator in California, USA. The emission of EM radiation (*i.e.* photons) from accelerated charged particles is one of the basic laws of Nature that is deduced from Maxwell's equations, and its mathematical development is shown in section 1.2.4.1. In this context, a high-energy electron beam that passes through a magnetic field is deviated from its initial trajectory, and leads to the emission of X-rays, called *Synchrotron* radiation. When insertion devices are placed at the end of electrons linacs, for example wigglers or undulators as shown in Figure 1.4, an intense emission of X-rays builds up as the electron beam travels through the device, and produces an ultra-bright, short pulsed (fs range), coherent X-ray light source called the X-ray Free Electron Laser (XFEL). In a similar fashion to conventional lasers in the UV-visible-infrared range, the gain medium of XFELs is the electron bunch itself that emits X-ray photons while traveling in an undulator, seeding an amplification process called Self-Amplified Spontaneous Emission (SASE). More precisely, the emitted X-ray photons further stimulate the emission process through constructive interference while traveling concomitantly with the relativistic electron bunch, which travels at the speed of light. An undulator or wiggler is designed as a series of magnetic dipoles in periodically alternating directions, making the charged particles to oscillate transversely as they travel in the longitudinal direction, and leads to the periodic emission of synchrotron radiation. The full mathematical derivation for the theoretical frequency distribution of radiated intensity $\frac{d^2I}{d\Omega d\omega}$ can be found in several textbooks on synchrotron radiation. This derivation implies to solve the so-called *radiation integral*, and has the following solution:

$$\frac{d^2I}{d\Omega d\omega}(\theta,\omega) = \frac{e^2}{16\pi^3\varepsilon_0 c}\left(\frac{2\omega R}{3c\gamma^2}\right)^2 (1+\gamma^2\theta^2)^2\left[K_{2/3}^2(\xi) + \frac{\gamma^2\theta^2}{1+\gamma^2\theta^2}K_{1/3}^2(\xi)\right] \tag{1.23}$$

$$\text{with} \quad \xi = \frac{\omega R}{3c\gamma^3}(1+\gamma^2\theta^2)^{3/2}$$

In equation (1.23), R is the particle's bending radius passing through the magnetic field (*i.e.* related to the magnetic rigidity shown in equation (1.33)), θ is the azimuthal angle of emission, ω is the frequency of the emitted wave, γ is the relativistic Lorentz factor and $K_i(\xi)$ is the modified Bessel function of the second kind. This rather complex distribution is characterized by two very important quantities, the critical energy $\mathcal{E}_c$ and the critical angle θ_c, obtained by the following relationships:

$$\mathcal{E}_c = \hbar\omega_c = \frac{3\hbar c}{2R}\gamma^3 \qquad \theta_c = \frac{1}{\gamma}\left(\frac{\omega_c}{\omega}\right)^{1/3} \tag{1.24}$$

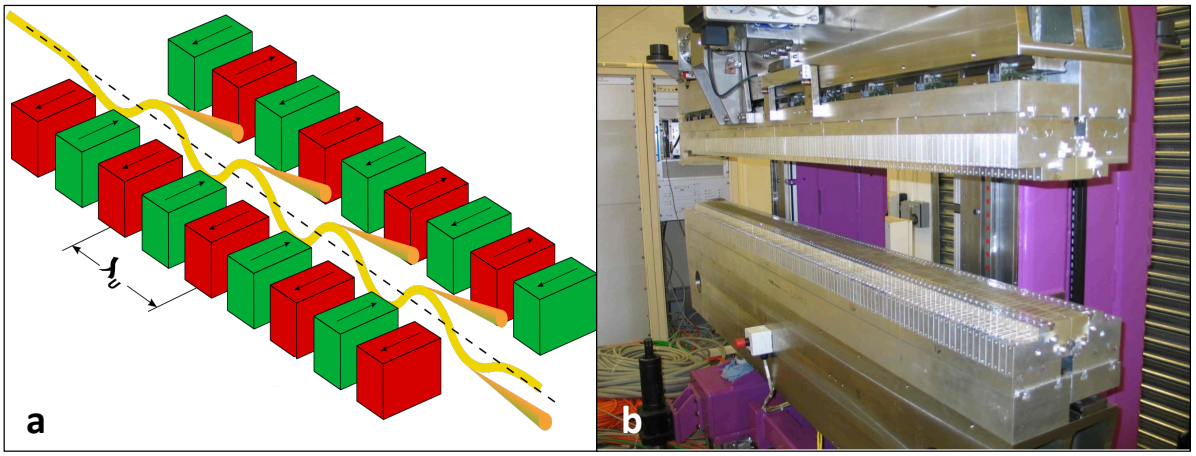

FIGURE 1.4: Emission of radiation from a high-energy electron beam using an undulator. (a) Schematic diagram of an undulator. (b) Experimental undulator used in an X-ray light source.

The critical energy $\mathcal{E}_c$ is the median emitted photon energy that delimits 50% of the total radiated energy above and below (strongly skewed distribution with its maximum occurring around $0.3\mathcal{E}_c$), and similarly for the critical angle θ_c. Since the radiative emission from an undulator is the result of constructive interference and of a resonant process, this leads to the emission of harmonics with wavelengths λ_n determined by the geometry of the undulator, expressed by the following equation:

$$\lambda_n = \frac{\lambda_u}{2\gamma^2 n}\left(1 + \frac{K^2}{2} + \gamma^2\theta^2\right) \quad \text{, with} \quad K = \frac{eB_0\lambda_u}{2\pi m_0 c} \tag{1.25}$$

In equation (1.25), n is the harmonic integer order, λ_u is the undulator's magnetic wavelength, B_0 in the on-axis undulator magnetic field and K is called the undulator parameter. The latter parameter K strongly defines the spectrum of harmonics emitted. For instance, small K value (*i.e.* $K \ll 1$, wiggler case) will generate an intense emission of low-order harmonics resulting from a narrow emission (small divergence angle θ), whereas large K values (*i.e.* $K \gg 1$, undulator case) will generate a broader spectrum with high-order harmonics, however with lower intensities due to a broader angular divergence. Finally, we can find the energy of the harmonic emitted using $\mathcal{E}_n = 2\pi\hbar c/\lambda_n$.

1.2.3 Cyclotrons

As the new discoveries in physics were blooming in the early 1900's, the need for higher charged particle kinetic energies to study the fundamental properties of matter was constantly

increasing, pushing engineers to develop new accelerating structures. Following the invention of the RF-based linear accelerator by Rolf Wideröe in 1928, Ernest O. Lawrence, associate professor at UC Berkeley at the time, looked at Wideröe's work (written in German) and had the brilliant idea to immerse the accelerating cavity into a constant magnetic field which would curve particle trajectories and allow to re-use the same cavity for acceleration, instead of having a linear series of accelerating cavities. This would be the birth of the cyclotron, and Pr Lawrence published the successful concept with his student Milton S. Livingston in 1932 [7], for which their received the Nobel Prize in Physics of 1939. The following sections are describing the relevant equations for the comprehension of basic particle dynamics in a cyclotron, along with the main key concepts.

1.2.3.1 Uniform circular motion in closed orbits

Let us first consider the simple case of a charged particle of mass m and charge q, traveling at a non-relativistic velocity v_θ in a uniform magnetic field B_z. The particle will therefore undergo the Lorentz force, and its equations of motion can be solved using Newton's law, which we will express in cylindrical coordinates for practical reasons:

$$\boldsymbol{F} = \frac{d\boldsymbol{p}}{dt} = q\boldsymbol{v} \times \boldsymbol{B}$$

$$m\langle \dot{v}_r, \dot{v}_\theta, \dot{v}_z \rangle = q \begin{vmatrix} \hat{e}_r & \hat{e}_\theta & \hat{e}_z \\ v_r & v_\theta & v_z \\ B_r & B_\theta & B_z \end{vmatrix} \tag{1.26}$$

Further developing the velocities and accelerations in cylindrical coordinates using $\boldsymbol{v} = \langle v_r, v_\theta, v_z \rangle = \langle \dot{r}, r\dot{\theta}, \dot{z} \rangle$ and $\dot{\boldsymbol{v}} = \langle \dot{v}_r, \dot{v}_\theta, \dot{v}_z \rangle = \langle \ddot{r} - r\dot{\theta}^2, r\dot{\theta} + 2\dot{r}\dot{\theta}, \ddot{z} \rangle$ gives the following set of equations:

$$\ddot{r} - r\dot{\theta}^2 = \frac{q}{m}\left(r\dot{\theta}B_z - \dot{z}B_\theta\right) \tag{1.27}$$

$$r\ddot{\theta} + 2\dot{r}\dot{\theta} = \frac{q}{m}\left(\dot{z}B_r - \dot{r}B_z\right) \tag{1.28}$$

$$\ddot{z} = \frac{q}{m}\left(\dot{r}B_\theta - r\dot{\theta}B_r\right) \tag{1.29}$$

Further considering that $\boldsymbol{B} = \langle B_r, B_\theta, B_z \rangle = \langle 0, 0, B_z \rangle$, equations (1.27), (1.28) and (1.29) now become:

$$\ddot{r} - r\dot{\theta}^2 = \frac{q}{m} r\dot{\theta} B_z \tag{1.30}$$

$$r\ddot{\theta} + 2\dot{r}\dot{\theta} = -\frac{q}{m}\dot{r} B_z \tag{1.31}$$

$$\ddot{z} = 0 \tag{1.32}$$

The solution of equations (1.30), (1.31) and (1.32) are uniform circular motion, for which the trajectory is a circle (also called closed orbit). In equation (1.30), the centripetal force $-mr\dot{\theta}^2$ balances out the Lorentz force $qr\dot{\theta}B_z$, which leads to:

$$m\frac{v_\theta^2}{r} = q v_\theta B_z \qquad \Longrightarrow \qquad B_z r = \frac{m v_\theta}{q} = \frac{p}{q} \tag{1.33}$$

Equation (1.33) is called the magnetic rigidity, showing that particles with increasingly higher velocities (or momentum p) will travel in circles with increasing radius r. The revolution frequency f_{rev} and its corresponding angular frequency ω_{rev} are given by:

$$f_{\text{rev}} = \frac{v_\theta}{2\pi r} \qquad \Longrightarrow \qquad \omega_{\text{rev}} = 2\pi f_{\text{rev}} = \frac{q B_z}{m} \tag{1.34}$$

which is also known as the Larmor precession frequency. Considering that the particle takes always the same time to perform one full revolution, called the *isochronism* condition, and further inserting an RF voltage source half-way through one rotation to accelerate the particle at each passage, it is necessary to adjust its frequency ω_{RF} such that it matches the particle's precession frequency ω_{rev}. Hence, we get the following timing condition, which is known as the *synchronism* condition:

$$\omega_{\text{RF}} = \alpha \omega_{\text{rev}} \tag{1.35}$$

where α is defined as an integer harmonic number. Thus, we see that by having a circular motion separated in two sections (called Dees) and by having proper phase matching with an alternating voltage source, it is possible to accelerate a particle in circular motion, as is shown on Figure 1.5. The particle bunch will therefore undergo a spiral motion since its momentum increases at every half turn which will increase its precession radius, as dictacted by the magnetic rigidity equation (1.33). Having more than one bunch accelerated at the same time implies to use only odd harmonic numbers $\alpha = 1, 3, 5, \ldots$ for proper phase matching to avoid

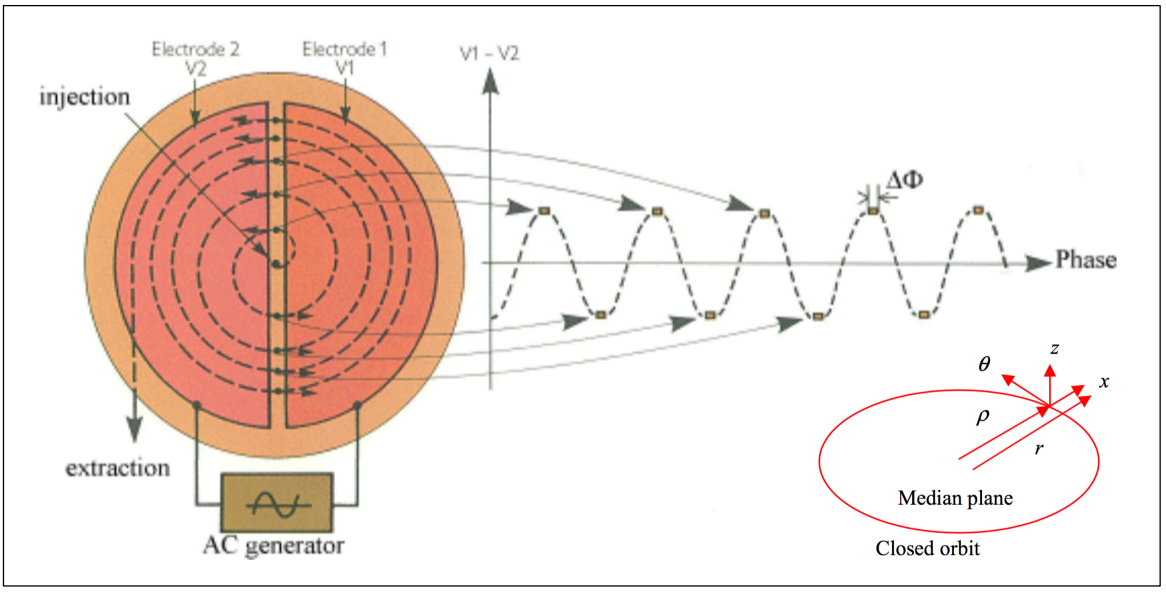

FIGURE 1.5: Cyclotron schematic diagram and coordinate system (inlet). This figure is adapted from [8].

decelerating the particle bunches. Hence, we see that the concept of cyclotrons allows to build devices that are relatively compact and cost-effective, as opposed to a very long series of RF cavities put linearly one after the other to reach the same particle energies. This innovative accelerator design has enabled several breakthroughs over time and now finds application in nuclear physics (from fundamental to applied research) and in the medical domain, in particular for radioisotopes production used in nuclear medicine as well as for cancer treatments (heavy ion radiotherapy).

1.2.3.2 Transverse dynamics

Horizontal stability

Let's now consider more realistic particle beams by including imperfections in the equations. The reference particles will travel along the aforementioned closed orbit rotations, but we will now consider the motion of particles with small orbit deviation x around the closed orbit or radius ρ, now with the position radius defined as:

$$r = \rho + x = \rho\left(1 + \frac{x}{\rho}\right) \tag{1.36}$$

Since the field B_z is never uniform in practical terms, we now develop the magnetic field B_z in Taylor series and keep the first order field defect:

$$B_z(r) = \sum_{n=0}^{\infty} \frac{\partial^n B_z}{\partial r^n}\bigg|_{r=\rho} (r-\rho)^n \approx B_0 + \frac{\partial B_z}{\partial x} x = B_0 \left(1 + \frac{\rho}{B_0}\frac{\partial B_z}{\partial x}\frac{x}{\rho}\right) = B_0 \left(1 - N\frac{x}{\rho}\right) \tag{1.37}$$

where B_0 is the zero-order uniform field, and we define $N = -\dfrac{\rho}{B_0}\dfrac{\partial B_z}{\partial x}$ as the field index. The parameter N represents the fractional change of the magnetic field along the radial axis. Being positive for a decreasing field $B_z(r)$ with radius r and negative for an increasing field in the outward direction. This small orbit deviation with a radially varying magnetic will induce a horizontal (radial) restoring force on the particles. Equation (1.30) now becomes:

$$\ddot{x} - \frac{v_\theta^2}{r} = \frac{q}{m} v_\theta B_z(r) \tag{1.38}$$

Using the following first-order Taylor series development for $1/r$:

$$\frac{1}{r} = \frac{1}{\rho + x} = \frac{1}{\rho\left(1 + \frac{x}{\rho}\right)} = \frac{1}{\rho}\left(1 + \frac{x}{\rho}\right)^{-1} \approx \frac{1}{\rho}\left(1 - \frac{x}{\rho}\right)$$

We can now re-write the force equation (1.38) as:

$$\ddot{x} - \frac{v_\theta^2}{\rho}\left(1 - \frac{x}{\rho}\right) = \frac{q}{m} v_\theta B_0 \left(1 - N\frac{x}{\rho}\right)$$

Further noting that $qB_0/m = v_\theta/\rho = \omega_0$, we find the following equation of movement:

$$\ddot{x} + \omega_0^2 (1 - N) x = 0 \tag{1.39}$$

Equation (1.39) is the well-known harmonic oscillator equation with angular frequency $\omega_r = \omega_0 \nu_r = \omega_0 \sqrt{1 - N}$. The parameter ν_r is called the horizontal betatron oscillation number, and is the ratio of the number of horizontal oscillations (also called betatron oscillations) around the closed orbit per full rotation. The horizontal stability is therefore achieved when $\nu_r = \sqrt{1 - N}$ is real, hence for $N < 1$. A field index $0 < N < 1$ corresponds to a decreasing field B_z with increasing closed orbit radius ρ, whereas $N < 0$ represents an increasing field B_z. An imaginary angular frequency ω_r (*i.e.* for $N > 1$) would produce unstable beam oscillations in the horizontal plane, leading to exponential beamsize growth and therefore to beam loss.

Vertical stability

Since the main field varies radially, *i.e.* $B_z = B_z(r)$, this induces a radial field component B_r as we can infer from Ampère's law, leading to:

$$\boldsymbol{\nabla} \times \boldsymbol{B} = 0 \quad \Longrightarrow \quad \frac{\partial B_r}{\partial z} - \frac{\partial B_z}{\partial r} = 0$$

$$\therefore \quad B_r = \int \frac{\partial B_z(r)}{\partial r} \mathrm{d}z = \frac{\partial}{\partial x}\left[B_0\left(1 - N\frac{x}{\rho}\right)\right] z = -N\frac{B_0}{\rho} z \tag{1.40}$$

Still considering that $B_\theta = 0$ and inserting equation (1.40) into (1.29) leads to:

$$\ddot{z} + \omega_0^2 N z = 0 \tag{1.41}$$

which is again the equation for harmonic oscillations, now with angular frequency $\omega_z = \omega_0 \nu_z = \omega_0 \sqrt{N}$. Similarly to its radial homologue, the parameter ν_z is called the vertical betatron oscillation number, and is the ratio of the number of vertical oscillations around the closed orbit per full rotation. Vertical stability is achieved when $\nu_r = \sqrt{N}$ is real, hence for $N > 0$. Hence, it appears that to achieve both horizontal and vertical beam stability at the same time, the field index must be $0 < N < 1$, which corresponds to a decreasing field $B_z(r)$ which increasing radius r. We will show that this particular condition in incompatible with the isochronism condition for relativistic particles, and therefore does not allow this type of cyclotrons to reach high energies, which are limited by the geometry of the system.

1.2.3.3 Isochronism and focusing conditions for relativistic beams

For relativistic particles, the mass increases as $m = \gamma m_0$, therefore ω_{rev} becomes:

$$\omega_{\text{rev}} = \frac{qB_z}{\gamma m_0} \tag{1.42}$$

Hence, to keep the isochronism condition, the ratio $B_z(r)/\gamma(r)$ must stay constant, and since $\gamma(r)$ is strictly increasing with radius r, then $B_z(r)$ must also increase. This implies that $N < 0$ as a necessary condition, as per its definition from equation (1.37), which is clearly incompatible with vertical focusing. Reaching increasingly higher kinetic energies necessarily leads to

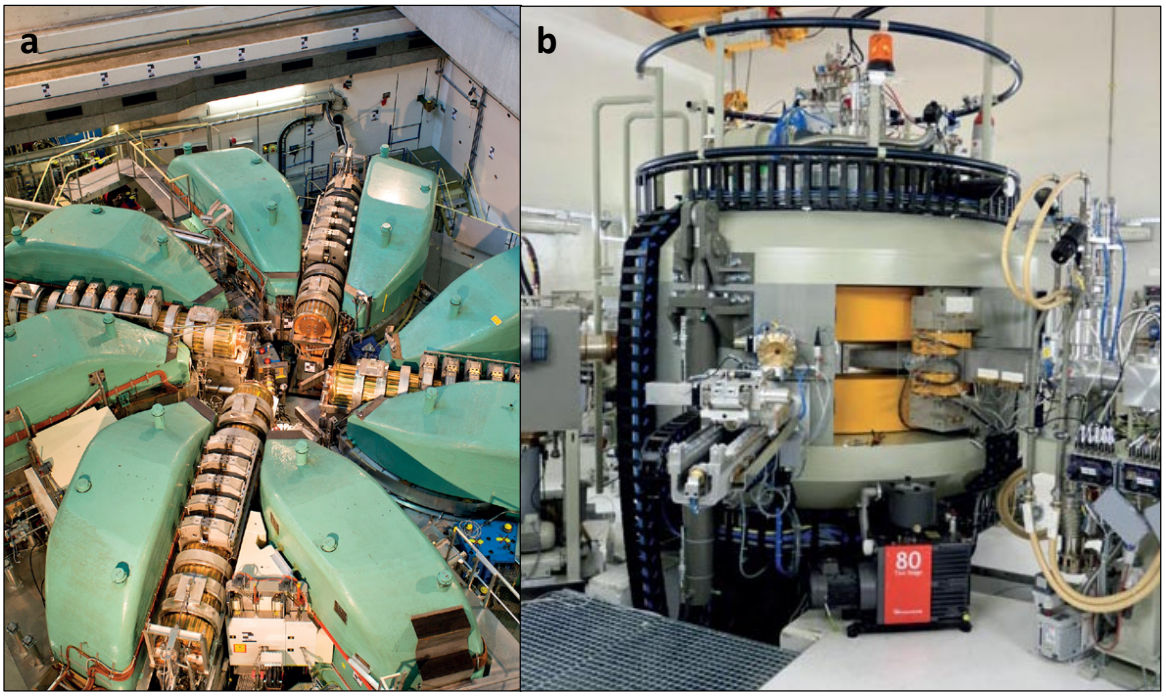

FIGURE 1.6: (a) 590 MeV cyclotron at the Paul Scherrer Institute (PSI). Photo credit: PSI. (b) Cyclone® 30 of 30 MeV for radioisotopes production from the company *IBA*. Photo credit: *IBA*.

unstable vertical oscillations and therefore to beam loss. This means that the maximum energy attainable is limited by the geometry of the machine. Additional vertical focusing must be inserted into the system, and this is done by including an azimuthal field component B_θ to compensate the instability as we recall from equation (1.29). An azimuthally varying field $B_z(r,\theta)$ will induce an azimuthal field component B_θ again from Ampère's law, which in turn will produce a vertical focusing force $F_z = q\dot{r}B_\theta$ to compensate the instability. This is the particular reason why cyclotrons with sectored magnets were developed, as can be seen in Figure 1.6.a with the 590 MeV proton cyclotron at the Paul Scherrer Institute (PSI) in Switzerland. This concept also avoided to produce cyclotrons with only one very large magnetic dipole, which are difficult to produce. Moreover, a greater number of RF cavities can be inserted between the sectored magnets, as can be noted from the four RF cavities in Figure 1.6.a. In Figure 1.6.b is shown a very compact 30 MeV commercial cyclotron that is used nowadays for the production of radioisotopes used in nuclear medicine.

1.2.3.4 Synchrocyclotrons

When high-energy relativistic particles are required for some applications, another cyclotron design can be done by continuously satisfying the synchronism condition from equation (1.35), even if the isochronism condition is not respected. Indeed, as the particles are accelerated by the RF fields, their kinetic energy increases and therefore also the relativistic factor $\gamma(r)$, which reduces the angular revolution frequency ω_{rev} as the mass of the particle increases. Hence, is it possible to synchronize the RF frequency ω_{RF} with the varying revolution frequency, by accelerating one particle bunch at a time from the injection to the extraction. This type of frequency-modulated cyclotron is thus necessarily pulsed, and is called synchrocyclotron. It is now becoming increasingly popular for high-energy applications like proton-therapy, for which 200-250 MeV protons are required in order to reach deep-seated tumors. Synchrocyclotrons avoid the need for vertical focusing with sectored magnets, have quasi-uniform magnetic field with a positive field index, and its design can be rather compact, hence being a very competitive alternative to sectored isochronous cyclotrons.

1.2.4 Synchrotrons

In 1943, a little more than a decade after the invention of the cyclotron, while working on RF sources for radar technologies at the University of Birmingham in England, the Australian Marcus Oliphant proposes the concept of a constant-orbit frequency-modulated particle accelerator, which would be called a synchrotron. Edwin McMillan, while working on the Manhattan Project for the development of transuranium elements, would further develop the concept of the synchrotron, independently and at the same time as the Soviet Vladimir Veksler. Recalling the magnetic rigidity equation (1.33), the concept of performing a frequency-modulated acceleration on a constant orbit necessarily requires that the steering magnetic field increases in time (*i.e.* using electro-magnets). The idea is to simultaneously ramp up the frequency of the RF source such as to keep the *synchronism* condition (see equation (1.35)) as the particles are accelerated, in order to constantly match the revolution frequency. They would both be acknowledged for establishing the so-called *phase stability principle* in 1945, which showed that proper RF phase matching would keep particles bunched together and thus provide a stable beam. Early synchrotrons have then successfully been built such as the 300 MeV electron synchrotron at the University of Michigan in 1949, as well as the 6 GeV proton synchrotron at UC

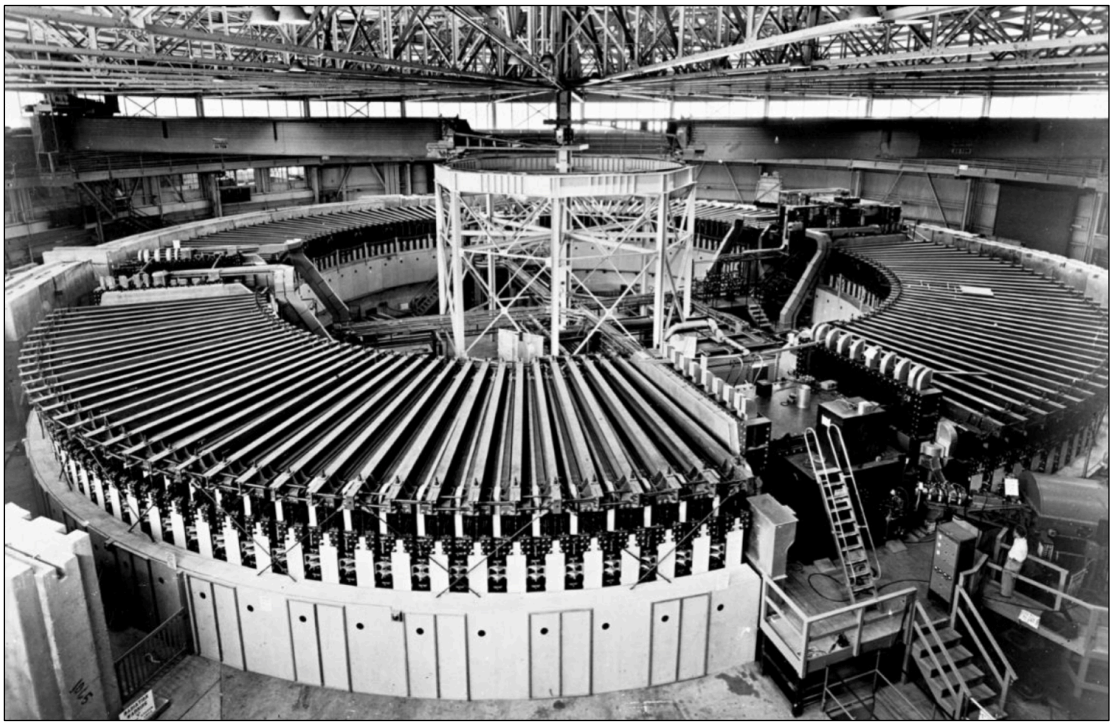

FIGURE 1.7: Early synchrotron: the 6 GeV proton synchrotron, named BeVatron at UC Berkeley in 1954, built for the discovery of the anti-proton which occurred in 1955. This figure is reproduced from [9].

Berkeley in 1954 tailored specifically for the discovery of the anti-proton which occurred the year after (see Figure 1.7). Proton synchrotrons were first used in fixed-target collisions, and are now used as head-on particle colliders in order to double the useful energy in the center-of-mass (COM). The largest proton synchrotron up to this day is the 7 TeV (*i.e.* 14 TeV in COM) Large Hadron Collider (LHC) at the Centre Européen pour la Recherche Nucléaire (CERN) located near Geneva, Switzerland, with part of the 27 km-long accelerator tunnel located in France. The development of the LHC led to the discovery of the Higgs boson in 2012 [10, 11] and completed the search for the missing particle in the Standard Model.

Concerning electron synchrotrons, experimental physicists working on early synchrotrons in the 1950's noticed parasitic emissions of X-ray radiation coming out of the bending magnets. These X-ray emissions were called synchrotron radiation. Indeed, the concept of radiation emission from accelerated charged particles was known at the time, however this effect was a direct demonstration of the Larmor relationship for radiative energy loss. More precisely, since the synchrotron radiative yield is proportional to $1/m^4$, electrons accelerated in synchrotrons

require substantial energy compensation with RF sources to balance the energy losses by synchrotron radiation emissions, and then be further accelerated, which prevents their acceleration to ultra-relativistic energies in the TeV range. Hence, the only option to reach TeV energies for electrons (and positrons) is a linear accelerator that avoids synchrotron radiative losses. In this context, the Compact Linear Collider (CLIC) is a concept being developed for the construction of a multi-TeV electron-positron linac collider, and is expected to be in operation in Geneva, Switzerland by 2035. The next section 1.2.4.1 discusses the mathematical framework of radiation emission from accelerated charged particles, and then shows how electron synchrotrons are used nowadays as storage rings to generate ultra-high brilliance light sources.

1.2.4.1 Emission of radiation by charged particles

The purpose of this section is to provide a mathematical basis for the comprehension of radiative emissions from an accelerated charged particle. The complete details of the derivations can be found in numerous textbooks on relativistic electromagnetism [12]. Several derivations can be very lengthy and go out of the scope of this dissertation. The goal of the following derivations will therefore be to give a framework to reach the main results, which are essential for the proper understanding of the phenomena occurring in the context of this doctoral work. Starting from Maxwell's equations, the general expressions for the electromagnetic wave equation using the scalar potential Φ and the vector potential $\boldsymbol{A}$, in the Lorenz gauge, can be written as shown in equations (1.11) and (1.12), where the charge density $\rho = \rho(\boldsymbol{r}, t)$ and current distribution $\boldsymbol{J} = \boldsymbol{J}(\boldsymbol{r}, t)$ are functions of space $\boldsymbol{r}$ and time t. The general solutions to these equations, in the Lorenz gauge, are expressed as:

$$\Phi(\boldsymbol{r}, t) = \frac{1}{4\pi\varepsilon_0} \iiint_{\mathbb{R}^3} \frac{\rho(\boldsymbol{r}', t_{\text{ret}})}{|\boldsymbol{r} - \boldsymbol{r}'|} \, \mathrm{d}^3\boldsymbol{r}' \tag{1.43}$$

$$\boldsymbol{A}(\boldsymbol{r}, t) = \frac{\mu_0}{4\pi} \iiint_{\mathbb{R}^3} \frac{\boldsymbol{J}(\boldsymbol{r}', t_{\text{ret}})}{|\boldsymbol{r} - \boldsymbol{r}'|} \, \mathrm{d}^3\boldsymbol{r}' \tag{1.44}$$

where $t_{\text{ret}} = t - \frac{1}{c}|\boldsymbol{r} - \boldsymbol{r}'|$ is the retarded time. This "retarded time" can be viewed as the propagation time of the EM wave from the point of emission to an observer. For a single charged particle, we use the following 3D Dirac distributions to describe a moving point charge:

$$\rho(\boldsymbol{r}, t_{\text{ret}}) = q\delta^3(\boldsymbol{r} - \boldsymbol{r}_0) \qquad \boldsymbol{J}(\boldsymbol{r}, t_{\text{ret}}) = q\boldsymbol{v}\delta^3(\boldsymbol{r} - \boldsymbol{r}_0) \tag{1.45}$$

We now define the absolute distance $R = \boldsymbol{R} \cdot \hat{n} = |\boldsymbol{r} - \boldsymbol{r}_0|$ from a point charge located at $\boldsymbol{r}_0$, along with its associated unit direction vector $\hat{n} = (\boldsymbol{r} - \boldsymbol{r}_0) \,/\, |\boldsymbol{r} - \boldsymbol{r}_0|$. After integration of the Dirac distributions in equations (1.43) and (1.44), we find:

$$\Phi(\boldsymbol{r}, t) = \frac{q}{4\pi\varepsilon_0} \left[\frac{1}{(1 - \hat{n} \cdot \boldsymbol{\beta}) R} \right]_{\text{ret}} \tag{1.46}$$

$$\boldsymbol{A}(\boldsymbol{r}, t) = \frac{q}{4\pi\varepsilon_0 c} \left[\frac{\boldsymbol{\beta}}{(1 - \hat{n} \cdot \boldsymbol{\beta}) R} \right]_{\text{ret}} \tag{1.47}$$

with $\boldsymbol{v} = \boldsymbol{\beta} c$ and where we have used $c = 1/\sqrt{\varepsilon_0 \mu_0}$. Equations (1.46) and (1.47) are the general expressions for the potentials of EM fields generated by a moving charged particle, and are called the Liénard-Wiechert potentials. The brackets $[...]_{\text{ret}}$ mean that they are evaluated at the retarded time $t_{\text{ret}} = t - R(t)/c$. The Liénard-Wiechert electric $\boldsymbol{E}$ and magnetic $\boldsymbol{B}$ fields can then be found using $\boldsymbol{E} = -\boldsymbol{\nabla}\Phi - \dfrac{\partial \boldsymbol{A}}{\partial t}$ and $\boldsymbol{B} = \boldsymbol{\nabla} \times \boldsymbol{A}$. After derivation and evaluation at the retarded time, we find the following expressions:

$$\boldsymbol{E}(\boldsymbol{r}, t) = \frac{q}{4\pi\varepsilon_0} \left[\frac{\hat{n} - \boldsymbol{\beta}}{\gamma^2 (1 - \hat{n} \cdot \boldsymbol{\beta})^3 R^2} \right]_{\text{ret}} + \frac{q}{4\pi\varepsilon_0 c} \left[\frac{\hat{n} \times (\hat{n} - \boldsymbol{\beta}) \times \dot{\boldsymbol{\beta}}}{(1 - \hat{n} \cdot \boldsymbol{\beta})^3 R} \right]_{\text{ret}} \tag{1.48}$$

$$\boldsymbol{B}(\boldsymbol{r}, t) = \frac{1}{c} \hat{n} \times \boldsymbol{E} \tag{1.49}$$

In equation (1.48), the first term is called the velocity field (or *near* field since effective for small R values as it follows $1/R^2$), whereas the second term is called the acceleration field (or *far* field since it is dominant for large R values as it follows $1/R$). Hence, the rest of the derivation will be concerned about the acceleration field and thus we will drop the velocity field, equivalent to evaluating the field with an observer placed far away from the charged particle. The power density of the radiated energy is found using the Poynting vector:

$$\boldsymbol{S} = \frac{\boldsymbol{E} \times \boldsymbol{B}}{\mu_0} \tag{1.50}$$

We will now distinguish two cases for the emission of radiation: The first case is when the acceleration $\dot{\boldsymbol{\beta}}$ is oriented parallel to the velocity of the charged particle $\boldsymbol{\beta}$, called *Bremsstrahlung* radiation. The second case is obviously when $\dot{\boldsymbol{\beta}}$ is perpendicular to the velocity of the charged particle $\boldsymbol{\beta}$, called *Synchrotron* radiation. We will start in the non-relativistic approximation (*i.e.* low β values) and then further generalize in the relativistic regime.

Acceleration parallel to velocity: Bremsstrahlung radiation

In the case for $\boldsymbol{\beta} \,||\, \dot{\boldsymbol{\beta}}$, called *Bremsstrahlung* radiation, and for non-relativistic velocities (*i.e.* $\beta \approx 0$), we find the following emitted power density distribution:

$$S(R,\theta) = |\boldsymbol{S}| = \frac{|\boldsymbol{E}||\boldsymbol{B}|}{\mu_0} = \varepsilon_0 c|\boldsymbol{E}|^2 = \frac{1}{\varepsilon_0 c}\left(\frac{q\dot{\beta}}{4\pi R}\right)^2 \sin^2\theta \tag{1.51}$$

where $\dot{\beta} = |\dot{\boldsymbol{\beta}}|$. We see from equation (1.51) that the emitted power follows $\sin^2\theta$, hence that the EM emission is maximal in the direction perpendicular to the velocity of the particle (*i.e.* $\theta_{\max} = \pi/2$), and falls off as $1/R^2$. The total power radiated is found by integration $S(R,\theta)$ over a surface area A:

$$P = \int S(R,\theta)\,\mathrm{d}A = \int S(R,\theta)R^2\,\mathrm{d}\Omega = \int_0^{2\pi}\int_0^{\pi} S(R,\theta)\; R^2 \sin\theta\,\mathrm{d}\theta\mathrm{d}\phi$$

$$\therefore \quad P = \frac{q^2\dot{\beta}^2}{6\pi\varepsilon_0 c} \tag{1.52}$$

which is the well-known Larmor formula for the power radiated by a non-relativistic point charge in motion. It predicts that the radiated power is proportional to the square of the particle's charge q^2 and to the square of the acceleration $\dot{\beta}^2$. The Larmor formula is one of the basic laws of Nature and can re-formulated as follows: Any time a charged particle undergoes an acceleration (or deceleration), it emits part of its kinetic energy in the form of Bremsstrahlung photons. In the relativistic case, the emitted power density is expressed as:

$$S(R,\theta) = |\boldsymbol{S}|\frac{dt}{dt_{\text{ret}}} = \varepsilon_0 c|\boldsymbol{E}|^2\,(1 - \hat{n}\cdot\boldsymbol{\beta})$$

$$\therefore \quad S(R,\theta) = \frac{1}{\varepsilon_0 c}\left(\frac{q\dot{\beta}}{4\pi R}\right)^2 \frac{\sin^2\theta}{(1-\beta\cos\theta)^5} \tag{1.53}$$

From equation (1.53), there is an additional factor $(1-\beta\cos\theta)^5$ in the denominator which has the effect of tipping forward the radiative emission as the velocity increases. This is due to the fact that the charged particle has more momentum in the forward direction. We can also note that using $\beta = 0$ reduces equation (1.53) to the initial non-relativistic equation (1.51). It is also straightforward to show that, using the typical optimum searching methods:

$$\theta_{\max} = \arccos\left[\frac{1}{3\beta}(\sqrt{1+15\beta^2}-1)\right] \tag{1.54}$$

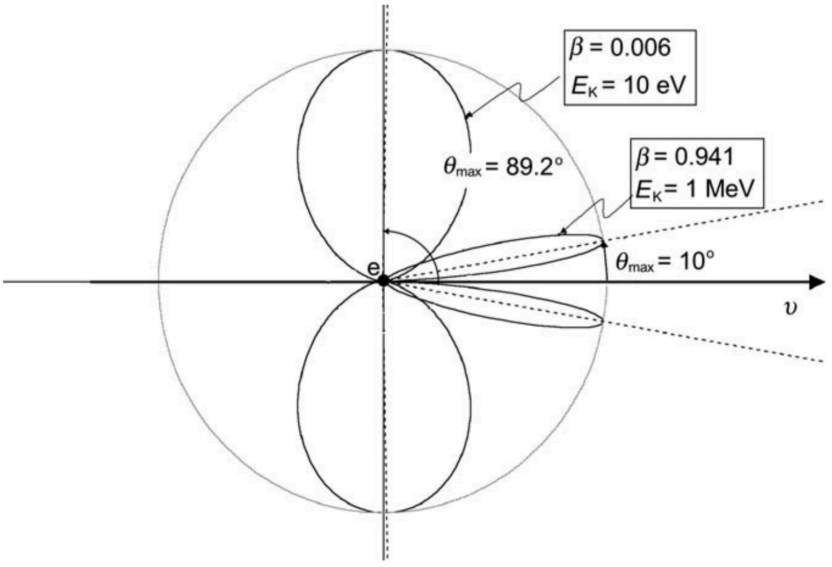

FIGURE 1.8: Angular distribution of Bremsstrahlung emissions for two electron kinetic energies of $\mathcal{E}_K = 10$ eV and $\mathcal{E}_K = 1$ MeV. Both radiation intensities are normalized to 1, however the emission intensity is 1.44×10^4 higher for the 1 MeV case. This figure is extracted and adapted from [13].

The expression shown in equation (1.54) reduces as expected to $\theta_{max} = \pi/2$ for $\beta \to 0$, moreover $\theta_{max} \to 0$ for $\beta \to 1$ (see Figure 1.8). The total power radiated, after integration over all angles, is now written as:

$$P = \frac{q^2 \dot{\beta}^2}{6\pi\varepsilon_0 c}\gamma^6 \tag{1.55}$$

which now exhibits an additional γ^6 factor, and thus becomes very important at relativistic velocities when $\gamma \gg 1$. Moreover, since $\gamma \propto 1/m_0$, it follows that the radiative yield is proportional to $1/m_0^6$, which means that the emission of radiation is extremely important for light charged particles like electrons compared to protons. More precisely, Bremsstrahlung radiation most often results from electrons experiencing acceleration when colliding with atomic nuclei, leading to momentum transfer and therefore to the emission of high-energy photons.

Acceleration perpendicular to velocity: Synchrotron radiation

In the case for $\boldsymbol{\beta} \perp \dot{\boldsymbol{\beta}}$, called *Synchrotron* radiation, and for the general case of relativistic energies, we can find the following power density from the acceleration field:

$$S(R,\theta) = \frac{1}{\varepsilon_0 c}\left(\frac{q}{4\pi R}\right)^2 \frac{\left|\hat{n} \times (\hat{n} - \boldsymbol{\beta}) \times \dot{\boldsymbol{\beta}}\right|^2}{(1 - \hat{n}\cdot\boldsymbol{\beta})^5}$$

$$\therefore \quad S(R,\theta) = \frac{1}{\varepsilon_0 c}\left(\frac{q\dot{\beta}}{4\pi R}\right)^2 \frac{1}{(1-\beta\cos\theta)^3}\left[1 - \frac{\sin^2\theta\cos^2\phi}{\gamma^2(1-\beta\cos\theta)^2}\right] \tag{1.56}$$

which now includes a dependence on the polar angle ϕ. After integration over all solid angles, the total radiated power now reads:

$$P = \int_0^{2\pi}\int_0^{\pi} S(R,\theta)R^2\sin\theta\,\mathrm{d}\theta\mathrm{d}\phi = \frac{q^2\dot{\beta}^2}{6\pi\varepsilon_0 c}\gamma^4 \qquad \Longrightarrow \qquad P_{\text{Brem}} = \gamma^2 P_{\text{Sync}} \tag{1.57}$$

Hence, this shows that the emission of radiation through Bremsstrahlung is greater than synchrotron radiation by a factor γ^2, noticeable only for relativistic velocities. In a synchrotron accelerator, the emission of radiation occurs mostly through synchrotron radiation due to the circular motion, and since $P \propto \gamma^4 \propto 1/m_0^4$, it follows that electrons loose approximately $(m_\text{p}/m_\text{e})^4 \approx 1836^4 \approx 10^{13}$ times more energy through synchrotron emissions than protons. As previously mentioned in the XFEL section 1.2.2.2, this is what limits electron synchrotrons to reach ultra-relativistic energies in the TeV range as opposed to proton synchrotrons like the LHC. For electrons, the only option to reach these energies is through linear accelerators in order to limit the radiative losses. As an example, to find the radiated power emitted in a bending magnet, one can use the centripetal acceleration $\dot{\beta} = a_\text{centri}/c = v^2/Rc = \beta^2 c/R$ and replace the curvature radius by the magnetic rigidity (1.33) $R = p/qB = \gamma\beta m_0 c/qB$. Hence, we find:

$$P = \frac{q^2}{6\pi\varepsilon_0 c}\gamma^4\left(\beta^2 c\frac{qB}{\gamma\beta m_0 c}\right)^2 = \frac{q^4\beta^2}{6\pi\varepsilon_0 m_0^4 c^5}\mathcal{E}^2 B^2 \tag{1.58}$$

where $\mathcal{E} = \gamma m_0 c^2$ is the total relativistic energy of the particle. Therefore, the synchrotron radiative yield is proportional to the square of the particle energy, and becomes very important at relativistic velocities. The angular emission cone as well gets narrower as the particle energy increases, as shown in Figure 1.9. Accelerators that benefit of this effect are called Synchrotron Light Source (SLS). A schematic diagram of basic SLS structure is shown in Figure 1.10.a. SLS consists of electron synchrotrons reaching several GeV of energy into which the accelerated pulsed (ps duration) electron beam is stored in a storage ring, giving rise to ultra-high luminosity synchrotron light emissions in the UV-soft X-ray range (tens of eV to tens of keV). Nowadays, SLS of the 3$^{\text{rd}}$ generation enhance the brilliance of light sources through the use of insertion devices like wigglers and undulators. SLSs presently constitute the most brilliant light sources on the planet, being outmatched only by XFELs, considered as the new 4$^{\text{th}}$ generation of accelerator-based Light Sources (see Figure 1.10.b).

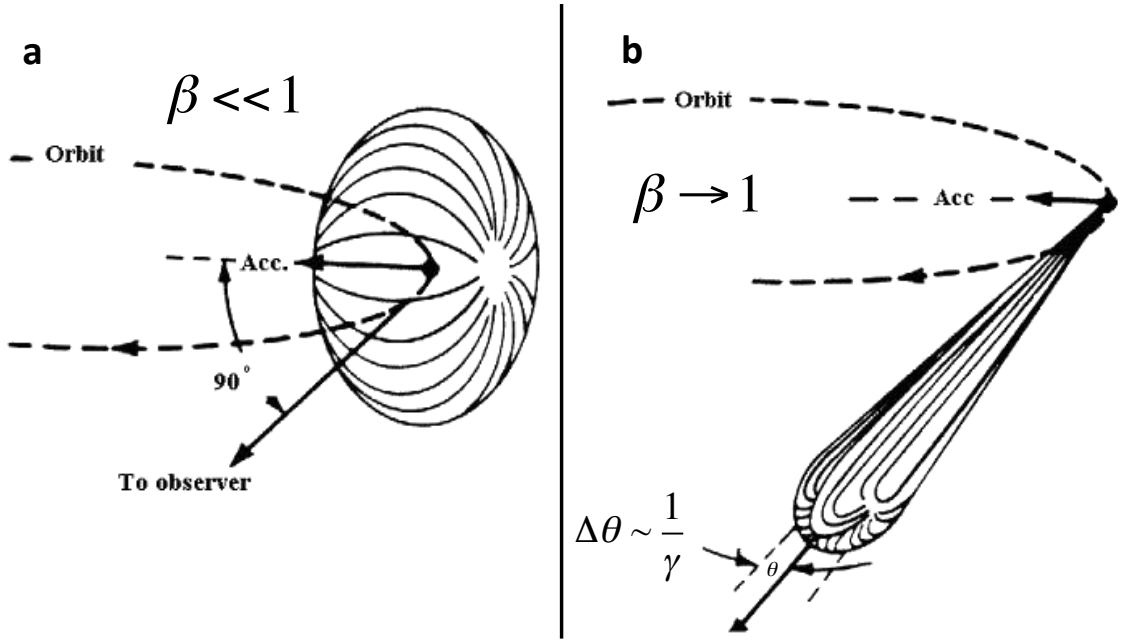

FIGURE 1.9: Angular distribution of synchrotron emissions for different electron velocities with (a) $\beta \ll 1$ and (b) $\beta \rightarrow 1$. The conical emission gets narrower with higher electron energies, $\Delta\theta \sim 1/\gamma$. This figure is extracted and adapted from [12].

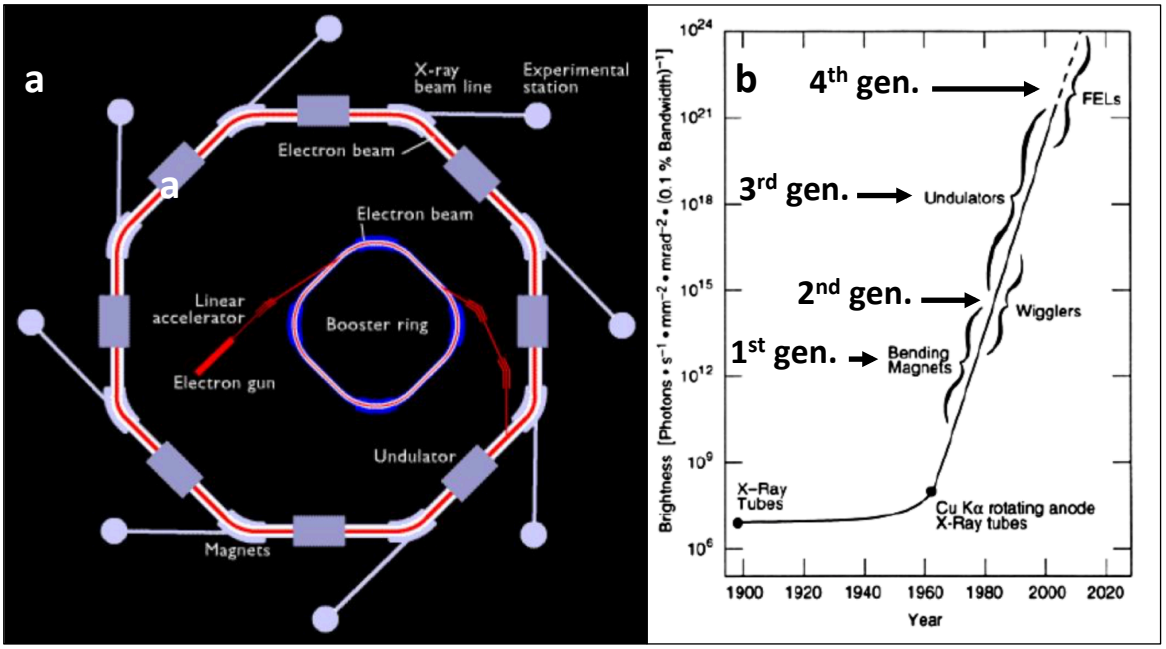

FIGURE 1.10: Synchrotron light source. (a) Schematic diagram of a Synchrotron Light Source (SLS). (b) Temporal evolution of X-ray light sources' brightness in the last century. Accelerator-based Light Source are grouped in four different generations of characterized by their emission intensities as the accelerator technologies improved over time. These figures are extracted and adapted from [14].

1.3 Laser-driven particle accelerators

1.3.1 High-power lasers and Chirped Pulse Amplification

Based on the theoretical work of Charles H. Townes and Arthur L. Schawlow [15], Theodore H. Maiman made the first laser operate in 1960, while working at Hughes Research Laboratory in California, using a ruby crystal and flash lamps with his work exposed in a groundbreaking publication in *Nature* [16]. The same paper was previously rejected from editors in *Physical Review Letters*, qualifying the work as "simply more of the same", considering the large amount of papers received at the time on the maser (microwave equivalent of the laser). Nevertheless, this historical paper revolutionized the modern world with its numerous applications. The light power within laser pulses rapidly climbed to MW and GW (10^6 - 10^9 W) with the further developments of *Q-switching* and *Mode Locking* techniques. In a famous paper of 1979, Toshiki Tajima and John M. Dawson published the concept of performing a laser-based electron accelerator using the strong plasma oscillations that high-power laser pulses can induce in their wake [17]. For increasing the feasibility of a laser-driven electron accelerator, they recommend in their work that "techniques of making short pulses have to be perfected". At the time, the production of high-energy pulses were possible for long pulse durations, as well as for low-energy short pulses, but not both at the same time (*i.e.* high-energy short pulse), since the amplifying crystals would get completely damaged as of strong over-heating from the high laser power. The turning point to this situation would come in 1985 from Donna Strickland and Gérard Mourou with the invention of the Chirped Pulse Amplification (CPA) technique [18] (see Figure 1.11), for which they would be awarded the Nobel Prize in Physics 2018. The modern method consists of using a short duration (tens of femtoseconds ranged) seed laser pulse from a broadband source, typically Ti:Sapphire technologies which was developed by Peter Moulton in 1986 [19], and first to stretch it in time to hundreds of picoseconds by giving a chirp (*i.e.* delay in time) to the different frequency components using a set of diffraction gratings. In this configuration, the stretched pulse can then safely be amplified to high energies without reaching the critical power damage threshold of the gain medium and related optics, to finally be compressed back to tens of femtoseconds by the conjugate operation of the stretcher using a second set of diffraction gratings, the latter being called the compressor. The CPA technique allowed to tremendously increase the delivered output power of lasers to the TW level (10^{12} W) and up to 10 PW (10^{15} W) at the time of writing these lines. This laser power

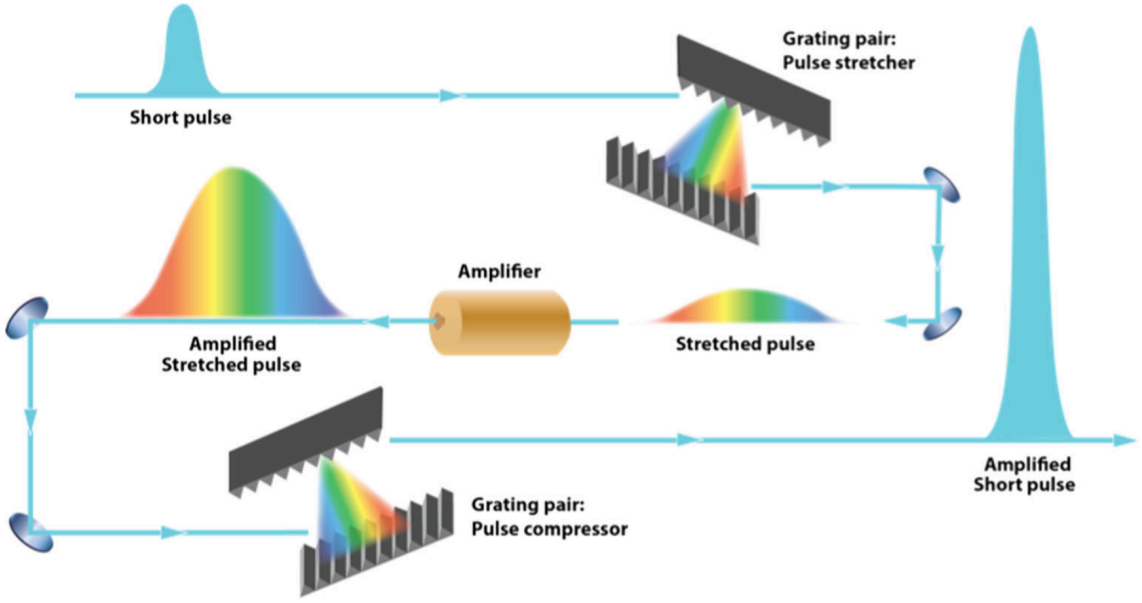

FIGURE 1.11: Schematic diagram of the Chirped Pulse Amplification technique. This figure is extracted and adapted from [20].

is currently in commissioning at the Extreme Light Infrastructure for Nuclear Physics (ELI-NP) facility in Magurele, Romania. The advent of CPA-based lasers would allow for a plethora of applications to be possible, such as eye surgeries for instance, as well as opening the new research field of relativistic optics, thereby making possible all-optical (*i.e.* laser-driven) charged particle accelerators. The next sections will be discussing the context of laser-driven electron (see section 1.3.2) and ion (see section 1.3.3) acceleration in further details.

1.3.2 Electron acceleration

This section is intended to give a brief overview of laser-driven electron acceleration, also called laser-plasma acceleration. The goal is not to cover laser-based electron acceleration in details as this is not the main subject of this doctoral work, but to overlay the main concepts and historical advances. For further details, there exist several excellent reviews of laser-plasma acceleration in the literature, from which this section is based on [21–25]. When sending a high-energy, short-duration laser pulse into a gaseous medium, the ponderomotive force (developed in section 2.1.3) pushes the electrons out of the laser pulse trajectory due to radiation pressure, thereby producing a strong charge separation that induces plasma oscillations in the wake of the laser pulse. These plasma waves can generate very high longitudinal electric fields, and

the injection of an electron bunch with the right phase velocity leads to its acceleration in the forward direction along the laser propagation axis, occurring naturally through the transverse re-circulation of the previously ejected electrons. This phenomenon is commonly referred to as Laser Wakefield Acceleration (LWFA). As shown in the work of Esarey *et al.* (2002) [23], inserting the plasma frequency $\omega_p = \sqrt{\frac{n_e e^2}{m_e \varepsilon_0}}$ in the expression of the supported electric field in a plasma E_0 leads to:

$$E_0 = \frac{c m_e \omega_p}{e} = \sqrt{\frac{n_e m_e c^2}{\varepsilon_0}} \tag{1.59}$$

where n_e is the electron density of the medium. Equation (1.59) shows that the maximal electric field sustainable in a plasma essentially depends on the electron density n_e, since the remainder of the expression is constituted of fundamental constants. Conventional gas jets have densities on the order of $n_e \sim 10^{18}$ cm^{-3}, after insertion into (1.59) leads to $E_0 \sim 100$ GV/m, which is three orders of magnitude higher than the maximal electric field reachable in RF cavities, being limited by the cavity material's electrical breakdown. This acceleration occurs over the dephasing length of the plasma wake, which is usually on the order of several tens to hundreds of micrometers, determined by the Rayleigh length of the focal volume. Hence, this enables the acceleration of electron bunches to energies that are equivalently reached in conventional accelerators that are several tens of meters long, compared to the sub-millimetric scale with LWFA. Nowadays, gas nozzle technologies underwent major developments, allowing to reach electron densities of $n_e \sim 10^{20} - 10^{21}$ cm^{-3}, thus opening the path to generate accelerating gradients on the order of several TV/m. Following the seminal paper of T. Tajima and J. M. Dawson in 1979 [17], along with the advent of CPA-based lasers [18] in 1985, several early experiments to perform all-optical electron acceleration occurred in the 1990's up to 2001. The resulting electron beams were characterized by $\sim$ 100 MeV maximal energy with Maxwellian energy spectrum (*i.e.* 100% energy spread exponentially decreasing with the vast majority in the lower energy section below 10 MeV) and large beam divergences [26–36]. In these experiments, the tested methodologies were using either the beat wave, wakefield or self-modulated wakefield acceleration schemes. The resulting beam qualities from these experiments were considered rather poor, partly since the injected electron bunch length was much longer than the plasma wavelength, hence leading to a tiny fraction of electrons being efficiently accelerated. The increasing laser power throughout the years lead in 2002 to the first demonstration of the so-called *Forced Laser Wakefield* into which electrons were accelerated up to 200 MeV with

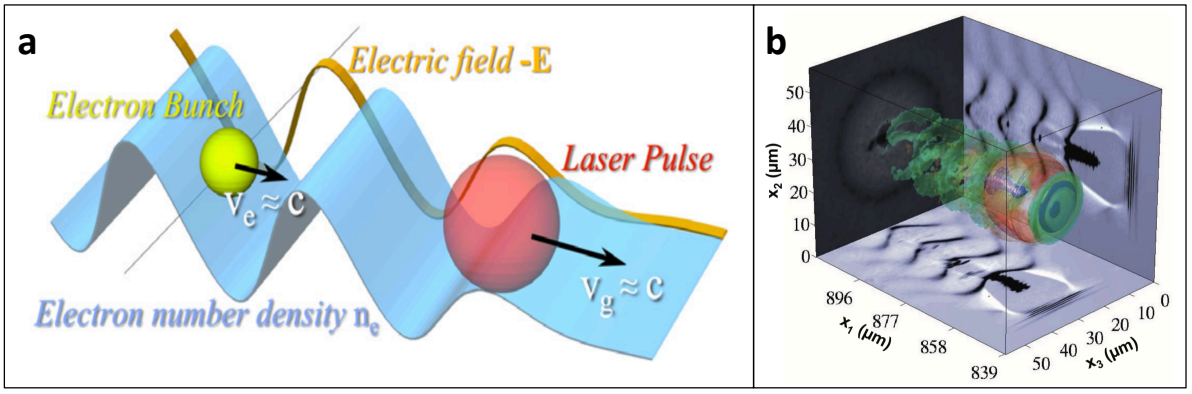

FIGURE 1.12: (a) Schematic diagram of Laser Wakefield Acceleration (LWFA). The high-intensity laser pulses drives a plasma wave in its wake which generates a longitudinal electric that accelerates an electron bunch. This figure is extracted and adapted from [56]. (b) 3D Particle-In-Cell (PIC) simulation of LWFA. This figure is extracted and adapted from [57].

rather low divergence ($\sim$ 100 mrad) by the work of Malka *et al.* (2002) [37]. This was made possible by strongly reducing the interaction between the laser pulse and the accelerated electron bunch using a high-power short-duration laser pulse, generating a highly relativistic plasma wave with strong accelerating gradients. The electron beam qualities significantly increased in 2004 when three independent groups [38–40] published groundbreaking experimental results appearing in the same issue of *Nature*. The electron bunches were characterized by high bunch charge (>100 pC), high energy ($\sim$ 100 MeV) monoenergetic spectra (few % of energy spread) and a few milliradians of beam divergence. These characteristics were obtained by using Joule-level short-duration (tens of femtoseconds ranged) laser pulses and focusing the laser energy in a sphere with a radius smaller than the plasma wavelength, which completely expels the electrons locally. This leads to the formation of positively charged cavity and thus to high electron trapping, a mechanism called the *bubble* or *blow out* regime depending on the laser intensity used (see Figure 1.12). The high-quality electron beams resulting from the bubble regime were rapidly perfected to reach 1 GeV electron energies in 2006 [41], and were further optimized through the recent years [42–51], as shown in Figure 1.13. The record electron energy of nearly 8 GeV was reached in 2019 by the work of Gonsalves *et al.* (2019) [52].

As described by the works of Esarey *et al.* (2002) [53] and Kostyukov *et al.* (2003) [54], the strong ionization provoked in the gaseous media during LWFA experiments leads to the formation of an ion channel that produces a restoring force on the expelled electrons. Hence, while being

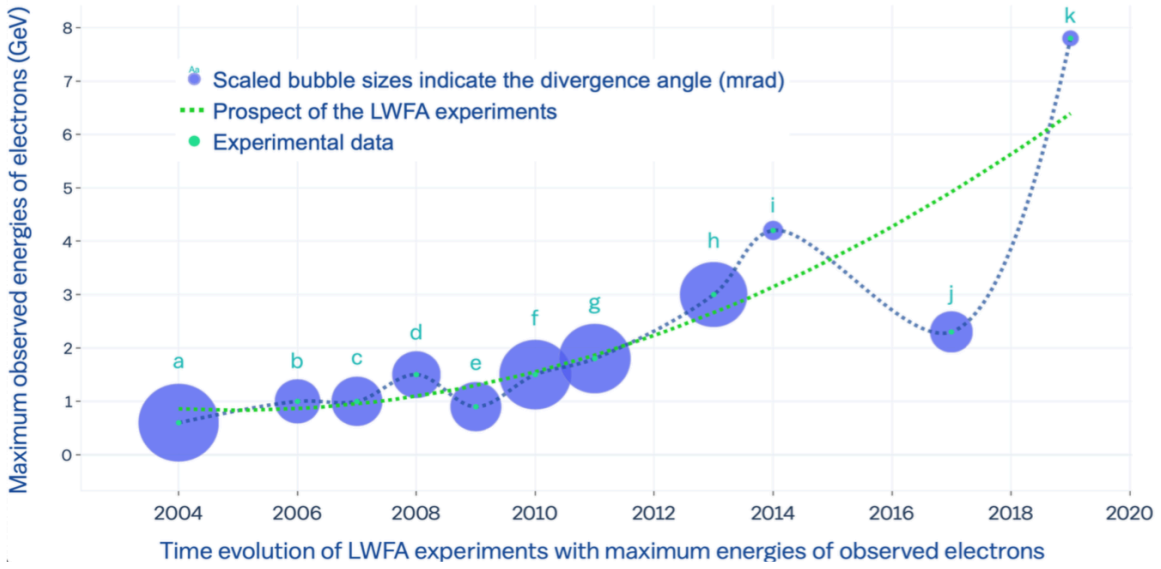

FIGURE 1.13: Electron acceleration by LWFA in the bubble regime throughout the recent years (a: [40], b: [41], c: [43], d: [44], e: [46], f: [47], g: [48], h: [49], i: [50], j: [51] and k: [52]). This figure is extracted and adapted from [25].

accelerated in the forward direction, the highly relativistic electrons undergo transverse oscillations due to the restoring force, equivalent to betatron oscillations in conventional accelerators, and therefore must also emit X-ray radiation through synchrotron emission while doing so (see section 1.2.4.1), commonly called *betatron* radiation (see Figure 1.14.a). More precisely, not only LWFA can be used to accelerate electron beams to highly-relativistic energies, but the plasma transverse oscillations act as a plasma wiggler at the same time. Hence, the resulting X-ray emissions are of short duration (tens of femtoseconds) and exhibit high spatial coherence, which make laser-driven betatron radiation sources very attractive. The emitted X-ray spectrum exhibits the same characteristics as previously described for undulators and wigglers in equations (1.23)-(1.24)-(1.25) (see section on XFELs 1.2.2.2). The first experimental demonstration of betatron radiation emission from LWFA experiment came in 2004 from the work of Rousse *et al.* (2004) [55]. Very good reviews on the recent advances of betatron sources from LWFA can be found in two papers from Albert *et al.* (2014, 2016) [56, 57]. The high coherence obtained from laser-based betatron radiation sources allows to perform an imaging technique called X-ray Phase Contrast Imaging (XPCI), into which the retrieval of the radiation phase strongly enhances the imaging resolution. XPCI is now done routinely in LWFA experiments, and the resulting X-ray radiation source yield from one single laser shot is very competitive but also offers complementary characteristics to Synchrotron Light Sources, as shown by the

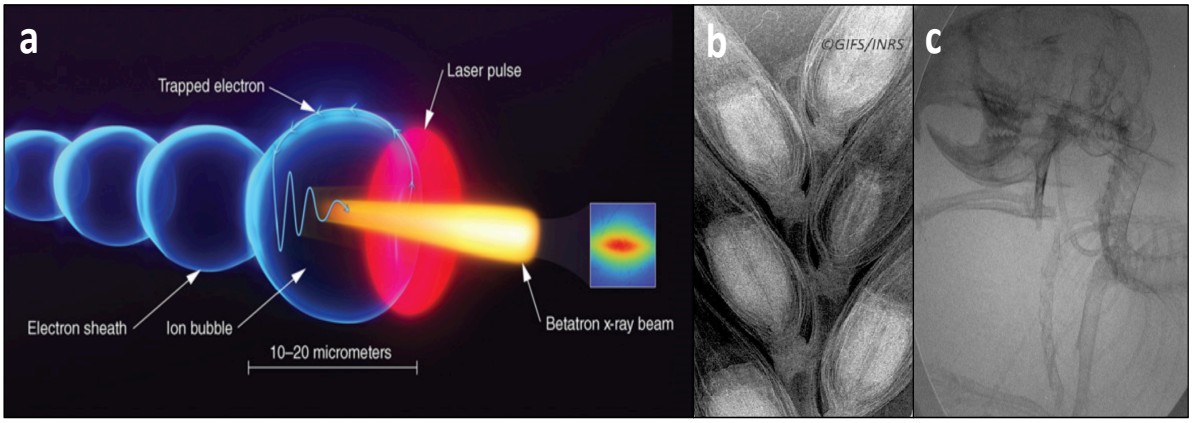

FIGURE 1.14: (a) Betatron radiation generated by LWFA. This figure is extracted and adapted from [56]. (b-c) Wheat seeds (b) and mouse head (c), extracted and adapted from [59].

works of Fourmaux *et al.* (2011, 2018, 2020) [58–60] and Hussein *et al.* (2019) [61].

1.3.3 Ion acceleration

This section aims at describing the context of laser-driven ion acceleration from the first experiments up to this day. Further development of the mathematical framework of laser-based ion acceleration can be found in Chapter 2 (see section 2.3). The overview presented in this dissertation is not extensive, and is based on several excellent detailed review papers on the subject [62–67]. Even before the invention of the laser in 1960, Vladimir I. Veksler, co-inventor of the synchrotron accelerator, proposes the concept of coherent acceleration of charged particles in plasmas in 1957 [68]. In this concept, the accelerating field is proportional to the number of accelerated particles, in a collective process that would automatically satisfy the synchronicity condition between the particles and the accelerating field (*i.e.* temporal coherence). Moreover, coherent acceleration would ultimately lead to quasi-neutral groups of particles, which would allow for high beam stability even for large number of particles per bunch. This type of acceleration would occur through the interaction between the particle bunch and dense targets, which can sustain high electric fields like plasmas. Research on laser-generated plasmas began in the 1970's for the development of nuclear fusion using high-energy lasers. In this context, CO_2 lasers operating at a central wavelength of $\lambda_0 = 10$ μm were driving the pre-heating and compression of plasma cores. Researchers soon found out that strong charge separation were producing energetic ions that expanded outward and transported the absorbed laser energy away from the compression zone, hence making the task more difficult. Nevertheless,

several important scientific advances were reported, such as extremely huge hot electron current densities produced with high-power lasers which could not be produced by any other method, also generating magnetic fields over a hundred of Teslas in a plasma [69]. The interest in producing high-energy ions through laser-plasma interactions continuously grew up with the escalation of laser intensities, and ions with energies of several MeV were reported in 1986 with solid thick foils ($\sim$ 150 μm) and using "long" nanosecond-ranged pulses [70], then followed by the use of "short" picosecond-ranged pulses after the advent of the CPA technique [71, 72]. Laser-driven energetic ion generation was also reported with other target types such as micrometric clusters [73] and gaseous targets [74, 75]. In all these experiments, the ion beam characteristics were not very attractive as they exhibited isotropic emissions and low particle numbers, thereby making them unsuitable ion accelerators for applications. The mechanism for generating these energetic ions was explained by a strong charge separation induced by the production of hot electrons through resonance absorption with high-energy laser pulses, then followed by a thermal plasma expansion. It was only in 2000 that three independent experiments [76–78] reported the production of intense ion beams (*i.e.* large particle numbers reaching 10^{13} particles per bunch) with kinetic energies reaching several tens MeV, along with high levels of collimation ($\sim 40^\circ$ conical divergence) and laminarity. These much more interesting characteristics were attained using either metallic or plastic foils of micrometric thicknesses, as well as high-intensity ($I_0 > 10^{18}$ W/cm^2) short pulses (≤ 1 ps) enabled through CPA-based lasers. The short pulse durations are essential for the efficiency of the process, as longer nanosecond-long pulses would completely destroy the foils before reaching the peak intensity, as a result of plasma expansion. The process also required sufficiently high laser-to-prepulse intensity contrast as to avoid the pre-expansion of the target before the interaction with the main pulse, which would degrade the ion generation efficiency. Indeed, a nanosecond-long contrast of at least 10^{-6} was necessary when using intensities above 10^{18} W/cm^2 since the ionization threshold for most atoms is around intensities of 10^{13} W/cm^2. The ionization of atoms before the main pulse causes a charge imbalance followed by a plasma expansion, which disturbs the laser pulse propagation before reaching the interaction point with the target bulk. These prepulses are coming both from the Amplified Spontaneous Emission (ASE) pedestal of the amplifying crystals and imperfect pulse stretching/compression preceding the interaction. Inconsistent explanations of the phenomenon driving the acceleration occurred among those publications. In particular, Clark *et al.* (2000) [76] and Maksimchuck (2000) *et al.* [78] claimed that ions were originating from the front target surface and crossed the full target thickness

before being detected on the rear side, whereas Snavely *et al.* (2000) [77] (see also Hatchett *et al.* (2000) [79]) were suggesting that the acceleration started directly at the rear side of the target. The explanation came the year after from the work of Wilks *et al.* (2001) [80], in a description of the mechanism called the Target-Normal Sheath Acceleration (TNSA), and received correct mathematical modeling of plasma expansion in vacuum in the work of Mora (2003) [81]. In this acceleration scheme, the focused laser pulse pushes the electrons from the front target surface in the forward direction through the relativistic ponderomotive force (described in section 2.1.3), some of them being retained near the back target surface, and thereby producing a sheath of hot electrons that establishes an intense quasi-static longitudinal electric field (up to the TV/m range, four orders of magnitude higher than the 100 MV/m found in conventional accelerators) that accelerates ions coming from hydrocarbon impurities and water molecules naturally adsorbed on the surface. Among the different ion species, protons absorb most of the energy from the electric field due to their greater charge-to-mass ratio, making them easier to accelerate and thus reacting more quickly to temporal variations of the sheath electric field. This acceleration takes place over a few tens of microns and leads to charged particle beams with ion kinetic energies up to several tens of MeV per charge state, but also have short bunch duration (ps to ns, three orders of magnitude shorter than what is achieved in conventional accelerators), high bunch charges of a few nC (*i.e.* kA current), have conical beam divergence of ($< 25^\circ$ half-angle), as well as an intrinsically low normalized transverse emittance (< 4 μm·mrad) [82–85] due to their high laminarity. The ions are surrounded by a co-moving electron cloud which forms a quasi-neutral plasma bunch that ensures beam stability and hence prevents its explosion due to electrostatic repulsion (*i.e.* the so-called "Coulomb explosion"). A schematic diagram of TNSA is shown in Figure 1.15.

Laser-driven proton beams seemed like a natural choice for being used in an application of fast-ignition of fuel cores for laser fusion, due to their "Bragg peaked" energy deposition profile. The investigation of this application started in the years that followed [87–89]. The novel characteristics of laser-accelerated proton beams soon attracted considerable attention for ion beam therapy of cancer tumors, opening the possibility to produce more compact and cheaper accelerators compared to conventional accelerators like cyclotrons or synchrotrons [90–93]. Again in the medical domain, the production of radioisotopes using laser-driven proton beams was also suggested, which triggered several feasibility investigations [94–98]. The low emittance exhibited by TNSA beams also favored their application for proton-based radiographies and

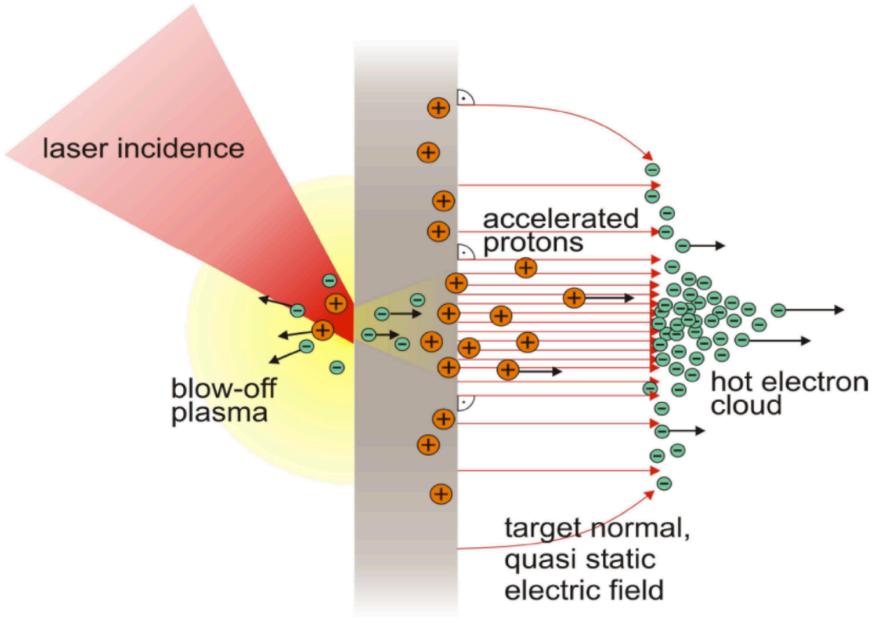

FIGURE 1.15: Simplified schematic diagram of ion acceleration with solid targets. This figure is extracted and adapted from [86].

imaging [83, 99, 100]. On that note, the broad energy spectrum along with the short duration of the proton bunch has further enabled the development of single-shot time-resolved probing of electromagnetic fields in laser-plasma interactions with picosecond temporal resolution [101, 102]. Again using imaging techniques, the radiographic methods turned out to be very valuable for the investigation of TNSA's own acceleration mechanism [103], as is shown in Figure 1.16.a. Hence, is it not surprising that TNSA-based proton beams, at the turn of the millennium and the decade that followed, triggered so much excitement in the scientific community. High-power laser facilities scattered all over the world started to perform laser-driven ion acceleration experiments to first increase our understanding of laser-plasma interactions, particularly in the TNSA regime (other acceleration regimes are discussed in section 2.3), but also to help and optimize the laser-based ion beam generation [105–125]. The quest for reaching the highest proton energies started with the 58 MeV in the work of Snavely *et al.* (2000) [77] at the Nova PW laser (423 J, 500 fs, 3×10^{20} W/cm^2), then surpassed to roughly 67 MeV from the work of Gaillard *et al.* (2011) [126] at the Trident laser (80 J, 670 fs, 1.5×10^{20} W/cm^2) using flat-top cone targets [121, 127] and much less laser energy, followed by the 85 MeV in the work of Wagner *et al.* (2016) [128] at the PHELIX laser (200 J, 500 fs, 2.6×10^{20} W/cm^2) using thin 1 μm-thick plastic targets, and finally up to nearly 100 MeV from the work of Higginson *et al.* (2018) [129] at the Vulcan laser (210 J, 900 fs, 3×10^{20} W/cm^2) using 100 nm-thick plastic foils.

The major disadvantage of lasers of that scale is their enormous shot-to-shot fluctuations and very low repetition rate, most of them requiring tens of minutes to hours between the shots for cooling down. This is why now strong interest is given to laser-driven sources of smaller scale (*i.e.* generating lower proton energies) but providing higher reliability and repetition rate for applications, able to run at a few Hz to tens of Hz as typically found with commercial TW-scale Ti:Sapphire lasers. Hence, we see from this path to attain record proton energies (although not being the only metric for evaluating beam quality) that an optimized laser-target interaction is found by both adjusting the proper laser parameters (energy per pulse, intensity, pulse duration, contrast, polarization, incidence angle) and also, with equivalent importance, by choosing the right target type (material composition, density, thickness, surface roughness, macroscopic shape). Scaling laws of proton energies and particle numbers with respect to laser parameters and target thicknesses can be found in pioneering publications from Fuchs *et al.* (2006) [112] and Robson *et al.* (2007) [116]. Further investigations with regards to target thicknesses can be found in several other publications (not all mentioned here) [125, 130, 131]. Another constraint on laser-based ion beam generation comes from the stringent target alignment requirements imposed by the use of large numerical apertures (*i.e.* tight focusing, see section 2.1.1 for Gaussian optics definitions) in order to produce high intensity laser-matter interactions within the focal volume. This is the subject of an investigation and development of a Target Positioning Interferometer (TPI) performed during this doctoral work, presented in Chapter 3. One of the main issues with the use of solid targets regards the target refreshment after each shot. Indeed, the interaction target gets completely evaporated within (and beyond) the interaction zone, and therefore gas jets appear as more viable solution to reach high-repetition rate in laser-driven ion acceleration. The ideal case is indeed to match the repetition rate of high-power lasers of several Hz to tens of Hz, thereby leading to high particle fluxes. However, gas jet targets have in general exhibited lower maximum energies, particle numbers as well as larger beam divergences, when compared to most solid target studies [132–138]. This is partly due to the fact that solid targets can maintain sharper density gradients leading to stronger accelerating fields. Nevertheless, important developments in gas nozzle technologies as well as the use of hybrid acceleration schemes have shown promising results in recent studies [139–142]. In Figure 1.16.b is shown the maximum proton energy $\mathcal{E}_{\mathrm{K,p}}^{\mathrm{max}}$ scaling for different laser intensities I_0 of some experiments reported up to 2008 [83], showing a dependence of $\mathcal{E}_{\mathrm{K,p}}^{\mathrm{max}} \propto (I_0\lambda^2)^{0.3-0.5}$.

In most laser-driven ion acceleration experiments, the main detector is a Thomson Parabola

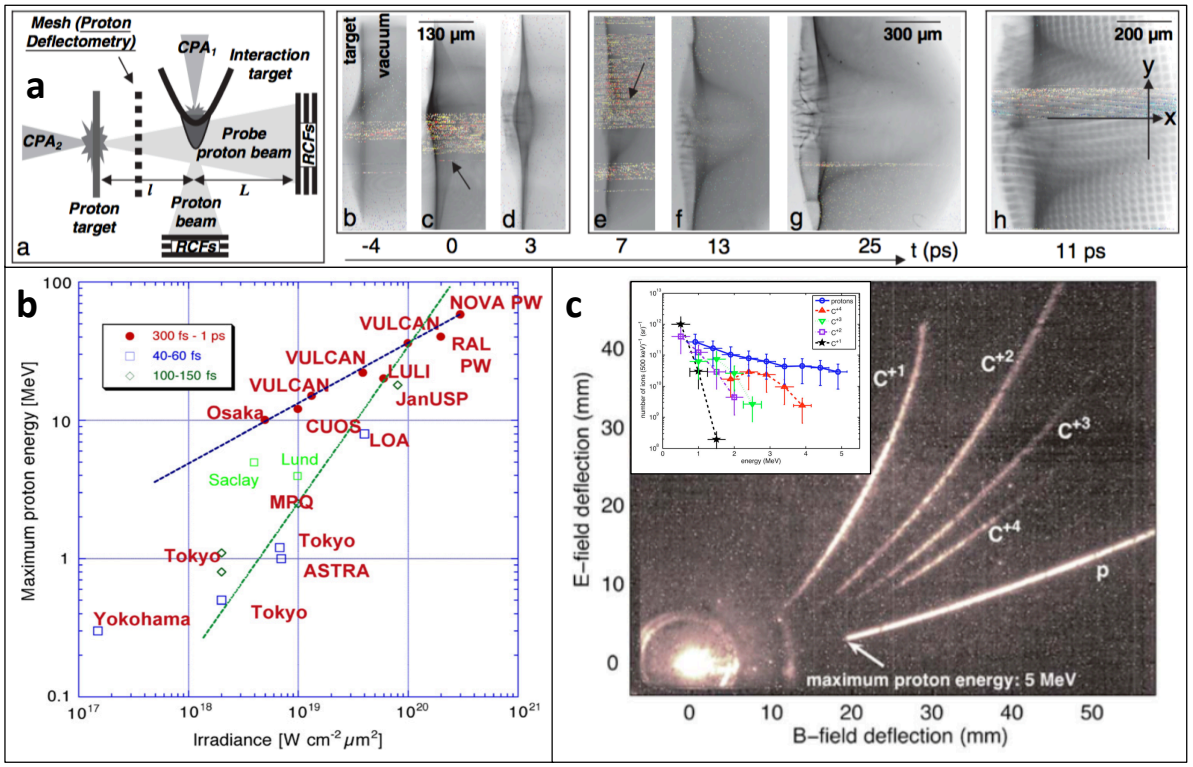

FIGURE 1.16: (a) Proton radiographies of the TNSA mechanism by probing the non-linear dynamics of plasma expansion. This figure is extracted and adapted from [103]. (b) Maximum energy scaling with respect to laser irradiance for selected experiments up to 2008. The maximum proton energy $\mathcal{E}_{K,p}^{max}$ approximately follows a $(I_0\lambda^2)^{0.3-0.5}$ dependence. This figure is extracted and adapted from [83]. (c) Thomson parabola spectrometer measurement of laser-accelerated ions species. The inlet is the ion spectra from the parabolas trace on the detector. This figure is extracted and adapted from [104].

(TP) spectrometer that uses static magnetic and electric fields to split the different ion energies and ion species in terms of their respective charge-to-mass ratio. A typical TP spectrometer measurement is shown in Figure 1.16.c, and the kinematics derivation for the equations of motion of charged particles passing through $\boldsymbol{E}$ and $\boldsymbol{B}$ fields is shown in Appendix A.2. Other charged particle diagnostics include Radiochromic Films (RCF), CR-39, Imaging Plates (IP), MicroChannel Plates (MCP), Time-of-Flight (TOF) delay lines with either plastic scintillators, SiN or diamond detectors, scintillators with hyperspectral imaging, as well as pixelated semiconductor detector, which are further discussed in Chapter 4. The use of surface micro- or nano-structuration of targets to increase the effective interaction surface with the laser pulse is as well the subject of an entire Chapter of this doctoral work, presented in Chapter 5.

Chapter 2

Background of Laser-Driven Ion Acceleration

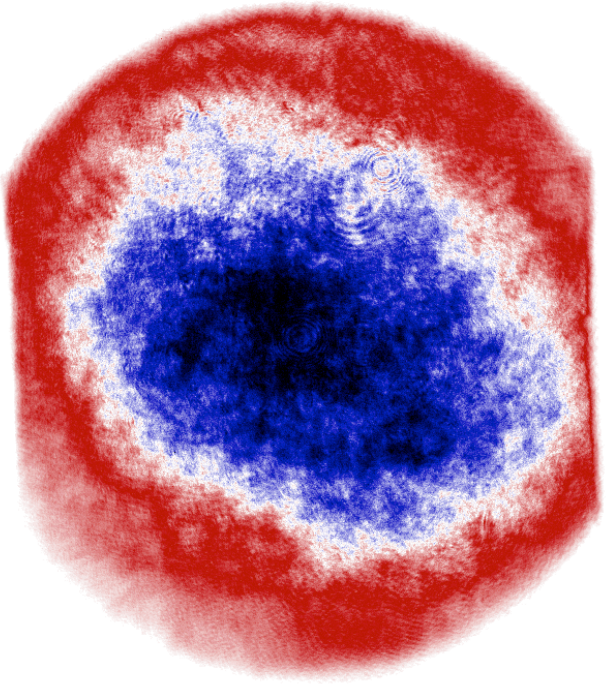

ALLS 100 TW post-compression beam with 2 J in 20 fs.

Chapter Content

The goal of this Chapter is to provide the necessary theoretical background for the proper comprehension of the work presented in this doctoral dissertation. The Chapter is divided into three parts, namely the laser-plasma interactions, the high-field absorption processes and, finally, the acceleration mechanisms relevant for these studies.

2.1 Laser-plasma interactions

In this section, we provide the theoretical background for several laser-plasma interaction concepts that are essential for this work. The section starts by invoking different well-established

concepts from Gaussian optics, then continues with a description of the electron interaction with a plane wave in vacuum and the ponderomotive force. The most established theories regarding ionization processes are discussed, the concepts regarding the propagation of a laser in a plasma are given, to finally provide insights related to the use of Particle-In-Cell simulations.

2.1.1 Gaussian optics

In this section, the main concept used in Gaussian optics are outlined. The derivation is not performed here as it can be found in numerous textbooks and on the web. The solution to the wave equation (1.12) expressed in cylindrical coordinates and in the paraxial approximation leads to the well-known expression for Gaussian beams propagating along the z-axis:

$$\boldsymbol{A}(r,z,t) = A_0 \frac{w_0}{w(z)} \exp\left[-\frac{r^2}{2w(z)^2} - i\phi(r,z)\right] e^{i\omega t} \ \hat{r} \tag{2.1}$$

with the EM field intensity expressed as:

$$I(r,z,t) = \frac{1}{2} c\varepsilon_0 |\boldsymbol{E}(r,z,t)|^2 = \frac{1}{2} c\varepsilon_0 \omega^2 |\boldsymbol{A}(r,z,t)|^2 \tag{2.2}$$

In equation (2.1), A_0 is the amplitude of the vector potential, w_0 is called the beamwaist (*i.e.* radius of the focal spot) found for $w(z=0)$ with $w(z)$ being the beam radius (at $1/e$ of on-axis amplitude) expressed as:

$$w(z) = w_0 \sqrt{1 + \left(\frac{z}{z_\mathrm{R}}\right)^2} \tag{2.3}$$

In equation (2.3), z_R is the Rayleigh length defined where $w(z=z_R) = \sqrt{2} w_0$, therefore at one half the peak intensity I_0, and determines the depth of focus $2z_\mathrm{R}$. It is related to the beamwaist by:

$$z_\mathrm{R} = \frac{1}{2} k w_0^2 \tag{2.4}$$

with $k = |\boldsymbol{k}| = 2\pi/\lambda$ being the wavenumber. Also note that temporal variation of equation (2.1) is described solely by the factor $e^{i\omega t}$ in the plane-wave approximation, with ω being the angular frequency. Furthermore in equation (2.1), we can note the phase $\phi(r,z)$ of the wave, written as:

$$\phi(r,z) = kz + k\frac{r^2}{2R(z)} - \psi(z) \tag{2.5}$$

with $R(z)$ being the curvature radius of the wave found with the following expression:

$$R(z) = z + \frac{z_R^2}{z} \tag{2.6}$$

The Gouy phase $\psi(z)$ is also defined as:

$$\psi(z) = \arctan\left(\frac{z}{z_R}\right) \tag{2.7}$$

and characterizes the abrupt phase advance around $z = 0$. Based on these concepts, several more practical parameters useful in the laboratory can derived, such as the angular divergence of the beam:

$$\theta = \lim_{z\to\infty} \arctan\left[\frac{w(z)}{z}\right] \tag{2.8}$$

This wave equation solution in the Gaussian beam approximation is the fundamental Transverse ElectroMagnetic (TEM_{00}) mode, for which the electric $\boldsymbol{E}$ and magnetic $\boldsymbol{B}$ fields are both perpendicular (*i.e.* oriented in the transverse direction) to the beam propagation direction along the wavevector $\boldsymbol{k}$ (z-axis here). When using focusing optics, and important parameter is the so-called f-number N, defined as $N = f/D$ with f being the focal length and D being the near-field beam diameter (*i.e.* before focusing). This allows to define one the most central concept in focusing optics, being the numerical aperture NA defined as:

$$\mathrm{NA} = n\sin\theta = n\sin\left[\arctan\left(\frac{D}{2f}\right)\right] \approx n\frac{D}{2f} = \frac{1}{2N} \tag{2.9}$$

The numerical aperture defines the focusing tightness, and is further related to the beamwaist by:

$$\mathrm{NA} \approx \frac{2k}{w_0} \tag{2.10}$$

Let's take a practical example with a focusing parabola, a reflective focusing device commonly used to focus high-power laser pulses. A common parabola type is said to be $f/3$, meaning $N = 3$. Therefore, this defines its numerical aperture of $\mathrm{NA} = 1/(2N) \approx 0.1667$. A commercial Ti:Sapphire laser most often has a central wavelength of $\lambda_0 = 800$ nm, hence defining the theoretical minimum beamwaist as $w_0 \approx 2k_0/\mathrm{NA} = \lambda_0/(\pi\mathrm{NA}) \approx 1.53$ μm, or a focal spot diameter of about 3.06 μm. Moreover, this also determines the Rayleigh length of $z_R = \frac{1}{2}kw_0^2 \approx \lambda_0/(\pi\mathrm{NA}^2) \approx 9.2$ μm, therefore a depth of focus of about 18.4 μm. This means that with an $f/3$ focusing optics and a "perfectly" Gaussian beam, the accuracy of the target positioning

must be within ± 9.2 μm to avoid losing one half of the peak intensity I_0 at $z = 0$. Moreover, note that this also allows to determine the distributions of $w(z)$, $R(z)$ and $\psi(z)$ along z, and in fact of almost everything $\boldsymbol{A}(r, z, t)$ except its amplitude A_0. The latter is determining I_0 and therefore the regime of the interaction. A more lengthy derivation of how to estimate I_0 with the measured laser pulse parameters (energy, duration and spot size) is shown in Appendix A.1, in terms of the Gaussian beam approximation.

2.1.2 Electron interaction with a plane wave in vacuum

Since electrons are $m_\mathrm{p}/m_\mathrm{e} \approx 1836$ times lighter than the lightest ions (*i.e.* protons), they react to much faster electromagnetic field oscillations and are thus the first actors to consider in laser-matter interactions. The ions being much heavier than electrons, we will show that their interaction is negligible for the calculations, as a first approximation, within the laser intensity range of interest for this dissertation ($I_0 \sim 10^{18} - 10^{21}$ W/cm^2). This range of considered laser intensities is the one for which the Target-Normal Sheath Acceleration, the acceleration process central to this dissertation, is the dominant acceleration mechanism when an EM wave interacts with a solid target. The interaction of a single electron in vacuum is described by equating Newton's second law with the Lorentz force as:

$$\frac{d\boldsymbol{p}}{dt} = -e(\boldsymbol{E} + \boldsymbol{v} \times \boldsymbol{B}) \tag{2.11}$$

Equation (2.11) is fully described in relativistic terms with the momentum $\boldsymbol{p} = \gamma m_\mathrm{e} \boldsymbol{v}$ and the Lorentz factor $\gamma = 1/\sqrt{1 - v^2/c^2} = \sqrt{1 + (p/m_\mathrm{e}c)^2}$. We now use again the definitions of $\boldsymbol{E} = -\boldsymbol{\nabla}\Phi - \dfrac{\partial \boldsymbol{A}}{\partial t}$ and $\boldsymbol{B} = \boldsymbol{\nabla} \times \boldsymbol{A}$ obtained in the Lorenz gauge, and insert them in equation (2.11) which gives:

$$\frac{d\boldsymbol{p}}{dt} = e\left(\boldsymbol{\nabla}\Phi + \frac{\partial \boldsymbol{A}}{\partial t} - \boldsymbol{v} \times \boldsymbol{\nabla} \times \boldsymbol{A}\right) \tag{2.12}$$

We now use the following vectorial identities:

$$\boldsymbol{v} \times \boldsymbol{\nabla} \times \boldsymbol{A} = (\boldsymbol{\nabla}\boldsymbol{A}) \cdot \boldsymbol{v} - (\boldsymbol{v} \cdot \boldsymbol{\nabla})\boldsymbol{A}$$

$$\frac{\partial \boldsymbol{A}}{\partial t} = \frac{d\boldsymbol{A}}{dt} - (\boldsymbol{v} \cdot \boldsymbol{\nabla})\boldsymbol{A}$$

and further insert them in equation (2.12), leading to:

$$\frac{d\boldsymbol{p}}{dt} = e\frac{d\boldsymbol{A}}{dt} + e\boldsymbol{\nabla}\Phi - e(\boldsymbol{\nabla}\boldsymbol{A})\cdot\boldsymbol{v} \quad \Longrightarrow \quad \frac{d(\boldsymbol{p}-e\boldsymbol{A})}{dt} = e\boldsymbol{\nabla}\Phi - e(\boldsymbol{\nabla}\boldsymbol{A})\cdot\boldsymbol{v} \tag{2.13}$$

Hence, we can note here that $e\boldsymbol{A}$ directly characterizes the momentum of the electron and has the same units. Let's now consider that we are in vacuum (*i.e.* $\Phi = 0 \ \forall \ \mathbb{R}^3$), with a wave propagating in the z-direction, polarized in the perpendicular xy-plane (*i.e.* $\boldsymbol{A} = \boldsymbol{A}_\perp$), and defining the normalized vector potential as:

$$\boldsymbol{a} = \frac{e\boldsymbol{A}}{m_e c} = \left\langle \delta a_0 \cos\phi, \sqrt{1-\delta^2}a_0 \sin\phi, 0 \right\rangle \quad \text{, with} \quad \phi = \omega t - kz \tag{2.14}$$

where $a_0 = eA_0/m_e c$ is the normalized amplitude of the vector potential, ϕ is the phase of the wave being a relativistic invariant, along with $\delta = \pm 1$ for linear polarization and $\delta = \pm 1/\sqrt{2}$ for circular polarization. It is common and very practical to use the dimensionless parameter a_0 to describe the "force" of the wave, and will be used very often hereinafter. Further considering that the electron is initially at rest leads to the following expressions:

$$\boldsymbol{p}_\perp = e\boldsymbol{A} \tag{2.15}$$

$$\boldsymbol{p}_z = \frac{\boldsymbol{p}_\perp^2}{2m_e c} \tag{2.16}$$

$$\gamma = \sqrt{1 + \left(\frac{p}{m_e c}\right)^2} = \sqrt{1 + \frac{p_\perp^2 + p_z^2}{(m_e c)^2}} = 1 + \frac{p_z}{m_e c} \tag{2.17}$$

Equation (2.15) show that the electron's transverse momentum $\boldsymbol{p}_\perp$ is only dictated by the vector potential $\boldsymbol{A}$, moreover that the forward momentum $\boldsymbol{p}_z$ is always related to the transverse momentum through equation (2.16). It also demonstrates that the electron comes back at rest after the passage of the wave (*i.e.* when $p_\perp \to 0$), and that it experiences always a positive drift in the forward direction. The fact that it comes back at rest is a representation of the Lawson-Woodard theorem, stating that plane electromagnetic waves cannot accelerate charged particles in vacuum. Nevertheless, there exists several schemes where electrons can gain the laser energy without losing the energy back after the passage of the wave, such as for instance:

1) Ionized electrons that can have the kinetic energy on the order of the ponderomotive potential (explained in section 2.1.4).

2) If the electron movement under the influence of the wave is abruptly stopped by an obstacle (*i.e.* a solid foil).

3) If there is plasma gradient or an external magnetic field that facilitates the exchange of energy with the wave.

4) Short duration pulse of a few optical cycles do not verify this theorem and can indeed accelerate electrons.

When one of the above situations occur, the electron acceleration process is referred to as Direct Laser Acceleration (DLA). Equation (2.17) gives a hint to the relationship between the Lorentz factor and the vector potential. We can find the expression of the Lorentz factor as:

$$\gamma_\perp = \sqrt{1 + a_0^2} \qquad\qquad \gamma = 1 + \frac{a_0^2}{2} \tag{2.18}$$

This gives direct and very simple expressions of the Lorentz factor with respect to the normalized amplitude of the vector potential, being the most central parameter of the interaction. We can express a_0 in more practical terms using $A_0 = E_0/\omega$, $\omega = 2\pi c/\lambda$ and $I_0 = \varepsilon_0 c E_0/2$. It then follows that:

$$a_0 = \frac{eA_0}{m_e c} = \sqrt{\frac{e^2 I_0 \lambda^2 \delta^2}{2\pi^2 m_e^2 c^5 \varepsilon_0}} \tag{2.19}$$

where equation (2.19) is a very well known equation used to easily calculate the normalized amplitude of the vector potential. It is commonly accepted that the electron's relativistic intensity regime starts when the oscillation energy eA_0c is as high as the electron's rest mass $m_e c^2$, in other words when the oscillation momentum $eA_0 = m_e c$ and hence for $a_0 = 1$. This relativistic regime threshold occurs at an intensity of $I_0 \approx 1.37 \times 10^{18}$ W/cm^2 for a wavelength of $\lambda = 1$ μm. Further solving for the equations of motion leads to the following expressions for the electron movement:

$$x(\phi) = \frac{a_0}{k}\delta \sin\phi \tag{2.20}$$

$$y(\phi) = -\frac{a_0}{k}\sqrt{1-\delta^2}\cos\phi \tag{2.21}$$

$$z(\phi) = \frac{a_0^2}{4k}\left[\phi + (\delta^2 - 1/2)\sin 2\phi\right] \tag{2.22}$$

We see from equations (2.20)-(2.22) that the electron undergoes oscillatory motion in the perpendicular xy-plane, however its longitudinal motion is characterized by a steadily growing

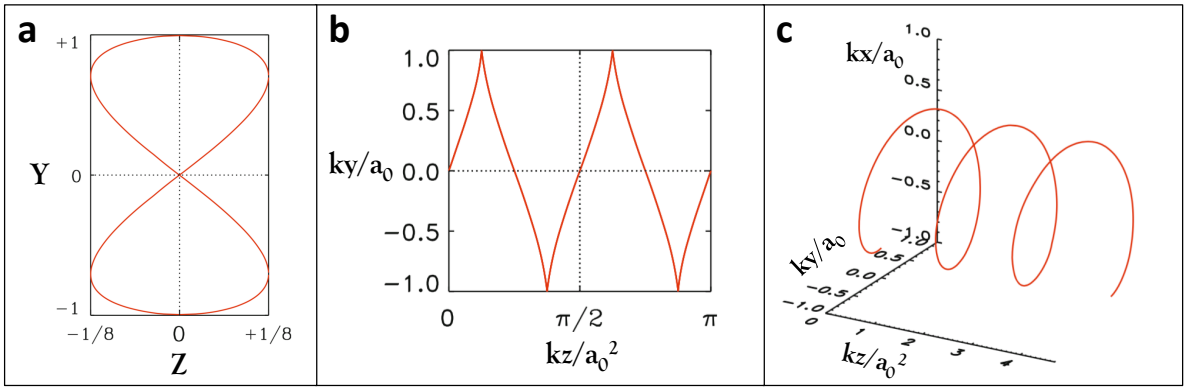

FIGURE 2.1: Relativistic electron motion under the influence and EM wave in vacuum. (a) So-called "figure-of-eight" obtained by computing the electron motion in the EM wave's reference frame for $p_z = 0$, in linear polarization (*i.e.* $\delta = \pm 1$). (b) Profile of the electron motion in the yz-plane for linear polarization (*i.e.* $\delta = \pm 1$). (c) Electron motion in circular polarization (*i.e.* $\delta = \pm 1/\sqrt{2}$). This figure is extracted and adapted from [143].

term ϕ and an oscillating term. Moreover, the longitudinal position $z(\phi)$ scales a_0^2 as opposed to the transverse motion scaling in a_0. Hence, as a_0 gets above unity in the relativistic regime, electrons get pushed strongly in the forward direction. Also note that in the case of circular polarization (*i.e.* $\delta = \pm 1/\sqrt{2}$), the oscillating term drops in equation (2.22), hence making the electron only drift forward. This also leads to helicoidal motion. Figure 2.1 exhibits the electron motion under different conditions.

2.1.3 Ponderomotive force

The ponderomotive force is an expression of the force that makes the electron oscillate. It can be derived directly from the relativistic equation of motion (2.13) presented in section 2.1.2, however we will start the derivation in the non-relativistic here for better pedagogical understanding. Let's first write Newton's second law for a plane electric wave as follows:

$$m_e \ddot{x} = -eE_0 \sin \omega t \tag{2.23}$$

This leads to the following expression for the electron velocity after integration:

$$\dot{x} = v_0 + \frac{eE_0}{m_e \omega} \cos[\omega(t - t_0)] \tag{2.24}$$

In equation (2.24), we define the classical oscillation velocity as $v_{\text{osc}} = eE_0/m_e\omega$. We see immediately that v_{osc} does not have a superior bound at c, since it is a classical definition. Nevertheless, it is used to express the transition to the electron's relativistic intensity regime, occurring when $v_{\text{osc}} = c$, as can be derived from the relativistic intensity threshold definition presented in the previous section (see section 2.1.2). Now assuming that the electron is initially at rest ($v_0 = 0$ at $t = t_0$), the kinetic energy is:

$$\mathcal{E}_{\text{K}}(t) = \frac{1}{2}m_e\dot{x}^2 = \frac{e^2E_0^2}{2m_e\omega^2}\cos^2[\omega(t-t_0)] \tag{2.25}$$

with the ponderomotive energy U_{pond} being the maximum oscillation kinetic energy of an electron in a laser field. It is related to the ponderomotive potential through $U_{\text{pond}} = q\Phi_{\text{pond}}$, and is defined as:

$$U_{\text{pond}} = \frac{e^2E_0^2}{2m_e\omega^2} \tag{2.26}$$

Its time-averaged value over one optical cycle therefore is:

$$\overline{U}_{\text{pond}} = \langle\mathcal{E}_{\text{K}}(t)\rangle = \frac{1}{2}U_{\text{pond}} = \frac{e^2E_0^2}{4m_e\omega^2} \tag{2.27}$$

Further replacing $A_0 = a_0m_ec/e$ in equation (2.27), we also have:

$$U_{\text{pond}} = \frac{1}{2}m_ec^2a_0^2 \qquad \Longrightarrow \qquad \overline{U}_{\text{pond}} = \frac{1}{4}m_ec^2a_0^2 \tag{2.28}$$

which shows that the ponderomotive energy of a charged particle influenced by a laser pulse is solely characterized by the normalized amplitude of the vector potential, again showing its central importance. For conservative forces such as in oscillatory motion, it is possible to write the force as the gradient of a potential energy, hence that $\boldsymbol{F}_{\text{pond}} = -\boldsymbol{\nabla}(U_{\text{pond}})$. More generally, we can write:

$$\boldsymbol{F}_{\text{pond}} = -\frac{e^2}{2m_e\omega^2}\boldsymbol{\nabla}(E_0^2) \tag{2.29}$$

Hence we see from equation (2.29) that the ponderomotive force is always oriented outward from the high-electric field regions due to the squared electric field, hence pushes the electrons away from high intensity gradients. Finally, using $E_0 = \omega A_0$ and in the relativistic regime ($m_e \to \gamma m_e$), we can write:

$$\boldsymbol{F}_{\text{pond}} = -\frac{e^2}{2\gamma m_e\omega^2}\boldsymbol{\nabla}(E_0^2) = -\frac{e^2}{2\gamma m_e}\boldsymbol{\nabla}(A_0^2) \tag{2.30}$$

In general terms, since the ponderomotive force is proportional to the square of the field, the force presented in equation (2.30) is composed of an average component and an oscillating term at frequency 2ω. The average component of this force is the actual ponderomotive force. It can therefore be re-written as:

$$\boldsymbol{F}_{\text{pond}} = -\frac{e^2}{2\langle\gamma\rangle m_\text{e}}\boldsymbol{\nabla}\langle\boldsymbol{A}^2\rangle \tag{2.31}$$

$$\text{with } \langle\gamma\rangle = \sqrt{1+\frac{\langle\boldsymbol{p}\rangle^2 + e^2\langle\boldsymbol{A}^2\rangle}{(m_\text{e}c)^2}} \tag{2.32}$$

It can be noted in equation (2.32) that the average relativistic factor $\langle\gamma\rangle$ is composed of the average momentum $\langle\boldsymbol{p}\rangle$ and the oscillating momentum $\langle\boldsymbol{p}_\perp\rangle = e\langle\boldsymbol{A}\rangle$. Further noting that only the oscillating part is space-dependent (the average momentum rather depends on time), we can re-write equation (2.31) as:

$$\boldsymbol{F}_{\text{pond}} = -m_\text{e}c^2\boldsymbol{\nabla}\langle\gamma\rangle \tag{2.33}$$

Equation (2.33) finally leads to the following expression for the relativistic ponderomotive energy:

$$U_{\text{pond}} = m_\text{e}c^2\left(\langle\gamma\rangle - 1\right) = m_\text{e}c^2\left(\sqrt{1+\langle\boldsymbol{a}^2\rangle} - 1\right) = m_\text{e}c^2\left(\sqrt{1+a_0^2/2} - 1\right) \tag{2.34}$$

2.1.4 Ionization processes

This section describes the main ionization processes of multiphoton absorption and tunnel ionization. The study of laser-plasma interactions indeed makes it relevant to wonder what is the minimum laser intensity required to ionize atoms. To have an order of magnitude at hand, let's first consider the Bohr radius (electron-proton distance in hydrogen atoms) as a starting point, being $a_\text{B} = 4\pi\varepsilon_0\hbar^2/m_\text{e}e^2 = 5.3\times10^{-11}$ m. The Coulomb electric field associated to this distance is therefore $E_a = e/4\pi\varepsilon_0 a_\text{B}^2 = 5.1\times10^{11}$ V/m, corresponding to an intensity of $I_a = \varepsilon_0 c E_a^2/2 = 3.5\times10^{16}$ W/cm^2. Is this value anywhere near the measured values? Of course not, ionization events happen at much lower intensities around 10^{12} W/cm^2, four orders of magnitude lower. A proper quantum mechanical modeling of field ionization came with the theory of Mstislav V. Keldysh in a famous paper of 1965 [144]. In this paper, Mstislav V. Keldysh derived a general equation to estimate the photoionization probability per unit time for an incoming EM wave of intensity I_0 and frequency ω, expressed by the following

equation:

$$W = A\omega \left(\frac{I_\mathrm{p}}{\hbar\omega}\right)^{\frac{3}{2}} \left(\frac{\gamma}{\sqrt{1+\gamma^2}}\right)^{\frac{5}{2}} S\left(\gamma, \frac{\widetilde{I}_\mathrm{p}}{\hbar\omega}\right) \exp\left[-\frac{2\widetilde{I}_\mathrm{p}}{\hbar\omega}\left(\operatorname{arcsin}\gamma - \gamma\frac{\sqrt{1+\gamma^2}}{1+2\gamma^2}\right)\right] \tag{2.35}$$

In equation (2.35), the so-called Keldysh parameter γ (not to be confused with the Lorentz factor) is defined as $\gamma = \sqrt{I_\mathrm{p}/U_\mathrm{pond}}$, where I_p is the static ionization potential and U_pond is the ponderomotive energy (see equation (2.26) section 2.1.3). The effective ionization potential $\widetilde{I}_p$ is rather defined as $\widetilde{I}_\mathrm{p} = I_\mathrm{p} + U_\mathrm{pond}/2$, and expresses the fact that half the ponderomotive energy serves to retain the electron bound to the atom (*i.e.* increasing the ionization potential) due to the oscillating nature of the wave. Hence, when ionized, an electron can acquire at least the other half ponderomotive energy above the ionization level in the continuum. Again in equation (2.35), A is a numerical constant close to 1, $S\left(\gamma, \frac{\widetilde{I}_\mathrm{p}}{\hbar\omega}\right)$ is a slowly varying function of the field and frequency, defined as:

$$\begin{aligned} S(\gamma, x) = \sum_{n=0}^{\infty} \exp\left[-2\left(\langle x+1\rangle - x + n\right)\left(\operatorname{arcsin}\gamma - \frac{\gamma}{\sqrt{1+\gamma^2}}\right)\right] \\ \times D\left[\sqrt{\frac{2\gamma}{\sqrt{1+\gamma^2}}\left(\langle x+1\rangle - x + n\right)}\right] \end{aligned} \tag{2.36}$$

with $x = \widetilde{I}_\mathrm{p}/\hbar\omega$, $\langle ... \rangle$ denotes the integer part of the argument and $D(z)$ is a Dawson integral of the form:

$$D(z) = \int_0^z e^{y^2 - z^2}\,\mathrm{d}y \tag{2.37}$$

As we can see from equation (2.35), the mathematical description of ionization events is a complex process, however it holds rather simple solutions in some selected cases, namely for *Multiphoton Ionization* (MPI) and high-field *Tunnel Ionization*. Both of these events are described in the next sections and are summarized in the schematic diagrams of Figure 2.2. These two cases occur either for $\gamma \gg 1$ or $\gamma \ll 1$, but of course events involving a combination of both cases happen in between the two when $\gamma \approx 1$ (*i.e.* multiphoton absorption + tunneling through the remainder of the potential barrier).

Multiphoton ionization

For the case when $\gamma \gg 1$ (*i.e.* low field, high frequency), the function $S\left(\gamma, \frac{\widetilde{I}_\mathrm{p}}{\hbar\omega}\right) \approx 1$ and equation (2.35) reduces to:

$$W \approx A\omega \left(\frac{I_\mathrm{p}}{\hbar\omega}\right)^{\frac{3}{2}} (2\gamma)^{-2\left\langle \frac{\widetilde{I}_\mathrm{p}}{\hbar\omega}+1 \right\rangle} = \sigma_n I_0^n \tag{2.38}$$

with $n = \left\langle \frac{\widetilde{I}_\mathrm{p}}{\hbar\omega} + 1 \right\rangle$ being the number of photons absorbed to bridge the gap of $\widetilde{I}_\mathrm{p}$. This process is called multiphoton ionization. If the frequency is high enough and therefore that ionization is possible with $n = 1$ photon, we have the well-known *photoelectric effect* explained by Albert Einstein in 1905, for which he received the Nobel Prize in Physics 1921. It is also possible for the electron to absorb more photons than required for passing over the barrier of $\widetilde{I}_\mathrm{p}$, thereby providing supplementary momentum to the electron and accumulating a kinetic energy of $\mathcal{E}_\mathrm{K} = n\hbar\omega - \widetilde{I}_\mathrm{p}$. This type of event is called *Above-Threshold Ionization* (ATI). Also note that $W \sim \sigma_n I_0^n$, which is the expected functional shape from measurements.

Tunnel ionization

For the next case when $\gamma \ll 1$ (*i.e.* high field, low frequency), $S\left(\gamma, \frac{\widetilde{I}_\mathrm{p}}{\hbar\omega}\right) \approx \sqrt{3\pi}/4\gamma^2$ and equation (2.35) reduces to:

$$W \approx A\frac{\sqrt{3\pi}}{4\gamma^2}\frac{I_\mathrm{p}}{\hbar}\sqrt{\gamma\frac{I_\mathrm{p}}{\hbar\omega}}\exp\left(-\frac{4}{3}\frac{I_\mathrm{p}}{\hbar\omega}\gamma\right) \tag{2.39}$$

where we have used:

$$\widetilde{I}_\mathrm{p} = I_\mathrm{p}\left(1 + \frac{1}{2\gamma^2}\right)$$

This case of figure is called tunnel ionization. In this situation, the Coulomb potential energy $U_\mathrm{C}(r)$ around the nucleus is strongly disturbed by the very intense incoming electric field wave, and can be expressed locally as:

$$U_\mathrm{C}(r) = -\frac{Ze^2}{4\pi\varepsilon_0|r|} - eEr \qquad \text{, for } r \in [-\infty, \infty] \tag{2.40}$$

Hence, the term eEr bends the Coulomb potential and reduces the height of the barrier required for the electron to reach the continuum. At a certain intensity, the electron can go through the

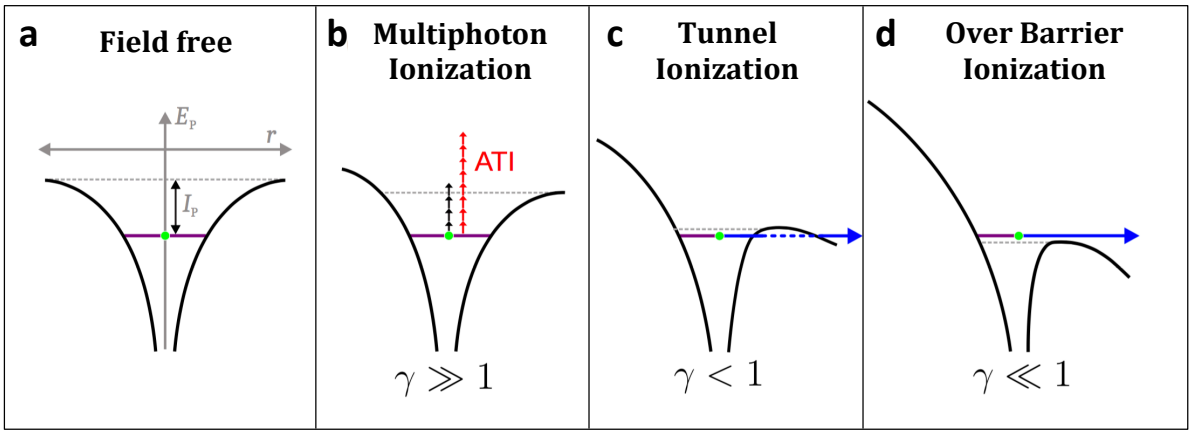

FIGURE 2.2: Schematic diagrams of strong field ionization events. (a) Field free Coulomb potential around the nucleus. (b) Multiphoton Ionization shown with an Above-Threshold Ionization event. (c) Tunnel Ionization event. (d) Over Barrier Ionization event. This figure is extracted and adapted from [145].

barrier by tunnel effect. Somewhere for large values of r, the barrier must be lower than the binding energy for the tunnel effect to occur. If the laser intensity is high enough and the barrier becomes lower than I_p everywhere, the electron will escape spontaneously. This effect is called *Over Barrier Ionization* (OBI). For relatively high intensities above 10^{15} W/cm^2, the Keldysh model diverges from what is observed experimentally. High-field tunnel ionization events are described more accurately by the ADK (Amonosov, Delone and Krainov) model [146] published in 1986. However, the ADK model is only valid in the tunnel regime. In laser-plasma interactions, when a high-intensity EM wave interacts with a target, the target is usually initiated in a stable non-ionized state. In high-intensity laser experiments, the ponderomotive energy is typically much higher than most ionization potentials of atoms, making them very easily ionized. Nevertheless, it is important to consider these models in order to properly estimate the ionization levels that are realistically reachable at a given intensity. The ionization models also describe the ionization physics happening during the steep power rise of a laser pulse, a few picoseconds before reaching the peak power. Moreover, the discussed Keldysh and ADK models are often included in Particle-In-Cell codes (see section 2.1.6) to give additional realism to the simulations, allowing to generate different ion species as a result of the strong laser-matter interactions.

2.1.5 Laser propagation in plasmas

The goal of this section is to derive the main concepts regarding the propagation of an EM wave in a plasma. These concepts are essential for the comprehension of this doctoral work, and form the basis of the absorption processes (see section 2.2) and acceleration mechanisms (see section 2.3) described further in this dissertation. In a uniform plasma, we can write the following expression for the perpendicular current density induced by an incoming EM wave traveling along the z-axis and polarized perpendicularly (*i.e.* $\boldsymbol{A} = \boldsymbol{A}_\perp$):

$$\boldsymbol{J}_\perp = -en_\mathrm{e}\boldsymbol{v}_\perp = -en_\mathrm{e}\frac{\boldsymbol{p}_\perp}{\gamma m_\mathrm{e}} = -\frac{n_\mathrm{e}e^2}{\gamma m_\mathrm{e}}\boldsymbol{A} \tag{2.41}$$

where we have used $\boldsymbol{p}_\perp = e\boldsymbol{A}$ from equation (2.15) and n_e is the electron density found by the classical relationship $n_\mathrm{e} = Z_\mathrm{eff}\rho N_\mathrm{A}/M$, where Z_eff is the effective ionization level, ρ is the mass density, N_A is Avogadro's number and M is the molar mass. Further replacing $\boldsymbol{J}_\perp$ in the wave equation for the vector potential (1.12) gives:

$$\boldsymbol{\nabla}^2\boldsymbol{A} - \frac{1}{c^2}\frac{\partial^2\boldsymbol{A}}{\partial t^2} = \mu_0\frac{n_\mathrm{e}e^2}{\gamma m_\mathrm{e}}\boldsymbol{A} \tag{2.42}$$

We now assume a plane wave distribution of the form $\boldsymbol{A} = \boldsymbol{A}_0 e^{i(kz-\omega t)}$, thus simplifying the second order derivatives, finally leading to the following dispersion relationship:

$$k^2c^2 = \omega^2 - \frac{\omega_{\mathrm{p,e}}^2}{\gamma} \tag{2.43}$$

where $\omega_{\mathrm{p,e}}$ the electron plasma frequency defined as:

$$\omega_{\mathrm{p,e}} = \sqrt{\frac{n_\mathrm{e}e^2}{m_\mathrm{e}\varepsilon_0}} \tag{2.44}$$

Therefore, we can further express the dispersion relationship as:

$$k = \sqrt{\varepsilon_\mathrm{eff}}k_0 = \sqrt{1 - \frac{\omega_{\mathrm{p,e}}^2}{\gamma\omega^2}}k_0 = \widetilde{n}k_0 \tag{2.45}$$

where ε_eff is the effective permittivity of the plasma, k_0 is the wavenumber in vacuum (*i.e.* without plasma) obtained with the usual expression $k_0 = \omega/c$ and $\widetilde{n}$ is the refractive index. We can

already see from equation (2.45) that the plasma imposes some limits on the wave propagation. In particular, if the argument in the square root of equation (2.45) becomes negative, this produces a complex refractive index that corresponds to an evanescent wave, characterized by a penetration depth (also called skin depth) of $l_s \approx c/\omega_{p,e}$. More precisely, let's consider that $\omega_{p,e} \gg \gamma\omega \approx \omega$, this gives the following index:

$$\tilde{n} = \sqrt{1 - \frac{\omega_{p,e}^2}{\gamma\omega^2}} \approx i\frac{\omega_{p,e}}{\omega} \qquad \Longrightarrow \qquad e^{ikz} = e^{i\tilde{n}k_0 z} = e^{-\frac{\omega_{p,e}}{\omega}k_0 z} = e^{-\frac{\omega_{p,e}}{c}z} = e^{-\frac{z}{l_s}}$$

Hence, as shown above, the skin depth l_s defines the effective penetration depth of the EM wave in a dense plasma. The EM wave cannot propagate in the plasma if $\sqrt{\gamma}\omega < \omega_{p,e}$. To better understand this transition, it is convenient to define the critical density of the laser n_c, for an EM wave interacting with a plasma at normal incidence, obtained by:

$$n_c = \frac{\varepsilon_0 m_e}{e^2}\omega^2 \tag{2.46}$$

For a typical Ti:Sapphire laser operating at a central wavelength of 800 nm, the critical density is around $n_c = 1.74 \times 10^{21}$ cm^{-3}. We can then note three cases of figure:

$n_e < \gamma n_c$: underdense plasma, EM wave is transmitted

$n_e = \gamma n_c$: resonance, maximal absorption

$n_e > \gamma n_c$: overdense plasma, EM wave is reflected

We can further write the refractive index of the plasma as:

$$\tilde{n} = \sqrt{\varepsilon_{eff}} = \sqrt{1 - \frac{n_e}{\gamma n_c}} \tag{2.47}$$

In general, metals have electron densities on the order of $10^{23} - 10^{24}$ cm^{-3} (*i.e.* hundreds to thousands of n_c), making them highly overdense and preventing visible light to propagate through, therefore explaining why they appear so reflective. Considering a low metallic density of $n_e = 100n_c$, EM waves penetrate in metals as evanescent wave on a distance of $l_s \approx c/\omega_{p,e} = 12.7$ nm, a penetration depth that decreases with increasing metallic density. On the contrary, gas jets have electron densities on the order of $10^{18} - 10^{19}$ cm^{-3}, (*i.e.* two to three orders of magnitude below n_c), making them highly transmissive. Another thing to note is the presence of the Lorentz factor γ in the dispersion relationship, which has the effect of

increasing the effective critical density when an EM wave with relativistic intensity propagates through a plasma. As the laser intensity increases towards the relativistic regime, the oscillating electrons see their mass increase due to their relativistic energy, and hence oscillate at a slower pace which reduces their effective plasma frequency as $\omega_{\mathrm{p,e}}/\sqrt{\gamma}$. This allows for the EM wave transmission to reach larger depths in a material that is classically overdense like metals. This effect is called *Self-Induced Relativistic Transparency* [147, 148] and is the subject of several acceleration schemes under investigation.

An important characteristic that plasmas can have is called *quasi-neutrality*. Locally, plasmas can sustain very strong electric fields, however after a certain distance positive and negative charges balance out and no net electric field can be perceived on macroscopic distances since they screen one another. Let's consider a fixed point charge $q\delta(r)$ placed at $\boldsymbol{r} = 0$ in a plasma with initial electron density of $n_{e,0}$, which is screened by a cloud of electrons locally. The distribution of the static electric potential is found by Poisson's equation as shown by:

$$\boldsymbol{\nabla}_r^2 \Phi(r) = -\frac{q\delta(r)}{4\pi\varepsilon_0} + \frac{e}{4\pi\varepsilon_0}\left[n_{\mathrm{e}}(r) - n_{\mathrm{e},0}\right] \tag{2.48}$$

where we assumed spherical symmetry and with $\boldsymbol{\nabla}_r^2$ being the Laplacian along r. Assuming a perfect electron gas with temperature T_{e} as well as $\Phi(r) \to 0$ for $r \to \infty$ and solving the equation, it can be shown that the electron cloud will follow a Boltzmann distribution:

$$n_{\mathrm{e}} \approx n_{\mathrm{e},0}\, e^{\frac{q\Phi(r)}{k_{\mathrm{B}}T_{\mathrm{e}}}} \tag{2.49}$$

Inserting expression (2.49) in equation (2.48) gives:

$$\frac{1}{r^2}\frac{\partial}{\partial r}\left[r^2\frac{\partial\Phi(r)}{\partial r}\right] = -\frac{q\delta(r)}{4\pi\varepsilon_0} - \frac{en_{\mathrm{e},0}}{4\pi\varepsilon_0}\left[1 - e^{\frac{q\Phi(r)}{k_{\mathrm{B}}T_{\mathrm{e}}}}\right] \tag{2.50}$$

Equation (2.50) is notoriously difficult to solve. In the weak coupling approximation (*i.e.* $q\Phi(r) \ll k_{\mathrm{B}}T_{\mathrm{e}}$), the solution is:

$$\Phi_{\mathrm{D}} = \frac{q}{4\pi\varepsilon_0 r}e^{-\frac{r}{\lambda_{\mathrm{D}}}} \tag{2.51}$$

Hence, we see that the typical Coulomb electric potential in $1/r$ is screened by an exponentially decreasing factor with characteristic length λ_{D}, which is called the Debye length. It is expressed

as:

$$\lambda_{\mathrm{D}} = \sqrt{\frac{\varepsilon_0 k_{\mathrm{B}} T_{\mathrm{e}}}{n_{\mathrm{e},0} e^2}} \tag{2.52}$$

The Debye length characterizes the radius of action after which the plasma is considered to be quasi-neutral. Hence, all the physics behind plasma waves must be considered within this distance to ensure a proper description of their kinetic evolution. This concept takes particular importance when performing Particle-In-Cell simulations (see section 2.1.6) and for the description of the acceleration mechanisms (see section 2.3).

2.1.6 Particle-In-Cell simulations

Modeling laser-plasma interactions is essential for the comprehension of the underlying acceleration mechanisms in laser-based particle acceleration. With the increasing available computational power over the past decades, virtual laser-plasma experiments performed through numerical modeling have become an invaluable tool to understand and develop new acceleration schemes. This requires to perform a kinetic evaluation of charged particles and their concomitant collective interactions with EM fields in the relativistic regime. The equation that describes this phenomenon was introduced by Anatoly Vlasov in 1945 [149]:

$$\frac{\partial f_{\mathrm{s}}}{\partial t} + \frac{\boldsymbol{p}_{\mathrm{s}}}{\gamma m_{\mathrm{s}}} \cdot \boldsymbol{\nabla} f_{\mathrm{s}} + q_{\mathrm{s}} \left(\boldsymbol{E} + \frac{\boldsymbol{p}_{\mathrm{s}}}{\gamma m_{\mathrm{s}}} \times \boldsymbol{B} \right) \cdot \frac{\partial f_{\mathrm{s}}}{\partial \boldsymbol{p}} = \left(\frac{\partial f_{\mathrm{s}}}{\partial t} \right)_{\mathrm{coll}} \tag{2.53}$$

Equation (2.53) is called the Vlasov-Maxwell equation, and was formely introduced without binary collisions (*i.e.* righthand side of equation set to 0). It describes the spatio-temporal evolution of a fluid of charged particles experiencing the Lorentz force from $\boldsymbol{E}$ and $\boldsymbol{B}$ fields arising from the Maxwell equations. The function $f_{\mathrm{s}} = f_{\mathrm{s}}(\boldsymbol{p}, \boldsymbol{r}, t)$ is a 6D particle density distribution defined per unit volume $d^3\boldsymbol{r} = dxdydz$ and momentum $d^3\boldsymbol{p} = dp_x dp_y dp_z$ that evolves over time t. The total number of particles N_{p} is thus found by integrating over the entire volume and all momenta:

$$N_{\mathrm{p}} = \sum_{\mathrm{s}} \iint f_{\mathrm{s}}(\boldsymbol{p}, \boldsymbol{r}, t)\, \mathrm{d}^3\boldsymbol{p}\, \mathrm{d}^3\boldsymbol{r} \tag{2.54}$$

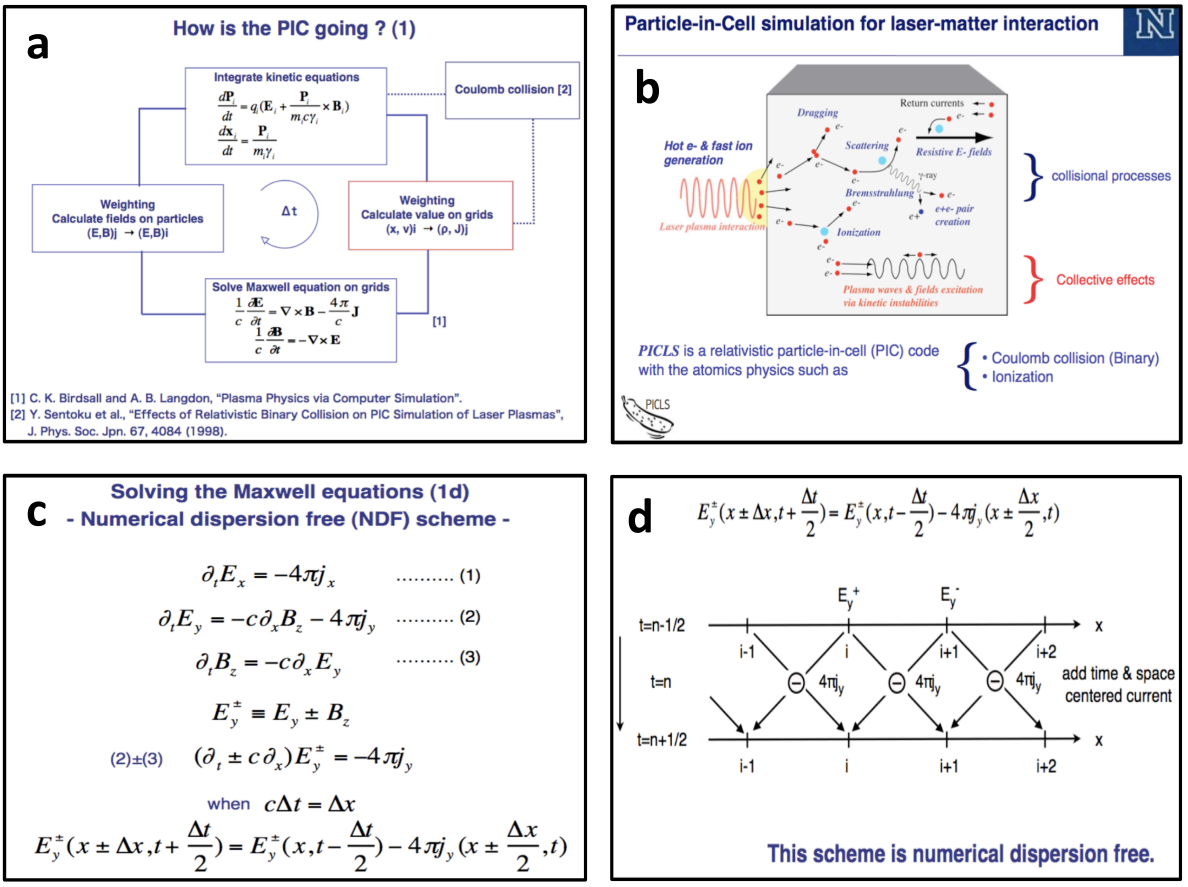

FIGURE 2.3: PICLS code framework schematic diagram used for developing PIC simulations. (a) Temporal iteration loop of PICLS for calculating the EM fields and the relativistic equations of motion using the particle distributions in phase space. (b) Schematic diagram of the different laser-matter interactions included in PICLS. (c) Finite Difference Time Domain scheme for field calculation. (d) Numerical Dispersion Free calculation scheme. This figure is extracted and adapted from [153].

The coupling with Maxwell's equations (1.6)-(1.9) is done through the calculation of the moments of f_s to find the charge density $\rho(\boldsymbol{r},t)$ and current density $\boldsymbol{J}(\boldsymbol{r},t)$:

$$\rho(\boldsymbol{r},t) = \sum_s q_s \int f_s \, \mathrm{d}^3\boldsymbol{p} \qquad \boldsymbol{J}(\boldsymbol{r},t) = \sum_s q_s \int f_s \frac{\boldsymbol{p}_s}{\gamma m} \, \mathrm{d}^3\boldsymbol{p} \tag{2.55}$$

Indeed, it can become rapidly heavy to compute f_s is in a 6D volume over time (*i.e.* effective 7D) within a spatial resolution below the Debye length λ_D for the proper evaluation of the generated plasma waves in the relativistic regime. As an example, let's consider we have an EM wave on the verge of the relativistic regime with $a_0 = 1$, leading to a Lorentz factor of $\gamma = \sqrt{1+a_0^2} = \sqrt{2}$. Let's assume a uniform electron plasma under the influence of the EM wave, hence with a temperature (average kinetic energy) of $k_B T_e = m_e c^2(\gamma - 1) \approx 211$ keV. For

a solid plasma density of $n_e \approx 10^{23}$ cm^{-3}, this gives a Debye length of $\lambda_D \approx 11$ nm. Let's now suppose we want to evaluate the evolution of an electron cloud within a focal volume of 1 μm^3 = 10^{-12} cm^3, over a fixed cartesian meshgrid (which is not a strict requirement for PIC codes). This gives a total of N_e = (10^{-12} cm^3)×(10^{23} cm^{-3}) = 10^{11} electrons to track over (1 μm/11 nm/2)^3 = 6×10^6 space voxels, where we have considered $\Delta x = \lambda_D/2$ to satisfy the Nyquist theorem. This is already a challenging task for a single computer workstation, also considering we need to discretize the momentum space as well. A solution to this problem was brought by a type numerical simulation called *Particle-In-Cell* (PIC), which solves the Vlasov-Maxwell equations using the method of the *macroparticle characteristics* [150, 151]. The distribution function f_s is discretized using so-called macroparticles, which are a statistical representation (with an associated statistical weight) of an ensemble of particles and models them in a collective motion. This allows for a significant reduction of the number of particles to be simulated, at the cost of an intrinsic numerical noise. Another advantage of PIC simulations is that they do not require the discretization of momentum space, hence not imposing maximum value. In fact, they avoid solving directly the Vlasov-Maxwell equation (2.53) and rather solve the relativistic equations of motion for all macroparticles sampling the plasma through the following equations:

$$\frac{d\boldsymbol{p}}{dt} = q\left(\boldsymbol{E} + \frac{\boldsymbol{p}}{\gamma m} \times \boldsymbol{B}\right) \qquad \frac{d\boldsymbol{r}}{dt} = \frac{\boldsymbol{p}}{\gamma m} \qquad \gamma = \sqrt{1 + \left(\frac{|\boldsymbol{p}|}{mc}\right)^2} \tag{2.56}$$

Particles can move freely (*i.e.* undiscretized) in space and momentum domains, a spatial meshgrid is used nevertheless to calculate the average electric and magnetic fields on spatial nodes from the particle phase space distribution, using a Finite Difference Time Domain (FDTD) scheme. The PIC code used in the context of this doctoral work is called PICLS [152]. The 2D3V version was used, meaning two degrees of freedom in space and all three kept in the momenta domain. A schematic diagram of the different steps done in each temporal iteration in PICLS is shown in Figure 2.3.a. The code also incorporates different binary events such as collisions, pair production, Bremsstrahlung production and ionization, as shown in Figure 2.3.b. A numerical dispersion free scheme is used, which is explicited in Figures 2.3.c-d.

2.2 High-field absorption processes

It should be first noted that the principal actors driving the laser energy absorption are the electrons and not the ions for the considered laser intensities of this dissertation. Indeed, the much higher mass of ions ($m_p \approx 1836 m_e$ for protons) makes them very slow compared to the laser frequency ($\omega_{p,p} \ll \omega$) and hence react to electric fields on longer timescales from collective effects. Replacing the mass of electrons m_e by the mass of protons m_p in equation (2.19), we find that the relativistic intensity threshold for protons is around $I_0 \approx 4.62 \times 10^{24}$ W/cm^2 for a laser with wavelength of 1 μm, beyond reach compared to the record laser intensity achieved today around 5.5×10^{22} W/cm^2 [154]. For laser-driven ion acceleration, the laser energy must necessarily be transferred intermediately to the electrons that are pushed by the ponderomotive force, gaining a maximal kinetic energy on the order of $U_{pond} = m_e c^2 a_0^2/2$. The oscillating electrons then undergo populational heating through collisions with the plasma. This in turn produces a strong charge separation that leads to the establishment of a high electrostatic potential which is responsible for ion acceleration. The relevant laser energy absorption processes in this context can be classified in terms of the intensity range into which they are effective, in particular being either non-relativistic ($a_0 < 1$) or relativistic events ($a_0 > 1$). Non-relativistic absorptions are characterized by the electric force $q\boldsymbol{E}$ being the dominant term in the two components of the Lorentz force. As the electric field intensity rises into the relativistic regime, the oscillation velocity of electrons in the EM field approaches the speed of light, hence making the magnetic force $q\boldsymbol{v} \times \boldsymbol{B}$ a significant term in the Lorentz force used to describe the electron motion. The next sections describe the laser energy absorption mechanisms from electrons in high-intensity regimes that are relevant for this doctoral work.

2.2.1 Collisional Absorption

Once the electrons have gained a kinetic energy on the order of the ponderomotive energy, they perform collisions with other charged particles, a process that transfers the radiation energy to the plasma. Since electron-electron collisions solely contribute to plasma thermalization and ion-ion collisions occur on much longer timescales than the one of interest (*i.e.* the electron interaction timescale of $\Delta t_e \sim 2\pi/\omega_{p,e}$), only electron-ion collisions are of importance for laser energy absorption. Nevertheless, ion-ion correlations remain of central importance for the study of Warm Dense Matter, and precise ion-ion correlations were reported experimentally in

the works of Ma *et al.* (2013, 2014) [155, 156] using X-Ray Thomson Scattering. While electrons collide with ions, they gain energy through the absorption of photons, which is why the effect is called *Inverse Bremsstrahlung* (*i.e.* Bremsstrahlung effect seen with reversed time axis). These electron-ion collisions can be modeled by inserting an additional loss term in the Lorentz force:

$$\frac{d\boldsymbol{p}}{dt} = -e(\boldsymbol{E} + \boldsymbol{v} \times \boldsymbol{B}) - m_e \nu_{ei} \boldsymbol{v} \tag{2.57}$$

where ν_{ei} is the electron-ion collision frequency. Collisional absorption occur over the full plasma length for underdense plasmas, and over the skin depth l_s for overdense plasmas. It leads to the following expression for the absorption coefficient A_{coll} and collision frequency [157]:

$$A_{coll} = \frac{\nu_{ei}}{c}\frac{n_e}{n_c}\left(1 - \frac{n_e}{n_c}\right)^{-1/2} \qquad \nu_{ei} = \frac{Ze^2 n_e \ln\Lambda}{3\varepsilon_0^2 m_e (2\pi T_e)^{3/2}} \tag{2.58}$$

where $\ln\Lambda$ is the Coulomb logarithm. Hence, we see that the collision rate follows $T_e^{-3/2}$, which makes electron-ion collisions less and less important as the laser intensity increases. Electron-ion collision rates in metals have typical values in the range of $\nu_{ei} \sim 10^{14} - 10^{16}$ Hz, making collisional absorption effective for relatively low intensities of $I_0 \leq 10^{15}$ W/cm^2 or in the first femtoseconds of the interaction when the laser intensity rises. As the laser intensity increases above 10^{15} W/cm^2, the plasma undergoes strong heating and the mean free path of electrons ($l_{MFP} = v_{th}/\nu_{ei}$, where v_{th} is the electron thermal velocity) becomes greater than the plasma skin depth due to the low collision frequency. In this situation, collisional absorption becomes negligible as the intensity climbs further and collisionless absorption mechanisms dominate the laser energy absorption from electrons. The most relevant mechanisms are discussed in the following sections.

2.2.2 Anomalous Skin Effect and Sheath Inverse Bremsstrahlung

As mentioned in the previous section, collisional absorption cannot be the dominant source of laser energy absorption as the intensity rises above 10^{15} W/cm^2, and collective effect become important since the electron's mean free path is larger than the plasma skin depth (*i.e.* $l_{MFP} \gg l_s$). Of particular importance here is the absorption occurring in steep density gradient with solid targets (*i.e.* overdense). Two mechanisms are known to explain laser energy absorption in the range in the intensity range of $I_0 \sim 10^{15} - 10^{17}$ W/cm^2, namely the *Anomalous*

Skin Effect and *Sheath Inverse Bremsstrahlung*. Both mechanisms have been demonstrated to be limit cases of the same absorption phenomenon, as explained in Yang *et al.* (1995) [158]. The *Anomalous Skin Effect* occurs when the thermal excursion length is much greater than the skin depth $l_{th} = v_{th}/\omega \gg l_s$, therefore the laser field oscillatory influence is transported beyond the skin depth [159] and electron thermalization occurs farther than l_s. In the other extreme case where $l_{th} = v_{th}/\omega \ll l_s$, electrons undergo several oscillatory cycles within the skin depth l_s and collectively bounce against ions as a sheath of electrons due to the strong charge separation. This effect is indeed analogous to inverse Bremsstrahlung absorption but now occurring a collective motion as a sheath, hence why it has been referred to *Sheath Inverse Bremsstrahlung* [160].

2.2.3 Resonance Absorption

The absorption mechanisms studied so far were for normal incidence with a plasma. Resonance absorption is a collisionless absorption process that occurs when a P-polarized EM wave is obliquely incident on a steep density gradient (*i.e.* with an electric field component along the density gradient, $\boldsymbol{E} \cdot \boldsymbol{\nabla} n_e \neq 0$). A schematic diagram of the geometrical concepts involved for resonance absorption is shown in Figure 2.4. The effective permittivity for an EM wave incident on a plasma with a angle θ is written as [157]:

$$\varepsilon_{eff}(\theta) = 1 - \frac{\omega_{p,e}^2}{\gamma\omega^2} - \sin^2\theta \tag{2.59}$$

Equation (2.59) implies that the EM wave can tunnel in the plasma within a skin depth to excite a resonance, and undergoes reflection at the plane $n_e = n_c \cos^2\theta \leq n_c$, where there is a match between laser frequency and the plasma frequency. This generates a plasma wave that amplifies during the first few optical cycles of the laser pulse, and then absorption occurs through wave damping from charged particle collisions, Landau damping and wave breaking [162, 163]. Considering a plasma density ramp of length L followed by a plateau at n_e, one can show that the absorption coefficient A_{ra} is given by:

$$A_{ra} \approx \frac{\phi^2(\xi)}{2} \quad \text{, where} \quad \phi(\xi) \approx 2.3\xi \exp\left(-\frac{2}{3}\xi^3\right) \quad \text{and} \quad \xi = (kL)^{1/3}\sin\theta \tag{2.60}$$

The function $\phi(\xi)$ exhibits an optimum for $\xi_{max} = 0.8$ with $A_{ra}^{max} = 0.86$. The incidence angle must therefore increase when the normalized plasma scale length L/λ decreases. Moreover,

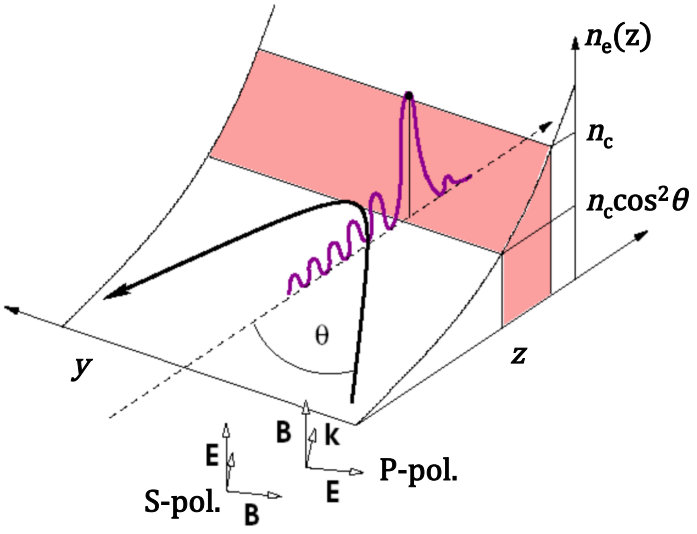

FIGURE 2.4: Schematic diagram of resonance absorption. Both linear polarizations are defined, the P-polarization being when the electric field is oriented in the EM wave's plane of incidence (yz-plane here) whereas the S-polarization is for an electric field oriented perpendicularly to the plane of incidence. This figure is extracted and adapted from [161].

when $L/\lambda \leq 0.08$ (*i.e.* very steep density gradient or very long wavelength), it is not possible anymore to reach $\xi_{\max} = 0.8$ since $\sin\theta \leq 1$, and therefore $A_{\text{ra}} < 0.86$. Resonance absorption in this case is said to be "not-so-resonant". It is important to note, however, that resonance absorption provides a minor contribution to electron heating when reaching the electron relativistic intensity threshold around 10^{18} W/cm^2 and becomes negligible thereafter. It is therefore not the dominant absorption mechanism for the TNSA mechanism, but is important nevertheless during the intensity rise of the laser pulse.

2.2.4 Vacuum Heating

As aforementioned in the previous section, when a P-polarized EM wave with oblique incidence encounters a very steep plasma density gradient (*i.e.* $L/\lambda \leq 0.08$), resonance absorption becomes "not-so-resonant" since the sharp gradient hinders the growth of plasma waves. This absorption mechanism was modeled in the work of François Brunel (1987) [164], and is called *Vacuum Heating* or *Brunel effect*. In this absorption mechanism, the quiver oscillation amplitude of electrons is much larger than the plasma scale length L. The longitudinal electric field component $\boldsymbol{E}_z$ (due to oblique incidence) pulls electrons out of the plasma edge in the first half

laser period, before changing direction and pushing electrons back into the target. When electrons reach the target, they have acquired a kinetic energy on the order of the ponderomotive energy which makes them travel far beyond the plasma skin depth and are therefore shielded by the plasma when the laser changes sign again. They are accelerated during a half-period in vacuum, which is why this absorption mechanism is called Vacuum Heating. The Brunel effect is one of the major absorption mechanisms for intensities in the range $10^{17} - 10^{19}$ W/cm^2, above which the $\boldsymbol{J} \times \boldsymbol{B}$ absorption mechanism dominates (see section 2.2.5). The Brunel absorption coefficient can reach $\sim 10\%$ for $a_0 = 1$. Indeed, an interesting feature is that it results in a pulsed electron bunch generation at the same repetition rate as the EM wave frequency $\nu = \omega/2\pi$. The electron temperature T_e^B generated by the Brunel modeling and the absorption coefficient A_B are given by:

$$T_e^B = 2m_e v_{osc}^2 \gamma^{-2} \sin^2\theta \qquad A_B \approx 0.05 a_0^{-1} \tan\theta \left[\sqrt{1 + a_0^2 \sin^2\theta} - 1\right] \tag{2.61}$$

It is rather straightforward to show that the electron temperature returned by the model are on the order of the ponderomotive energy, as is observed experimentally. The original Brunel work exhibited maximal absorption for large incidence angles around $\theta = 70°$, however a proper PIC modeling of the phenomenon has shown an absorption maximum for $\theta = 45°$ [165].

2.2.5 J × B Heating

For relativistic EM field intensities with $a_0 > 1$, more precisely for laser intensities above 10^{18} W/cm^2 for $\lambda_0 = 1$ μm, the oscillation velocity of electrons in the EM field approaches the speed of light, and the $\boldsymbol{v} \times \boldsymbol{B}$ term becomes of preponderant importance in the Lorentz force. The $\boldsymbol{J} \times \boldsymbol{B}$ Heating is effective for both linear polarizations S and P, however completely suppressed for circular polarization. The intense electric field first makes the electrons oscillate from the ponderomotive force in the transverse plane, providing them with a relativistic velocity $\boldsymbol{v}_\perp$ and driving a current density $\boldsymbol{J}_\perp$. The steadily growing current density $\boldsymbol{J}_\perp$ then concomitantly interacts the $\boldsymbol{B}$-field of the EM wave, and generates a Lorentz force that pulls the electrons out of the target to finally re-inject them back in. Since $\boldsymbol{v}$ and $\boldsymbol{B}$ both oscillate at a frequency of ω, the resulting term oscillates at a frequency of 2ω and therefore re-injects electron

bunches in the target twice per laser period. The relativistic electrons that acquire a kinetic energy on the order of the ponderomotive potential go far beyond the skin depth l_s and the Debye length λ_D, which makes them shielded from the laser field thereafter. This absorption mechanism occurs in similar fashion to Vacuum Heating with the presence of steep-edged density gradients and high intensities however, in the $\boldsymbol{J} \times \boldsymbol{B}$ mechanism, the $\boldsymbol{B}$-field is non-negligible and pushes the relativistic electrons along the longitudinal axis even for S-polarization, being most effective for normal incidence. It is the combination of both the effects of electrons oscillating at relativistic velocities and the non-negligible $\boldsymbol{B}$-field in the Lorentz force that gives rise to the $\boldsymbol{J} \times \boldsymbol{B}$ Heating as a non-linear ponderomotive force. This absorption process dominates the TNSA mechanism for intensities in the range $10^{18} - 10^{20}$ W/cm^2, and was explained in 1985 from the work of William L. Kruer and Kent Estabrook [166]. A few years after, the pioneering work from Wilks *et al.* (1992) [167] has shown through simulations that the average kinetic energy of the relativistic electrons re-entering the target, also called hot electron temperature $k_B T_e^{hot}$, can be properly estimated by the relativistic ponderomotive energy as previously obtained from equation (2.34):

$$\overline{\mathcal{E}}_K = k_B T_e^{hot} \approx U_{pond} = (\gamma_\perp - 1) m_e c^2 = \left(\sqrt{1 + a_0^2} - 1 \right) m_e c^2 \tag{2.62}$$

Equation (2.62) would become central thereafter to explain laser energy absorption from electrons in the relativistic regime with steep density gradients. It is also the starting point for the development of a theoretical model for the TNSA mechanism in laser-driven ion acceleration. It is important to note here that the ponderomotive energy is a reasonable estimate for the electron temperature and provides the proper scaling, but does not provide a rigorous description of electron heating. The absorption coefficient $A_{\boldsymbol{J}\times\boldsymbol{B}}$ can be written as follows:

$$A_{\boldsymbol{J}\times\boldsymbol{B}} \sim \frac{1}{2\pi} \left[1 - \left(1 + a_0^2 \right)^{-1/2} \right] \tag{2.63}$$

Similarly to the Brunel effect, the $\boldsymbol{J} \times \boldsymbol{B}$ absorption coefficient will reach an asymptotic value with increasing laser intensity, going up to 20% for $a_0 > 1$.

2.3 Acceleration mechanisms

This section is dedicated to detail the main principles behind the most prominent laser-driven ion acceleration mechanisms relevant to this doctoral work. They arise from a combination of all the theoretical concepts previously discussed on laser-plasma interactions (see section 2.1) and the absorption processes that drive electron heating at high laser intensities (see section 2.2). Indeed, a particular attention is given to *Target-Normal Sheath Acceleration*, not only being by far the most studied ion acceleration mechanism up to the present time, but also because the mechanism is central to this work. The section as well covers the concepts and scaling laws of *Radiation Pressure Acceleration* and *Collisionless Shock Acceleration* to give a wider perspective on the context of laser-based ion acceleration.

2.3.1 Target-Normal Sheath Acceleration

As aforementioned in section 1.3.3, the Target-Normal Sheath Acceleration mechanism occurs when a high-intensity ($I_0 > 10^{18}$ W/cm^2 or $a_0 > 1$) short duration (≤ 1 ps) laser pulse interacts with a relatively thin target of micrometric thickness. In addition, the plasma generated by the laser-matter interaction must be maintained somewhat unexpanded at the arrival of the main pulse by ensuring a high prepulse contrast ratio of at least 10^6 with respect to maximum intensity, up to nanoseconds before the interaction. The intense EM wave above the electron's relativistic intensity threshold pushes the electrons from the target, which are easily ionized mainly through high-field tunnel ionization, in the laser's forward direction through the relativistic ponderomotive force. The accelerated electrons undergo strong populational heating mostly through $\boldsymbol{J} \times \boldsymbol{B}$ and Vacuum Heating absorption mechanisms in the intensity range of $10^{18} - 10^{20}$ W/cm^2. Hot electrons then propagate through the target at relativistic velocities, and exit the target's rear side where some of them are retained due to strong charge separation, based on the target's capacitance, and form an electron cloud (the "sheath") that establishes an intense quasi-electrostatic electric field over a distance on the order of the Debye length λ_D. The longitudinal electric field completely ionizes water molecules and hydrocarbon impurities instantaneously, which are naturally present on the surface, and ions get accelerated along the target-normal direction by the electron sheath. The acceleration terminates when both ejected ion and electron populations have reached the same thermal velocities to form a quasi-neutral plasma bunch. Different ion species can be accelerated by this mechanism, however protons

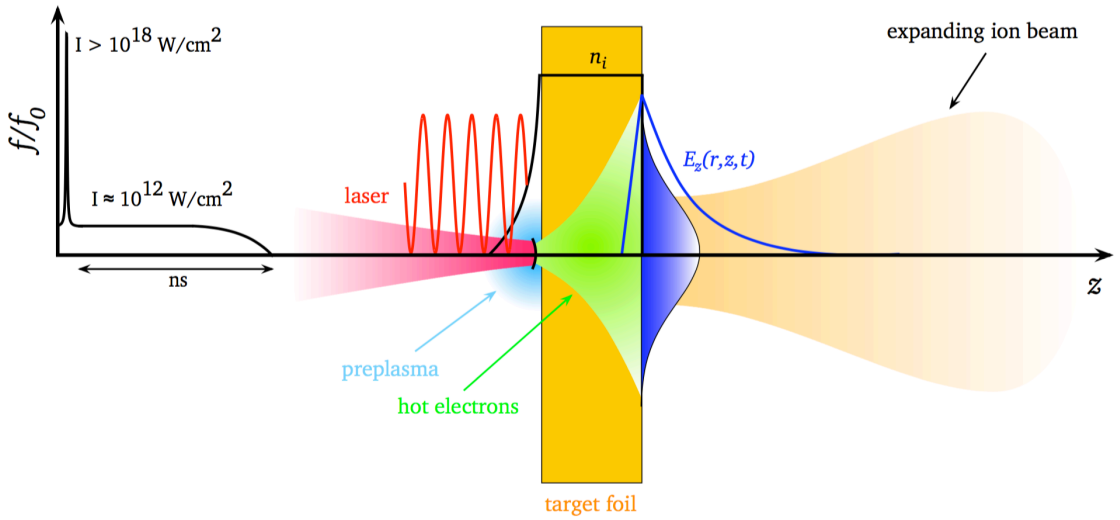

FIGURE 2.5: Schematic diagram of TNSA mechanism for ion acceleration with solid targets, resulting from plasma expansion into vacuum. This figure is extracted and adapted from [67].

are of particular interest since they respond more quickly to the accelerating electric field which results in stronger energy absorption from the hot electron cloud, owing to their higher charge-to-mass ratio compared to carbon ion species, for instance. The same plasma expansion also occurs on the target's front surface, however the acceleration is more efficient from the rear surface in the forward direction as a result of sharper density gradients, leading to stronger electric fields. More precisely, the front surface's plasma gradient is more affected by the EM wave's perturbation that produces a blow-off plasma, which hinders the conservation of a steep plasma density gradient. The high intensity of the EM wave, combined with the fact that ions start at rest on a cold surface, lead to strongly forward-oriented (*i.e.* non-isotropic) and relatively low divergence energetic ion beams, hence providing high beam quality. The short laser pulse duration ensures the generation of a steep hot electron density gradient and thus of a strong accelerating electric field. Another crucial factor is the laser contrast, which must be high enough to prevent a too strong target decompression before the interaction with the main pulse. The TNSA mechanism therefore relies on the generation of a dense hot electron cloud as an intermediate step in the laser-to-proton energy transfer. The acceleration process is explained by a plasma expansion model [80, 81] which is detailed below. A schematic diagram of TNSA is also shown in Figure 2.5. Finally, this section gives insights on the main experimental beam characteristics of laser-driven ion beams obtained through TNSA.

Plasma expansion model

The interaction of an EM wave with relativistic intensity ($a_0 > 1$) and a sharp plasma interface leads to strong electron heating through the different aforementioned absorption processes (see section 2.2). As noted by Wilks *et al.* (1992) [167], the average kinetic energy of the hot electron population, also called hot electron temperature, can be estimated by the ponderomotive energy:

$$k_B T_e^{hot} \approx U_{pond} = m_e c^2 \left(\sqrt{1 + a_0^2} - 1 \right) \quad \text{, with } a_0 \propto \sqrt{I_0 \lambda^2} \tag{2.64}$$

This assumption received further validation in the work of Hatchett *et al.* (2000) [79] to explain their experimental results. In equation (2.64), we recall that the normalized amplitude of the vector potential a_0 is given from equation (2.19), moreover that $a_0 = 1$ for $I_0 = 1.37 \times 10^{18}$ W/cm^2 and $\lambda = 1$ μm. A fraction η of the laser pulse energy $\mathcal{E}_L$ is transferred to hot electrons, for which the maximum electron density $n_{e,0}^{hot}$ generated can be estimated by the following semi-empirical relationship [112]:

$$n_{e,0}^{hot} = \frac{\eta \mathcal{E}_L}{c \tau_L S_{sheath} k_B T_e^{hot}} \qquad \eta = \alpha I_0^{0.74} \tag{2.65}$$

with $\alpha = 1.2 \times 10^{-15}$ (cm^2/W)$^{0.74}$ and the intensity in expressed in W/cm^2 [112]. In equation (2.65), τ_L is the laser pulse duration, c is speed of light and S_{sheath} is the surface area that covers the electron sheath. By inserting a few reasonable numerical values (e.g. $I_0 = 1.37 \times 10^{18}$ W/cm^2, $\eta = 3\%$, $k_B T_e = 0.211$ MeV, $\mathcal{E}_L = 1$ J and $\tau_L = 30$ fs) into equation (2.65), it is rather straightforward to remark that the number of hot electrons $N_{e,0}^{hot} = \eta \mathcal{E}_L / k_B T_e^{hot}$ traversing the target in the forward direction will generate currents that are several hundred times higher ($\sim 280\times$ using the chosen values) than the Alfvén current limit of $i_A = 4\pi\varepsilon_0 m_e c^3 / e \approx 17$ kA [168]. The Alfvén current limit is reached when a flux of charged particles is high enough so that its own magnetic field (produced by Ampère's law (1.9)) bends its trajectory back towards the source. Hence, strong return currents going in the backward direction are induced in the plasma by the hot electrons going in the forward direction such that the net current does not exceed the Alfvén current limit, and therefore minimizes the generated magnetic field. The radius of the hot electron sheath r_{sheath} can be estimated by the laser beamwaist w_0, target thickness d and electron beam divergence angle θ using:

$$r_{sheath} = w_0 + d \tan\theta \qquad S_{sheath} = \pi r_{sheath}^2 = \pi \left[w_0 + d \tan\theta \right]^2 \tag{2.66}$$

The hot electrons will exit the target's rear side while some of them will be backholded and undergo transverse re-circulation, as a result of the strong charge separation inducing a restoring force, to form an electron sheath. We can simplify the situation by a 1D problem and obtain the electric potential resulting from this charge separation from Poisson's law:

$$\frac{\partial^2 \Phi}{\partial z^2} = \frac{e}{\varepsilon_0}\left[n_{\mathrm{e},0}^{\mathrm{hot}}(z) - Z n_{\mathrm{i}}(z)\right] \qquad n_{\mathrm{e}}^{\mathrm{hot}}(z) = n_{\mathrm{e},0}^{\mathrm{hot}}\, e^{-\frac{\mathcal{E}_{\mathrm{K}}}{k_{\mathrm{B}} T_{\mathrm{e}}^{\mathrm{hot}}}} = n_{\mathrm{e},0}^{\mathrm{hot}}\, e^{\frac{e\Phi(z)}{k_{\mathrm{B}} T_{\mathrm{e}}^{\mathrm{hot}}}} \tag{2.67}$$

Equation (2.67) assumes a global charge quasi-neutrality (*i.e.* with $n_{\mathrm{e},0}^{\mathrm{hot}} = Z n_{\mathrm{i},0}$) assumption. The hot electron density is characterized by a Boltzmann distribution in energy (more precisely a Maxwell-Jüttner distribution in the relativistic case), where we have used $\mathcal{E}_{\mathrm{K}} = -e\Phi$. More in general regarding the Boltzmann distribution, one can also write the following expression starting from the expression of $n_{\mathrm{e}}^{\mathrm{hot}}(z)$ in equation (2.67):

$$e\Phi(z) = k_{\mathrm{B}} T_{\mathrm{e}}^{\mathrm{hot}} \left\{ \ln\left[n_{\mathrm{e}}^{\mathrm{hot}}(z)\right] - \ln\left[n_{\mathrm{e},0}^{\mathrm{hot}}\right] \right\} \tag{2.68}$$

Taking the gradient of equation (2.68) and further noting that $\boldsymbol{E} = -\boldsymbol{\nabla}\Phi$ leads to the following relationship:

$$-e\boldsymbol{E} n_{\mathrm{e}}^{\mathrm{hot}} = k_{\mathrm{B}} T_{\mathrm{e}}^{\mathrm{hot}} \boldsymbol{\nabla}(n_{\mathrm{e}}^{\mathrm{hot}}) \tag{2.69}$$

Equation (2.69) expresses the fact that electric fields in plasmas arise from steep charge density gradients, a well-known concept in plasma physics. In this particular case, the sharp density gradient is induced by the high-intensity, short duration EM wave. As initial conditions for solving equation (2.67), we consider that $n_{\mathrm{i}}(z < 0) = n_{\mathrm{i},0}$ and $n_{\mathrm{i}}(z > 0) = 0$, with a sharp border at $z = 0$. The solution to this problem is obtained by Crow *et al.* (1975) [169] and is expressed as:

$$\Phi(z) = -\frac{2k_{\mathrm{B}} T_{\mathrm{e}}^{\mathrm{hot}}}{e} \ln\left[1 + \frac{z}{\sqrt{2\mathrm{e}}\lambda_{\mathrm{D},0}}\right] - \frac{k_{\mathrm{B}} T_{\mathrm{e}}^{\mathrm{hot}}}{e} \tag{2.70}$$

with the initial Debye length $\lambda_{\mathrm{D},0} = \sqrt{\varepsilon_0 k_{\mathrm{B}} T_{\mathrm{e}}^{\mathrm{hot}} / n_{\mathrm{e},0}^{\mathrm{hot}} e^2}$ and noting $\mathrm{e} = \exp(1) = e^1$. Hence, taking the derivative along z leads to the expression for the longitudinal electric field $E_z(z)$:

$$E_z(z) = -\frac{\partial \Phi}{\partial z} = \frac{2k_{\mathrm{B}} T_{\mathrm{e}}^{\mathrm{hot}}}{e} \frac{1}{z + \sqrt{2\mathrm{e}}\lambda_{\mathrm{D},0}} \tag{2.71}$$

One can therefore find the maximum electric field at $z = 0$:

$$E_z^{\max} = E_z(z=0) = \sqrt{\frac{2}{\mathrm{e}}} E_{z,0} \qquad E_{z,0} = \frac{k_\mathrm{B} T_\mathrm{e}^\mathrm{hot}}{e\lambda_{\mathrm{D},0}} = \sqrt{n_{\mathrm{e},0}^\mathrm{hot} k_\mathrm{B} T_\mathrm{e}^\mathrm{hot}/\varepsilon_0} \tag{2.72}$$

Equation (2.72) is central to plasma physics. It shows that the maximum sustainable electric field in a thermal plasma is given solely by the square-root of the product $n_{\mathrm{e},0}^\mathrm{hot} k_\mathrm{B} T_\mathrm{e}^\mathrm{hot}$. Another intuitive way to see it is by noting that an electric field is defined as a potential (*i.e.* here the ponderomotive potential $\Phi_\mathrm{pond} = \dfrac{k_\mathrm{B} T_\mathrm{e}^\mathrm{hot}}{e}$) per unit length (*i.e.* the Debye length $\lambda_{\mathrm{D},0}$). To obtain the temporal variation for $t > 0$, we consider an isothermal expansion of the hot electrons, hence in equilibrium with the potential Φ. For the expansion of ions, a fluid model is used to write the equations of continuity and momentum conservation (Euler's equation):

$$\frac{\partial n_\mathrm{i}}{\partial t} + \frac{\partial (n_\mathrm{i} v_\mathrm{i})}{\partial z} = 0 \qquad \frac{\partial v_\mathrm{i}}{\partial t} + v_i \frac{\partial v_\mathrm{i}}{\partial z} = -\frac{Ze}{m_\mathrm{i}} E_z(z) \tag{2.73}$$

where v_i is the ion velocity and m_i is the ion mass. We then use the self-similar variable $\xi = z/c_\mathrm{s} t$ with $c_\mathrm{s} = \sqrt{Z k_\mathrm{B} T_\mathrm{e}^\mathrm{hot}/m_\mathrm{i}}$ being the ion sound speed. The system of equations (2.73) has a self-similar solution of the form:

$$v_\mathrm{i} = c_\mathrm{s} + \frac{z}{t} \qquad n_\mathrm{i} = n_{\mathrm{i},0}\, e^{-\frac{v_\mathrm{i}}{c_\mathrm{s}}} = n_{\mathrm{i},0}\, e^{-(1+\frac{z}{c_\mathrm{s} t})} \tag{2.74}$$

Expressions in (2.74) lead to a time-dependent Debye length $\lambda_\mathrm{D}(z,t)$ of the form:

$$\lambda_\mathrm{D}(z,t) = \sqrt{\frac{\varepsilon_0 k_\mathrm{B} T_\mathrm{e}^\mathrm{hot}}{n_\mathrm{e}^\mathrm{hot} e^2}} = \lambda_{\mathrm{D},0}\, e^{\frac{1}{2}(1+\frac{z}{c_\mathrm{s} t})} \tag{2.75}$$

Indeed, this solution predicts infinite acceleration for large z. This is a consequence of the isothermal expansion (*i.e.* $T_\mathrm{e}^\mathrm{hot}$ is constant everywhere) model. However, in reality the electron temperature decreases while the energy is transferred to the ions. The acceleration stops when ion and electron populations form a co-moving quasi-neutral plasma bunch, a condition reached when the populations have the same thermal velocities. This is modeled by imposing a stopping condition through a finite acceleration time called t_acc, as indicated in the work of Fuchs *et al.* [112]. The expression for the maximum ion energy is obtained by finding the velocity at the ion front, developed in the accurate model of Mora (2003) [81], and is written

as:

$$\mathcal{E}_{\mathrm{K,i}}^{\max} = 2Zk_{\mathrm{B}}T_{\mathrm{e}}^{\mathrm{hot}}\left[\ln\left(\tau_{\mathrm{i}} + \sqrt{1+\tau_{\mathrm{i}}^2}\right)\right]^2 \quad \text{, with } \tau_{\mathrm{i}} = \frac{\omega_{\mathrm{p,i}} t_{\mathrm{acc}}}{\sqrt{2\mathrm{e}}} \tag{2.76}$$

with $\omega_{\mathrm{p,i}} = \sqrt{n_{\mathrm{e,0}}^{\mathrm{hot}} Ze^2/m_{\mathrm{i}}\varepsilon_0}$ being the ion plasma frequency and τ_{i} is called the normalized acceleration time. In the work of Fuchs *et al.* (2006) [112], the acceleration time is semi-empirically modeled from experiments as $t_{\mathrm{acc}} \approx 1.3(\tau_{\mathrm{L}} + t_{\mathrm{min}})$, with $t_{\mathrm{min}} = 60$ fs being the minimum required time for the energy transfer from the hot electrons to ions. An important fact to note from (2.76) is that the maximum ion energy is linearly dependent on the hot electron temperature $k_{\mathrm{B}}T_{\mathrm{e}}^{\mathrm{hot}}$, but depends mildly on the hot electron density $n_{\mathrm{e,0}}^{\mathrm{hot}}$. However, the hot electron density linearly influences ion number as we shall see further, coming from the quasi-neutral assumption. From the self-similar solution of equation (2.74) and using the non-relativistic kinetic energy $v_{\mathrm{i}} = \sqrt{2\mathcal{E}_{\mathrm{K,i}}/m_{\mathrm{i}}}$, we can calculate the ion energy spectrum:

$$\frac{dn_{\mathrm{i}}}{d\mathcal{E}_{\mathrm{K,i}}} = \frac{dn_{\mathrm{i}}}{dv_{\mathrm{i}}}\frac{dv_{\mathrm{i}}}{d\mathcal{E}_{\mathrm{K,i}}} = \frac{n_{\mathrm{i,0}}}{\sqrt{2\mathcal{E}_{\mathrm{K,i}} Zk_{\mathrm{B}}T_{\mathrm{e}}^{\mathrm{hot}}}} e^{-\sqrt{\frac{2\mathcal{E}_{\mathrm{K,i}}}{Zk_{\mathrm{B}}T_{\mathrm{e}}^{\mathrm{hot}}}}} \tag{2.77}$$

Then, for the particular case of protons ($Z = 1$), we find the famous truncated exponential relationship for the proton number energy spectrum $\frac{dN_{\mathrm{p}}}{d\mathcal{E}_{\mathrm{K,p}}}$:

$$\frac{dN_{\mathrm{p}}}{d\mathcal{E}_{\mathrm{K,p}}} = c_{\mathrm{s}} t_{\mathrm{acc}} S_{\mathrm{sheath}} \cdot \frac{dn_{\mathrm{p}}}{d\mathcal{E}_{\mathrm{K,p}}} = \frac{n_{\mathrm{e,0}}^{\mathrm{hot}} c_{\mathrm{s}} t_{\mathrm{acc}} S_{\mathrm{sheath}}}{\sqrt{2\mathcal{E}_{\mathrm{K,p}} k_{\mathrm{B}} T_{\mathrm{e}}^{\mathrm{hot}}}} e^{-\sqrt{\frac{2\mathcal{E}_{\mathrm{K,p}}}{k_{\mathrm{B}}T_{\mathrm{e}}^{\mathrm{hot}}}}} \quad \text{, for } \mathcal{E}_{\mathrm{K,p}} \leq \mathcal{E}_{\mathrm{K,p}}^{\max} \tag{2.78}$$

We note from equation (2.78) that the proton spectrum is completely determined by the hot electron population with $n_{\mathrm{e,0}}^{\mathrm{hot}}$ and $k_{\mathrm{B}}T_{\mathrm{e}}^{\mathrm{hot}}$, moreover is in agreement with experiments. Schematic diagrams of the self-similar solution for isothermal plasma expansion are shown in Figure 2.6.

Beam characteristics

After the groundbreaking experiments of the year 2000 [76–78], laser-driven ion beams received thorough experimental characterizations, in the years that followed, by several experiments worldwide [82, 84, 85, 120, 170–174]. The ion beam source size emerging from the rear

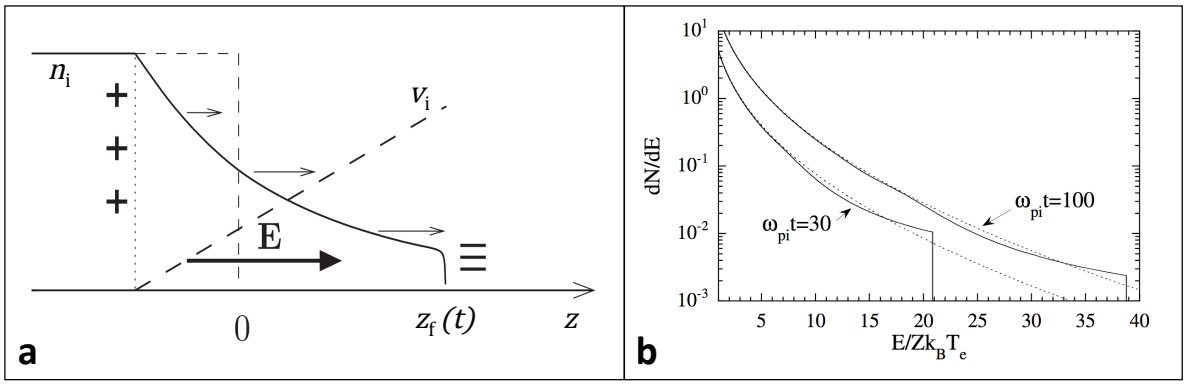

FIGURE 2.6: (a) Schematic diagram of the self-similar solution found for the isothermal plasma expansion, as obtained from equation (2.74). This figure is extracted and adapted from [64] (b) Simulated (full lines) and analytical (dotted lines) solutions ion spectra obtained for the isothermal plasma expansion model, calculated for two normalized acceleration times. This figure is extracted and adapted from [81].

target surface was determined to be a few tens up to a few hundreds of micrometers in diameter, depending on the laser characteristics and the target thickness, with decreasing size for increasing kinetic energies. Moreover, the divergent cone half-angle was measured to be in the tens of degrees ($15° - 30°$) for the full beam (*i.e.* all energies) with decreasing divergence with increasing proton kinetic energy. These types of measurement are typically performed using RCF stacks for beam profiling at different energies, usually combined with either grooves placed on the target or by using fine metallic meshgrids placed between the ion source and the RCF stack used for source size measurement. Combining the values of source size and divergence half-angle allows to model the ion cone beams originating from a virtual point source placed several hundreds of micrometers, depending on the energy, before the interaction target front. Schematic diagrams characterizing the proton beam features are shown in Figure 2.7.

Another characteristic worth noting is the increasing maximum proton energy with decreasing target thickness. PIC simulations insights from the work of Dong *et al.* (2003) [130] showed that increased proton energies are obtained with decreasing target thickness due to a combination lower energy loss and lower conical dispersion of hot electrons traversing the target. A lower energy loss of hot electrons leads to higher hot electron temperatures and densities at the target's rear side, and thus to higher proton energies as shown from equation (2.76). Assuming ultra-high laser-to-prepulse contrast ($> 10^{10}$ down to a few tens of picoseconds before the main pulse), a sub-optimal target thickness is found when the target becomes more transparent to the laser, *i.e.* on the order of the skin depth l_s, leading to a decreased energy transfer and hence to lower proton energies. In practice, achieving ultra-high contrast for high-intensity

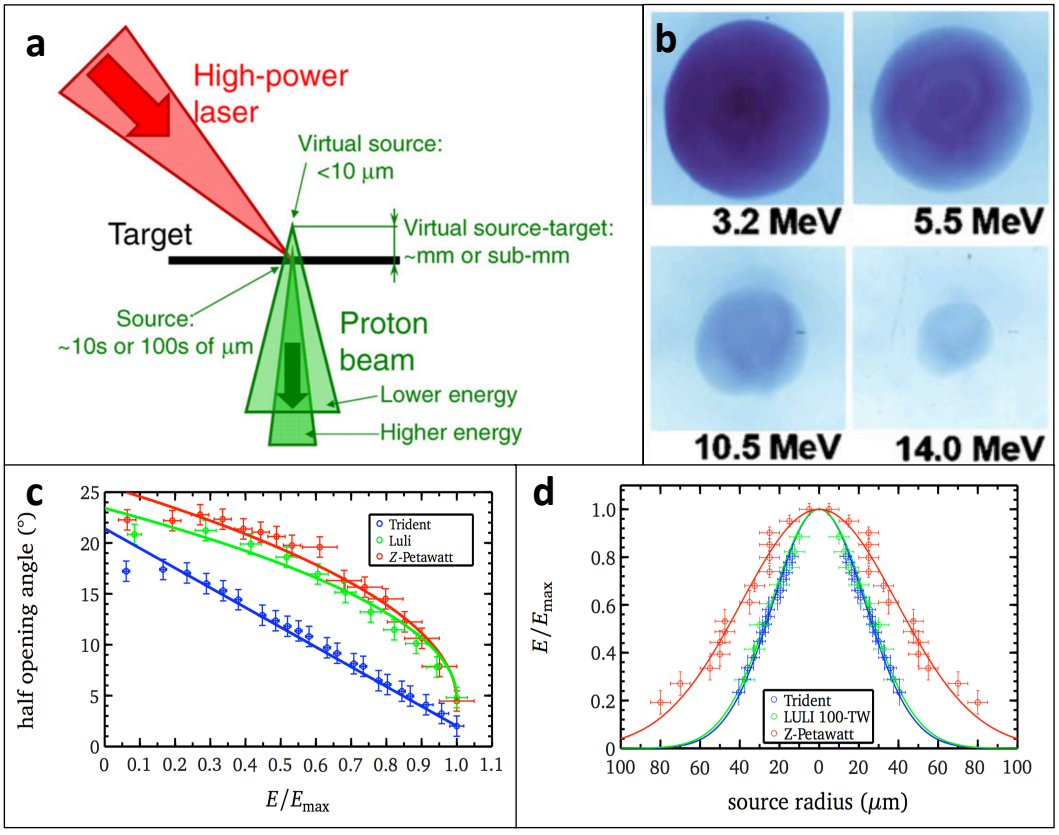

FIGURE 2.7: (a) TNSA beam source size and divergence characteristics. This figure is extracted and adapted from [65] (b) Use of radiochromic films to determine beam divergence, particle energy and particle numbers. The reported energy, from the stopping power values, is the one having its Bragg peak energy deposition in the corresponding layer of the RCF stack. This figure is extracted and adapted from [85]. (c-d) Cone half-angle variation (c) and source size variation (d) with energy. These figures are extracted and adapted from [67].

laser pulses is not a simple task and requires the use of several beam cleaning techniques such as saturable absorbers, cross-wave polarizers (XPW) and plasma mirrors (PM) [175]. The latter is a type of mirror made of polymer that is initially transparent to the laser and gradually absorbs energy from the ASE pedestal and prepulses that initiates a plasma expansion at its front. As the laser intensity rises, the plasma expansion reaches a point for which the electron density is higher than the laser's critical density, hence becoming reflective when the main pulse hits the plasma mirror. The position where the laser hits the PM needs to be changed at every shot, making its use more cumbersome than without PM. In the end, the optimal target thickness yielding the highest proton energies is ultimately dictated by the intensity regime and the laser-to-prepulse contrast [112, 125, 131]. A too thin target ($<$ 100 nm) used with a low laser contrast ($< 10^6$) will undergo strong ionization, expand and disrupt before the main pulse arrives, producing an inefficient TNSA mechanism. Contrast enhancement using plasma

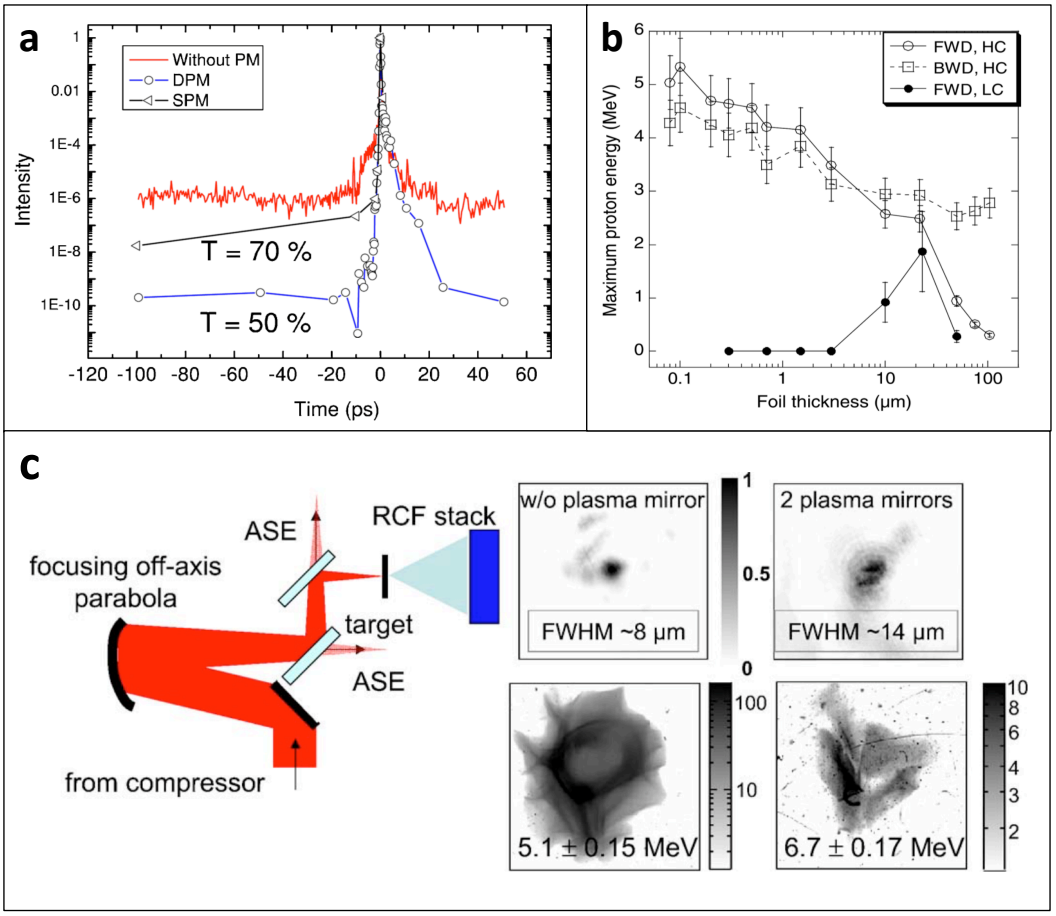

FIGURE 2.8: (a) Enhanced contrast with single and double plasma mirrors. This figure is extracted and adapted from [176]. (b) Investigation of maximum ion energy with high laser contrast (HC) compared to low laser contrast (LC), for different target thicknesses. Forward (FWD) and backward (BWD) accelerations are also investigated. This figure is extracted and adapted from [115]. (c) Increased proton energies when using plasma mirrors and ultrathin foils. The gray levels shown for the RCFs are in Gy. This figure is extracted and adapted from [117].

mirrors and optimal target thickness for laser-driven ion acceleration have been investigated in the literature [115, 117, 176, 177], and examples are shown in Figure 2.8. In particular, Figure 2.8.a shows that an enhanced laser contrast comes at the expense of an energy loss in the laser pulse, hence to lower intensities, reaching around 50% of transmission when using two plasma mirrors at 45° of incident, commonly called Double Plasma Mirror (DPM) [178, 179]. The energy transmission of a PM (and DPM) varies for different laser fluences and PM material, hence the experimental endpoint must be evaluated thoroughly. The lower proton energies, resulting from the lower laser intensities when using a DPM, are compensated by the use of ultra-thin foils yielding higher proton energies, up to the optimal thickness. This effect is shown in Figure 2.8.b. One needs to note that the contrast comparisons are often performed

at equivalent laser intensities, hence why the low contrast case appears so inferior to the high contrast cases. Indeed, using a DPM can be a double-edged knife since lower energy transmission with thinner targets can yield lower proton energies than the full laser power with thicker targets. Hence, the net gain of using PM is strongly dependent on the laser characteristics used and the type of contrast obtained, making it difficult to estimate directly. Another example of higher proton energies obtained using a DPM is shown in Figure 2.8.c. As we can notice from the intensity levels on the RCFs of Figure 2.8.c, higher proton energies obtained with a DPM can also come at the expense of lower particle yield due to a smaller amount of hot electrons generated, reaching nearly ten-fold of difference in this particular case. Indeed, as the laser intensities escalate with larger laser facilities being built over time, beam cleaning techniques are increasingly becoming a necessity, otherwise targets undergo plasma expansion too early before the interaction with main pulse, which ultimately decreases the acceleration efficiencies. However, some acceleration schemes are benefiting from a larger plasma scale length provided by a preplasma to deliberately induce self-focusing within the plasma, thereby increasing the energy transfer [180, 181].

2.3.2 Radiation Pressure Acceleration

If the laser intensity climbs above 10^{20} W/cm^2, another acceleration mechanism comes into competition with TNSA when using overdense targets, namely the Radiation Pressure Acceleration (RPA). The RPA mechanism was first suggested in the work of Esirkepov *et al.* (2004) [182] for intensities in excess of 10^{23} W/cm^2, in an intensity range of strong predominance with respect to TNSA. In this mechanism, the momentum carried by the EM wave is so high that it pushes directly the target, providing collective thrust to the particles. This results in a forward-oriented beam of particle emerging from the radiative pressure upon EM wave's impact with the front target surface, and is only effective for very thin targets (typically submicrometric thicknesses). If the impact is strong enough, the accelerated ions from the front surface in the laser's forward direction can reach velocities higher than the ions emerging from the rear target surface through the TNSA mechanism, in addition to exhibiting a low energy dispersion. A way to further increase its predominance is to use circularly polarized waves such as to quench hot electron generation, in particular through complete inhibition of $\boldsymbol{J} \times \boldsymbol{B}$ absorption (see section 2.2.5), and conserve only the drifting term in the longitudinal equation of motion (see equation (2.22)) [183]. The radiative pressure P_{rad} of a laser pulse of peak intensity I_0 upon

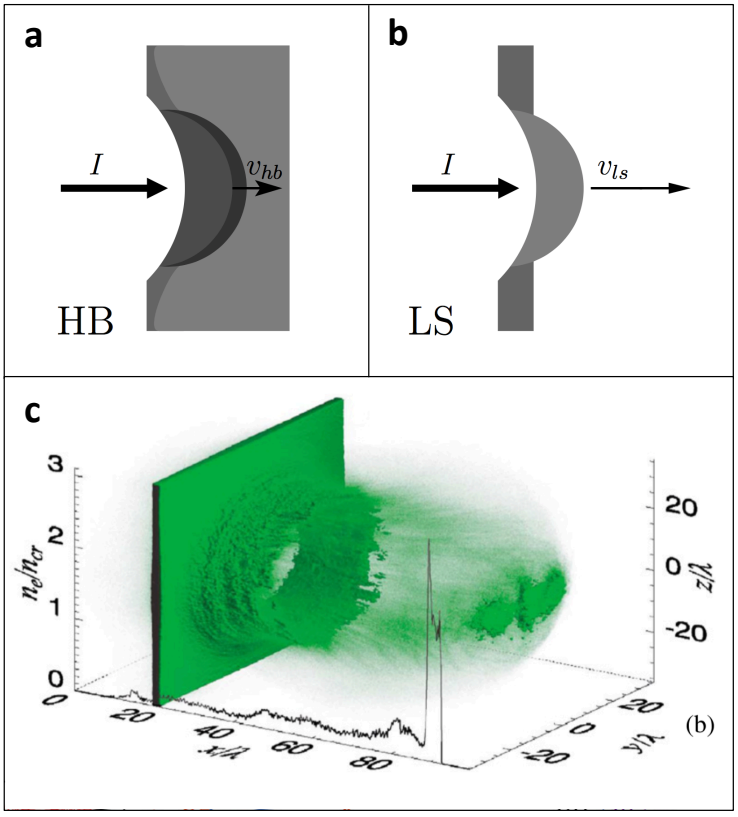

FIGURE 2.9: Schematic diagrams of the Radiation Pressure Acceleration mechanism. (a-b) Two distinct acceleration cases within RPA are the Hole Boring (a) and Light-Sail (b) regimes. These figures are extracted and adapted from [63]. (c) 3D PIC simulations exhibiting the strong radiative pressure of an ultra-intense laser pulse impacting a thin overdense target. This figure is extracted and adapted from [131].

impact with a target can be expressed as [64]:

$$P_{\text{rad}} = (1 + \mathcal{R} - \mathcal{T})\frac{I_0}{c} = (2\mathcal{R} + \mathcal{A})\frac{I_0}{c} \tag{2.79}$$

where $\mathcal{R}$, $\mathcal{T}$ and $\mathcal{A}$ are the reflection, transmission and absorption coefficients, respectively. In equation (2.79), we have imposed the conservation of energy through the relationship $\mathcal{R} + \mathcal{T} + \mathcal{A} = 1$. One can expect a maximum pressure, in an ideal case called the "perfect" relativistic mirror for $\mathcal{T} = \mathcal{A} = 0$ and therefore $\mathcal{R} = 1$, leading to $P_{\text{rad}}^{\text{max}} = 2I_0/c$. It is possible to distinguish two regimes of acceleration with RPA, one in the case of thick targets called *Hole Boring* (HB) regime and another for thin target called the *Light Sail* (LS) regime. Schematic diagrams for both cases are shown in Figure 2.9 as well as further explanations given in the next sections.

2.3.2.1 Hole Boring regime

The Hole Boring regime (also called the laser piston regime) occurs when the laser pulse does not penetrate through the target, as a result of using a "thick" target (*i.e.* much thicker than the laser penetration skin depth, $d \gg l_s$), and pushes the particles to continuously increase the local density from its pressure. This steepens the density of the target as the laser acts on the surface like a piston. This ultimately bores a hole in the plasma and accelerates particles up to a velocity called the "hole boring velocity" v_{HB}, thereby defining the target thickness condition of $d > v_{HB}\tau_L$, with τ_L being the laser pulse duration. Estimations of the HB velocity are found by balancing out the the EM and mass momentum flows in planar geometry [184, 185]. This leads to the following kinetic energy scaling for ions:

$$\mathcal{E}_K^{HB} = 2m_e c^2 Z \frac{n_c}{n_e} a_0^2 \tag{2.80}$$

Hence, we see from equation (2.80) that ion kinetic energy scales as $\mathcal{E}_K^{HB} \propto a_0^2 \propto I_0$, compared to $\mathcal{E}_K^{TNSA} \propto a_0 \propto \sqrt{I_0}$ for the TNSA mechanism, explaining why RPA triggers so much attention in the laser acceleration community. We can also note that $\mathcal{E}_K^{HB} \propto 1/n_e$, and thus high electron densities are not prone to produce high ion energies in HB-RPA. The target density must therefore be reduced close to $n_e \sim n_c$ but not below, since the target would become transparent which would reduce the reflection coefficient and the strength of the impact. Moreover reducing the target thickness helps to increase ion energies by minimizing collisional energy losses. Promising theoretical estimates when using $I_0 > 10^{22}$ W/cm^2 and near-critical targets of micrometric thickness are predicting proton energies above 100 MeV and quasi-monoenergetic beams [186–188].

2.3.2.2 Light Sail regime

If the target thickness d is reduced such that $d < v_{HB}\tau_L$, with v_{HB} being the hole boring velocity and τ_L the laser pulse duration, the ion front reaches the other side of the target before the end of the laser pulse. In this situation, the entire target thickness is accelerated within the focal volume, and the effect is described as a thin relativistic mirror propelled by radiation pressure, called the Light Sail regime. This particular case limits particle energy losses since there is no plasma background, and continuously accelerates the same ion mass already compressed by

the laser. Ion energy estimations in this regime yield the following expression for ion kinetic energy scaling [64, 189, 190]:

$$\mathcal{E}_{\mathrm{K}}^{\mathrm{LS}} = m_{\mathrm{p}}c^2 \frac{F^2}{2(1+F)} \qquad F = 2Z\frac{n_{\mathrm{c}}}{n_{\mathrm{e}}}\frac{m_{\mathrm{p}}}{m_{\mathrm{e}}}\frac{\tau_{\mathrm{L}}c}{d}a_0^2 \tag{2.81}$$

where F is the dimensionless laser fluence $F = (2/\sigma c^2)\int I(t)\mathrm{d}t$ with $\sigma = m_{\mathrm{i}}n_{\mathrm{i}}d$ being the mass surface density. Similarly to the HB regime, $\mathcal{E}_{\mathrm{K}}^{\mathrm{LS}} \propto a_0^2 \propto I_0$ and $\mathcal{E}_{\mathrm{K}}^{\mathrm{LS}} \propto 1/n_{\mathrm{e}}$. However, the target thickness d appears in equation (2.81), as opposed to being absent for the HB regime, and the ion energy follows $\mathcal{E}_{\mathrm{K}}^{\mathrm{LS}} \propto 1/d$. Hence, it appears clear that reducing the target thickness as much as possible further boosts the ion kinetic energy $\mathcal{E}_{\mathrm{K}}^{\mathrm{LS}}$. However, the LS regime is limited at a point where the self-induced relativistic transparency becomes important, making the target more transparent and thus reducing the radiative pressure imposed on the target. We have seen in section 2.1.5 that a target is underdense (*i.e.* transparent to the laser) if $n_{\mathrm{e}} < \gamma n_{\mathrm{c}}$. Hence, when the laser intensity a_0 increases, so does γ, and thus an overdense target can become transparent to the laser if the intensity is high enough. Since the laser impact also compresses the target and locally steepens the electron density n_{e}, the relativistic transparency condition does not occur directly when $\gamma = n_{\mathrm{e}}/n_{\mathrm{c}}$. When $d \ll \lambda$, the work from Vshivkov *et al.* (1998) [191] showed that the relativistic transparency condition is of:

$$a_0 > \xi = \pi\frac{n_{\mathrm{e}}d}{n_{\mathrm{c}}\lambda} \tag{2.82}$$

We see from equation (2.82) that reducing the target thickness also reduces the intensity threshold for which the relativistic transparency commences. Another acceleration scheme involving the relativistic transparency is called the BreakOut Afterburner (BOA) [192, 193]. The BOA mechanism benefits from the Self-Induced Relativistic Transparency with a target that is normally overdense, to have the laser pulse penetrate deeper into the target and hence increase the laser-to-target energy transfer. This yields a hotter and denser electron cloud on the target's rear side, leading to an acceleration scheme comparable to TNSA enhanced by relativistic transparency. The LS-RPA optimal point is found at the regime boundary condition found in equation (2.82), after being inserted in equation (2.81) and considering $F \ll 1$, leads to:

$$\mathcal{E}_{\mathrm{K}}^{\mathrm{LS,\,opt}} = 2\pi^2 m_{\mathrm{e}}c^2\frac{m_{\mathrm{e}}}{m_{\mathrm{p}}}\left(\frac{Z}{A}\frac{\tau_{\mathrm{L}}c}{\lambda}a_0^2\right)^2 \tag{2.83}$$

Current record laser intensities [154] yield optimal target thicknesses in the tens of nanometers, which is enabled by current target production technologies. For instance, considering $I_0 = 10^{22}$ W/cm^2 (*i.e.* $a_0 \approx 100$) with a solid target density of $n_e = 400 n_c$ and $\lambda = 1$ μm yields an optimal target thickness of $d_{opt} \approx 80$ nm. However, producing ultra-thin targets of this thickness range is still a challenge today, moreover conserving an ultra-high laser contrast at these laser intensities is probably the detail that backholds most experimental campaigns. Indeed, a laser-to-prepulse contrast as high as 10^{10} at peak intensities of 10^{23} W/cm^2 leads to prepulses and ASE intensities around 10^{13} W/cm^2. These intensities are indeed well above the target's ionization threshold, and therefore destroy the target before the main pulse arrives.

2.3.3 Collisionless Shock Acceleration

The generation of ion beams in plasmas via electrostatic shocks triggers a lot of attention in the laser-based ion acceleration community. It has been shown through PIC simulations from the works of Delavit *et al.* (1992) [194] and Silva *et al.* (2004) [132] that supersonic shocks of high Mach numbers ($M \sim 2-3$) can be produced in plasmas, with $v_i = M c_s$ being the ion velocity, M is the Mach number and $c_s = \sqrt{Z k_B T_e^{hot}/m_i}$ is the ion sound speed estimated from the electron temperature. Due to the relativistic intensities typically involved in this acceleration scheme ($a_0 > 1$), the electrostatic shocks grow only through strong charge separation without the presence of collisions between particles, hence why the mechanism is called Collisionless Shock Acceleration (CSA). In the CSA scheme, the ponderomotive force from a high-intensity laser pulse drives a sharp increase of electron density, hence giving rise to a high electric field, that propagates in a plasma medium. The ions inside the plasma are then pulled by the strong charge separation, and acceleratd by the spiked electric field, driving another spike themselves in their wake. In a similar fashion to the Hole Boring case, the radiative pressure drives a shock velocity v_{shock} and ion kinetic energy $\mathcal{E}_K^{CSA}$ that can be estimated by momentum conservation with the following expressions in the non-relativistic case:

$$v_{shock} = \sqrt{\frac{(1+\mathcal{R})I_0}{m_i n_i c}} \qquad \mathcal{E}_K^{CSA} = \frac{1}{2} m_i (2 v_{shock})^2 = 2\frac{Z}{A} M^2 T_e^{hot} \tag{2.84}$$

The quasi-electrostatic field induced from shock produces a high potential barrier Φ for ions inside the plasma. In the shock's moving frame, ions undergo a reflection on the potential

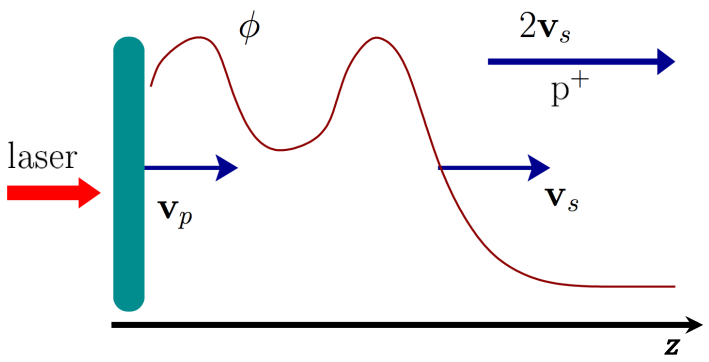

FIGURE 2.10: Schematic diagram of the Collisionless Shock Acceleration mechanism. The ions are reflected on the shock front and gain twice the shock velocity. These figure is extracted and adapted from [63].

barrier if $Ze\Phi > m_\mathrm{i}v_\mathrm{i}^2/2$. Upon reflection on the shock wave, ions can reach maximum velocities of twice the shock velocity (*i.e.* $v_\mathrm{i}^\mathrm{max} = 2v_\mathrm{shock}$). A schematic diagram of CSA is shown in Figure 2.10. The CSA mechanism predicts highly monoenergetic ion spectra [195], as long as the shock propagates with the same velocity. Equation (2.84) shows an energy scaling that follows $M^2T_\mathrm{e}^\mathrm{hot}$ and therefore $\mathcal{E}_\mathrm{K}^\mathrm{CSA} \propto a_0^2 \propto I_0$. In order to maximize v_shock, one would want to reduce the density ion density n_i to the near-critical point since $v_\mathrm{shock}^2 \propto 1/n_\mathrm{i}$, and therefore maximize the laser energy absorption which will drive the strong electrostatic shock. To do so, one important experiment [135] used CO_2 laser (central wavelength of 10 μm) in order to benefit from a lower critical density closer to gas jets produced in the laboratory. The resulting ion energy spread was indeed very narrow (1%), however particle numbers were very low, on the order of 10^7 protons/sr. Other experiments use so-called exploded foils and deliberately induce solid target plasma expansion with a second high-power laser before the interaction with the main laser pulse [196–198]. Another recent experiment [142] rather used supersonic H_2 gas jets which boosted the ion density to the near-critical regime and thus lead to an increased laser-to-particle energy transfer. Ion beams of up to 6 MeV were observed, however with nearly isotropic emissions. Different strategies to maximize the shock density and velocity are thus under investigation. Nevertheless, the generation of strong shocks within the CSA scheme is still a very challenging task as of today, although promising experiments are presently planned.

Chapter 3

Submicrometric Solid Target Alignment

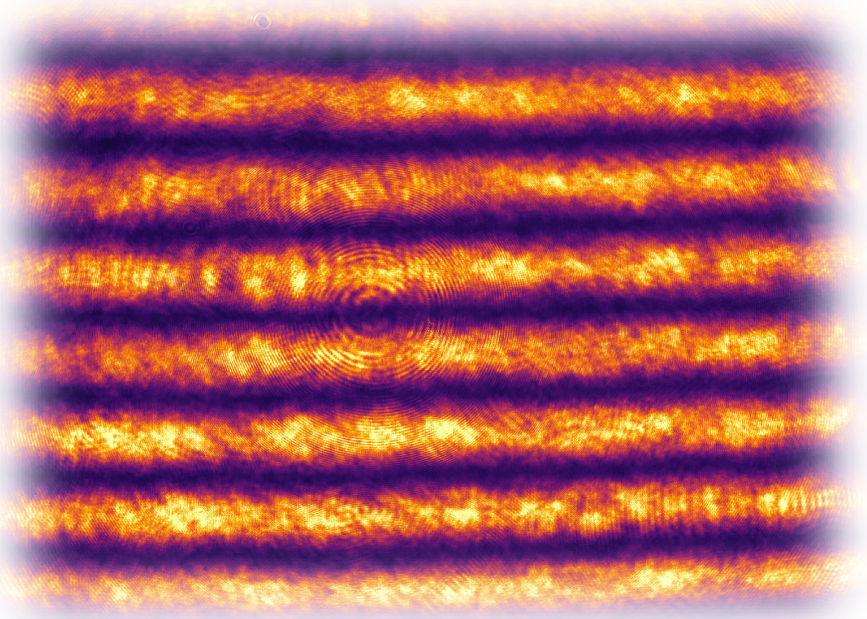

Interferogram obtained for metallic thin foil alignment.

Chapter Content

3.1 Foreword

This Chapter details a study performed to improve target alignment systems in laser-driven ion acceleration with solid targets. The Chapter starts by overviewing the most used conventional alignement procedures in the laser-based ion acceleration community, then continues by exposing the work done within this doctoral degree, to finally end with perspectives and recommendations for further developments. I was the project lead of this work in a narrow collaboration with an undergraduate summer intern that I supervised, Charles Bienvenue, which resulted in the following publication:

— C. Bienvenue*, **S. Vallières***, S. Payeur & P. Antici, "Submicrometric Absolute Positioning of Flat Reflective Surfaces Using Michelson Interferometry", *Review of Scientific Instruments*, vol. 90, 123702 (2019). ***Equivalent first-author contributions.**

3.2 Conventional target alignment procedures

As previously mentioned in section 2.1.1, typical tight-focusing off-axis parabolas used to focus high-power laser beams have Rayleigh lengths z_R on the order of a few tens of micrometers, depending on the numerical aperture NA and the central wavelength λ_0 used. As per the definition of the Rayleigh length, the laser intensity obtained at a distance of $z = \pm z_R$ away from the focal spot center is half the peak intensity I_0 obtained at the focus position $z = 0$. Hence, the Rayleigh length delimitates the uncertainty Δz on the solid target positioning along the longitudinal axis to maximize the intensity of the desired laser-matter interaction. The two most simple and direct solid target alignment techniques use conventional imaging in two different planes, namely shadowgraphic and transverse plane imaging, which are shown on Figure 3.1. Whilst only one of them is necessary for placing the interaction target in the focal plane of the laser, often both methods are used in conjunction to ensure alignment redundancy at each laser shot. Moreover, they are sometimes used with concomitant white light imaging cameras (not shown on Figure 3.1), placed outside the vacuum chamber, looking at the Target Chamber Center (TCC). Again, this is done to verify the agreement with the pre-defined coordinates system of the chamber and provide backup imaging if one system fails. The positioning accuracies of shadowgraphic and transverse plane imaging techniques are on the order of 10 μm down to a few microns when using diffraction-limited optics, depending on the lens and objectives used in the setup. Hence, having a positioning uncertainty of about the same magnitude as the Rayleigh length directly induces an uncertainty as high as 50% on the laser intensity obtained at the interaction point, in addition to shot-to-shot fluctuations in laser energy. Indeed, using optical components with high numerical apertures above NA = 0.3 for imaging reduces the obtained positioning uncertainty, however this also reduces so much the Field-of-View that the technique becomes not practical anymore for use. Moreover, highly accurate positioning makes the technique very sensitive to acousto-mechanical vibrations in the laboratory. Hence, we desired to develop a robust target positioning device that allows for submicrometric (*i.e.* at least an order of magnitude below the Rayleigh length) positioning accuracies using interferometry. Ensuring consistent accurate positioning within the Rayleigh length at every laser shot minimizes the fluctuations in the resulting ion beam generated within the TNSA regime, therefore increasing the source's reliability and stability. The next sections are detailing the study on a Target Positioning Interferometer (TPI) developed for solid target alignment used for generating a highly reliable and repeatable laser-based ion source in the TNSA scheme.

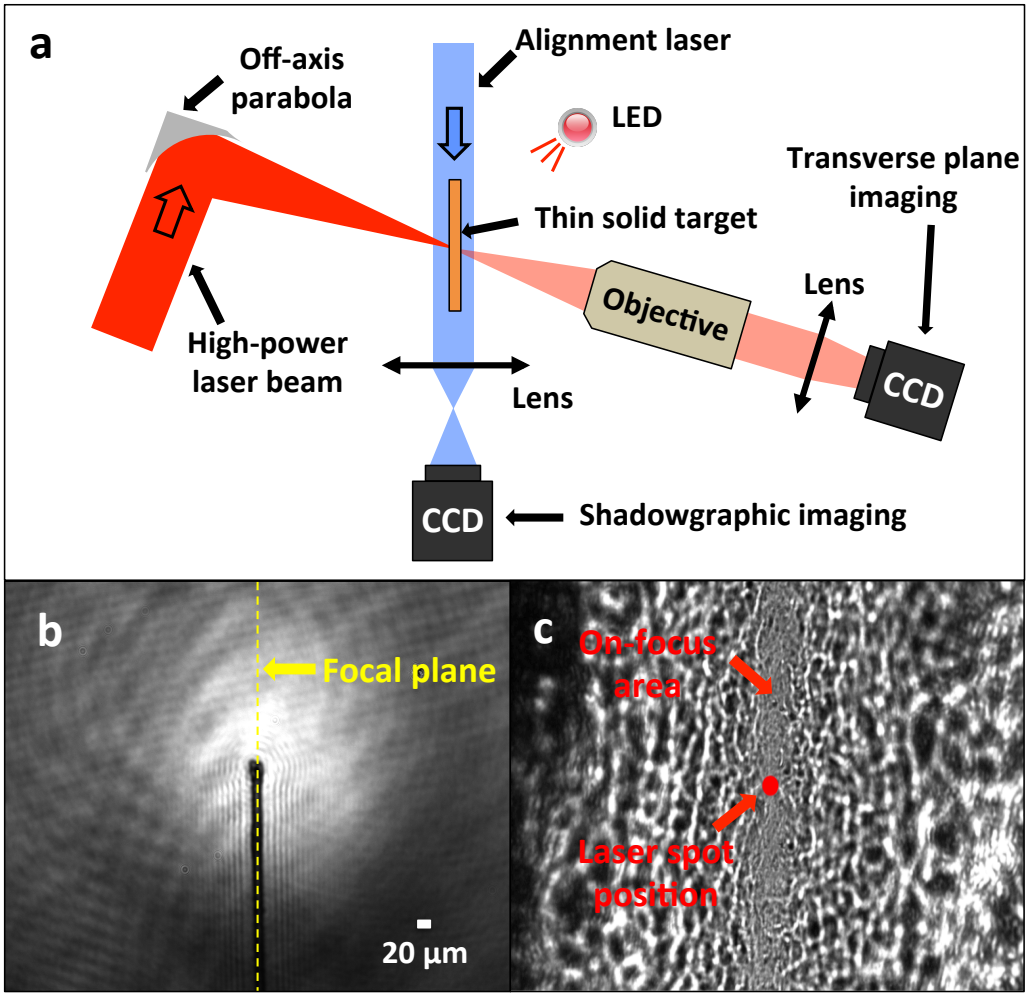

FIGURE 3.1: Conventional solid target alignment techniques used in laser-driven ion acceleration. (a) Schematic diagram of the two most used method for solid target alignment in the laser's focal plane, namely shadowgraphic and transverse plane imaging of the target. (b) Shadowgraphic image of a target's shadow, with pre-calibrated focal plane position. (c) Transverse plane imaging using a 10X microscope objective and diffused light from a LED on target. The laser's focal plane position is found by an on-focus section in the image.

3.3 Submicrometric Absolute Positioning of Flat Reflective Surfaces Using Michelson Interferometry

3.3.1 Abstract

We present a Target Positioning Interferometer (TPI), a system that uses variations of the wavefront curvature to position solid reflective surfaces with submicrometric precision. The TPI is a Michelson interferometer into which a lens is inserted in the target arm and the mirror of the

reference arm is slightly tilted. The TPI configuration presented in this work allows to position the surface of reflective target on a beam focus within an uncertainty of 350 nm (2σ) in a sub-second timeframe, using a lens with numerical aperture of NA $= 0.20$. We support our experimental findings with numerical simulations of the interference pattern using the $ABCD$ matrices method, allowing to define scaling laws for using the TPI with different optics and environments, as well as suggestions to improve the TPI accuracy and adapt the system to different applications. This system is very well suited for accurate and repeatable target positioning used in laser-driven ion acceleration, where a precise alignment is key to optimize the proton acceleration mechanism.

3.3.2 Introduction

Several applications require reliable, accurate, precise and affordable absolute positioning. The use of these devices can be as diverse as high-precision machining in industrial manufacturing or laser-matter interactions. It is important to distinguish relative and absolute positioning: classical interferometers currently achieve displacement measurements with subnanometric precision. However, when using monochromatic laser sources, they cannot be used to perform an absolute measurement because of the inherent half-wavelength ambiguity, which is usually on the order of a few hundreds of nanometers. An absolute positioning system can, if reaching the ambiguity range in accuracy, be used with conventional monochromatic interferometers to achieve subnanometric accuracy. A handful of methods are used to accomplish absolute measurements, based on triangulation, microscopy[1], self-mixing interferometry[2,3], and several other techniques. However, only few close the gap between relative and absolute positioning, such as techniques based on multi-wavelength interferometry[4-11], optical frequency combs[8-18], femtosecond time-of-flight[18,19] and combinations of these measurement techniques. Wavelength scanning interferometry combines measurements at different wavelengths, generating a synthetic wavelength which is stretching up the ambiguity range to convert a relative positioning system into an absolute one. Time-of-flight techniques use a short pulse and the travelling delay to determine the absolute distance. Finally, optical frequency comb methods take profit of the well-defined spectrum and highly stability of mode-locked femtosecond lasers.

In this paper, we introduce a novel absolute distance measuring device, the Target Positioning Interferometer (TPI) which allows unambiguous submicrometric measurements using a fiber-based monochromatic source. It was initially developed to achieve precise local positioning of reflective thin foils used for laser-driven ion accelerators, avoiding physical contact with the used thin foil. In laser-plasma ion acceleration, a solid metallic foil of micrometric thickness (0.1-20 μm) is irradiated by a short-pulse (tens to hundreds of fs) high-intensity laser. The energy of the laser-accelerated particles heavily depends on the focused laser intensity that under high vacuum conditions typically reaches values up to 10^{18}-10^{21} W/cm^2. The Rayleigh length of the focused down laser beam typically employed in such experiments (in this case an $f/3$ off-axis parabola focusing a beam with transverse size of 100 mm down to a focal spot of about 3 μm in diameter) is about 10 μm. In such cases, a displacement error of only 10 μm on the target's position can result in a decrease of the intensity by a factor 2, by definition of the Rayleigh length z_R in Gaussian optics, excluding shot-to-shot fluctuations of the laser. This strongly reduces the achievable proton energies and justifies the need for an accurate positioning system in order to maximize the acceleration mechanism. Pre-alignment systems based on optical lenses (microscopy) allow positioning the target around the required position, typically within a range of a few tens of microns. Since the foils used are very thin, they are often deformed or curved on the millimeter scale because they are soft, and thus a lack of foil flatness can prevent a good alignment of the targets within the focal spot of the laser. However, only a transverse area with a size similar to the focal spot needs to be locally precisely aligned along the laser propagation axis, and this is possible with the small probe size of the TPI. Many applications in the field of particle acceleration require not only high particle energy, but also intense flux[20-25], which can be obtained by increasing the shot-to-shot repeatability.

The aforementioned target positioning methods were not used in our facility because they unfortunately do not respond to some of our needs. The required alignment system has to achieve at least micron-scale positioning of a small area of already tiny targets (a few mm^2 area), at 5 cm from a lens that is placed approximately at 50 cm from the chamber wall inside a vacuum chamber. It has to measure the position in a few seconds to increase repetition rate of the laser-driven ion accelerator. Moreover, we considered important for the positioning system to be rather affordable and easy to use towards future deployments of laser-driven accelerator for applications. Time-of-flight interferometric methods are not viable solutions because obtaining 1 μm accuracy requires to measure a femtosecond-ranged time difference, which is

difficult to monitor. Also, since we only need to probe a small area (about 10 μm in diameter) with our positioning system, this cannot be done with the other interferometers, even when adding a convergent lens, because the wavefront shape will change with the target position, as described later in this work. The paper is organized as follows: We first present the TPI experimental setup and its operating principles. We then present analytical and numerical calculations based on Gaussian optics. Afterward, the numerical method we used to analyze the interference pattern and automate the TPI is proposed. Finally, we provide experimental results for our setup and propose ways to improve the performance or adapt the TPI for different applications.

3.3.3 Materials and Methods

3.3.3.1 Experimental Setup

A schematic diagram of the setup used for the TPI is presented in Figure 3.2.a. Pictures of the experimental setup are shown in Figure 3.2.b-c. The purpose of this system is to accurately position reflective surface at the focus point (*i.e.* $z = 0$) of lens L2 (*i.e.* the target arm). The TPI has a Michelson-like configuration. The laser beam coming from the source through an optical fiber is diverging at its end into the lens L1, which is use to have a collimated beam. Then, the collimated beam is separated by the beam splitter BS between the target and the reference arms. The target arm has an aspherical lens L2, which focuses the beam on the tested reflective target without spherical aberrations. The reference arm has the mirror M1 at its end, which has a small angle with respect to the target arm, in order to obtain slightly non-collinear beams. Both beams are returning in the imaging arm and are focused by the lens L3 into the camera CCD. We used a Fabry-Perot benchtop laser source with central wavelength of $\lambda_0 = 785$ nm and maximum output power 20 mW (used power of 0.5 mW) from *Thorlabs* (S1FC785). This working wavelength has been chosen since it provides high reflectance on metallic surfaces and transmission in optics of the system, resulting in a high signal-to-noise ratio (SNR). The working principle of this system is illustrated in Figure 3.3. In Gaussian optics, the wavefronts are curved before (positive curvature) and after (negative curvature) the focus point along the propagation line. At the exact focus point, the wavefront can be considered as straight. The fringes on the interference pattern collected by the CCD camera (we used a 16-bits image sensor of 1288×964 square pixels of 3.75 μm with an integration time of 200 ms) of the TPI

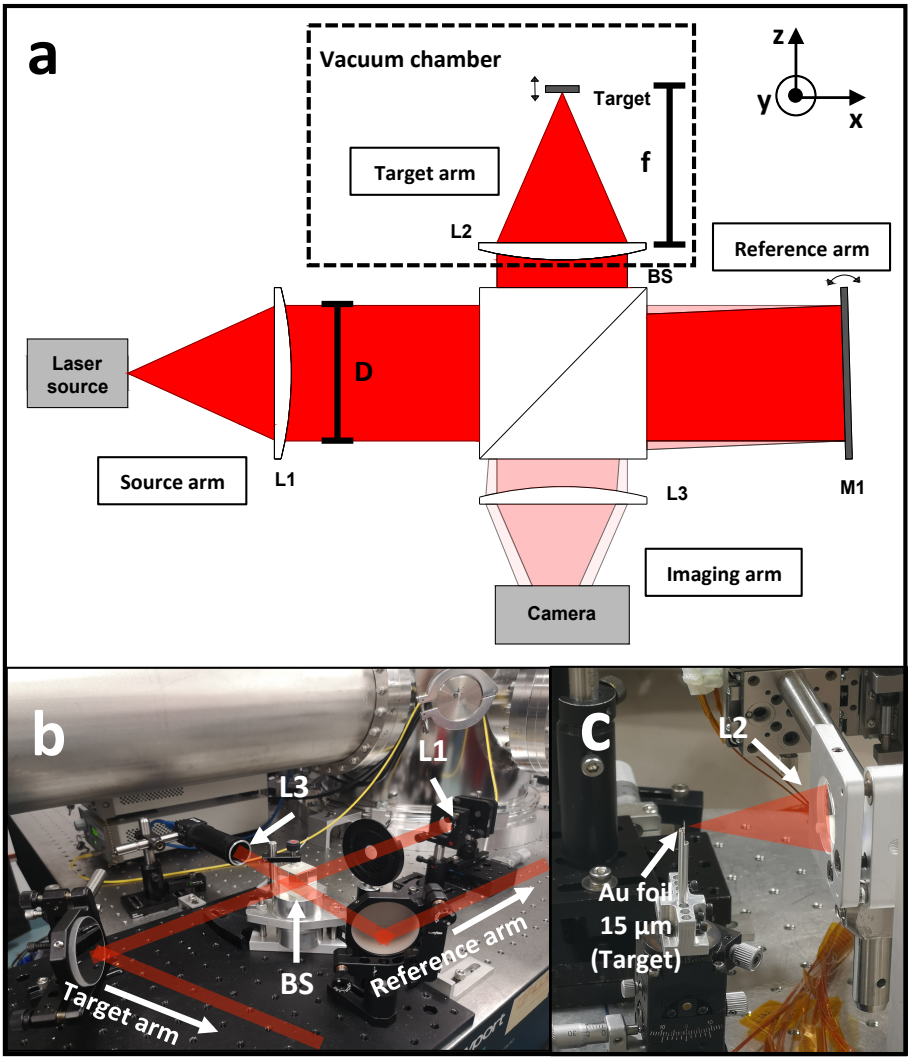

FIGURE 3.2: Experimental setup of the TPI. (a) Schematic setup of the TPI. The intensities of the laser beam are represented with shades of red. The mirror M1 has a non-zero angle with the incident beam. (b) Picture of the experimental setup of the Michelson interferometer. (c) Picture of the setup around lens L2 inside the experimental chamber, focusing a $D = 2$ cm beam on a focal length of $f = 5$ cm (*i.e.* NA = 0.2) onto a 15 μm-thick flat gold thin foil.

will be straight if a flat reflective surface is placed at the focus point of lens L2 (when the wavefront's curvature is zero). When the target is not at that exact position, the fringes have either positive or negative curvature, depending on which side of the focus point the target is placed. The curvature increases when the target is located further away from the focus point. This fringes behavior is unique along the propagation line after the lens L2 and thus there is no ambiguity on the position. We demonstrate this phenomenon using numerical simulations, for which further details are presented in section 3.3.3.2. Hence, the choice of lens L2 is critical for the precision of the TPI, the most important parameter being its numerical aperture (NA). A higher value of NA increases the beam curvature around the focus point. This improves the

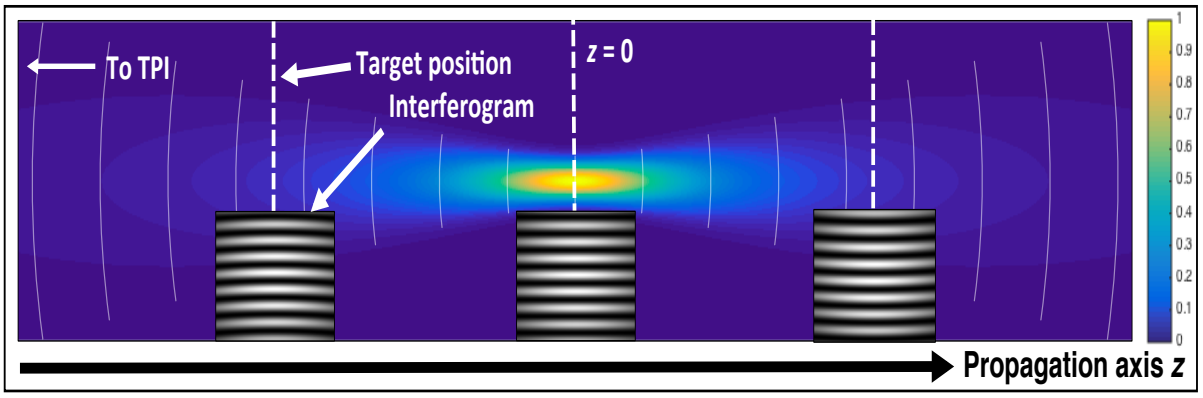

FIGURE 3.3: Side view of the focal spot profile after the lens L2 with normalized color-represented intensities. The wavefronts are represented by white continuous lines and they are distanced by $c\Delta t$ = 5 μm in the direction of the light propagation. The lens L2 is at the left of the image and examples of target positions around the focal spot are represented with dashed white lines with their corresponding interference pattern recorded on the CCD camera. From the left to the right, the fringes curvature is negative, straight and positive. The target positions along the focal spot are respectively z = -22.5 μm, z = 0 μm and z = 22.5 μm.

accuracy since the spatial variation of the fringe curvature is more pronounced, which makes it easier to distinguish straight fringes from curved ones. However, this implies placing the lens very close to the target (*i.e.* short focal distance f), or having larger optics (larger beam diameter D). When configurating the TPI, there is a compromise to make between having a high NA while not being too close to the target. Based on typical technical constraints and optics used in laser-plasma acceleration, a lens L2 with NA = 0.2 was chosen.

3.3.3.2 Simulation of the Interference Pattern

To support the experimental observations and assumptions, along with providing a better understanding of the influence of each parameter on the TPI, we have simulated the interference pattern using the expression of the transverse electromagnetic mode of a Gaussian beam for both returning beams in the imaging arm of the interferometer. The electric field for each arm can be calculated at the position $\boldsymbol{r} = x\hat{x} + y\hat{y}$ on the CCD camera, with x and y being the positions in the transverse plane and their related unit direction vectors $\hat{x}$ and $\hat{y}$:

$$\boldsymbol{E}_j(\boldsymbol{r}) = \boldsymbol{E}_0(\boldsymbol{r})\,\frac{w_{j,0}}{w_j(z_j)}\,\exp\left[-\frac{\rho_j^2(\boldsymbol{r})}{w_j^2(z_j)} - i\phi_j\right]\hat{\rho}_j \tag{3.1}$$

with the phase:

$$\phi_j = k_0 z_j + k_0\frac{\rho_j^2(\boldsymbol{r})}{2R_j(z_j)} - \psi_j(z_j) \tag{3.2}$$

for $j = 1, 2$ corresponding to each returning beam, $k_0 = 2\pi/\lambda_0$ is the central wavenumber, $z_j = z_j(\boldsymbol{r})$ is the position on the wave propagation axis, $\rho_j(\boldsymbol{r})$ is the transverse distance from the propagation axis of the beam, $\hat{\rho}_j$ the unit direction vector of ρ_j, $w_j(z_j)$ is the beam width at a distance z_j of the beamwaist $w_{j,0}$, $R_j(z_j)$ is the beam's wavefront radius of curvature at z_j, ψ_j is the Gouy phase at z_j and $\boldsymbol{E}_0$ is the amplitude of the electric field at $z_j = 0$. Ray transfer matrix analysis for Gaussian beam, also known as the *ABCD* matrix method, is used to model the beam propagation in the TPI and determine the values of the previous parameters. The intensity at a position $\boldsymbol{r}$ on the observation plane is then calculated according to the following equation:

$$I(\boldsymbol{r}) = I_1(\boldsymbol{r}) + I_2(\boldsymbol{r}) + 2\sqrt{I_1(\boldsymbol{r})I_2(\boldsymbol{r})}\cos\left[\Delta\phi(\boldsymbol{r})\right] \tag{3.3}$$

with the intensities of both beams at position $\boldsymbol{r}$ being:

$$I_j(\boldsymbol{r}) = \frac{\left|\boldsymbol{E}_j(\boldsymbol{r})\right|^2}{2\eta} \tag{3.4}$$

where $\Delta\phi$ is the phase difference between the two beams, and η is the propagation medium impedance. A MATLAB® routine was developed to calculate the intensity on each pixel of the CCD and generate a synthetic image of the expected interference pattern. An example of these images as a function of the position from the focus point is shown in Figure 3.3. The simulations are very well in agreement with the experimental observations (see section 3.3.4) and validate the hypothesis for which the fringes are straight when the target is at the focus point. However, this model is valid only within the paraxial approximation, *i.e.* when the numerical aperture of the lens L2 is small enough such that the beamwaist w_0 satisfies the following condition[26]:

$$w_0 \gg \frac{\lambda_0}{\pi\sqrt{2}} = 0.18\ \mu\text{m} \tag{3.5}$$

For NA = 0.25, we have:

$$w_0 \approx \frac{\lambda_0}{\pi\text{NA}} = 1.00\ \mu\text{m} \tag{3.6}$$

In accordance with the condition of equation (3.5), we set the value of NA $= 0.25$ as the upper bound for our simulations. Beyond this value, we consider the paraxial approximation is not applicable anymore. The interference pattern simulation allows to understand, predict and optimize the behavior of the TPI before and during experimental testing.

3.3.3.3 Numerical Method for Fringe Analysis

As can be noted from calculations, the determination of the focus point is strictly related to the position where the fringes are fully parallel. To determine this longitudinal position z_0, we developed a numerical method to analyze the fringes using their Orientation Density Function (ODF). This metric is extensively used in nervous fiber tracking for diffusion-tensor Magnetic Resonance Imaging and tractography[27-31]. In the aforementioned papers, the fibers orientation analysis is highly multi-dimensional as they evaluate the 3D orientation of nervous fibers in each voxel of a 3D image, whereas in the present study the orientation evaluation is performed on a 2D image $I(x, y)$. Two rectangular sub-images I_1 and I_2 are extracted from the original image I, as shown on the Figure 3.4.a. The full height is taken to include all the fringes in the signal, and the width can be chosen to split the image through the center. However, slightly overlapping the two sub-images helps to reduce the windowing artifact, allowing in turn to reduce the noise in the ODF calculation. This is a compromise with the system's sensitivity, but increases the SNR. The optimal width is very specific to each system, and was found to be around $2/3$ of the full width in the case of the present study. The mean orientation, noted $\bar{\theta}$, of the fringes in these images can be evaluated with the following methodology. The ODF is calculated for each sub-image I_i through a radial integral of the Fourier space in polar coordinates, as shown by equations (3.7) and (3.8), which allows to rule out the dependence on the fringe's wavenumber amplitude $k = (k_x^2 + k_y^2)^{1/2}$, and thus only conserves the dependence on the orientation angle $\theta \in [0, 2\pi]$ for further analysis.

$$\mathrm{ODF}_i(\theta) = \int_0^\infty \hat{I}_i(k, \theta)\, k \, \mathrm{d}k \tag{3.7}$$

$$\hat{I}_i(k_x, k_y) = \mathcal{F}_{x,y}[I_i(x, y)] = \int_{-\infty}^{\infty} \int_{-\infty}^{\infty} I_i(x, y)\, e^{-i(k_x x + k_y y)}\, \mathrm{d}x\mathrm{d}y \tag{3.8}$$

In order to reduce the calculation time and numerical noise introduced by the 2D Fourier transform and as well by the 2D interpolation when using polar coordinates, we use the Radon transform of the fringes, as defined by equation (3.9). This allows obtaining their projections $p_i(s, \theta)$, where s is the space coordinate perpendicular to the integration direction. The Radon transform unfolds directly in a polar coordinate system which makes further analysis in the polar system fast and convenient. At the same time, it inherently applies a data smoothing step

due to its integral operator nature. If we then take the 1D Fourier transform of the projections along s, $\hat{p}_i(k,\theta)$, we can use the Central Slice Theorem as per equation (3.10), and thus to link with the radial lines in Fourier space passing by the origin, as required by equation (3.7). We therefore obtain the ODF calculation method used in this work, as shown by equation (3.11):

$$p_i(s,\theta) = \mathcal{R}[I_i(x,y)] = \int_{\substack{-\infty \\ l=x\cos\theta+y\sin\theta}}^{\infty} I_i(x,y)\,\mathrm{d}l \tag{3.9}$$

$$\hat{p}_i(k,\theta) = \mathcal{F}_s[p_i(s,\theta)] = \hat{I}_i(k,\theta) \tag{3.10}$$

$$\mathrm{ODF}_i(\theta) = \int_{-\infty}^{\infty} \hat{p}_i(k,\theta)\,|k|\,\mathrm{d}k = \int_{-\infty}^{\infty} \mathcal{F}_s\left\{\mathcal{R}\left[I_i(x,y)\right]\right\}\,|k|\,\mathrm{d}k \tag{3.11}$$

An important point to note from equation (3.11) is that we have changed the integration limits by taking the absolute value of the Jacobian $|k|$ and by having $\theta \in [0,\pi]$. This simple change permits to reduce information redundancy from $\theta \in [\pi, 2\pi]$, lowers calculation time while increasing the signal-to-noise ratio (SNR) since we integrate through both Fourier peaks at once. The effect of the Jacobian $|k|$, also known as Ram-Lak filter in tomographic reconstruction, allows to reduce the influence of the strong zero-frequency peak, but it also increases high frequency noise as a side-effect. It is possible to attenuate this side-effect by using a Hann or cosine filter. For better visualization of the process, we show a sample fringes image $I(x,y)$ in Figure 3.4.a. The two sub-images extracted from it are shown with red and blue rectangles. The Figure 3.4.b presents the 2D Fourier transform of the image I_2. The Fourier space consists of a central peak, which is the zero-frequency component of the image, along with two well-defined peaks, which is what we expect from the Fourier transform of a sinusoidal wave. We can also notice a cross-like blurring effect on the peaks due to the image windowing, which produces a *sinc* function artifact that can be overcome by applying a circular binary mask to the image in real space. The 1D Fourier transform of the projections, $\hat{p}_2(k,\theta)$, is the signal along the radial lines as shown in Figure 3.4.b. After integrating every $\hat{p}_2(k,\theta)$ along k for all θ, we obtain the $\mathrm{ODF}(\theta)$ function of the image I_2 as shown on Figure 3.4.c, exhibiting a strong signal peak at $\bar{\theta}_2 = 91.5°$, which is the orientation of the two peaks in the Fourier plane. We track this information about the fringes through a Gaussian fit performed directly on the thresholded peak of the ODF, recording its mean value $\bar{\theta}_2$. The same procedure is applied on the image I_1. If the fringes are curved, the two half-images I_1 and I_2 will not return the same $\bar{\theta}$, and therefore the determination of the focus point position is defined by the condition presented in equation

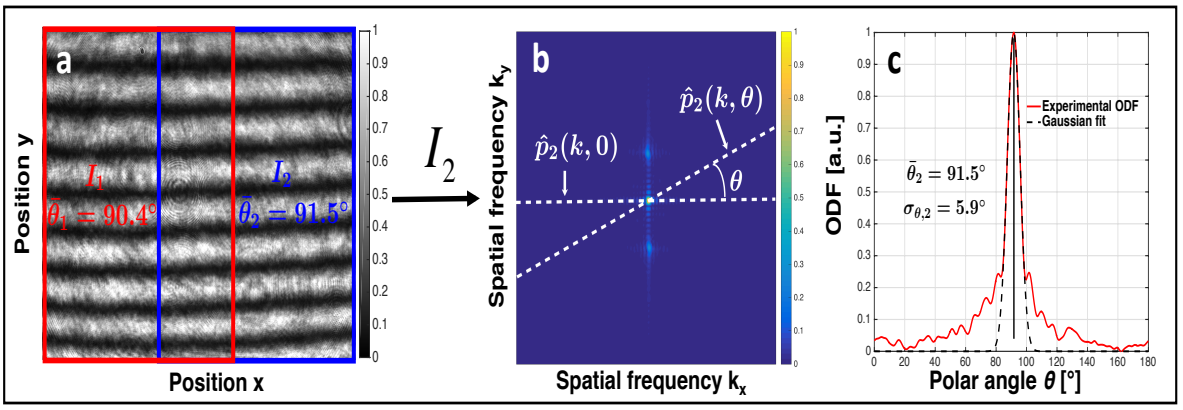

FIGURE 3.4: Numerical analysis methodology. (a) Image of the experimental fringes collected on the CCD, which is separated into two rectangular sub-images I_1 and I_2 represented by red and blue rectangles. Their orientation $\bar{\theta}_i$ is also provided. The value of the parameter $\Delta\theta$ for this image is 1.1°. (b) Fourier transform of the sub-image I_2 and its radial lines $\hat{p}_2(k,\theta)$. (c) Orientation Density Function (ODF) of the sub-image I_2 fringes in normalized arbitrary units [a.u.], exhibiting a strong signal peak at $\bar{\theta} = 91.5°$ and having a standard deviation of $\sigma_\theta = 5.9°$ ($2\sigma_\theta/180° = 6.6\%$). Gaussian fit has $R^2 > 0.99$.

(3.12):

$$\Delta\theta = \bar{\theta}_2 - \bar{\theta}_1 = 0 \tag{3.12}$$

For the image I presented on Figure 3.4.a, the value of $\Delta\theta$ is of 1.1°. We perform an experimental calibration of the positioning system by moving the target along the propagation axis z using a calibrated piezoelectric actuator Picomotor™ with 30 nm step size. The calibration procedure consists in measuring $\Delta\theta$ at different positions z from an arbitrarily chosen origin around the focus point, then find the position that fulfills the condition in equation (3.12) with a level of confidence of 95% (*i.e.* 2σ) and finally determine a fitting function g to have an equation of the form $z = g(\Delta\theta)$. When the TPI is calibrated, it can be used to do single measurements of $\Delta\theta$ and then the position z can be obtained with the function g. All the data analysis is performed on a MATLAB® routine that is linked with an in-house LabVIEW™ program to automate the target's actuator movement.

3.3.4 Results

The first step to study the performance of the TPI is to compare the experimental and simulated fringes in similar working conditions. A comparison of both cases is shown in Figure 3.5, for three different positions along the focal axis of lens L2. The first pair of images (Figures

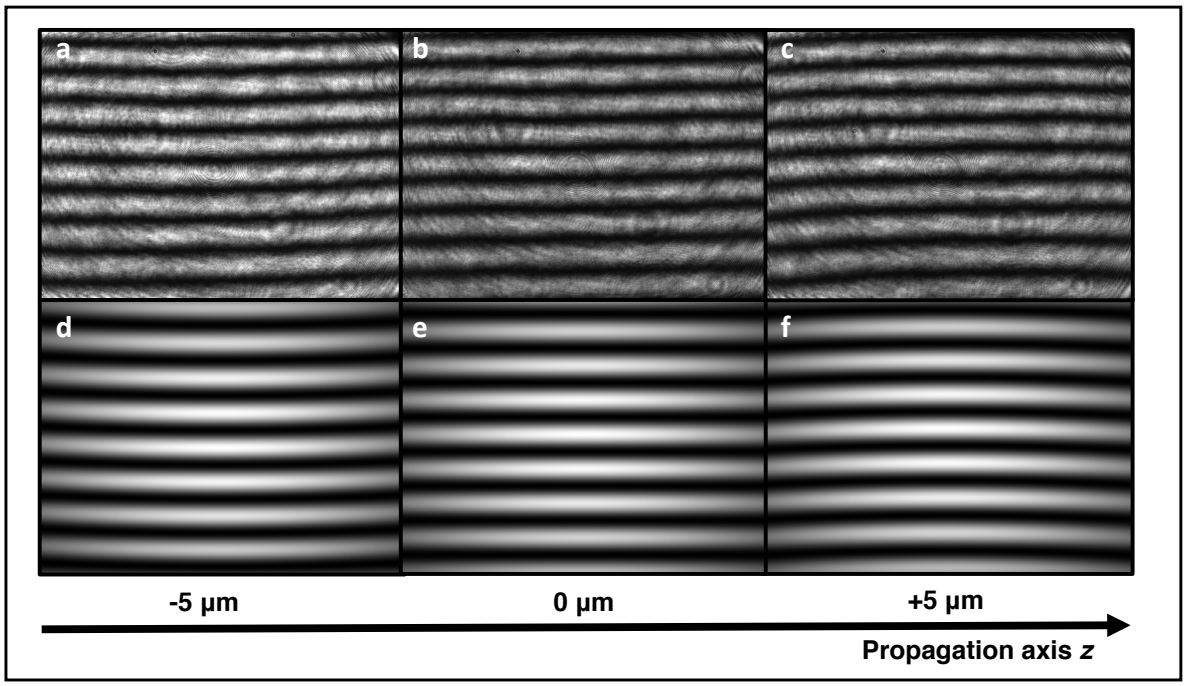

FIGURE 3.5: Experimental (a-c) and simulated (d-f) interference patterns for different distances along focal axis z of -5 μm (a and d), 0 μm (b and e) and +5 μm (c and f). The position uncertainty on these experimental images is of 1.3 μm (2σ).

3.5.a and 3.5.d) show the fringes at 5 μm before the focus point, where the fringes are curved upward (positive curvature). Despite the intrinsic experimental noise in Figures 3.5.a, there is an excellent agreement between experimental observations and simulations. The middle pair of images (*i.e.* Figures 3.5.b and 3.5.e) allows to observe the straight fringes at the focus point, as obtained by the simulations and the experiment. Again, there is an excellent agreement between the experimental and simulated fringes. The same applies for the last pair of images (Figures 3.5.c and 3.5.f). As expected, we observe a symmetrical behavior between the images related to a position at -5 and +5 μm.

As a next step we input a series of experimental images, corresponding to different positions along the focal axis, in the numerical method for fringe analysis. We obtain the positioning calibration graph along the focal spot positions as shown on Figure 3.6. The data points (z, $\Delta\theta$) were observed to be always linear within the tested experimental conditions up to several tens of micrometers. To estimate the focal spot position, we perform a linear regression through a least-squares minimizing algorithm. We then determine its uncertainty Δz by finding the linear curves containing the points within a 2σ interval, such that the distance from the focus point (z_0) to the confidence interval lines, along $\Delta\theta = 0°$, is $z_0 \pm \Delta z$. The experimental TPI

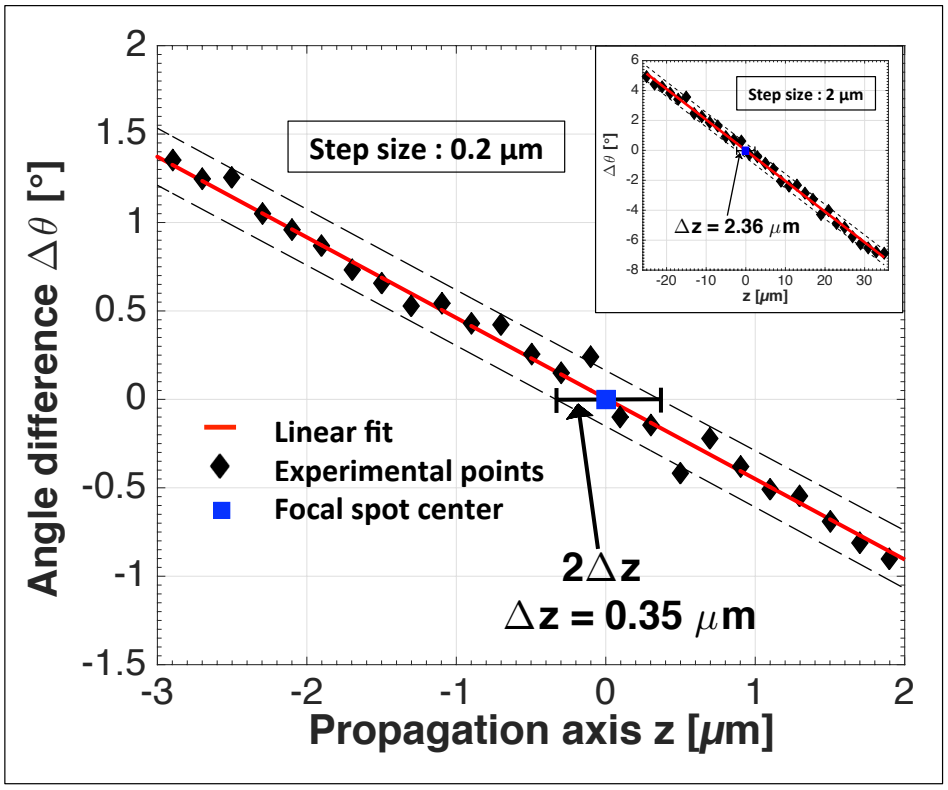

FIGURE 3.6: Experimental positioning calibration curve through the focal spot. The experimental data points are shown in black diamonds for an acquisition range of 5 μm (step size of 0.2 μm), a linear regression is shown in full red line, along with its 2σ (95%) level of confidence margins in dashed black lines. The focus point position is also shown (blue square) with its associated uncertainty Δz of of 0.35 μm. The experimental workpoint is shown in blue square. A least-squares minimizing linear regression was performed with $R^2 > 0.99$. The inlet is an experimental acquisition over 60 μm (step size of 2 μm), exhibiting the long-range linear behavior, providing an uncertainty of Δz = 2.36 μm in this case.

achieves a positioning uncertainty Δz of 350 nm (2σ), which is smaller than $\lambda_0/2$, corresponding to a variation in intensity applied on the target's front surface of less than 0.2% excluding variations in the incident laser properties, thus providing shot-to-shot repeatability. Benefiting from an automated system, with a piezoelectric actuator (Picomotor^{TM}) and running on a Intel Core i5-3470 CPU @ 3.2 GHz processor with 8 Gb of RAM, it is possible to do the calibration procedure, acquiring and analyzing the data for 30 points over a range of 60 μm in less than 60 seconds. The inlet of Figure 3.6 shows that this longer-range acquisition also exhibits a linear behavior, even over several Rayleigh lengths z_R. When the calibration is done, a single position measurement is then a sub-second process. The calibration data points exhibit a very linear behaviour, most probably due to the subtraction of equivalent non-linear behaviors from $\bar{\theta}_1$ and $\bar{\theta}_2$. Since the image I is centered with the fringe curvature and the two sub-images I_1 and I_2 are taken left-right separated through the center, the variation of $\bar{\theta}_1$ is equivalent to $\bar{\theta}_2$, which

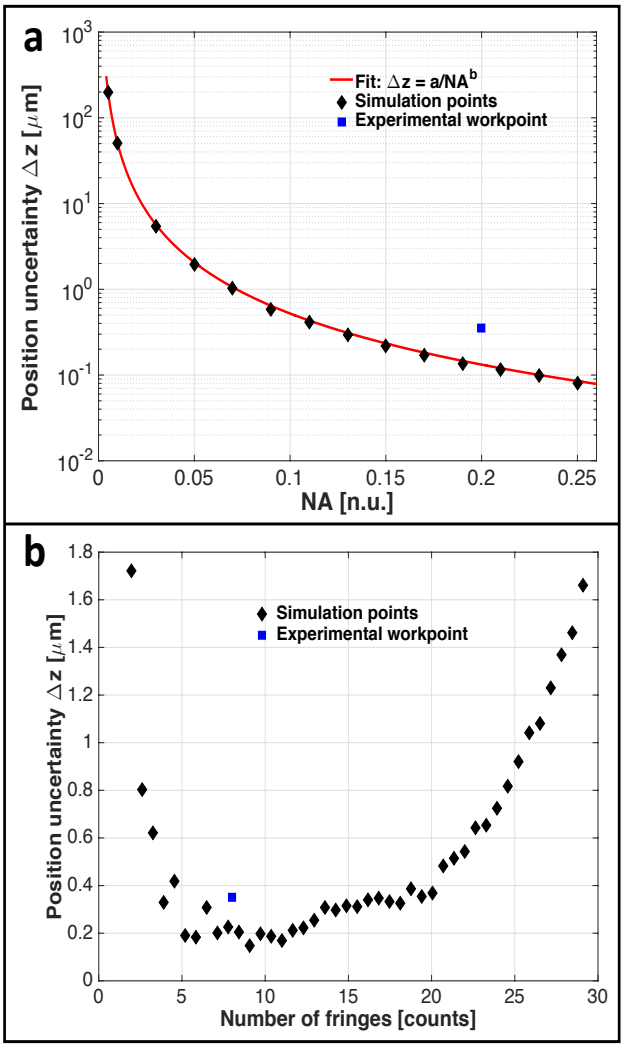

FIGURE 3.7: Uncertainty analysis for the TPI. (a) Uncertainty (2σ) on the position measurement with NA. The returned fit parameters for NA variation are of $a = 0.005468$ μm and $b = 1.98$, with $R^2 > 0.999$. (b) Uncertainty (2σ) on the position measurement against the number of fringes recorded on the CCD.

linearizes the problem. Again due to the azimuthal symmetry the fringes, one could have the same interference pattern recorded in a random orientation θ and the numerical method would still work, as long as the curvature is roughly centered to have enough interferometric information covering both sub-images I_1 and I_2.

In order to better understand and enhance the performance of the system through Δz, we have performed a series of simulations for different NA of lens L2 and number of fringes recorded on the CCD, for which the results are shown on Figures 3.7.a-b. We can first note on Figure 3.7.a that Δz decreases very rapidly with the numerical aperture of lens L2, nearly following an inverse-square law as the fit (full red curve) is suggesting. Indeed, this is in excellent agreement

with Gaussian optics if we estimate that Δz is proportional to the Rayleigh length z_R of the focal spot, as shown by equation (3.13). Comparing with the experimental workpoint for NA = 0.2, simulations suggest a Δz of 132 nm compared to 350 nm (2σ), which gives a percent difference of 62%. The difference between experiments and simulations can be due to several technical and environmental factors: acoustic vibrations in the building, laser source noise, parasite reflections, imperfect optics, *etc.* Nevertheless, this is still very close from theory, and thus it is very useful to test numerical fringes with different optical parameters before testing them experimentally. As noted from (3.13), spatial resolution Δz can be improved significantly through a higher NA, and therefore with a lens L2 closer to the target (*i.e.* smaller f) and larger beam diameter, with the NA of the system defined as:

$$\Delta z \propto z_R \approx \frac{\lambda_0}{\pi \mathrm{NA}^2} \tag{3.13}$$

$$\mathrm{NA} = n \sin\left[\arctan\left(\frac{D}{2f}\right)\right] \approx \frac{nD}{2f} \tag{3.14}$$

where n is the refractive index, f is the focal length of lens L2 and D is the transverse beam diameter. Concerning Figure 3.7.b, we can note that there is an optimal range of operation between 4 to 20 fringes recorded on the CCD. This is adjustable by slightly tilting mirror M1 to vary the phase difference $\Delta\phi$ between the two returning beams in the CCD. We can see in Figure 3.7.b that the position uncertainty of the system slowly increases up to 20 fringes before increasing significantly above that limit. This is first due to the decreasing curvature of the interference pattern as we get far away from the central interference lobe. Moreover, when the width of the fringes gets comparable to the pixel size, the contrast in the Fourier plane gets lower and thus the numerical method does not conserve a high SNR. On the other end of the graph, where there is only a few fringes on the image (*i.e.* less than 4), this produces a widening of the signal due to strong windowing, hence decreasing the performance significantly (*i.e.* higher Δz). In the end, the optimal workpoint seems to be around 8 fringes per image, combining strong fringe curvature and high SNR. This is observed in both simulations and experiments.

3.3.5 Discussion

The numerical aperture is the most crucial parameter of the TPI, defined in the present case by lens L2. The choice of lens L2 depends on the constraints related to the TPI, for instance on the

parameters defining the NA of the system through the transverse beam diameter D and the focal length f. For example, one could need to maintain a distance of a meter between the lens and the target, *i.e.* $f = 1$ m, and having $D = 2.5$ cm, which altogether provides a NA of 0.0125 in vacuum. Using the fitted equation of the Figure 3.7.a, the uncertainty for this application of the TPI would be around 32 μm (2σ). Similarly, one could have the same accuracy than our TPI configuration at a 25 cm distance of the target with a beam diameter of 10 cm. Moreover, even though the paraxial approximation is not valid above NA $= 0.25$, which prevents to simulate realistic cases using the $ABCD$ matrix method, it is expected that the performance of the system will continue to increase, since the curvature of the focal spot will increase as well. However, there are some experimental limitation of using high NA, such as higher spherical aberrations (aspherical lens L2 was used in this case to limit this effect), cumbersome optics for large beam diameters and high space constraints for systems using very short focal distances.

Aside from the numerical aperture, there are several other important points to consider. Regarding the targets, their surface roughness has to be low (< 0.2 μm Ra $\approx \lambda_0/4$, *i.e.* significantly lower than the half-wavelength ambiguity), otherwise the wavefront will be too distorted and its interference with the almost flat wavefront of the reference arm will be totally unusable (*i.e.* too low SNR). Concerning the orientation of the target, the reflected beam must be within $\pm 0.5^\circ$ to provide a good performance, otherwise it is possible to obtain aberrations in the target beam due to a misalignment with the center of lens L2, strong phase difference between the two returning beams (as shown on Figure 3.7.b) as well as significant loss of information on the CCD. Achieving this precision was not a limiting factor for the presented research since we used a target pre-alignment bench that is spatially calibrated with the reference system of the experimental chamber[32]. More precisely, in addition to the focal axis alignment of reflective targets, the TPI can potentially also be used for fine-tuning the target's orientation by maximizing the returning signal in the interferometric imaging, thereby serving multiple purposes. To achieve a positioning uncertainty of Δz = 350 nm, the returning beam of the target arm was superimposed on the incoming beam and placed on the CCD with a precision of 1 mm over a target arm length of 2 m, which gives a maximal angular deviation of 0.03° (*i.e.* nearly perpendicular). One might note that the TPI can work in an environment with vibrations since their effect on the precision can be easily measured. The frequency of the vibration must ideally be lower than the acquisition rate of the CCD to ensure the best fringe measurement. Moreover, the calibration procedure takes less than a minute and takes into account random errors when

evaluating the uncertainty in the given environment. For example, the TPI is installed nearby an experimental chamber onto which are connected vacuum pumps for maintaining a high vacuum (10^{-6} mbar). Comparing the calibration with and without the pumps being operational produced a difference of roughly 1 μm between both case. Furthermore, the TPI offers a low-cost and simple method for achieving high-accuracy positioning in absolute terms. Given the above mentioned facts, the TPI has a strong potential for a wide use in other applications.

The TPI system achieves measurements within an uncertainty of $\Delta z = 350$ nm (2σ), which is smaller than $\lambda_0/2$ = 393 nm, and thus also resolves the half-wavelength ambiguity of classical interferometer. There is not a large difference between both values, but the performance of the system can still be increased: the TPI was not vibrationally isolated or boxed to reduce air turbulence, and its precision can certainly be enhanced significantly with a lens having a higher NA. Since the gap is closed between relative and absolute measurements, the TPI could be modified to a conventional Michelson interferometer, which is widely used for relative distance measurements, to achieve subnanometric absolute positioning. Furthermore, with additional computing power, the TPI could use multiple images instead of one for each position, averaging for each point (z, $\Delta\theta$), reducing again the uncertainty. A further benefit of the TPI comparing to the aforementioned systems is that it also allows high-precision positioning of microscopic objects, such as electronic components, since the laser used for the alignment converges in a small spot (in our TPI configuration, the focal spot was $w_0 = 1.25$ μm).

3.3.6 Conclusion

Experimental measurements have demonstrated that the TPI can achieve precise and accurate positioning of reflective flat targets with an uncertainty of a few hundreds of nanometers. The TPI, using a lens with numerical aperture of 0.2, allows positioning with an uncertainty down to 350 nm (2σ). This result is also supported by numerical simulations based on Gaussian optics, providing scaling laws for using the TPI in different conditions. Further steps for improving the system will include adapting the TPI for highly-absorbing solid targets used in laser-driven ion acceleration experiments, such as metallic targets nanostructured with nanowires[32] or nanospheres[33] that increase the laser energy absorption, which is key to enhance the performance of laser-driven proton acceleration. Surface nanostructuration intrinsically distorts

the incoming wavefront, which in turn will yield a very noisy measurement. The SNR of the system must therefore be tuned high enough such that it is still possible to properly position the target within the beam focus while compromising with a larger uncertainty. When successfully incorporated into the accelerator, the TPI will allow increasing the reliability of the laser-matter interactions, thus providing repeatable proton spectra. Finally, the accuracy of the TPI was more than sufficient for our needs, but it would be possible to further increase its measurement precision through higher NA using a lens with higher numerical aperture, averaging on multiple images and combining with conventional interferometric measurements.

3.3.7 Acknowledgments

This work is supported by the National Sciences and Engineering Research Council of Canada (NSERC) (Discovery Grant RGPIN-2018-05772, Alexander-Graham-Bell Graduate Scholarship for S.V. and Undergraduate Student Research Awards for C.B.), FRQNT (nouveaux chercheurs, Grant No. 174726, Equipe 2016-PR-189974 and Supplements of the NSERC Undergraduate Student Research Awards for C.B.), Compute Canada (Job: pve-323-ac) as well as the Canada Foundation for Innovation (CFI). This study has also received financial support from the French State, managed by the French National Research Agency (ANR) in the frame of "the Investments for the future" Programme IdEx Bordeaux - ANR-10-IDEX-03-02. We would like to thank Pilar Puyuelo-Valdes and Martina Salvadori for the technical support.

3.3.8 References

[1] Y. Shou, Y. Geng, Q. Liao, J. Zhu, P. Wang, M. Wu, C. Li, X. Xu, R. Li, H. Lu, Y. Zhao, W. Ma, C. Lin & X. Yan, "Laser proton accelerator with improved repeatability at Peking University", *J. Phys.: Conf. Ser.*, vol. 874, 012043 (2017).

[2] M. Norgia, G. Giuliani & S. Donati, "Absolute distance measurement with improved accuracy using laser diode self-mixing interferometry in a closed loop", *IEEE Trans. Instrum. Meas.*, vol. 56, 1894-1900 (2007).

[3] D. Guo & M. Wang, "Self-mixing interferometry based on a double-modulation technique for absolute distance measurement", *Appl. Opt.*, vol. 46, 1486-1491 (2007).

[4] O. P. Lay, S. Dubovitsky, R. D. Peters, J. P. Burger, S.-W. Ahn, W. H. Steier, H. R. Fetterman & Y. Chang, "MSTAR: A submicrometer absolute metrology system", *Opt. Lett.*, vol. 28, 890-892 (2003).

[5] Y. Kuramoto & H. Okuda, "High-accuracy absolute distance measurement by two-wavelength double heterodyne interferometry with variable synthetic wavelengths", *e-print arXiv*:1402.5575 (2014).

[6] K. Alzahrani, D. Burton, F. Lilley, M. Gdeisat & F. Bezombes, "Automatic absolute distance measurement with one micrometer uncertainty using a Michelson interferometer", *Lecture Notes in Engineering and Computer Science*, vol. 2, (2011).

[7] K. Falaggis, D. Towers & C. Towers, "Multiwavelength interferometry: Extended range metrology", *Opt. Lett.*, vol. 34, 950-952 (2009).

[8] N. Schuhler, Y. Salvadé, S. Lévêque, R. Dändliker & R. Holzwarth, "Frequency-comb-referenced two-wavelength source for absolute distance measurement", *Opt. Lett.*, vol. 31, 3101-3103 (2006).

[9] S. Hyun, Y.-J. Kim, Y. Kim, J. Jin, and S.-W. Kim, "Absolute length measurement with the frequency comb of a femtosecond laser", *Meas. Sci. Technol.*, vol. 20, 095302 (2009).

[10] Y. Salvadé, N. Schuhler, S. Lévêque & S. L. Floch, "High-accuracy absolute distance measurement using frequency comb referenced multiwavelength source", *Appl. Opt.*, vol. 47, 2715-2720 (2008).

[11] G. Wang, Y.-S. Jang, S. Hyun, B. Chun, H. Jay Kang, S. Yan, S.-W. Kim & Y.-J. Kim, "Absolute positioning by multi-wavelength interferometry referenced to the frequency comb of a femtosecond laser", *Opt. Express*, vol. 23, 9121 (2015).

[12] K.-N. Joo & S.-W. Kim, "Absolute distance measurement by dispersive interferometry using a femtosecond pulse laser", *Opt. Express*, vol. 14, 5954-5960 (2006).

[13] K. Minoshima & H. Matsumoto, "High-accuracy measurement of 240-m distance in an optical tunnel by use of a compact femtosecond laser", *Appl. Opt.*, vol. 39, 5512-5517 (2000).

[14] T.-A. Liu, N. R. Newbury & I. Coddington, "Sub-micron absolute distance measurements in sub-millisecond times with dual free-running femtosecond Er fiber-lasers", *Opt. Express*, vol. 19, 18501-18509 (2011).

[15] E. Baumann, F. R. Giorgetta, I. Coddington, L. C. Sinclair, K. Knabe, W. C. Swann & N. R. Newbury, "Comb-calibrated frequency-modulated continuous-wave ladar for absolute distance measurements", *Opt. Lett.*, vol. 38, 2026-2028 (2013).

[16] H. Zhang, H. Wei, X. Wu, H. Yang & Y. Li, "Absolute distance measurement by dual-comb nonlinear asynchronous optical sampling", *Opt. Express*, vol. 22, 6597-6604 (2014).

[17] M. Cui, M. G. Zeitouny, N. Bhattacharya, S. A. van den Berg & H. P. Urbach, "Long distance measurement with femtosecond pulses using a dispersive interferometer", *Opt. Express*, vol. 19, 6549-6562 (2011).

[18] I. Coddington, W. C. Swann, L. Nenadovic & N. R. Newbury, "Rapid and precise absolute distance measurements at long range", *Nat. Photonics*, vol. 3, 351-356 (2009).

[19] J. Lee, Y.-J. Kim, K. Lee, S. Lee & S.-W. Kim, "Time-of-flight measurement with femtosecond light pulses", *Nat. Photonics*, vol. 4, 716 (2010).

[20] U. Linz and J. Alonso, "What will it take for laser driven proton accelerators to be applied to tumor therapy?", *Phys. Rev. Spec. Top. - Accel. Beams*, vol. 10, 1-8 (2007).

[21] V. Malka, J. Faure, Y. A. Gauduel, E. Lefebvre, A. Rousse, and K. Ta Phuoc, "Principles and applications of compact laser-plasma accelerators", *Nat. Phys.*, vol. 4, 447-453 (2008).

[22] M. Barberio, S. Vallières, M. Scisciò, G. Kolhatkar, A. Ruediger & P. Antici, "Graphitization of diamond by laser-accelerated proton beams", *Carbon*, vol. 139, 531-537 (2018).

[23] M. Barberio, M. Scisciò, S. Vallières, F. Cardelli, S. N. Chen, G. Famulari, T. Gangolf, G. Revet, A. Schiavi, M. Senzacqua & P. Antici, "Laser-accelerated particle beams for stress testing of materials", *Nat. Commun.*, vol. 9, 372 (2018).

[24] M. Barberio, S. Veltri, M. Scisciò & P. Antici, "Laser-accelerated proton beams as diagnostics for cultural heritage", *Sci. Rep.*, vol. 7, 40415 (2017).

[25] M. Barberio & P. Antici, "Laser-PIXE using laser-accelerated proton beams", *Sci. Rep.*, vol. 9, 6855 (2019).

[26] A. April, "Ultrashort, strongly focused laser pulses in free space", *Coherence and Ultrashort Pulse Laser Emission*, F. J. Duarte, IntechOpen, 355-382 (2010).

[27] M. Descoteaux, R. Deriche, T. R. Knosche & A. Anwander, "Deterministic and probabilistic tractography based on complex fibre orientation distributions", *IEEE Trans. Med. Imaging*, vol. 28, 269-286 (2009).

[28] B. Pourdeyhimi, R. Dent & H. Davis, "Measuring fiber orientation in nonwovens. Part III: Fourier transform", *Text. Res. J.*, vol. 67, 143-151 (1997).

[29] J.-D. Tournier, F. Calamante, D. G. Gadian & A. Connelly, "Direct estimation of the fiber orientation density function from diffusion-weighted MRI data using spherical deconvolution", *NeuroImage*, vol. 23, 1176-1185 (2004).

[30] A. Tristàn-Vega, C.-F. Westin & S. Aja-Fernàndez, "Estimation of fiber orientation probability density functions in high angular resolution diffusion imaging", *NeuroImage*, vol. 47, 638-650 (2009).

[31] V. Wedeen, T. Reese, J. G. Dou, R. Weisskoff & D. Chesler, "Mapping fiber orientation spectra in cerebral white matter with Fourier-transform diffusion MRI", *Proceedings of the 8th Annual Meeting of ISMRM*, Denver, Colorado, USA (2000).

[32] S. Vallières, P. Puyuelo-Valdes, M. Salvadori, C. Bienvenue, S. Payeur, E. d'Humières & P. Antici, "The laser-driven ion acceleration beamline on the ALLS 200 TW for testing nanowire targets", *Proc. SPIE 11037*, 1103703 (2019).

[33] S. Vallières, M. Barberio, M. Scisciò, E. d'Humières & P. Antici, "Enhanced laser-driven proton acceleration using ultrasmall nanoparticles", *Phys. Rev. Accel. Beams*, vol. 22, 091303 (2019).

3.4 Perspectives

It is observed during experiments for the development of the TPI that positioning uncertainties of metallic foils can reach as low as $\Delta z = 350\,\text{nm} \approx \lambda_0/2$, thus ensuring reliable on-target laser intensity evaluation. Indeed, this level of precision corresponds to an on-target laser intensity uncertainty below 0.2% due to target positioning. This is achieved by using a Michelson interferometer modified with a focusing lens in the target arm, and proper tilt adjustments on the reference arm to enhance the device's sensitivity. This precision level is far more than required in the context of laser-driven ion acceleration, considering that $T_e^{\text{hot}} \propto a_0 \propto \sqrt{I_0}$ for the TNSA mechanism, moreover that shot-to-shot energy fluctuations of the ALLS 100 TW laser are of 2.5% RMS at a pulse energy of $\mathcal{E}_L = 2\,\text{J}$. Nevertheless, the developed TPI is strongly minimizing one source of uncertainty on the peak intensity evaluation, thus increasing the laser-based ion source's reliability and shot-to-shot repeatability. The TPI can also be used on other high-power laser facilities, however for lasers delivering very high energy above tens of Joules per

pulse and/or exhibiting lower pre-pulse contrast, the focal spot center might not be the optimal point in space for target alignment, as a results of plasma expansion and strong target decompression. In these situations, the optimal alignment position must be found beforehand by scanning the focal positions to find the one that maximizes the ion yield, and then calibrate the TPI with respect to this position.

One of the downsides of having a high-precision device such as the TPI is its sensitivity to environmental factors in the laboratory which hinder its proper use. Acousto-mechanical vibrations from the building's ventilation, from the vacuum pumps, from the nearby elevator, from people walking or simply talking around the chamber were generating fluctuations in the interferometric fringes that were noticeable with the naked eye on the acquisition images. The uncertainty Δz climbs easily well above the Rayleigh length z_R if precautions are not taken to reduce the environmental noise. To palliate to this problem, better acoustic isolation of the experimental vacuum chamber must be ensured, as well as encasing the TPI section and optics that are in-air as to limit noise from air turbulence.

Strictly speaking in the context of ion acceleration with solid targets in the TNSA regime, target fabrication is also a crucial factor for the proper use of the TPI. If the interaction targets are not perfectly flat or if the surface roughness is larger than $\lambda_0/4$, this produces strong wavefront distortions upon reflection on the metallic foil in the target arm beam, making the task very difficult for the TPI to estimate an absolute position. For example, a non-negligible tilt on the target makes the reflected beam arrive outside the CCD camera serving for interferometric measurements, hence making the TPI unusable. In an ideal case, the interaction targets must come from the same uncut large area thin foil, moreover being reflective as much as possible. The use of a multi-hole target holder, manufactured as a metallic cartesian meshgrid with equally spaced holes into which a single polished foil is inserted in between two twin parts of the holder, is recommended (typically a few hundred to a thousand holes in a grid is easily achievable). Assuming a polished foil is properly inserted into a multi-hole holder, this configuration increases the chance of having a globally flat foil, thereby limiting target-to-target variability and hence increasing the shot-to-shot consistency. In this situation, the TPI can be used to evaluate four points in the holder's transverse plane (*i.e.* left, right, top, bottom as far as possible from the target holder's center), and iteratively adjust the focal position z of the entire target holder beforehand of the shot series. This assumes that the tilts (θ_x and θ_y) on the multi-hole target holder are properly adjusted, which is usually the case in most laser-driven

ion acceleration facilities since target pre-alignment is performed before pumping. A blind and automated raster series of hundreds of shots can then be performed with high shot rate, ideally reaching the repetition rate of the laser.

One of the goals on the ALLS 100 TW ion beamline is to use the TPI to align nanostructured targets that enhance the TNSA mechanism (discussed further in Chapter 5). Since nanostructured targets typically have sub-wavelength transverse density variations and therefore high surface roughness, they inherently distort the wavefront upon reflection and may cause important problems for the analysis of interferometric data. Two solutions are foreseen to this problem; either the alignment is calibrated directly on the reflective front surface of the multi-hole target holder (if metallic-made such as in aluminum or stainless steel), or the alignment is done on the target's non-nanostructured rear surface. The latter technique would bring a slightly higher positioning uncertainty since it requires an additional longitudinal target movement to correctly position the front surface, based on a measurement from the rear surface. However if targets used are thin enough, on the order of 1 μm or $\ll z_R$, it should minimize this issue and yield intensity uncertainties due to target positioning around 1%.

Last but not least, the time constraint is an important factor to evaluate. As previously mentioned, the TPI absolute calibration sequence takes a few minutes, then a single position measurement is a sub-second process. The limiting factor in terms of time constraint is the motorized translation of lens L2, which typically takes a few seconds to go "in" and "out" of the main laser beam. Hence, the ideal case is to avoid using the TPI before every shot, otherwise this will inhibit the quest for reaching high shot rates. Again, no matter what type of target holder is used, the pre-alignment of the whole shot sequence using four points, as aforementioned above, is highly recommended for achieving high-repetition rate laser-driven ion sources with solid targets. Considering the very high sensitivity of interferometers that induces unstable fringe measurements, performing submicrometric alignment brings very restrictive constraints to achieve higher shot rates. Hence, if a global submicrometric target holder alignment using four selected points is not possible, and that single target alignment must be done, keeping the more robust conventional target alignment techniques (shadowgraphic and/or transverse plane imaging) is recommended for ensuring a high ion source reliability.

Chapter 4

Efficient Particle Diagnostics

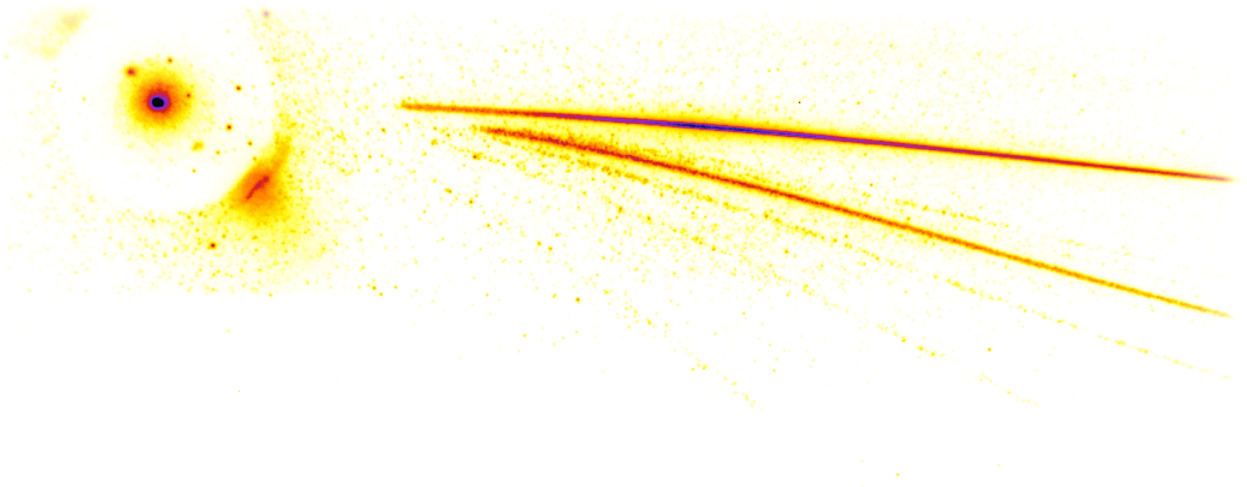

Thomson parabolas of protons and carbon ions impacting a microchannel plate detector.

Chapter Content

4.1 Foreword

This Chapter details two studies performed to develop efficient particle diagnostics to be incorporated on the ALLS 100 TW laser-driven ion beamline. The Chapter starts by overviewing some of the most common particle detectors used in the laser-based ion acceleration community, then continues by exposing the work done within this doctoral degree, to finally end with perspectives and recommendations for further developments. I was the project lead for both works which resulted in the following two publications:

— **S. Vallières**, C. Bienvenue, P. Puyuelo-Valdes, M. Salvadori, E. d'Humières, F. Schiettekatte & P. Antici, "Low-Energy Proton Calibration and Energy-Dependence Linearization of EBT-XD Radiochromic Films", *Review of Scientific Instruments*, vol. 90, 083301 (2019).

— **S. Vallières**, M. Salvadori, P. Puyuelo-Valdes, S. Payeur, F. Consoli, C. Verona, E. d'Humières, M. Chicoine, S. Roorda, F. Schiettekatte & P. Antici, "Thomson Parabola and Time-of-Flight Detector Cross-Calibration Methodology on the ALLS 100 TW Laser-Driven Ion Acceleration Beamline", *Review of Scientific Instruments*, vol. 91, 103303 (2020).

4.2 Conventional detectors used in laser-driven ion acceleration

This section aims to provide an overview of the most used particle diagnostics in laser-driven ion acceleration, along with the experimental constraints that they need to comply with. This section is based on excellent review articles available on these types of particle diagnostics [65, 199, 200], and their reading (with references therein) is encouraged to obtain further information. One of the most useful detectors used for ion beam profiling and (coarse) spectrum recovery are Radiochromic Films (RCF) [85]. They consist of plastic (polyester) sheets encompassing an active layer of micrometric thickness that darkens upon irradiation. They are sensitive to all ionizing radiation (UV, X-rays, electrons, ions, *etc.*) and hence precautions must be taken when one desires to measure one radiation type among several emerging from a source. In the context of laser-based ion acceleration with large energy spreads, RCFs are often placed in sheet stacks to measure the deposited dose (*i.e.* leading to the retrieval of particle numbers) corresponding to a narrow kinetic energy window in each sheet, due to the Bragg peak energy deposition profile from charged particles. Hence, in one laser shot, it is possible

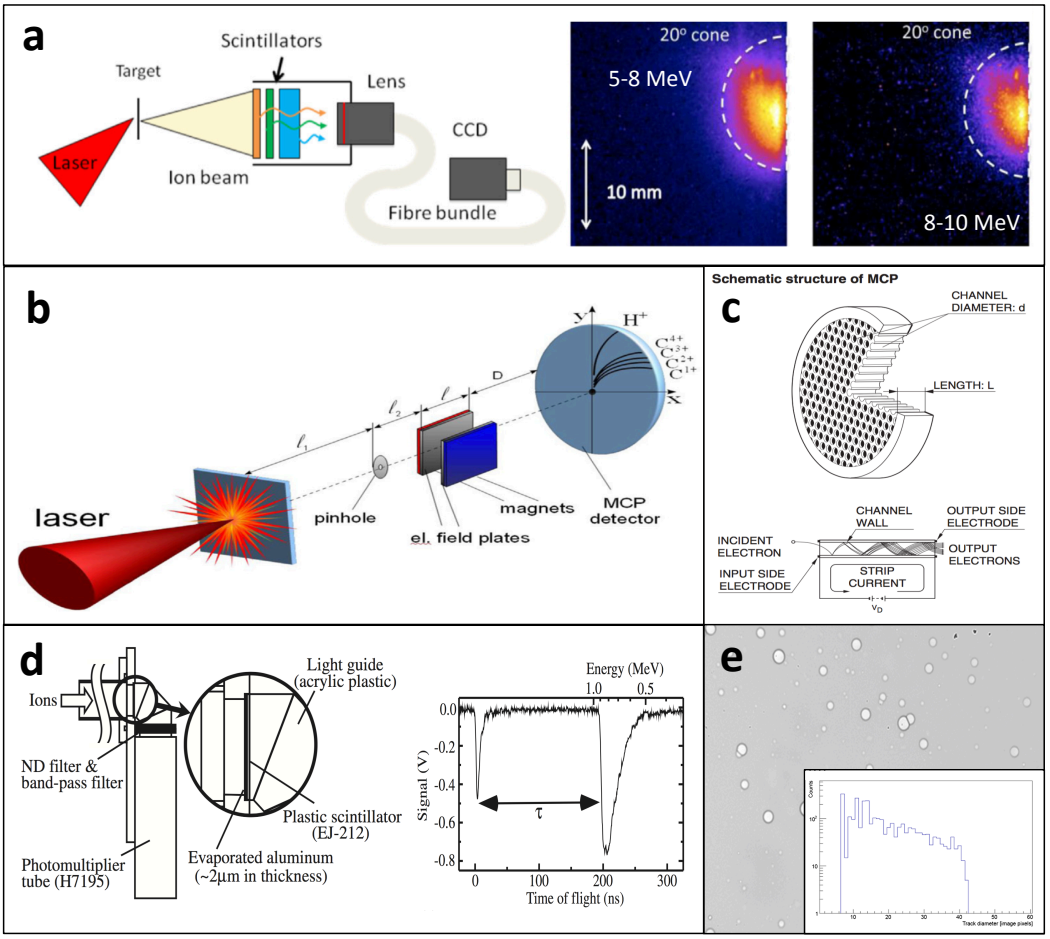

FIGURE 4.1: Common particle diagnostics used in laser-driven ion acceleration. (a) Ion beam profiler using scintillators and an associated imaging system. This figure is extracted and adapted from [200]. (b) Thomson parabola spectrometer used to spatially disperse different ion species in terms of their kinetic energy and charge-to-mass ratio. This figure is extracted and adapted from [200]. (c) Schematic diagram of a microchannel plate used as a high-gain single particle detector. This figure is extracted and adapted from [201]. (d) Time-of-Flight setup that uses a plastic scintillator and a photomultiplier tube for signal acquisition. This figure is extracted and adapted from [202]. (e) Impacts on CR-39 detector along with its associated spectrum reconstruction. The diameter of an impact corresponds to a specific particle kinetic energy. This figure is extracted and adapted from [203].

to obtain a coarsely reconstructed particle energy spectrum along with the energy-dependent conical beam divergence that is typical to TNSA ion beams. Post-processing of RCFs requires their scanning with flatbed scanners which can necessitate chamber venting and re-pumping for detector replacement. These detectors are therefore not suitable for high repetition-rate setups however, given their relatively fast particle detection readout, they are still very practical in the initial stages of a beamline for beam characterization. A suggested solution to this problem is to use a stack of scintillators emitting at different wavelengths [204] (see Figure 4.1.a), coupled to an imaging system using a CCD, allowing for a fully digitized beam profiling at

each shot. This interesting alternative to RCFs has its own limitations such as lower spatial resolution, broader energy bins, optical signal overlap, low flux saturation threshold and being easily damageable. One of the most common technique used for charged particle spectral reconstruction is a Thomson Parabola (TP) spectrometer (see Figure 4.1.b), in which static electric and magnetic fields are placed in parallel to disperse the particle trajectories in terms of their kinetic energy and charge-to-mass ratio, at the same time. Using the TP method, particle beams containing multiple ion species, such as TNSA ion beams with solid targets for instance, can receive simultaneous spectrum reconstruction for each species in one single shot. The incoming particles first go through a pinhole for momentum selection, cross the electric and magnetic field regions for spatial splitting, and then are collected on a spatially resolved detector such as an Image Plate [205], scintillators coupled to an Electron Multiplying CCD (EMCCD) [206] or a MicroChannel Plate (MCP) [104] (see Figure 4.1.c). Single particle track detectors such as CR-39 are also used for absolute particle number determination (see Figure 4.1.e). Impacts of particles on CR-39 produce defects in the resin with the appearance of holes that allow to track the energy deposition profile of a single particle, with the hole radius varying with the incident particle's kinetic energy. Indeed, CR-39 detectors are very inconvenient due to their analog nature, requiring an etching process in NaOH during several minutes before being analyzed under a microscope. Another popular methodology for spectrum retrieval is the Time-of-Flight (TOF) technique, in which a delay line of a few meters long is typically used to disperse in time the different energies within a particle bunch, similar to providing a "chirp", before collecting them with a temporally-resolved detection system [202] (see Figure 4.1.d). Some advantages of TOF lines is that they can provide an online, fast particle detection at each shot without the need for venting and re-pumping, moreover being much less cumbersome than most TP spectrometers. However, in the context of TNSA ion beams, the deconvolution of the different ion species is still a task that presents some difficulties, requiring very long delay lines, spectral shape assumptions and crude approximations. Aside from being usable online and fully digital to ensure a high repetition-rate, particle diagnostics used in the context of laser-driven ion acceleration must also face the challenges of being placed in an environment highly polluted by optical light, strong RF waves in the hundreds of kV/m amplitude range resulting from the interaction (referred to as ElectroMagnetic Pollution or EMP), as well as various ionizing radiation types such as high-energy electrons, X-ray photons, neutrons and heavy ions. The next sections are detailing two studies on particle diagnostics performed during this doctoral work, for their subsequent implementation on the ALLS 100 TW ion acceleration beamline. In

particular, we performed an absolute number calibration of the recently developed EBT-XD RCF on a Tandem Van de Graaff particle accelerator, for further use as TNSA beam profilers in the initial stage of the beamline. Moreover, we also present a TP-TOF cross-calibration study that shows their efficient incorporation on the recent laser-based ion beamline on ALLS 100 TW, along with the absolute spectral characterization of the generated ions species.

4.3 Low-Energy Proton Calibration and Energy-Dependence Linearization of EBT-XD Radiochromic Films

4.3.1 Abstract

In this work we calibrate the newly developed EBT-XD Radiochromic films (RCF) manufactured by Gafchromic^{TM} using protons in the energy range of 4-10 MeV. The irradiation was performed on the 2×6 MV Tandem Van de Graaff accelerator located at the Université de Montréal. The RCFs were digitized using an *Epson Perfection V700* flatbed scanner using both the RGB and grayscale channels. The proton fluences were measured with Faraday Cups (FC) calibrated in absolute terms. The Linear Energy Transfer (LET) function within the active layer of the films was calculated using the mass stopping power tables coming from the PSTAR database from the National Institute of Standards and Technology (NIST) to allow retrieval of the deposited dose. We find that the calibration curves for 7 and 10 MeV protons are nearly equivalent. The 4 MeV calibration curves exhibit a quenching effect due to the Bragg peak that falls close to the active layer. A linearization of this energy dependence was developed using a semi-empirical parametric model to allow the generation of calibration curves for any incident proton energy within the present range. Very good correspondence (<5% dose difference for the same netOD) of the 10 MeV calibration curves was noted when compared to existing high-energy proton (148.2 MeV) calibration curves reported in literature. Our calibration extends the range of operation of EBT-XD films to low-energy proton beam dosimetry.

4.3.2 Introduction

One of the most commonly used diagnostics for the detection of ionizing radiation are radiochromic films (RCF). These films consist of a polyester foil with thickness in the hundreds

of microns and have embedded an active layer sensitive to the radiation. Given their relatively easy use, their cheap costs, and - more importantly - their fast readout, they are extensively used whenever a quick and precise information about a wide range of deposited dose is needed (mGy up to kGy). RCFs allow detecting doses produced upon irradiation of ions, photons or electrons and are broadly employed in different applications such as medical dosimetry, nuclear physics or industry. A large selection of RCF types is available in order to better suit the different applications requesting diverse dose values. Several types of RCFs have been manufactured in the last years, in particular by the manufacturer Gafchromic^{TM} (HS, HD-810, MD, EBT) with different updates of specific types of RCFs coming up whenever a product could be improved (the MD-55 RCF type was replaced by the MD-V2 type, The EBT films were replaced successively by the EBT1, EBT2 and EBT3 films).

The easiest way to measure the deposited dose is by scanning the films using commercially available flatbed scanners that allow digitalizing the information in the film with micrometer resolution. Based on the retrieved optical density of the scanned surface, several published papers provide calibrations for the different types of existing RCFs, scanned using a variety of flatbed scanners, and taking into consideration the different issues and caveats that this procedure presents (e.g. scanning orientation, required time for dose saturation, etc)[1,2]. Gafchromic^{TM} released a new type of RCF in 2015, the EBT-XD. Compared to its predecessor, the EBT3, these films have a 25 μm thick active layer instead of 28 μm thick active layer, still placed between two 125 μm thick transparent polyester layers, for a total thickness of 275 μm per sheet. The manufacturer mentions that a different dopant composition of the active layer allows for a larger dynamic dose range up to 60 Gy, compared to 40 Gy for EBT3[3], which makes them better suited for Stereotactic Radiosurgery (SRS) and Stereotactic Body Radiotherapy (SBRT). Several absolute calibration papers have followed its release, especially high-energy photon calibrations for immediate use in medical dosimetry[4-9]. Concerning ion beam investigations, very few of them are available, namely a carbon ion calibration (290 and 400 MeV/u) from Yonai *et al.* (2018)[10], a high-energy proton (97.4 and 148.2 MeV) calibration from Khachonkham *et al.* (2018)[11] and a Monte Carlo derivation of the mass stopping powers for high-energy protons in the range of 50-400 MeV[12]. To our knowledge, no low-energy proton investigations have been published, yet calibration curves exist for EBT/MD-V2-55[13], EBT3[14-17] or for HD-V2/MD-V3[18] films, which allow for comparison. Calibrations for a lower energy range are particularly needed for high Linear Energy Transfer (LET) radiobiological

studies with cells and for laser-plasma accelerated proton beams, where typical energies that can be routinely produced by commercially available lasers are yielding currently at maximum a few tens of MeV. While producing lower energies, they are important for numerous applications[19-22].

In this work, we provide an absolute calibration of the EBT-XD with low-energy proton irradiations (4, 7 and 10 MeV), performed on the 2×6 MV Tandem Van de Graaff accelerator from the Université de Montréal. Results are presented for all channels in the RGB format as well as for grayscale representation. We show that the calibration depends on the incident particle energy, especially when the Bragg peak is near the sensitive layer of the film (*i.e.* for 4 MeV protons). The dose error incurred when neglecting this quenching effect is insignificant for the $7-10$ MeV energy range, ensuring less than 5% dose difference for the same net Optical Density (netOD). However, the dose error reaches up to 50% at 4 MeV, a non-linearity caused by the large stopping power distribution inside the sensitive layer when the Bragg peak is located close to it. A semi-empirical model is proposed to linearize the energy-dependence, providing dose estimations errors below 2% for the full dose range and for all energies in the $4-10$ MeV range.

4.3.3 Materials & Methods

4.3.3.1 Film scanning and net optical density evaluation

The EBT-XD Gafchromic^{TM} films were bought from the company *Ashland* and had dimensions of 20.32×25.40 cm^2 coming from the same box (lot No.10231802). The films were cut into 2×7 cm^2 sections using a guillotine cutter. Films were scanned on a *Epson Perfection V700* scanner in transmission mode, both in 48-bits RGB and 16-bits grayscale, then saved in uncompressed Tagged Image File Format (TIFF) data formats. All color corrections were disabled in the acquisition software, and a resolution of 600 dpi (42.3 μm/pixel) was used. Films were scanned prior to irradiation and after a 24h post-exposure in darkness to leave enough time for proper polymerization completion of the active layer. The selected region-of-interest (ROI) on each film section was a 5×5 mm^2 rectangle, for which the mean pixel value $\overline{\text{PV}}$ and standard deviation $\sigma_{\overline{\text{PV}}}$ were computed. Film uniformity was noted to be below 0.5%. The netOD evaluation

TABLE 4.1: Summary of relevant parameters to describe the delivered dose for 3 proton energies (4, 7 and 10 MeV).

$\mathcal{E}_{K,0}$ [MeV]	$\overline{LET}_{film}$ [MeV/cm]	$\sigma_{LET_{film}}/\overline{LET}_{film}$ [%]	$\overline{D}_{film}$ [Gy]	$\sigma_{D_{film}}/\overline{D}_{film}$ [%]	$\dot{\overline{D}}_{film}$ [Gy/min]
4	207	5.9	12 - 96	9.2	72
7	88	0.9	5.1 - 41	7.1	30
10	62	0.4	3.6 - 29	7.1	21

and its uncertainty were calculated following the method presented by Devic *et al.* (2004)[2]:

$$\text{netOD} = \text{OD}_{\text{exp}} - \text{OD}_{\text{unexp}} = \log_{10}\left(\frac{\overline{\text{PV}}_{\text{unexp}} - \overline{\text{PV}}_{\text{bckg}}}{\overline{\text{PV}}_{\text{exp}} - \overline{\text{PV}}_{\text{bckg}}}\right) \tag{4.1}$$

$$\sigma_{\text{netOD}} = \frac{1}{\ln(10)}\sqrt{\frac{\sigma^2_{\overline{\text{PV}}_{\text{unexp}}} + \sigma^2_{\overline{\text{PV}}_{\text{bckg}}}}{(\overline{\text{PV}}_{\text{unexp}} - \overline{\text{PV}}_{\text{bckg}})^2} + \frac{\sigma^2_{\overline{\text{PV}}_{\text{exp}}} + \sigma^2_{\overline{\text{PV}}_{\text{bckg}}}}{(\overline{\text{PV}}_{\text{exp}} - \overline{\text{PV}}_{\text{bckg}})^2}} \tag{4.2}$$

In the above equations (4.1) and (4.2), $\overline{\text{PV}}_{\text{unexp}}$ is the mean pixel value of an unexposed film, $\overline{\text{PV}}_{\text{exp}}$ is the mean pixel value of an irradiated (opaque) film, $\overline{\text{PV}}_{\text{bckg}}$ is the zero-light transmitted mean pixel value, and $\sigma_{\overline{\text{PV}}_{\text{unexp}}}$, $\sigma_{\overline{\text{PV}}_{\text{exp}}}$ and $\sigma_{\overline{\text{PV}}_{\text{bckg}}}$ are their corresponding standard deviations.

4.3.3.2 Proton irradiations and dose evaluations

The samples were irradiated using incident proton energies of $\mathcal{E}_{K,0} = 4$, 7 and 10 MeV. Film sections were placed in stacks of 6 superimposed sections using *Kapton* tape and mounted on a copper target holder (see Figure 4.2.a). This configuration allows to verify the depth-dose dependences at different depths and also prevents from collecting a parasite dose from X-rays generated by energetic protons hitting the copper target holder. For the data analysis of this calibration, only the dose deposited in the first film was used. A tantalum mask with square opening of 8×8 mm^2 was placed half a meter upstream from the target holder, directly followed by voltage-biased (+200 V) metal plates to collect parasite electrons generated by protons hitting the edges of the mask opening. All irradiations were performed under high vacuum (10^{-7} mbar) with a collimated and strongly defocused beam to achieve high uniformity in its central section (fluence fluctuations $\leq$1.2%) as can be noted from perpendicular intensity profiles in the inlet of Figure 4.2.b. Each irradiation was performed twice in order to ensure repeatability of the results. Delivered proton charges ranged from $Q = 50$ - 400 pC by steps of $\Delta Q = 50$

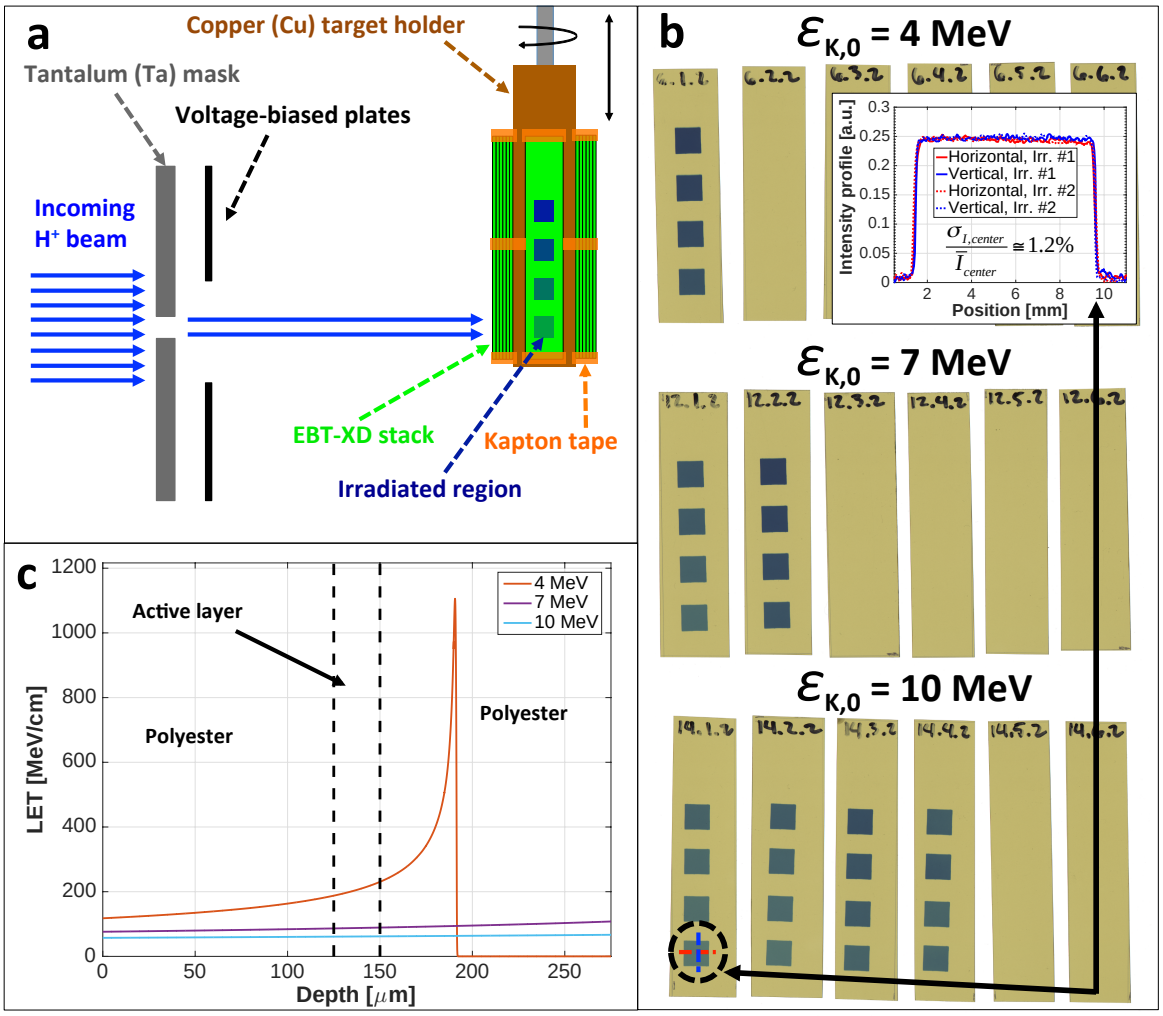

FIGURE 4.2: Sketch of the experimental setup on the 2 × 6 MV Tandem Van de Graaff accelerator from the Université de Montréal. (a) Experimental setup. (b) Scanned film stacks (consisting of 6 film) after irradiation for the three incident proton energies. The RCF facing the incident proton beam is shown on the left, the other films shown on the right follow the stack sequence. Each RCF stack displays the irradiation with 4 different fluences as denoted by the 4 visible squares on the films. Inlet figure shows perpendicular intensity profiles taken for the lowest fluence at 10 MeV, for both irradiation. All profiles have fluence fluctuations in the central section on the order of 1.2%. (c) LET calculation against depth in film for initial proton energies of 4, 7 and 10 MeV.

pC, with a mean irradiation current $\bar{I} \pm \sigma_{\bar{I}} = 5 \pm 0.35$ pA, which corresponds to 8 fluences in the range of $\phi = (0.49 - 3.9) \times 10^9$ protons/cm^2, with a fluence uncertainty of $\sigma_\phi / \phi = 7\%$. All charges were measured first with a Faraday Cup (FC) calibrated in absolute terms before each irradiation series, as well as with a simultaneous relative charge measurement collected from the tantalum mask. Since the dose rate of the Tandem can fluctuate during the irradiation and knowing the ratio between absolute and relative charge measurements, a mechanical shutter was set to close at the desired relative charge to be collected for each case. Hence, this

method also allows to achieve high repeatability for the same irradiation case. Deposited doses $D(\mathcal{E}_{K,0}, z)$ for a given initial kinetic energy $\mathcal{E}_{K,0}$ and depth z in films were evaluated using the following relationship:

$$D(\mathcal{E}_{K,0}, z) = \frac{\text{LET}(\mathcal{E}_{K,0}, z)}{\rho} \cdot \phi \tag{4.3}$$

In equation (4.3), ρ is the film mass density (1.35 g/cm^3) and $\text{LET}(\mathcal{E}_{K,0}, z)$ corresponds to the LET value calculated using the mass stopping power tables of tissue-equivalent polyester (polyethylene terephthalate, known as Mylar) found on the PSTAR database from the National Institute of Standards and Technology (NIST)[23] (see Figure 4.2.c), which are rigorously consistent with values found in the ICRU Report 49[24] and the stopping power tables as provided by SRIM[25]. The average deposited dose to a film $\overline{D}_{\text{film}}$ was calculated using the average LET inside the active layer $\overline{\text{LET}}_{\text{film}}$ along with its standard deviation $\sigma_{\text{LET}_{\text{film}}}$. The dose uncertainty in the film $\sigma_{D_{\text{film}}}$ was thus evaluated as:

$$\frac{\sigma_{D_{\text{film}}}}{\overline{D}_{\text{film}}} = \sqrt{\left(\frac{\sigma_{\text{LET}_{\text{film}}}}{\overline{\text{LET}}_{\text{film}}}\right)^2 + \left(\frac{\sigma_\phi}{\phi}\right)^2} \tag{4.4}$$

A scheme of the experimental setup is presented in Figure 4.2.a. Since the mean LET in the active layer $\overline{\text{LET}}_{\text{film}}$ is different for every proton energy that we used (4, 7 and 10 MeV), the prescribed dose varies with proton initial energy, even if the delivered fluence is the same for all energies. Therefore, it is very important to discriminate the different deposited dose ranges according to each initial kinetic energy using equations (4.3) and (4.4). A summary of the relevant parameters to describe these dose ranges is presented in Table 4.1. As shown in the paper of Vadrucci *et al.* (2015)[14], the deposited dose in EBT3 films is independent of the dose rate, and since EBT3 and EBT-XD are very similar in composition and construction, we do not expect the dose rate to be a significant variable in the present study.

4.3.4 Results

The calibration curves, dose (Gy) vs netOD (no units or n.u.), were fitted with the following functional form, as proposed by Devic *et al.* (2004)[2]:

$$D(\text{netOD}) = b \cdot \text{netOD} + c \cdot \text{netOD}^n \tag{4.5}$$

In equation (4.5), b and c are the fitting parameters and n is chosen among values ranging from $\frac{1}{2} - 5$, in half-integer steps, providing the best fit. The parameter b thus characterizes the linear part of equation (4.5), whereas c and n determine the degree of non-linear behavior, for a particular color channel. The calibration curves for the three initial proton kinetic energies are presented in Figure 4.3. The Red channel shows the greatest non-linear behavior ($n = 3$) and also highest sensitivity, followed by Green and Gray channels which are essentially equivalent ($n = 2$). Finally, the Blue channel ($n = \frac{1}{2}$) exhibits very low sensitivity. For low dose evaluations ($D < 10$ Gy), it is more advisable to use the Red channel in order to benefit from the higher sensitivity, however one needs to be aware that this channel shows quicker netOD saturation with dose. Hence, for dose evaluation exploiting the full dose range of the films (up to 60 Gy, as recommended by the manufacturer), it is better to use either the Green or Gray channel that exhibit slower netOD saturation with deposited dose. The obtained calibration curves show a very good correspondence to the curves obtained in the paper of Khachonkham *et al.* (2018)[11], especially for proton energies of 7 and 10 MeV. The curves for 4 MeV protons, however, shift from the 7 and 10 MeV curves. We can get a better insight of this behavior by regrouping them in different color channels, as presented by Figure 4.4. From Figure 4.4 we note that the calibration curves for 7 MeV and 10 MeV are very similar since they fall within the respective error bars. One would not make a significant dose evaluation error (<5%) by choosing either the 7 MeV or 10 MeV curve. However, going to 4 MeV causes a very significant curve shift as can be seen in all color channels of Figure 4.4. This is due to the significantly higher LET inside the active layer, *i.e.* when the Bragg peak falls close the sensitive layer depth, as is the case for the 4 MeV LET curve presented in Figure 4.2.c. This is known as the quenching effect, resulting from the saturation of polymerization sites inside the sensitive layer, which causes an under-response of the film. This quenching is well-known for EBT with high LET particles and has been reported previously in literature[13,15-17,26-28]. In Figure 4.2.c, one can note that the LET is constant over the entire active layer for 7 and 10 MeV protons.

This is the major benefit of a thin active layer, as it allows to have a constant dose over the whole sensitive volume and thus permits to perform precise dose measurements for clinical purposes. In the case of 4 MeV protons, the presence of a LET distribution inside the active layer leads to a broadened dose distribution and thus to a greater uncertainty on the deposited dose. Concerning the previously mentioned quenching effect with 4 MeV protons, which leads to a film under-response (lower netOD for the same dose), it causes dose differences in the Red

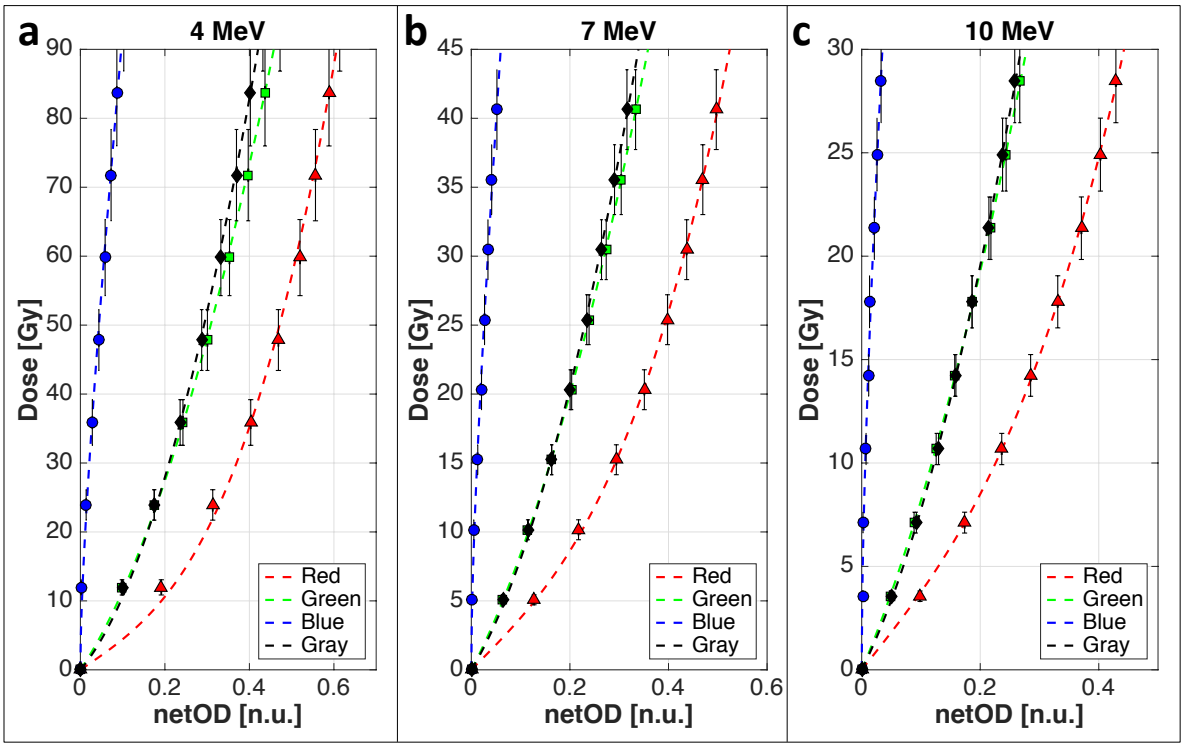

FIGURE 4.3: Calibration curves for four color channels (Red, Green, Blue and Gray) with initial proton kinetic energy of (a) $\mathcal{E}_{K,0} = 4$ MeV, (b) $\mathcal{E}_{K,0} = 7$ MeV and (c) $\mathcal{E}_{K,0} = 10$ MeV. All fits have $R^2 > 0.99$. The fitting exponent n of equation (4.5) are of 3, 2, $\frac{1}{2}$ and 2 for Red, Green, Blue and Gray channels, respectively. Markers are experimental data points and dashed lines are fitted curves.

TABLE 4.2: Calibration fit parameters b and c for all color channels and initial kinetic energies.

Color Channel	Energy [MeV]	b [Gy/OD]	c [Gy/OD^n]
Red ($n = 3$)	4	41.44	291.1
	7	35.86	181.8
	10	35.99	162.2
Green ($n = 2$)	4	91.02	230.7
	7	160.8	67.92
	10	67.27	145.7
Blue ($n = 1/2$)	4	502.7	133.2
	7	336.7	102.0
	10	287.0	106.9
Gray ($n = 2$)	4	72.05	337.7
	7	58.59	218.7
	10	57.26	202.1

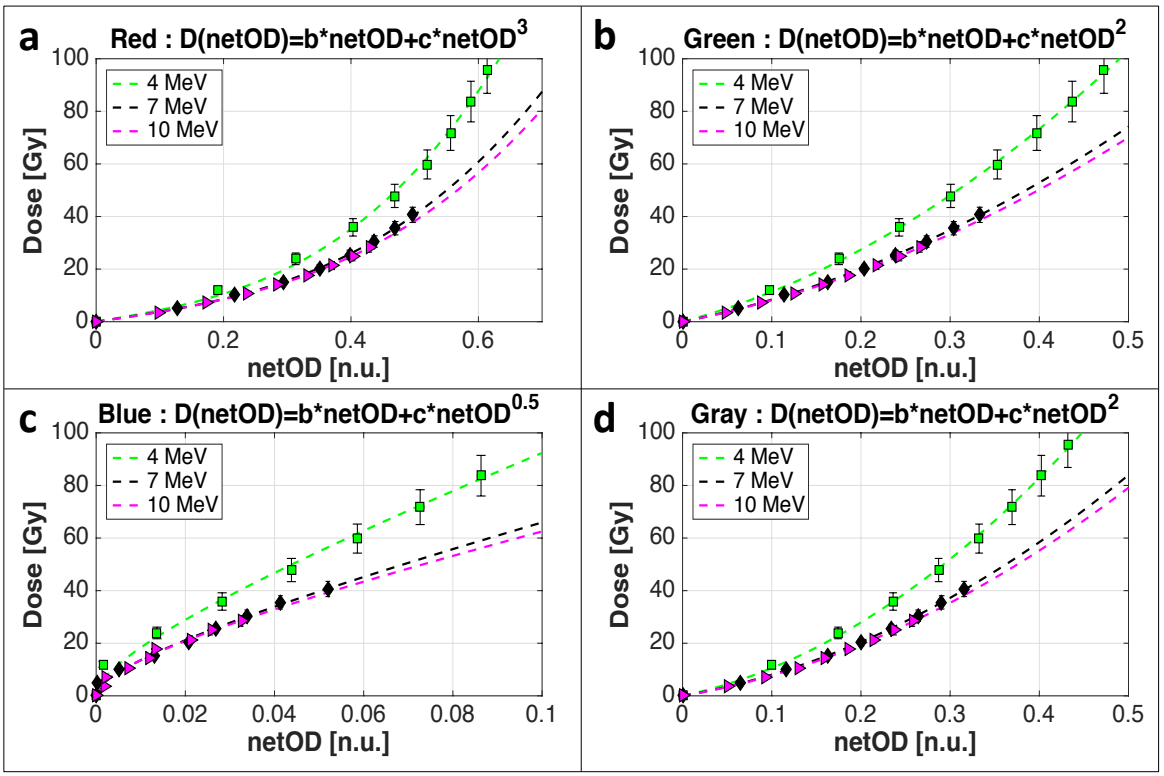

FIGURE 4.4: Calibration curves of the three initial proton kinetic energies (4, 7 and 10 MeV) relative to the four different color channels. (a) Red channel (b) Green channel (c) Blue channel (d) Gray channel. Markers are experimental data points and dashed lines are fitted curves.

channel between 4 and 10 MeV curves for the same netOD of 27% at low doses ($D = 8.6$ Gy at netOD = 0.2 for 10 MeV protons as reference) which is consistent with what is observed by Reinhardt *et al.* (2015)[17], reporting 26% at 6 Gy on EBT3 for a comparison of 4 MeV and 11 MeV protons. This further confirms the similarities between EBT types of RCF. The dose difference reaches 44% at intermediate doses ($D = 25$ Gy at netOD = 0.4 for 10 MeV protons) and finally 56% at high doses ($D = 57$ Gy at netOD = 0.6 for 10 MeV protons). We give only information for the Red channel since this channel is widely used by RCF users and serves as a reference. Moreover, the Red channel is the only one available for comparison with Reinhardt *et al.* (2015)[17], and for these reasons we did not find it relevant to present the differences for the other color channels. This high dose difference cannot be neglected, and this effect is expected to increase as the Bragg peak approaches the active layer of the RCF (*i.e.* 3.2 MeV $< \mathcal{E}_{K,0} <$ 4 MeV). To further investigate the quenching effect, we evaluated the change in sensitivity of the films, defined by the variation rate of netOD with respect to dose, calculated through equation (4.6). Since the 7 MeV curves are very similar to those of 10 MeV protons, sensitivity curves are presented in Figure 4.5 only for the 4 and 10 MeV protons. From Figure 4.5, it is possible to

note the downshift of 4 MeV sensitivity curves with respect to 10 MeV, for all color channels. The zero-dose sensitivity percent differences between 10 MeV and 4 MeV reach up to 13% for the Red channel, 24% for the Green channel, 24% for the Blue channel and 21% for the Gray channel. These percent differences are indeed expected to increase as the Bragg peak gets closer to the active layer (*i.e.* down to 3.2 MeV).

$$\frac{d(\text{netOD})}{dD} = \left[\frac{dD}{d(\text{netOD})}\right]^{-1} = \frac{1}{b + c \cdot n \cdot \text{netOD}^{n-1}} \tag{4.6}$$

In light of these high dose and sensitivity differences for various initial kinetic energies, there is a need to develop a methodology that allows an estimation of the fit parameters b and c, at least for any initial energy in the 4-10 MeV range. We propose a method to linearize this energy-dependence of $b(\mathcal{E}_{K,0})$ and $c(\mathcal{E}_{K,0})$, consisting in normalizing the calibration fit parameters b and c by the mean LET inside the active layer, as shown by equations (4.7) and (4.8), in order to limit the influence of the continuously increasing stopping power as the Bragg peak approaches the active layer.

$$\frac{b}{\overline{\text{LET}}_{\text{film}}} = b_1 \cdot \mathcal{E}_{K,0} + b_2, \tag{4.7}$$

$$\frac{c}{\overline{\overline{\text{LET}}}_{\text{film}}} = c_1 \cdot \mathcal{E}_{K,0} + c_2. \tag{4.8}$$

This allows to extract the first order LET dependence from the film response. A subsequent fit of $b/\overline{\text{LET}}_{\text{film}}$ and $c/\overline{\text{LET}}_{\text{film}}$ vs $\mathcal{E}_{K,0}$ was performed in order to determine the sub-parameters b_1, b_2, c_1, c_2. This sub-parametrization allows full flexibility and control on the calibration curve at least for all energies contained in the range $\mathcal{E}_{K,0} = 4 - 10$ MeV. The results of this linearization are shown in Figure 4.6. As noted from Figure 4.6, a very good linearization of the effect is obtained for all channels. Complete characterization of the calibration curve over the present energy range can be achieved by referring to the sub-parameters b_1, b_2, c_1, c_2. Final values for each color channel are presented in Table 4.3. Table 4.3 allows providing a calibration curve (dose vs netOD) for any initial proton kinetic energies contained in the range $\mathcal{E}_{K,0} = 4 - 10$ MeV. Further details and comments related to this curve reconstruction are provided in the *Discussion* (see section 4.4.5).

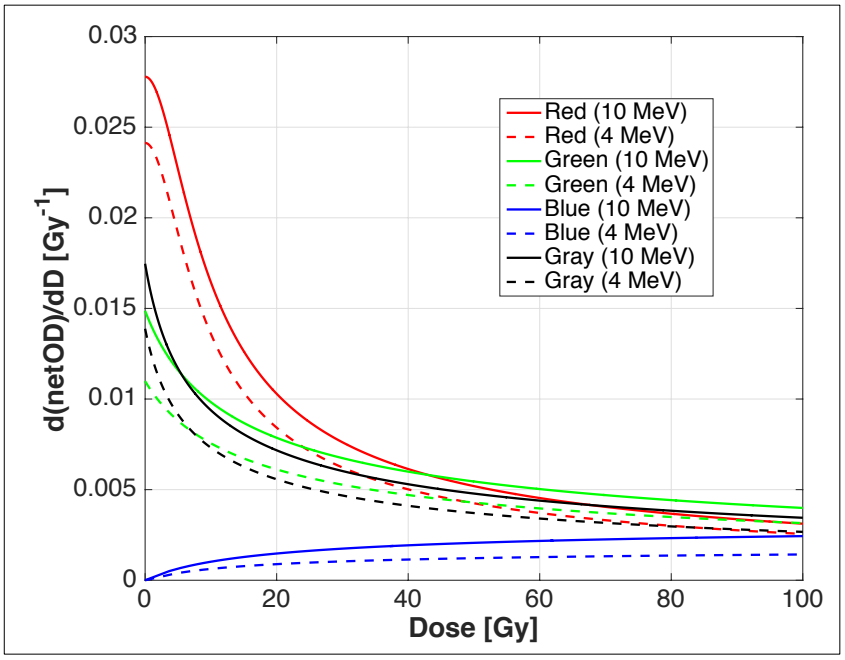

FIGURE 4.5: Influence of quenching effect on the film's sensitivity curves of RGB and Gray channels. Full lines and dashed lines are for 10 MeV and 4 MeV protons, respectively.

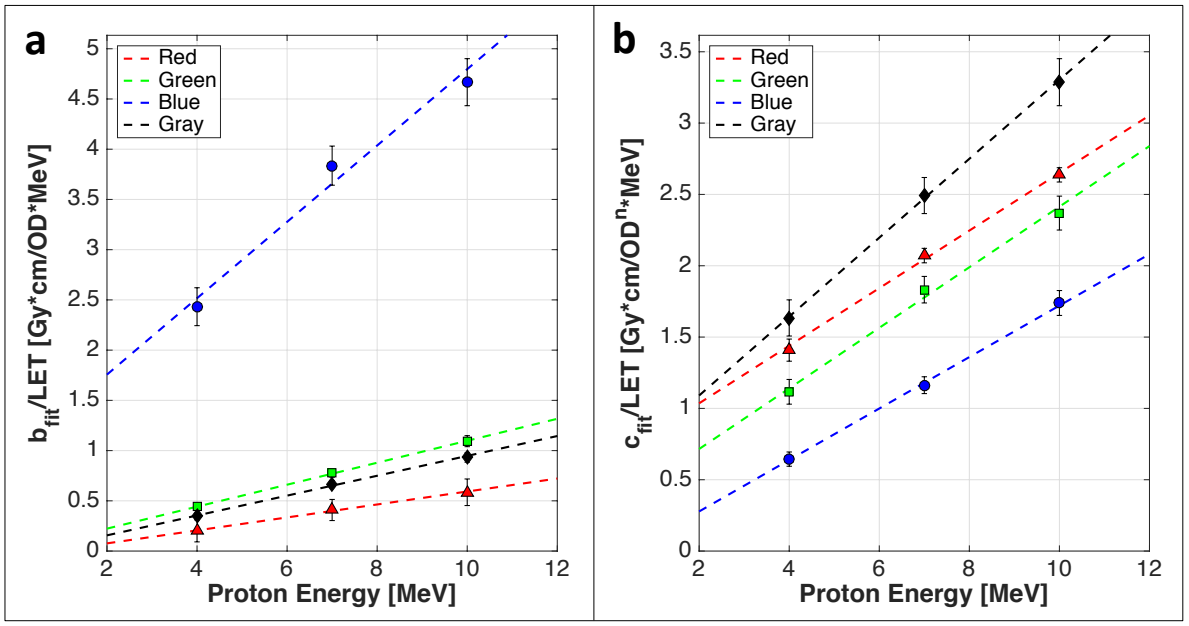

FIGURE 4.6: Proton energy-dependence linearization of the normalized calibration parameters $b/\overline{\text{LET}}_{\text{film}}$ (a) and $c/\overline{\text{LET}}_{\text{film}}$ (b), as per equations (4.7) and (4.8). All fits have $R^2 > 0.98$. Markers are data points and dashed lines are fitted curves for the Red ($n = 3$), Green ($n = 2$), Blue ($n = 1/2$) and Gray ($n = 2$) channels.

TABLE 4.3: Fit parameters for energy-dependence linearization.

Color Channel	b_1 [a]	b_2 [b]	c_1 [c]	c_2 [d]
Red ($n = 3$)	0.0645	-0.0524	0.2018	0.6322
Green ($n = 2$)	0.1093	0.0047	0.2123	0.2910
Blue ($n = 1/2$)	0.3800	0.9965	0.1804	-0.0829
Gray ($n = 2$)	0.0989	-0.0413	0.2765	0.5376

[a] Gy·cm/OD·MeV^2
[b] Gy·cm/OD·MeV
[c] Gy·cm/OD^n·MeV^2
[d] Gy·cm/OD^n·MeV

4.3.5 Discussion

Using the data provided in Table 4.3, it is possible to generate a calibration curve for any specific proton energy near our testing range, in a few numerical steps. The description of the method is as follows:

(i) For a given proton initial kinetic energy $\mathcal{E}_{K,0}$ and color channel, calculate the normalized fit parameters $b/\overline{\text{LET}}_{\text{film}}$ and $c/\overline{\text{LET}}_{\text{film}}$ through the energy linearization equations (4.7) and (4.8), using the sub-parameter values (b_1, b_2, c_1, c_2) provided in Table 4.3.

(ii) Calculate the average LET inside the active layer $\overline{\text{LET}}_{\text{film}}$ using either mass stopping power tables from the NIST-PSTAR database[23], SRIM/TRIM[25] calculations or with a suitable Monte Carlo code.

(iii) Calculate the specific calibration fit parameters b and c.

(iv) Generate the required calibration curve $D(\text{netOD})$ through equation (4.5), using the measured netOD, the calculated b and c values and the corresponding exponent n for a particular color channel.

For instance, the calibration curve parameters for 10 MeV protons with the Red channel ($n = 3$) is found by computing $b(\mathcal{E}_{K,0} = 10\,\text{MeV}) = \overline{\text{LET}}_{\text{film}} \cdot (b_1 \cdot \mathcal{E}_{K,0} + b_2) = 36.45$ Gy/OD and $c(\mathcal{E}_{K,0} = 10\,\text{MeV}) = \overline{\text{LET}}_{\text{film}} \cdot (c_1 \cdot \mathcal{E}_{K,0} + c_2) = 163.0$ Gy/OD^3. If one performs these calculation steps as proposed above for initial kinetic energies of $\mathcal{E}_{K,0}$ = 4, 7 and 10 MeV to recover the experimental calibration curves, one obtains an error on the dose calculation of less than 2.5% over the full netOD range evaluated here, for all energies. This shows that even if the

linearization fit was performed on only three data points, $b/\overline{\text{LET}}_{\text{film}}$ and $c/\overline{\text{LET}}_{\text{film}}$ are slowly varying functions against $\mathcal{E}_{\text{K},0}$, as opposed to the strongly non-linear behavior of $b(\mathcal{E}_{\text{K},0})$ and $c(\mathcal{E}_{\text{K},0})$, hence providing robustness to the semi-empirical model. One of the questions that arise is concerning the range of validity in terms of proton energies. As mentioned previously in this text, this semi-empirical model is at least valid in the range of $\mathcal{E}_{\text{K},0} = 4 - 10$ MeV. However, for energies below 4 MeV, the average LET inside the active layer increases up to 3.5 MeV, where the Bragg peak enters the sensitive volume. At that point, $\sigma_{\text{LET}_{\text{film}}}$ is on the order of 30% of the mean value, and then explodes up to 200% at 3.2 MeV, to finally fall back to zero when the Bragg peak is before the active layer ($\mathcal{E}_{\text{K},0} < 3.2$ MeV), a case for which the films are of no purpose anymore. For these reasons, it is not recommended to use this model below 3.6 MeV (15% standard deviation of LET, leading to a dose uncertainty of 17%), where the Bragg peak singularity causes enormous non-linearities in the dose distribution. However, one cannot be sure that the linearity holds with the extrapolation between 3.6 MeV and 4 MeV, hence it would be conservative to estimate 20% of uncertainty on the determination of dose at 3.6 MeV. On the other side of the energy range, however, the model is much more reliable for extrapolation since the LET decreases very slowly with increasing $\mathcal{E}_{\text{K},0}$ and, in addition, the LET distribution in the active layer becomes more constant. As a comparison, the dose values obtained in our measurements for proton energies of 7 and 10 MeV correspond to within 5%, *i.e.* below our dose uncertainty of 7%, to what is obtained by Khachonkham *et al.* (2018)[11] on EBT-XD for the same netOD with protons of initial kinetic energy of 148.2 MeV. The semi-empirical model for calibration curve generation, however, can diverge with an extrapolation that is far from the energy range evaluated in this study, since the behavior of the function is not necessarily linear and thus its behavior is unknown. It is noted with this model that no significant variation of the calibration curve generation occurs up to $\mathcal{E}_{\text{K},0}$ = 30 MeV, hence delimiting a safe upper bound to this model. Nevertheless, because of this strong correspondence with other works in literature, one can generate the curve for 10 MeV and safely use it for a proton energy between 10 and 148.2 MeV. For higher energy protons, it is recommended to repeat this analysis with a robust peer-reviewed Monte Carlo code such as Geant4[29]. Ideally, one should perform absolute dose measurements with a cross-calibrated ionization chamber for better correlation with netOD, when the proton energy allows for it, such as with protons of 100 MeV. In the end, the best practice is to use this model with low-energy protons not far from the experimental energy range of this paper (*i.e.* $\mathcal{E}_{\text{K},0} = 4 - 10$ MeV), or also above by using the 10 MeV curve.

4.3.6 Conclusion

In this study, we presented the experimental calibration of EBT-XD radiochromic films for kinetic energies of $\mathcal{E}_{K,0} = 4$, 7 and 10 MeV, performed on the 2×6 MV Tandem Van de Graaff accelerator from the Université de Montréal. A strong correspondence was observed between the calibration curves of 7 MeV and 10 MeV (<5% dose difference), and these two also precisely correspond to the proton calibration proposed by Khachonkham *et al.* (2018)[11] with 148.2 MeV protons (also <5% dose difference, which is below our dose uncertainty of 7%). However, the calibration curve for 4 MeV protons was observed to exhibit a quenching effect due to higher LET inside the active layer. Dose differences between the 4 MeV curves and the 10 MeV curves reach up to 50%, hence resulting in a non-negligible energy-dependence of the films. To palliate this, we have developed a semi-empirical model to linearize the energy dependence, thus allowing to generate calibration curves for any incident proton energies in the range $\mathcal{E}_{K,0} = 4 - 10$ MeV. It is not recommended to use this model below 3.6 MeV due to the strong non-linearity caused by the Bragg peak entering in the active layer. However, the very good correspondence between the 10 MeV curves and other calibrations in the literature (up to 148.2 MeV) suggest that it is safe to use the 10 MeV curves without strong discrepancies in the evaluation of dose. As such, we can safely estimate that our calibration curves are valid up to this energy range. For higher energy protons it is recommended to re-perform this analysis with a robust, peer-reviewed Monte Carlo code such as, e.g., Geant4[29] or to perform absolute dose measurements with a cross-calibrated ionization chamber for better correlation with netOD.

4.3.7 Acknowledgments

This work is supported by FRQNT (nouveaux chercheurs, Grant No. 174726, Equipe 2016-PR-189974), the National Sciences and Engineering Research Council of Canada (NSERC) (Discovery Grant RGPIN-2018-05772 and the Alexander-Graham-Bell Graduate Scholarship for S.V.), Compute Canada (Job: pve-323-ac) as well as the Canada Foundation for Innovation (CFI). This study has also received financial support from the French National Research Agency (ANR) in the frame of "the Investments for the future" Programme IdEx Bordeaux - ANR-10-IDEX-03-02. The authors wish to thank L. Godbout for maintaining the EN-1 Tandem accelerator and M. Chicoine for the fruitful discussions and support.

4.3.8 References

[1] S. N. Chen *et al.*, "Absolute dosimetric characterization of Gafchromic EBT3 and HDv2 films using commercial flat-bed scanners and evaluation of the scanner response function variability", *Rev. Sci. Instrum.*, vol. 87, 073301 (2016).

[2] S. Devic *et al.*, "Dosimetric properties of improved GafChromic films for seven different digitizers", *Med. Phys.*, vol. 31 (9), 2392 (2004).

[3] EBT-XD specifications, Gafchromic™ documentation. http://www.gafchromic.com/documents/EBTXD_Specifications_Final.pdf

[4] M. P. Grams, J. M. Gustafson, K. M. Long & L. E. Fong de los Santos, "Technical Note: Initial characterization of the new EBT-XD Gafchromic films", *Med. Phys.*, vol. 42 (10), 5782-5786 (2015).

[5] D. F. Lewis & M. F. Chan, "Technical Note: On GAFChromic EBT-XD film and the lateral response artifact", *Med. Phys.*, vol. 43 (2), 643-649 (2016).

[6] A. L. Palmer, A. Dimitriadis, A. Nisbet & C. H. Clark, "Evaluation of Gafchromic EBT-XD film, with comparison to EBT3 film, and application in high dose radiotherapy verification", *Phys. Med. Biol.*, vol. 60, 8741-8752 (2015).

[7] H. Miura, S. Ozawa, F. Hosono, N. Sumida, T. Okazue, K. Yamada & Y. Nagata, "Gafchromic EBT-XD film: Dosimetry characterization in high-dose, volumetric-modulated arc therapy", *J. of Appl. Clin. Med. Phys.*, vol. 17 (6), 312-322 (2016).

[8] A. A. Schoenfeld, S. Wieker, D. Harder & B. Poppe, "Changes of the optical characteristics of radiochromic films in the transition from EBT3 to EBT-XD films", *Phys. Med. Biol.*, vol. 61, 5426 (2016).

[9] S. Devic, N. Tomic & D. Lewis, "Reference radiochromic film dosimetry: Review of technical aspects", *Physica Medica*, vol. 32, 541-556 (2016).

[10] S. Yonai, C. Arai, K. Shimoyama & N. Fournier-Bidoz, "Experimental Evaluation of Dosimetric Characterization of Gafchromic EBT3 and EBT-XD Films for Clinical Carbon Ion Beams", *Rad. Protec. Dosim.*, vol. 180 (1-4), 314-318 (2018).

[11] S. Khachonkham, R. Dreindl, G. Heilemann, W. Lechner, H. Fuchs, H. Palmans, D. Georg & P. Kuess, "Characteristic of EBT-XD and EBT3 radiochromic film dosimetry for photon and proton beams", *Phys. Med. Biol.*, vol. 63, 065007 (2018).

[12] C. Shi, C. C. Chen, D. Mah & M. F. Chan, "Monte Carlo calculation of the mass stopping power of EBT3 and EBT-XD films for protons for energy ranges of 50-400 MeV", *Prec. Radiat. Oncol.*, vol. 2 (4), 106-113 (2018).

[13] D. Kirby, S. Green, H. Palmans, R. Hugtenburg, C. Wojnecki & D. Parker, "LET dependence of GafChromic films and an ion chamber in low-energy proton dosimetry", *Phys. Med. Biol.*, vol. 55, 417-433 (2010).

[14] M. Vadrucci, G. Esposito, C. Ronsivalle, R. Cherubini, F. Marracino, R. M. Montereali, L. Picardi, and M. Piccinini, M. Pimpinella, M. A. Vincenti & C. De Angelis, "Calibration of GafChromic EBT3 for absorbed dose measurements in 5 MeV proton beam and ^{60}Co γ-rays", *Med. Phys.*, vol. 42 (8), 4678-4684 (2015).

[15] M. C. Battaglia, D. Schardt, J. M. Espino, M. I. Gallardo, M. A. Cortés-Giraldo, J. M. Quesada, A. M. Lallena, H. Miras & D. Guirado, "Dosimetric response of radiochromic films to protons of low energies in the Bragg peak region", *Phys. Rev. Accel. Beams.*, vol. 19, 064701 (2016).

[16] M. C. Battaglia, J. M. Espino, M. I. Gallardo, A. M. Lallena, B. Fernandez, M. A. Cortés-Giraldo, J. M. Quesada & D. Schardt, "EBT3 film calibration in the Bragg peak region for proton beams below 5 MeV", *Nuclear Inst. and Methods in Physics Research B*, vol. 444, 117-124 (2019).

[17] S. Reinhardt, M. Wurl, C. Greubel, N. Humble, J. J. Wilkens, M. Hillbrand, A. Mairani, W. Assmann & K. Parodi, "Investigation of EBT2 and EBT3 films for proton dosimetry in the 4-20 MeV energy range", *Radiat. Environ. Biophys.*, vol. 54, 71-79 (2015).

[18] A. S. Cucoanes, M. Gugiu, F. Rotaru, F. Negoita, L. Tudor, S. Kisyov, C. Manailescu & V. Nastasa, "Radiochromic film calibration at 9 MV accelerator of IFIN-HH", *ACS Photonics*, vol. 2 (2), 208-2015 (2015).

[19] M. Barberio, M. Scisciò, S. Vallières, S. Veltri, A. Morabito & P. Antici, "Laser-Generated Proton Beams for High-Precision Ultra-Fast Crystal Synthesis", *Sci. Rep.*, vol. 7, 12522 (2017).

[20] M. Barberio, M. Scisciò, S. Vallières, F. Cardelli, S.N. Chen , G. Famulari, T. Gangolf, G. Revet, A. Schiavi, M. Senzacqua & P. Antici, "Laser-accelerated particle beams for stress testing of materials", *Nat. Comm.*, vol. 9, 372 (2018).

[21] M. Barberio, S. Vallières, M. Scisciò, G. Kolhatkar, A. Ruediger & P. Antici, "Graphitization of diamond by laser-accelerated proton beams", *Carbon*, vol. 138, 531-537 (2018).

[22] M. Barberio & P. Antici, "Laser-PIXE using laser-accelerated proton beams", *Sci. Rep.*, vol. 9, 6855 (2019).

[23] Mass Stopping Power Tables, NIST-PSTAR database. https://physics.nist.gov/PhysRefData/Star/Text/PSTAR.html.

[24] ICRU, "Stopping powers and ranges for protons and alpha particles", ICRU Report No. 49, International Commission of Radiation Units, Bethesda, MD, (1993).

[25] J. F. Ziegler, M. D. Ziegler & J. P. Biersack, "SRIM - The stopping and range of ions in matter (2010)", *Nucl. Inst. & Meth. in Phys. Res. B*, vol. 268, 1818-1823 (2010).

[26] M. Martisikova & O. Jakel, "Dosimetric properties of Gafchromic EBT films in monoenergetic medical ion beams", *Phys. Med. Biol.*, vol. 55, 3741-3751 (2010).

[27] L. Zhao & I. J Das, "Gafchromic EBT film dosimetry in proton beams", *Phys. Med. Biol.*, vol. 55, N291-N301 (2010).

[28] G. Angellier, M. Gautier & J. Hérault, "Radiochromic EBT2 film dosimetry for low-energy protontherapy", *Med. Phys.*, vol. 38 (11), 6171-6177 (2011).

[29] S. Agostinelli *et al.*, "Geant4 - a simulation toolkit", *Nucl. Inst. & Meth. in Phys. Res. A*, vol. 506 (3), 250-303 (2003).

4.4 Thomson Parabola and Time-of-Flight Detector Cross-Calibration Methodology on the ALLS 100 TW Laser-Driven Ion Acceleration Beamline

4.4.1 Abstract

We report on the cross-calibration of Thomson Parabola (TP) and Time-of-Flight (TOF) detectors as particle diagnostics, implemented on the most recent setup of the ALLS 100 TW laser-driven ion acceleration beamline. The Microchannel Plate (MCP) used for particle detection in the TP spectrometer has been calibrated in intensity on the Tandem Van de Graaff accelerator from Université de Montréal. The experimental data points of the scaling factor were obtained by performing a pixel clusters analysis of single proton impacts on the MCP. A semi-empirical model was extrapolated and fitted to the data to apply the calibration also

to higher kinetic energies and to extend it to other ion species. Two TOF lines using diamond detectors, placed at $+6^\circ$ and -9° with respect to the target-normal axis, were benchmarked against the TP spectrometer measurements to determine the field integrals related to its electric and magnetic dispersions. The mean integral proton numbers obtained on the beamline were about 4.1×10^{11} protons/sr with a standard deviation of 15% in the central section of the spectrum around 3 MeV, hence witnessing the high repeatability of the proton bunch generation. The mean maximum energy was of 7.3 ± 0.5 MeV, well in agreement with similar other 100 TW-scale laser facilities, with the best shots reaching 9 MeV and nearly 10^{12} protons/sr. The used particle diagnostics are compatible with the development of a high-repetition rate targetry due to their fast on-line readout, and are therefore a crucial step in the automation of any beamline.

4.4.2 Introduction

The precise measurement of particle characteristics is of the utmost importance when it comes to using particle beams for different applications. The development of particle diagnostics heavily depends on its features, *e.g.* the energy range to be detected, the bunch charge and particle charge state, the intensity of the beam, the beam profile, the required sensibility, resolution, *etc.* For these reasons, a plethora of different diagnostics have been developed and tested in the past for measuring particle beams, taking into consideration the multiple criteria that they need to satisfy[1]. High-intensity, short-pulse laser-driven proton beams, discovered nearly two decades ago[2], and today routinely accelerated with the so-called Target-Normal Sheath Acceleration (TNSA) mechanism[3], have triggered the development of new diagnostics. These laser-driven particle beams have the advantage of being very short in duration (ps at the source)[4], high in current (kA)[5], with a large energy spread and low emittance[6], can be operated at Hz repetition rate[7], and can generate strong ElectroMagnetic Pulses (EMPs) during their production[8]. This requires detectors that are highly versatile, since they need to allow for a quick acquisition time, high dynamic range, wide-range energy response, quick on-line readout and high resistance to EMPs. Combining all these requirements is challenging and not always possible using detectors typically employed in the conventional accelerator community.

Numerous detectors have been developed and tested in the last years to measure laser-accelerated protons. Among the most used detectors are stacks of Radiochromic Film (RCF),

which are polyester sheets with a sensitive layer that darken upon exposure to ionizing radiation. They allow for a discrete spectrum and 2D beam profile reconstruction, but are not suitable for high-repetition rate detection since their readout requires the use of a scanner as a subsequent step after the irradiation to post-process the data. They are also not sensitive to low particle intensities and to low proton energies (< 1 MeV), energy-region where the proton number is significant for laser-driven sources. A faster and more sensitive readout is performed by replacing RCFs with scintillators[9]. Thomson Parabolas (TP) allow for an almost continuous spectrum retrieval in one dimension. The detection of the protons is performed either using Image Plates, semiconductor-based detectors or Microchannel Plates (MCP). The latter two have the advantage of being usable with higher repetition-rate and have therefore been employed in several experiments where a quick analysis was needed (see review articles on TNSA experiments[2,10,11] and references therein). The Time-of-Flight (TOF) technique[12,13] is another well-established method used to retrieve information about the spectrum of the accelerated particles. Recently, TOF delay lines were used employing Chemical Vapor Deposition Diamond Detectors (CVD-DD)[14]. These detectors are characterized by a fast temporal response compared to scintillator-based detectors[15], provide a high energy resolution and are optimized to work in environments highly polluted by EMPs. The compactness of these detectors allows to place several TOF lines at different angles, providing a simultaneous measurement of the accelerated particle beam even within a rather small cone of 20° half-angle, *i.e.* the typical beam aperture of laser-accelerated proton beams. TOF detectors can be employed simultaneously with a Thomson Parabola which, on the other hand, provides information about the ion species but generally is more cumbersome and has a lower energy resolution than TOF. A detector based on acoustic waves (I-BEAT) has been lately proposed to overcome EMP problems and enable high-repetition rate online reconstruction of the absolute depth-dose distribution at application sites[16]. However, this diagnostic has not yet been extensively used by other groups. Among all the above cited diagnostics, MCP-TP and TOF coupled with diamond detectors (DD-TOF) are consolidating as being the most promising and appropriate route to diagnose intense proton beams as obtained on commercially available high-repetition rate laser-systems.

In this study, we present a method to calibrate MCPs used with TP and we use two different Diamond Detectors employed as TOF detectors. The MCP used for the particle detection with the TP spectrometer has been calibrated in intensity on the 2 × 6 MV Tandem Van de Graaff

accelerator from Université de Montréal, to retrieve the particle scaling factor that is needed to determine the particle numbers observed in the MCP-TP spectrometer for protons and carbon ions. We then perform a cross-calibration between the different diagnostics in a real-setting scenario, highlighting benefits and drawbacks: using the maximum proton energies obtained from the CVD-DD we calibrate the relevant parameters of the TP spectrometer required for the kinetic energy retrieval, and using the calibration of the proton numbers obtained on the Tandem accelerator, we validate the calibration of the CVD-DD. The detectors are used to optimize the proton beam generation on the recently installed ALLS 100 TW laser-driven ion acceleration beamline. The work is organized as follows: we first present the methodology for calibrating the response of a MCP using a pixel cluster analysis. The results of the MCP calibration allows us to establish a semi-empirical modeling of the response function, applicable for similar MCP types. In the second section of this paper, we present a description of the setup on the laser-driven ion acceleration beamline, along with a cross-calibration methodology for the calibration of the field integrals to determine the particle's kinetic energy with the TP spectrometer. We describe the implementation of the diagnostics on the Advanced Laser Light Source (ALLS) 100 TW laser-driven ion beamline and its use for maximizing the ion yield.

4.4.3 Absolute MCP Response Calibration

In this section, we detail how to relate the absolute particle number to the intensity of an MCP image as read by the CCD camera, through the measurement of the kinetic energy-dependent scaling factor SF for ions.

4.4.3.1 MCP detection system

We consider the MCP detection system as the interplay between the image acquisition system coupled to the MCP-phosphor assembly. In our setup, we used a double MCP detector in Chevron configuration with 97×79 mm^2 sensitive area, 8° bias angle pores of 25 μm in diameter with 1:40 aspect ratio, providing very high gain (10^6-10^7) suitable for particle counting, acquired from the company *Photonis*[17]. The Chevron MCP is assembled with a P43 phosphor, well-known for its high light yield but slow decay time of 3.2 ms at 1% of maximum intensity. Nevertheless, the detector refreshment time far more than sufficient for the present study and allows for potential repetition rates of hundreds of Hz. The MCP was imaged by an $f/2.4$

objective lens placed at 52 cm behind the phosphor, mounted on a 1.3 MegaPixels Blackfly PoE GigE CCD camera from *FLIR*[18], using a 12-bits dynamic range. A potential difference of -1.5 kV was applied between the entrance (cathode) and the exit (anode) of the MCP to drive the electron avalanche. The output electrons were then accelerated by a +5 kV potential placed on the phosphor screen for additional gain through light conversion.

4.4.3.2 Calibration on Tandem Accelerator

To calibrate the MCP detection system, different proton irradiations were performed on the 2×6 MV Tandem Van de Graaff accelerator from Université de Montréal, using incident proton kinetic energies of $\mathcal{E}_{K,0}$ = 1, 2.5, 5, 7.5, 10 and 11.5 MeV. A 2×2 mm^2 collimated square transverse profile, non-divergent and monoenergetic proton beam was incident on a 1 cm^2, 100 nm thick gold thin foil used as a Rutherford scatterer, placed at 45° with respect to proton incidence. Due to the used kinetic energies and the very small thickness of the foil, the vast majority of incident protons was transmitted through the Au foil and was collected by a Faraday Cup (FC) calibrated in absolute terms for charge monitoring. We used transmitted currents of $\dot{Q} = 0.1$, 1 and 10 nA for each chosen kinetic energy. The transmitted currents were compared to current measurements without gold foil to determine the proton current that was incident on the foil during the acquisitions. This technique allows to compensate *in situ* for the strongly-varying scattering cross-section with kinetic energy within the range of 1-11.5 MeV, and ensured that we had sufficient scattering events collected by the detector. A voltage bias of +200 V was applied on the foil to collect electrons ejected due to physical processes. All irradiations were performed in the dark and under high vacuum (10^{-7} mbar) with the camera acquisition time set to 400 ms. Acquisitions were repeated $N = 10$ times for each irradiation type, to ensure significant particle counting statistics. Hence, for each camera acquisition, incident proton fluences on the gold foil varied in the range of $\phi = (0.7 \text{ - } 21.2) \times 10^{11}$ protons/cm^2. The scattered protons were impacting the MCP's surface, located perpendicularly to the proton incidence direction at a distance of 88 cm from the gold foil, over a 5×4 cm^2 area, giving a particle collection solid angle of 2.6 msr. We performed scattering event simulations with the software *SIMNRA*[19], a Rutherford Backscattering Spectroscopy (RBS) calculation tool used for RBS analysis. This helped to ensure proper matching between simulated and detected scattered proton numbers, as well as to retrieve the kinetic energies of the protons scattered on the MCP, which are used for further analysis. The number of scattered protons hitting the MCP

per camera acquisition varied from a few tens to a few hundreds counts depending on the used kinetic energy, hence allowing to discriminate single particle events over the 20 cm^2 detection surface. A schematic diagram of the experimental setup is shown in Figure 4.7.

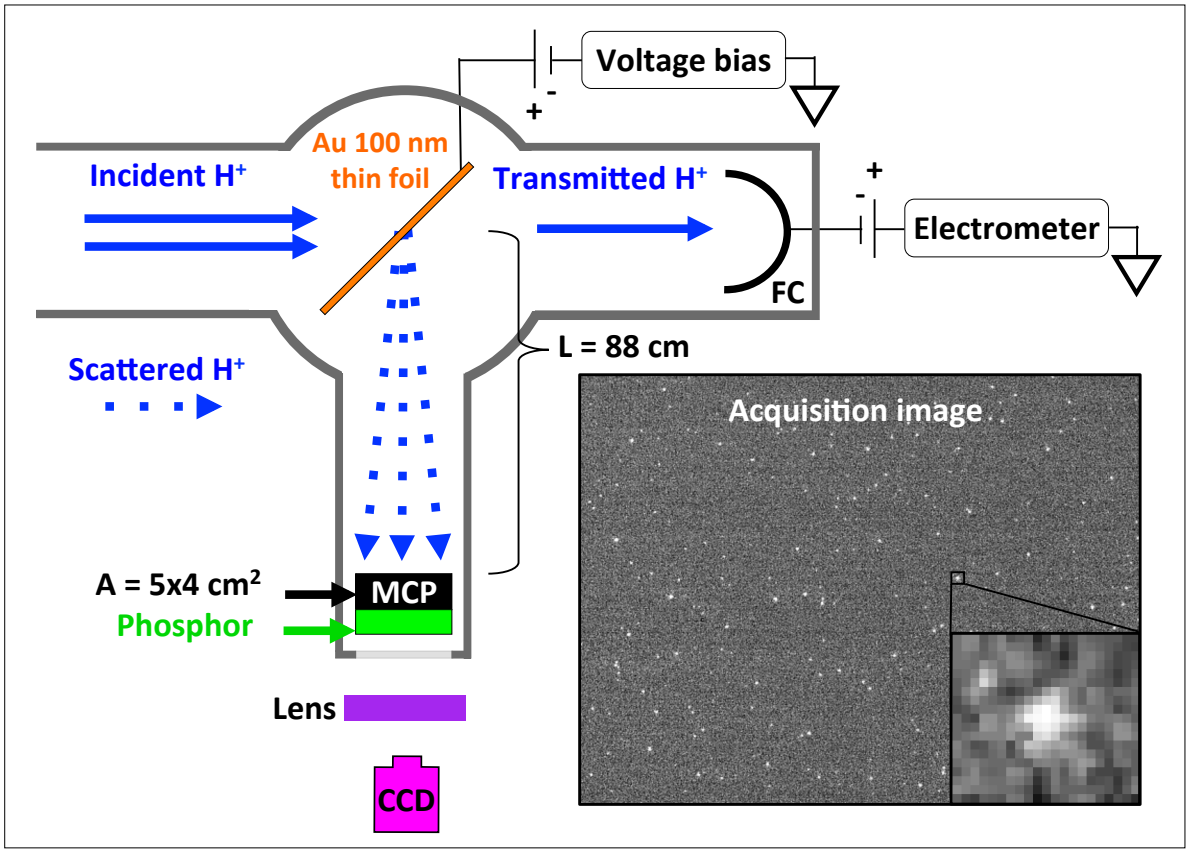

FIGURE 4.7: Experimental setup for measuring scattered proton irradiations on the Tandem particle accelerator from Université de Montréal. A 2×2 mm^2 collimated square transverse profile, non-divergent and monoenergetic proton beam is incident on a gold thin foil acting as a Rutherford scatterer. Most protons are transmitted through the gold foil and are collected by a Faraday Cup for fluence monitoring, whereas a fraction of the scattered protons are incident on the MCP detection system for calibration. The inset is an acquisition image of the phosphor by the CCD camera.

4.4.3.3 Pixel clustering analysis

In order to analyze the intensities of the pixel clusters on the image recording the MCP irradiated using monoenergetic protons, as shown in the inset of Figure 4.7, a numerical method was developed based on the work of Baumann *et al.* (2018)[20]. Since the number of scattered protons hitting the detector is on the order of a few tens to a few hundreds protons per camera acquisition, the probability of having two protons hitting the same microchannel within this timeframe is sufficiently low (probability $< 5 \times 10^{-4}$), such that we can reasonably assume that

the pixel clusters observed on the acquisition image are cones of light emitted by the phosphor from single proton events. The spatial resolution for this kind of MCP detection system is limited by the Point Spread Function (PSF) of the phosphor, which generates cones of light spatially larger than the diameter of a microchannel (25 μm) and of the pixel size of the image acquisition system which, using a lens magnification, relays a surface size on the MCP of 90 μm onto a single CCD pixel. In the X-ray photon counting method using pixelated semiconductor X-ray detectors, it is possible that one X-ray photon produces a single pixel event with no charge leakage to the surrounding pixels. Here it is necessary to analyze the pixel intensity distribution for each cluster produced by independent protons. Therefore, this issue prevents us from using single pixel events for histogram reconstruction. The intensity distributions were evaluated in the filtered domain using equation (4.9):

$$I_{\text{filt}}(i,j) = [I(i,j) - I_{\text{blank}}(i,j)] \star \frac{1}{2\pi} e^{-\frac{i^2+j^2}{2}} \; > \; T_{\text{noise}} \tag{4.9}$$

where $I(i,j)$ is the raw acquisition image evaluated at the pixel coordinates (i,j), $I_{\text{blank}}(i,j)$ is a blank image acquired without proton current (*i.e.* $\dot{Q}$=0), $\star$ denotes the cross-correlation operator and T_{noise} is an intensity threshold used for background suppression. A 2D cross-correlation with a normalized Gaussian kernel with unitary standard deviation is performed as a noise reduction technique and to enhance the cluster intensities with respect to the background, hence increasing the signal-to-noise ratio (SNR) and thus facilitating the search for the local maximum at each pixel cluster. The intensity threshold T_{noise} is defined empirically as the minimum intensity value such that $I_{\text{filt}}(i,j)$ encompasses only the pixel clusters coming from proton hits, and is kept constant for all images throughout the analysis. The retrieval of the mean pixel intensity is then based on the *Clustering* method described in Baumann *et al.* (2018)[20]. The method consists in considering the first neighbors around the maximum pixel position within a cluster (*i.e.* a 3×3 array), and then taking the average value of the pixels above T_{noise}. This method, as opposed to other techniques like *4-Pix* (*i.e.* 2×2 array), *Cross Shape* or *Nearest Neighbors* also shown in Baumann *et al.* (2018)[20], allows to consider a general shape that the pixel cluster might have, hence not limiting the search to a particular cluster shape which could induce a misestimation of the mean intensity value. The proton scaling factor $\text{SF}_{\text{protons}}$ is obtained as follows: We produce histograms with the cluster intensity (x-axis) and its occurrence (y-axis). We cumulate this process over $N = 10$ images to ensure sufficient particle counting statistics. $\text{SF}_{\text{protons}}$ is calculated by taking the mean cluster intensity of the

distribution (x-axis). The total standard deviation of $\mathrm{SF}_{\mathrm{protons}}$, σ_{SF}, obtained by independent observations from each image acquisition is given by equation (4.10).

$$\sigma_{\mathrm{SF}} = \sqrt{\left[\sum_{n=1}^{n=N}\left(\frac{1}{\sigma_n^2}\right)\right]^{-1}} \tag{4.10}$$

4.4.3.4 Experimental results

In this section, we detail the experimental results obtained on the Tandem accelerator and the semi-empirical modeling of the scaling factor SF function. Based on several previous works[21-25], we have modeled the intensity response of the MCP, $\mathcal{R}_{\mathrm{MCP}}$, for MeV-ranged ions with the following equation (4.11), as proposed by Prasad *et al.* (2010)[26] and Jeong *et al.* (2016)[27]:

$$\mathcal{R}_{\mathrm{MCP}}(\mathcal{E}_{\mathrm{K},0}) \propto \int_0^l \left[\frac{d\mathcal{E}_{\mathrm{K}}}{dz}\right]_{\mathrm{e}} (\mathcal{E}_{\mathrm{K},0}, z)\ e^{-\frac{z}{l_g}}\,\mathrm{dz} \tag{4.11}$$

In equation (4.11), $\left[\frac{d\mathcal{E}_{\mathrm{K}}}{dz}\right]_{\mathrm{e}}$ is the electronic stopping power for a particular ion species in a given material, $e^{-\frac{z}{l_{\mathrm{g}}}}$ models the MCP's exponential gain variation with microchannel penetration depth z, l_{g} is the characteristic gain length, l is the microchannel length and $\mathcal{E}_{\mathrm{K},0}$ is the initial kinetic energy of the particle incident on the detector. Indeed, an energy deposition through ion impact ionization at the entrance of a microchannel will generate a stronger electron avalanche than farther in the channel, justifying the choice of the exponential gain weight. The output response is thus modeled as the sum over the entire channel length of all incremental gain-weighted energy depositions as a function of depth. The amplitude scaling of the gain from the MCP detection system is then obtained by a linear fitting to scale the MCP response function $\mathcal{R}_{\mathrm{MCP}}$ to the particle scaling factor SF as measured by CCD camera counts per incident particle, estimated by equation (4.12).

$$\mathrm{SF} = a \cdot \mathcal{R}_{\mathrm{MCP}} + b \tag{4.12}$$

We note that a, b and l_{g} are characterized merely by the MCP detection system and are therefore particle-independent, whereas the particle dependence is solely considered in the electronic stopping power. For the modeling of experimental data, we have used the proton electronic stopping power in leaded-glass, which is the main material of the microchannels, as computed by the software *SRIM*[28]. Using the experimental data points for the proton scaling

factor $SF_{protons}$, we have iteratively varied l_g and subsequently fitted a and b, until best match was achieved by minimizing the Sum of Squared Errors (SSE) as a cost function over the sampled kinetic energy data points. The results of this best match modeling are shown in Figure

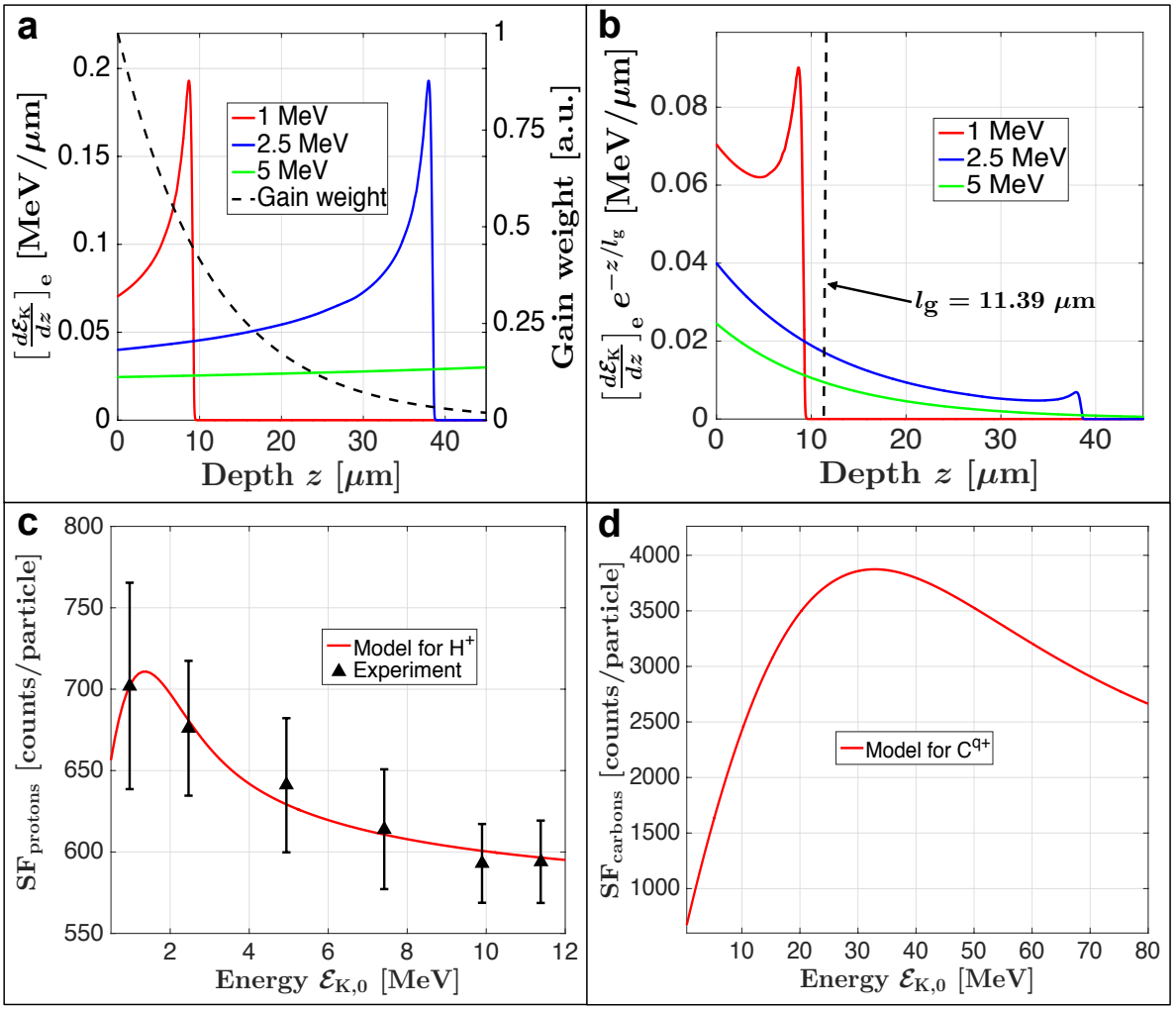

FIGURE 4.8: MCP detection system experimental response and semi-empirical modeling. (a) Proton electronic stopping power in leaded-glass as a function of depth (Bragg peak) for different initial kinetic energies of $\mathcal{E}_{K,0}$ = 1 (full red curve), 2.5 (full blue curve) and 5 MeV (full green curve), along with the best-matching exponential gain weight as a function of depth z (dashed black curve), obtained for l_g = 11.39 μm. (b) Gain-weighted electronic stopping power variation with depth. (c) Experimental proton scaling factor $SF_{protons}$ (black triangles) and and best fit model (full red curve), with $R^2 = 0.976$. In the presented case, the best fit is obtained for $a = 221.7$ counts/particle/MeV and $b = 563.6$ counts/particle. (d) Extrapolation of the best fit model for carbon ions.

4.8. At first, it is possible to observe, in Figure 4.8.a, the numerically generated Bragg peaks for three incident protons energies of 1, 2.5 and 5 MeV, overlaid by a plot of the exponential gain weight $e^{-\frac{z}{l_g}}$ that provides the best matching of the model with the experimental data (see right scale in Figure 4.8.a). We find a fit optimum for l_g = 11.39 μm, along with the linear scaling

parameters of $a = 221.7$ counts/particle/MeV and $b = 563.6$ counts/particle. For low-energy protons, for instance 1 MeV (full red curve in Figure 4.8.a), the entire energy deposition of the particle occurs at the front surface of the MCP within the first few microns, where the gain is highest. As the incident kinetic energy increases, for instance with 2.5 and 5 MeV protons (full blue and green curves in Figure 4.8.a respectively), the position of the Bragg peak shifts to after the high gain zone, where we consider the region located before l_g as the high gain zone. This decreases the gain-weighted energy deposition variation with depth, as shown in Figure 4.8.b. The integral of the curves presented in Figure 4.8.b for different kinetic energies $\mathcal{E}_{K,0}$, generates the output response variation with energy. This response curve $\mathcal{R}_{MCP}(\mathcal{E}_{K,0})$ is then linearly fitted to scale to the experimental data points, and allows retrieving the parameters a and b in equation (4.12). The result of this scaling (full red curve), together with the experimental values (black triangles), is presented in Figure 4.8.c. We show the model for protons (full red curve) along with the experimental data points (black triangles) obtained through the pixel clusters analysis described above. It is possible to note that the response function reaches its maximum when the travel range of protons $R(\mathcal{E}_{K,0})$ is approximately equal to l_g, occurring at $\mathcal{E}_{K,0} = 1.4$ MeV. This particular initial energy maximizes the overlap between the exponential gain weight and the stopping power variation with depth x. For $R(\mathcal{E}_{K,0}) < l_g$, the gain is high but a smaller amount of energy is deposited in the detector, explaining the continuously increasing response with increasing proton energy up to 1.4 MeV, in agreement with what is observed in the literature for keV-ranged proton detection using MCPs[29,30]. For $R(\mathcal{E}_{K,0}) > l_g$, the response decreases since most of the particle's energy is deposited farther in the microchannel, where the gain is lower due to a shorter distance available for electron avalanche amplification. This effect is in agreement with previous works on MeV-ranged proton[26,27,31]. To retrieve the scaling factor for carbon ions, we use the same parameters l_g, a and b, as obtained for the best fit of protons. We then implement the calculations using the electronic stopping power of carbon ions in leaded-glass, as obtained from *SRIM*, to generate the scaling factor function for carbon ions, as shown in Figure 4.8.d. As is shown experimentally also in the work of Jeong *et al.* (2016)[27], the response function for carbon ions is charge state-independent for this particular MeV range of energies since their Bragg peaks are positioned very close to the surface in the first few microns, hence making the response mostly energy-dependent. It is possible to observe in Figure 4.8.d that the model for carbon ions has the same shape as for protons, but with its peak shifted at around 32 MeV, and also scaled up in intensity because the stopping power of carbon ions at the Bragg peak is much higher than for protons ($\sim 13\times$). We would

like to stress that this methodology can be applied for other MCP detectors. In order to retrieve the response function, it is however necessary to measure at least three energy points, such as to define completely and univocally equation (4.12). To produce better results it is advisable to use more data points, in particular if the working energies are around the peak of the curve.

4.4.4 The Laser-Driven Ion Acceleration Beamline on ALLS 100 TW

4.4.4.1 Experimental setup

We tested the absolute intensity calibration of our MCP-TP on the ALLS 100 TW ion acceleration beamline located at the Institut national de la recherche scientifique (INRS) in Varennes close to Montréal, Canada. The Ti:Sapphire ALLS 100 TW laser[32], operates at repetition rate of 2.5 Hz at a central wavelength of $\lambda_0 = 800$ nm and comprises a double-CPA[33] system delivering laser pulses with an energy on target of $\mathcal{E}_L = 2$ J, in a pulse duration of $\tau_L = 20$ fs. Using an $f/3$ off-axis parabola, the 100 mm beam size (at e^{-2}) is focused down to a spot size of $w_{FWHM} = 5$ μm, leading to a peak intensity of $I_0 \sim 1.3 \times 10^{20}$ W/cm^2. The laser beamline benefits of a cross-wave polarizer (XPW) as part of a beam cleaning technique before injecting in the second CPA, which leads to an Amplified Spontaneous Emission (ASE) pre-pulse contrast of $< 10^{-10}$ at -100 ps before the main pulse, along with a steep power rise with contrast of $< 10^{-6}$ at -3 ps. The p-polarized laser pulses are incident with an angle 20° with respect to target-normal on thin copper foils with thickness of 5 μm for performing laser-driven ion acceleration in the TNSA regime. The targets are mounted on a multi-target holder allowing for 16 shots per pumping cycle. The targets are first pre-aligned on a target alignment bench outside the interaction chamber, and subsequently undergo micrometric precision alignment under vacuum using shadowgraphic imaging in the transverse plane, along with a target positioning interferometer[34]. The accelerated ions are monitored by three particle diagnostics, one Thomson Parabola (TP) spectrometer placed at 0° with respect to target-normal axis along with two TOF diagnostic lines, one positioned at +6° and the other at -9°. A schematic diagram of the setup is shown in Figure 4.9.a. Concerning the geometrical layout of the TP shown in Figure 4.9.a, the ions are first entering through a 500 μm pinhole placed 1.8 m away from the interaction point (*i.e.* collection solid angle of 6×10^{-8} sr) before passing in between two 6 cm-long copper electrodes which are separated by 2 cm and operated at $\pm$7.5 kV. The particles then go through a 0.46 T, 10 cm-long magnetic field generated by permanent magnets,

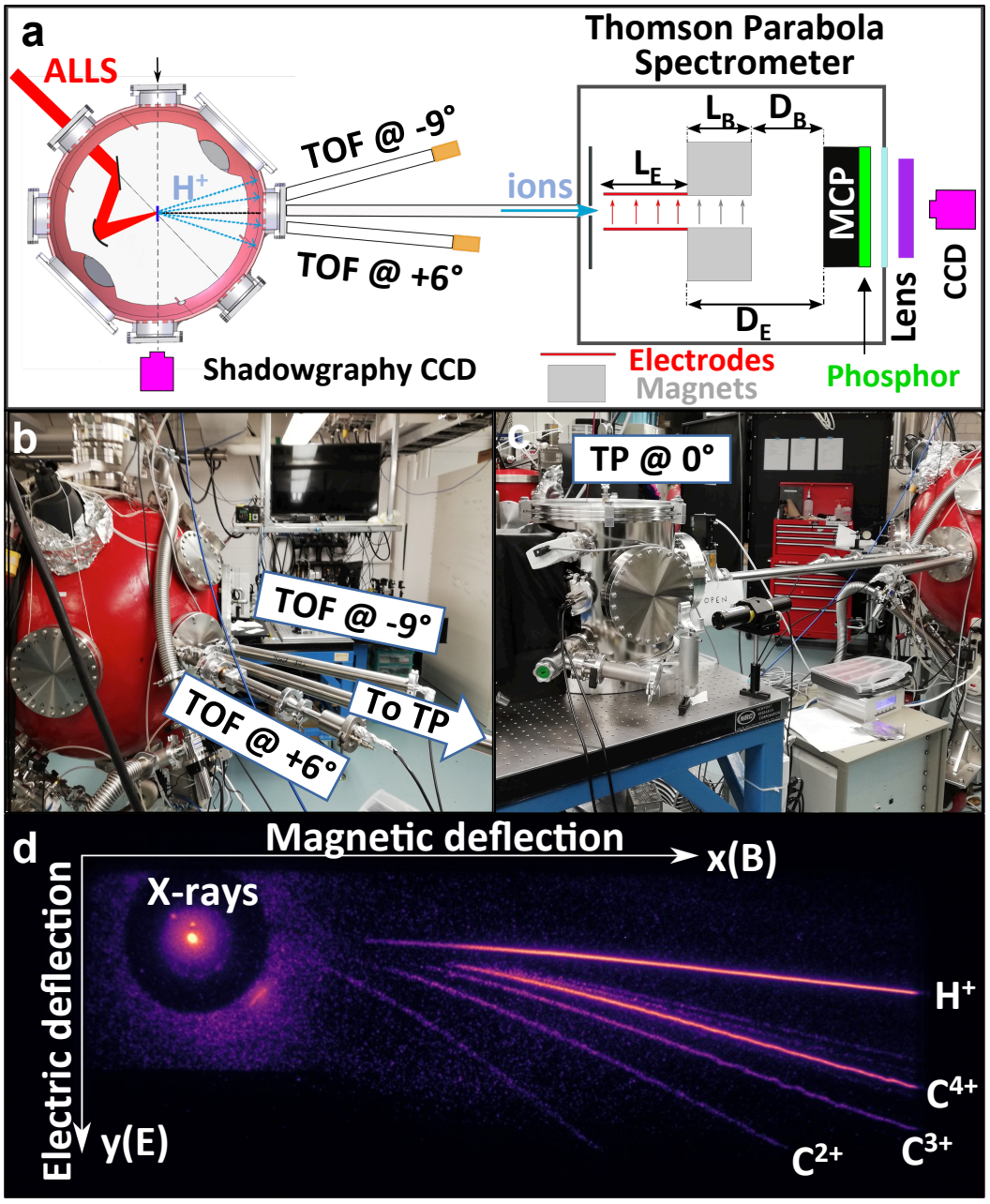

FIGURE 4.9: (a) Experimental chamber layout and the TP spectrometer layout. (b) Picture of the experimental chamber and (c) a view from the rear side of TP spectrometer experimental chamber. (d) A typical image obtained from the TP spectrometer. The other unlabeled parabola traces are the other carbon species which were not considered in the analysis of the present study, due to their too low intensity, as well as for better visualization purposes. In particular the one on the left of C^{2+} is C^{+}, along with the two above C^{4+} being C^{5+} and C^{6+}.

before spatially dispersing for 7.5 cm, after which they are detected by the aforementioned MCP detection system that acquires a laser-triggered image of the different particle parabolas (see Figure 4.9.d). The TOF lines are equipped with CVD-DD[14]. Both diamond detectors have an active layer of thickness 50 μm grown on a commercial $4 \times 4 \times 0.5$ mm High Pressure

High Temperature (HPHT) substrate, but are presenting two different electrode layouts. The interdigit, or planar detector, placed at -9° has superficial interdigital Aluminum contacts of 20 μm width and 20 μm spacing[35,36]. The sandwich, or transverse detector, placed at $+6^\circ$ has a layered structure consisting of a metal electrode deposited on the intrinsic diamond (*i.e.* the active volume of the detector) which in turn is in contact with a p-doped diamond[37]. The two have different sensitivities for different energy ranges, the planar diamond is more suitable for measurements of moderate-low energy protons and is characterized by a high temporal resolution due to the reduced distance between the electrodes. The transverse configuration is slightly slower but guarantees a quasi-uniform electric field throughout the whole thickness of the detector, providing a high Charge Collection Efficiency (CCE) for a wider energy range. Due to the different sensitivities for distinct energy range, the use of two types of diamond detectors ensured that we did not produce any systematic error in the estimation of the proton maximum energy nor of the proton yield. Since CVD-DD are only sensitive to the energy deposited in their active layer, they are not able to distinguish different ion species. As we are mainly interested in retrieving proton spectra, both the detectors were supplied with a 10 μm aluminum filter which provides a partial shielding from heavier ion contribution at the expense of loosing information on low-energy protons. From simulations performed using *SRIM*, it was possible to retrieve the maximum energies stopped by this filter which are: 750 keV for protons, 11.45 MeV for carbon ions, 13.7 MeV for nitrogen and 15.84 MeV for oxygen ions which are the main ion species accelerated during the interaction. Moreover, the filter provides a cut-off energy of $\simeq$ 45 MeV for copper ions coming from the bulk target. To have an accurate estimation of the actual temporal response of the detectors, both detectors were calibrated by exposing them to 5.486 MeV α-particles produced by the radioactive decay of Americium[38]. The signal collected by the CVD-DD was sent to a *Tektronix* DPO 7104 scope (1 GHz bandwidth and 5 Gsamples/s sampling rate) through 15 m long calibrated RG 223 cables. The transmission line was characterized by measuring its total S_{21} scattering parameter using the Agilent E8364B Network Analyzer. The employment of long cables, together with the optimized shielding of the detectors itself[35,39,40], provided a good mitigation of the effects of EMPs that are generated during the laser-matter interaction[41]. These EMPs, which can reach orders of hundreds of kV/m, can affect all the electronic devices placed nearby the experimental chamber. The proton spectra recorded by the diamond detectors located at $+6^\circ$ and -9° were computed following the procedure described in Salvadori *et al.* (2020)[42], while the TP

spectrometer allowed to simultaneously obtain the ions spectra at 0°. The particle number estimation retrieved from the parabolic traces shown in Figure 4.9.d was obtained with the pixel intensity calibration of the MCP detection system performed on the Tandem accelerator from Université de Montréal (see section 4.4.3.2).

4.4.4.2 Cross-calibration of the field integrals

In order to properly analyze the images obtained on the MCP when used as detector inside the TP spectrometer, it is necessary to follow correctly the traces of the trajectories belonging to the different ions traveling with different energies inside a magnetic and electric field. The magnetic and electric fields might not be completely uniform during the particle's trajectory, it is therefore better to introduce two field integrals I_B and I_E, defined by equations (4.13) and (4.14). As shown in the work of Ducret *et al.* (2018)[43], characterizing the field integrals allows to bring a more general representation of the electric $\boldsymbol{E} = E_0(z)\,\hat{y}$ and magnetic $\boldsymbol{B} = B_0(z)\,\hat{y}$ fields used for TP spectrometers, avoiding the need to assume top-hat field distributions along the longitudinal axis z. The values of I_B and I_E can further be inserted in the well-known non-relativistic, non-paraxial dispersion equations for the solution of charged-particle kinematics traversing static electric and magnetic fields for the case of Thomson Parabolas, as shown by equations (4.15) and (4.16).

$$I_B = \int_0^{L_B} B_0(z)\,\mathrm{d}z = \overline{B}_0 \cdot L_B \tag{4.13}$$

$$I_E = \int_0^{L_E} E_0(z)\,\mathrm{d}z = \overline{E}_0 \cdot L_E \tag{4.14}$$

$$x(\mathcal{E}_\mathrm{K}, I_B) = \frac{\sqrt{2\mathcal{E}_\mathrm{K} m}L_B}{qI_B}\left\{\cos\left[\arcsin\left(\frac{qI_B}{\sqrt{2\mathcal{E}_\mathrm{K} m}}\right)\right] - 1\right\} - D_B \tan\left[\arcsin\left(\frac{qI_B}{\sqrt{2\mathcal{E}_\mathrm{K} m}}\right)\right] \tag{4.15}$$

$$y(\mathcal{E}_\mathrm{K}, I_E) = \frac{qI_E}{2\mathcal{E}_\mathrm{K}}\left(\frac{L_E}{2} + D_E\right) \tag{4.16}$$

In equations (4.15) and (4.16), q, m and $\mathcal{E}_\mathrm{K}$ are the particle-dependent parameters, namely its charge, mass and kinetic energy respectively. The field-related distances L_B, D_B, L_E and D_E are respectively the magnetic field length, the magnetic drift distance, the electric field length and the electric drift distance. All of the aforementioned field-related distances are measured experimentally, and hence are known values. Therefore, a proper calibration of the field integrals I_B and I_E allows to completely define the system in terms of the particle's kinetic energy

$\mathcal{E}_K$ and charge-to-mass ratio q/m. Using the results and formulas above, we have all tools at disposal to absolutely measure laser-accelerated protons in numbers and in kinetic energy using a MCP-TP system. In order to cross-calibrate the above mentioned particle diagnostics, we adopted the following methodology:

(i) The magnetic field B_0 was measured with a calibrated gaussmeter. We used L_B as a first approximation to determine I_B.

(ii) We move the TOF detector temporarily on the 0° axis. Over a statistically significant amount of laser shots, we measure the maximum proton energy.

(iii) After placing back the TOF and the TP to their initial positions, we adjust I_B until we get a good match between the two maximum energies obtained on the 0° axis by the TOF and TP. The maximum proton energy ratios at different angles (*i.e.* energy at +6° vs 0°) should be in agreement with typical TNSA-based proton beam values found in literature[44,45].

(iv) Both the voltage across the electrodes ΔV and the electrode's separation distance d including their length L_E are measured and used as a first approximation to determine I_E.

(v) For a given ion species (protons for instance), I_E is incremented until best match is achieved with the theoretical curves from equations (4.15) and (4.16) and the experimental positions on the detector.

(vi) As a final verification, the theoretical curves can be generated for other ion species (carbon ions for instance) using (4.15) and (4.16), and should match with experimental positions on the detector. This confirms the correct parameters I_B and I_E.

One should note that the above methodology can be applied if there is at least one TOF line as a complementary particle diagnostics to the TP spectrometer. This particle diagnostic configuration allows using detectors located away from the 0° axis to retrieve indirectly the characteristics of the beam on the central axis.

4.4.4.3 Experimental results

Since the TOF technique coupled with diamond detectors ensures an accurate measurement of the maximum proton energy[42,46,47], this technique was used to validate the kinetic energy estimations obtained by the TP spectrometer using the aforementioned cross-calibration methodology of the field integrals (see Section 4.4.4.2). In Figure 4.10.a is shown a comparison between the maximum proton energy estimated by the TP and the two TOF lines for different shots performed in similar conditions (*i.e.* using the same laser pulse energy and copper 5 μm targets). The mean maximum energy of the selected shots is of 6.6 $\pm$ 0.9 MeV for the TP at 0°, 5.9 $\pm$ 0.8 MeV for the TOF at +6° and 4.9 $\pm$ 0.7 MeV for the TOF at -9°. It is possible to observe a good agreement between all the three diagnostics which respond similarly for each shot. All shots exhibit small shot-to-shot fluctuations with a standard deviation on the maximum energy of 14% for the three diagnostics, indicating a good repeatability. In Figure 4.10.b, the proton spectrum obtained with the TP spectrometer during a typical shot is shown together with the spectra provided by both TOF lines. The lower energy limit in the TOF spectra is determined by the growing tolerances due to the presence of the filter that produce higher uncertainty for energies close to its proton energy cut-off. For higher energies two different ranges have to be taken into account. Up to 3 MeV, the behavior of the two diamond detectors is well characterized[35,47] since protons are completely stopped inside the active thickness of the detector, depositing all their kinetic energy. Above 3 MeV, a correction factor has to be introduced to properly estimate the proton numbers. The uniform response of the diamond detector in transverse configuration (*i.e.* $+6°$) allows to easily take this into account[46]. On the other hand, the energy-dependent charge collection efficiency of the planar configuration (*i.e.* $-9°$)[42,47] does not allow to follow the same procedure, and hence a new methodology has to be implemented if a calibration with high-energy proton is not available, which will be the subject of a subsequent study. Consequently, the spectrum estimated by the TOF placed at $-9°$ results to be underestimated for energies higher than 3 MeV (dashed green line in Figure 4.10.b), whereas a reliable behavior is ensured for proton energies below 3 MeV (full green line in Figure 4.10.b). Nevertheless, the spectra obtained by the TP spectrometer and both TOF lines are exhibiting a very typical TNSA-like shape, with the ratio of their cutoff energies in agreement with other reported TNSA divergences in the literature[44,45]. Concerning Figure 4.10.c, we note an excellent agreement between the analytical curves, generated using equations (4.15) and (4.16) that were calibrated for their field integrals, and the experimental TP data points for different ion

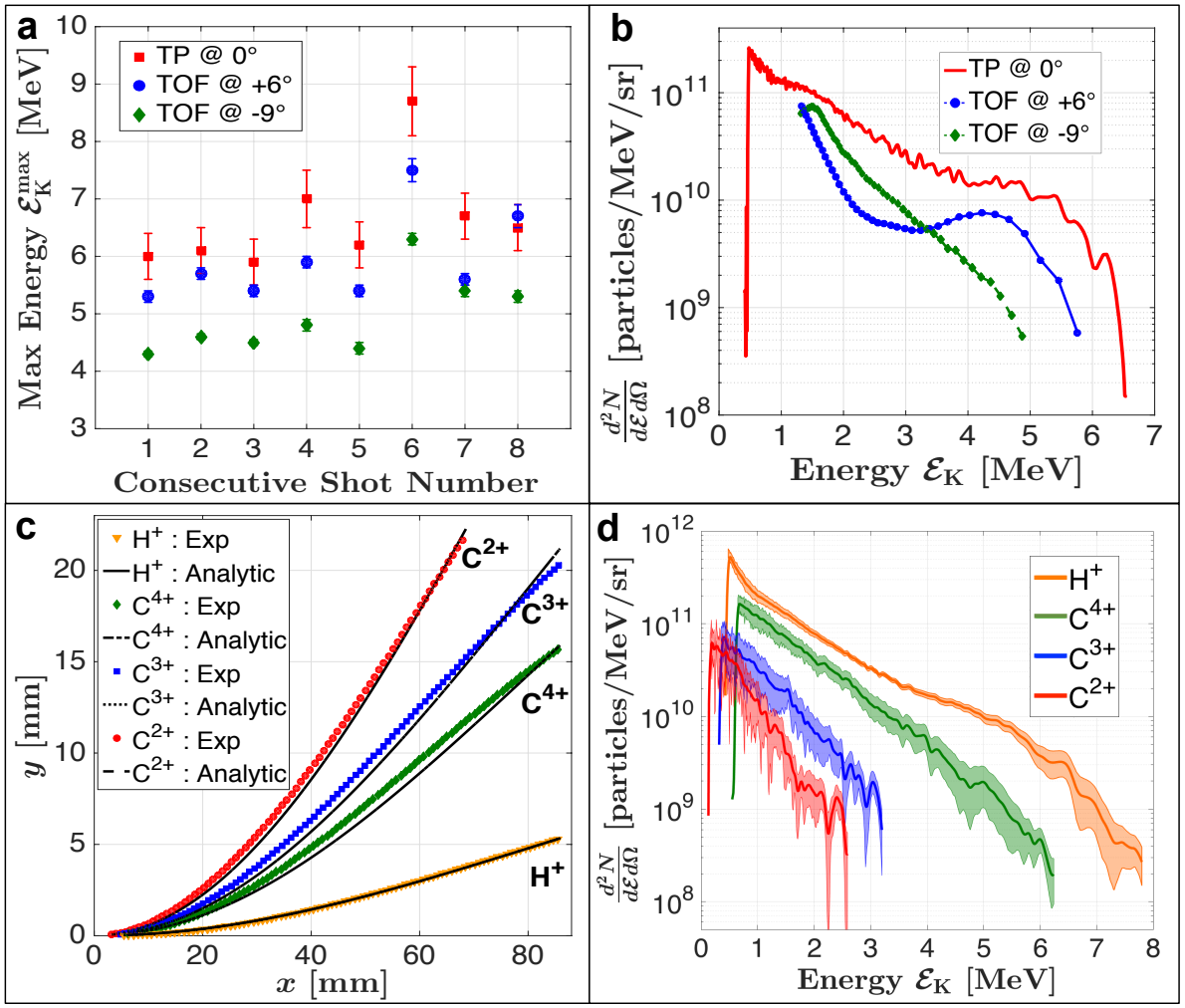

FIGURE 4.10: (a) Maximum proton energies at different angles obtained by the three used diagnostics: The two TOF lines placed at -9° and +6°, as well as the TP spectrometer placed at 0°. All the data are obtained with shots performed on 5 μm copper targets. Measurement were performed over 8 shots during which all diagnostics were operational. (b) Comparison among the spectra obtained by the aforementioned diagnostics for a typical shot. (c) Analytical parabolas (lines) calculated from equations (4.15) and (4.16), along with experimental points (markers) obtained with physical distances measures on the MCP detection system. (d) Spectra obtained for different ion species (H^+ in orange, C^{4+} in green, C^{3+} in blue and C^{2+} in red) from the TP spectrometer. Each spectrum is an average of ten shots, and the uncertainties are calculated using the standard error of the mean.The low-energy cutoff corresponds to the lowest kinetic energy detectable for each ion species, and only particle numbers above the background floor are displayed.

species as obtained by the MCP detection system. The matching is increasingly better with lower charge state, being best for protons, then for C^{2+}, *etc.* The divergence from the analytical equations is due to the fringe fields at the extremities of the magnets and the electrodes, which bring higher-order field components to deflections. Another source of error comes from the fact

that equations (4.15) and (4.16) are considering $\boldsymbol{E}$ and $\boldsymbol{B}$ fields that are invariant in the transverse plane, hence only varying along the longitudinal axis z. This changes the amplitude of the dispersion, but is of negligible importance compared to the effects of the fringe fields, since its effect can be incorporated within the calibration of the field integrals. Nevertheless, due to the relatively compact TP setup (*i.e.* small dispersion distances D_B and D_E), the types of errors are minimized and the effect of the zero-order field components are dominant, as can be noted with the strong agreement for the proton parabola over a large magnetic deflection distance of $x = 85$ mm. The very good agreement with the analytical equations along with the consistency observed within the three diagnostics validate the method we chose to cross-calibrate the TP spectrometer using the information retrieved by the two TOF lines. In Figure 4.10.d, we present the mean particle spectra for four ion species (H^+, C^{4+}, C^{3+} and C^{2+}), which are averaged over 10 shots and presented with their respective particle number uncertainty using the standard error of the mean. Similarly to the observations regarding the maximum energy in Figure 4.10.a, we can again note the high proton beam stability (orange curve in Figure 4.10.d) compared to similar laser-driven ion acceleration experiments, with a standard deviation of 15% for the amount of particles in its central section around 3 MeV. This is due to both the very small shot-to-shot fluctuations of the laser (2.5% RMS fluctuations in laser pulse energy) and the repeatable, high-precision (< 10 μm) alignment of the targets. The mean integrated proton number over the entire spectrum is in excess of 4.1×10^{11} particles/sr, as there is a substantial amount of undetected protons below the lower energy detection threshold of 0.4 MeV. The mean maximum energy is around 7.3 ± 0.5 MeV. Concerning the other presented ion species, the most favorably accelerated is C^{4+} for this laser energy value, as is clearly observed in Figures 4.9.d and Figures 4.10.d. The mean integrated number of C^{4+} ions within the spectra is in excess of 1.7×10^{11} particles/sr, about 2.4$\times$ lower than protons, with a standard deviation in its central section of 55%. The mean maximum energy for C^{4+} is around 6.2 ± 0.4 MeV. The two other presented carbon ion species (C^{3+} and C^{2+}) appear in much smaller quantities, with a mean integrated number of particles in the first half of 10^{10} particles/sr, an order of magnitude lower than protons, with their maximum energies in the range of (2.2 - 3.2) MeV.

4.4.5 Discussion

4.4.5.1 Particle number scaling factor

A proper characterization of the MCP's response is essential for the retrieval of the particle number scaling factor. By comparing the response function for MeV-range ions obtained in this study and the one from the work of Jeong *et al.* (2016)[27], we can first note a good agreement in terms of functional shape, but also with regards to their peak positions. For instance, the modeling of Jeong *et al.* (2016)[27] yields a peak of the response around 4 MeV compared to our 1.4 MeV for protons, and 24 MeV compared to our 32 MeV for carbon ions. Several factors explain these differences, the dominant factors are the different MCP characteristics (pore diameter, channel length and pitch) along with the use of a single MCP compared to Chevron MCP used in the present study. This yields to different and very detector-specific responses. Moreover, their modeling includes an angular variation of the response to correct for the different particle incidences at different energies. Their absolute particle number calibration was obtained *in situ* with a TP spectrometer and CR-39 detectors, rather than on a conventional particle accelerator as proposed here. The geometry of the presented setup allowed to neglect the angular variation of the response function since the collection solid angle was negligibly small (2.6 msr) to account for, as shown recently by the works of Fehre *et al.* (2018)[48] and Blase *et al.* (2017)[49]. Nevertheless, the peak positions of the response functions for protons and carbons obtained in the present study are still in the same range of energies (few MeV) as in the work of Jeong *et al.* (2016)[27]. This can be explained by the fact that both MCPs come from the same company and therefore the global response is similar. Concerning the work of Harres *et al.* (2008)[31], the presented response function follows the same trend as the one shown here, in particular the function has a decreasing scaling factor with increasing proton energy above 2 MeV. Moreover, the amplitude of the scaling factor, *i.e.* the number of counts per particle, is similar to ours since they also use a double MCP in Chevron configuration yielding a similar output gain. The modeling presented in the work of Harres *et al.* (2008)[31] considers the surface (*i.e.* $z = 0$ μm) electronic stopping power in Inconel for protons above 2 MeV, hence does not include the variation of the stopping power with depth in the channel. This explains why there is no observation of a peak in their scaling factor function and also prevents to properly model carbon ions as is mentioned in their work. In light of these observations, it appears very important to properly model the response of an MCP detection system using the full stopping

power dependence with depth (the full Bragg peak) in the correct material (leaded-glass here). As shown in several instances in the literature and again in the present study, approximating the depth-dependence of the MCP gain through a channel using an exponential behavior gives satisfying results.

Another important observation concerns the position of the peak at 1.4 MeV displayed in Figure 4.8.c for the scaling factor of protons. By looking carefully at Figure 4.9.d, it is possible to note on the proton parabola that there is a "high signal region" (hot spot) with more intense pixel intensities located around the middle of the parabola/detector. The position of this high signal region does not move from shot to shot, and since proton numbers are decreasing with increasing kinetic energy, it means that this effect is not related to particle numbers but rather to a higher response of the MCP at this particular proton energy. The proton kinetic energy related to this high signal region is about 1.5 MeV, which can also be noted as a small bump in the proton signal of Figure 4.10.b (red full line). The fact that the high signal region is located around the peak of the scaling factor function supports the correctness of our particle energy cross-calibration. Conversely, no high signal region is observed on the carbon parabolas of the MCP, since the carbon kinetic energies generated during the acceleration process are lower than the peak position of its scaling factor function located around 32 MeV. In the energy range of the 0-10 MeV, as observed in the spectra, the response function is still ramping up monotonously (see Figure 4.8.d).

4.4.5.2 Performance of the beamline

The mean proton number and their maximum kinetic energy obtained on our facility (Figure 4.10.d) are in agreement with what is found on other 100 TW-range laser facilities[50-55]. These facilities are reporting best proton numbers (typically obtained on the 0° axis) in the range of 10^{11} protons/sr, along with maximum kinetic energies in the range of 3-17 MeV depending on the used target thickness and the use of pre-pulse contrast enhancement techniques, in agreement with the 4.1×10^{11} protons/sr and 7.3 ± 0.5 MeV reported here as mean integral proton number and mean maximum kinetic energy, respectively. The mean ratios of maximum kinetic energies obtained at $+6^\circ$ and -9° with respect to 0° are of 0.92 ± 0.08 and 0.75 ± 0.08, respectively. These values are well in agreement with experimental measurements of TNSA proton beams reported in literature[44,45], although slightly lower of 6% and 12%, respectively for $+6^\circ$ and -9°. This discrepancy is due to several factors, namely the laser pulse energy, the

pulse duration, the numerical aperture of the off-axis parabola used and the target thickness, which will all together influence the divergence of the proton source. It is important to note that our laser configuration was not including a deformable mirror which could have further improved the performance of the beamline. Best shots are reaching nearly 10^{12} protons/sr and 9 MeV on the 0° axis with our 5 μm thick targets. It is likely that thinner targets (*e.g.* 1 μm-thick targets, not available during this experiment) might favor an enhanced proton yield and higher maximum energy. However, we note a high reliability of the beamline, providing a standard deviation of 15% both in proton numbers in the central energy section and maximum energy. In addition, having one TOF line on each side of the 0° line allows to determine after the shot if the target was tilted in the laser's plane of incidence. This allows to easily discard bad shots or to improve the target alignment system, which further enhances the beam reliability. Moreover, having both TOF disposed at different angles allows to have a better estimation of the beam divergence. All these criteria are extremely important when it comes to using laser-driven beamlines to reliably test numerous applications, such a radiation stress testing[56], ultrafast nanocrystal generation[57], radiation-induced morphological changes[58] and laser-PIXE[59,60]. In particular in the latter, the irradiation of a secondary target might block the diagnostic at 0°, but not the TOF lines at other angles. The testing of the aforementioned applications will be the subjects of subsequent studies on the beamline.

4.4.6 Conclusion

In summary, the presented study illustrates the most recent setup of the ALLS 100 TW laser-driven ion acceleration beamline which uses cross-calibrated TP-TOF detectors as particle diagnostics. The MCP used for particle detection in the TP spectrometer has been calibrated in intensity, on the 2 × 6 MV Tandem Van de Graaff accelerator from Université de Montréal, using single proton impacts to retrieve the particle scaling factor that is used to determine and benchmark the particle numbers observed in the TP for protons and carbon ions. The experimental data points of the scaling factor were obtained by performing a pixel clusters analysis of the proton impacts on the MCP, and a semi-empirical model was fitted to the data to extrapolate the calibration to higher kinetic energies and also to extend it to other ion species. The methodology of this intensity calibration is universal and can be applied to other kinetic energies in the tens keV to tens of MeV range, to different ion species or to other types of MCP detectors, hence making the technique broadly applicable. In our findings, we highlight

the importance of modeling the full depth-dependence for the stopping power (*i.e.* the Bragg peak) which allows to properly model the non-linearities of the response function. Two TOF lines using diamond detectors, placed at $+6^\circ$ and -9° with respect to target-normal axis, were used to determine the field integrals related to the electric and magnetic dispersions for the TP spectrometer. The two TOF lines allow to verify the proton beam alignment on a shot-to-shot basis and to characterize the beam divergence. This opens the possibility to know the proton beam characteristics on shots where the 0° axis of the TP spectrometer is blocked by a secondary target, but not the axes of the TOF lines, enabling diverse laser-driven proton beam applications that require reliable data. The used particle diagnostics are compatible with the development of a high-repetition rate targetry, as opposed to the use of radiochromic films or image plates, and are therefore a crucial step in the planned automation of the beamline. The testing of laser-driven proton beam applications using very high number of shots to ensure good statistics will be the subject of subsequent studies.

4.4.7 Acknowledgements

This work is supported by FRQNT (nouveaux chercheurs, Grant No. 174726, Equipe 2016-PR-189974), the National Sciences and Engineering Research Council of Canada (NSERC) (Discovery Grant RGPIN-2018-05772 and the Alexander-Graham-Bell Graduate Scholarship for S.V.), Compute Canada (Job: pve-323-ac) as well as the Canada Foundation for Innovation (CFI). This study has also received financial support from the French National Research Agency (ANR) in the frame of "the Investments for the future" Programme IdEx Bordeaux - ANR-10-IDEX-03-02. The work of F.C. has been carried out within the framework of the EUROfusion Consortium and has received funding from the Euratom research and training program 2014-2018 and 2019-2020 under grant agreement No. 633053. The authors wish to thank L. Godbout for maintaining the EN-1 Tandem accelerator, J.-C. Kieffer for the support and F. Fillion-Gourdeau for the help during the experimental campaign.

4.4.8 References

[1] M. C. Downer, R. Zgadzaj, A. Debus, U. Schramm & M. C. Kaluza, "Diagnostics for plasma-based electron accelerators", *Rev. Mod. Phys.*, vol. 90, 035002 (2018).

[2] H. Daido, M. Nishiuchi, A. S. & Pirozhkov, "Review of laser-driven ion sources and their applications", *Rep. Prog. Phys.*, vol. 75, 056401 (2012).

[3] S. C. Wilks, W. L. Kruer, M. Tabak & A. B. Langdon, "Absorption of Ultra-Intense Laser Pulses", *Phys. Rev. Lett.*, vol. 69, 1383 (1992).

[4] J. Fuchs *et al.*, "Comparison of Laser Ion Acceleration from the Front and Rear Surfaces of Thin Foils", *Phys. Rev. Lett.*, vol. 94, 045004 (2005).

[5] J. Fuchs *et al.*, "Comparative spectra and efficiencies of ions laser-accelerated forward from the front and rear surfaces of thin solid foils", *Phys. Plasmas*, vol. 14, 053105 (2007).

[6] A. Kemp, J. Fuchs, Y. Sentoku, V. Sotnikov, M. Bakeman, P. Antici & T. Cowan, "Emittance growth mechanisms for laser-accelerated proton beams", *Phys. Rev. E*, vol. 75, 056401 (2007).

[7] Y. Gao *et al.*, "An automated, 0.5 Hz nano-foil target positioning system for intense laser plasma experiments", *High P. Las. Sci. Eng.*, vol. 5, e12 (2017).

[8] F. Consoli *et al.*, "Laser produced electromagnetic pulses: generation, detection and mitigation", *High P. Las. Sci. Eng.*, vol. 8, e22 (2020).

[9] J. Metzkes, L. Karsch, S. D. Kraft, J. Pawelke, C. Richter, M. Schörer, M. Sobiella, N. Stiller, K. Zeil & U. Schramm, "A scintillator-based online detector for the angularly resolved measurement of laser-accelerated proton spectra", *Rev. Sci. Instrum.*, vol. 83, 123301 (2012).

[10] A. Macchi, M. Borghesi & M. Passoni, "Ion acceleration by superintense laser-plasma interaction", *Rev. Mod. Phys.* vol. 85, 2 (2013).

[11] A. Macchi, "A Review of Laser-Plasma Ion Acceleration", *arXiv:1712.06443*, (2017).

[12] E. Woryna, P. Parys, J. Wołowski & W. Mróz, "Corpuscular diagnostics and processing methods applied in investigations of laser-produced plasma as a source of highly ionized ions", *Laser Part. Beams*, vol. 14, 293 (1996).

[13] V. Scuderi *et al.*, "Time of Flight based diagnostics for high energy laser-driven ion beams", *J. Instrum*, vol. 12, C03086 (2017).

[14] M. Marinelli, E. Milani, A. Paoletti, A. Tucciarone, & G. Verona Rinati, "High-quality diamond grown by chemical-vapor deposition: Improved collection efficiency in α-particle detection", *App. Phys. Lett*, vol. 75, 20 (1999).

[15] S. Nakamura *et al.*, "Real-Time Optimization of Proton Production by Intense Short-Pulse Laser with Time-of-Flight Measurement", *Jap. J. of App. Phys.*, vol. 45 (34), pp. L913-L916 (2006).

[16] D. Haffa *et al.*, "I-BEAT: Ultrasonic method for online measurement of the energy distribution of a single ion bunch", *Sci. Rep.*, vol. 9, 6714 (2019).

[17] APD 2 PS 97X79/32/25/8 I 40:1 NR P43, *Photonis USA, Inc.*, https://www.photonis.com.

[18] BFLY-PGE-13H2M-CS, *FLIR Integrated Imaging Solutions, Inc.*, https://www.flir.com.

[19] M. Mayer, "SIMNRA User's Guide", Report IPP 9/113, Max-Planck-Institut für Plasmaphysik, Garching, Germany (1997).

[20] J. Baumann, R. Gnewkow, S. Staeck, V. Szwedowski-Rammert, C. Schlesiger, I. Mantouvalou & B. Kanngießer, "Photon event evaluation for conventional pixelated detectors in energy-dispersive X-ray applications", *J. Anal. At. Spectrom.*, vol. 33, 2043 (2018).

[21] R. J. Beuhler & L. Friedman, "A model of secondary electron yields from atomic and polyatomic ion impacts on copper and tungsten surfaces based upon stopping-power calculations", *J. Appl. Phys.*, vol. 48, 3928 (1977).

[22] E. J. Sternglass, "Theory of Secondary Electron Emission by High-Speed Ions", *Phys. Rev.*, vol. 108, 1 (1957).

[23] F. J. Frischkorn & K. O. Groeneveld, "Heavy Ion Induced Electron Emission from Solid Surfaces", *Phys. Scripta*, vol. T6, 89-93 (1983).

[24] P. H. Soltz, M. A. Furman, J.-L. Vay, A. W. Molvik & R. H. Cohen, "Numerical simulation of the generation of secondary electrons in the High Current Experiment", *Phys. Rev. Accel. Beams*, vol. 6, 054701 (2003).

[25] P. Thieberger, A. L. Hanson, D. B. Steski, V. Zajic, S. Y. Zhang & H. Ludewig, "Secondary-electron yields and their dependence on the angle of incidence on stainless-steel surfaces for three energetic ion beams", *Phys. Rev. A*, vol. 61, 042901 (2000).

[26] R. Prasad *et al.*, "Calibration of Thomson parabola-MCP assembly for multi-MeV ion spectroscopy", *Nucl. Instrum. and Meth. in Phys. Res. A*, vol. 623, 712-715 (2010).

[27] T. W. Jeong, P. K. Singh, C. Scullion, H. Ahmed, K. F. Kakolee, P. Hadjisolomou, A. Alejo, S. Kar, M. Borghesi & S. Ter-Avetisyan, "Experimental evaluation of the response of microchannel plate detector to ions with 10s of MeV energies", *Rev. Sci. Instrum.*, vol. 87, 083301 (2016).

[28] J. F. Ziegler, M. D. Ziegler & J. P. Biersack, "SRIM - The stopping and range of ions in matter (2010)", *Nucl. Inst. & Meth. in Phys. Res. B*, vol. 268, 1818-1823 (2010).

[29] J. L. Wiza, "Microchannel plate detectors", *Nucl. Inst. & Meth.*, vol. 162, 587-601 (1979).

[30] G.W. Fraser, "The ion detection efficiency of microchannel plates (MCPs)", *Intern. J. of Mass Spectro.*, vol. 215, 13-30 (2002).

[31] K. Harres *et al.*, "Development and calibration of a Thomson parabola with microchannel plate for the detection of laser-accelerated MeV ions", *Rev. Sci. Instrum.*, vol. 79, 093306 (2008).

[32] S. Vallières, P. Puyuelo-Valdes, M. Salvadori, C. Bienvenue, S. Payeur, E. d'Humières & P. Antici, "The Laser-Driven Ion Acceleration Beamline on ALLS 200 TW for Testing Nanowires Targets", *Proc. of SPIE*, vol. 11037, 1103703-1 (2019).

[33] D. Strickland & G. Mourou, "Compression of amplified chirped optical pulses", *Opt. Commun.*, vol. 56, 219 (1985).

[34] C. Bienvenue, S. Vallières, S. Payeur & P. Antici, "Submicrometric absolute positioning of flat reflective surfaces using Michelson interferometry", *Rev. Sci. Instrum.*, vol. 90, 123702 (2019).

[35] M. Marinelli *et al.*, "Analysis of laser-generated plasma ionizing radiation by synthetic single crystal diamond detectors", *Appl. Surf. Sci.*, vol 272, 104 (2013).

[36] V. I. Polyakov *et al.*, "Photodetectors with CVD diamond films: electrical and photoelectical properties photoconductive and photodiode structures", *Diam. and Rel. Mat.*, vol. 7, 821 (1998).

[37] S. Almaviva *et al.*, "Chemical vapor deposition diamond based multilayered radiation detector: Physical analysis of detection properties", *J. of Appl. Phys.*, vol. 107, 014511 (2010).

[38] M. Cipriani *et al.*, "Spectral characterization by CVD diamond detectors of energetic protons from high-repetition rate laser for aneutronic nuclear fusion experiments", *J. Instrum.*, vol. 14, C01027 (2019).

[39] R. De Angelis *et al.* ," High performance diagnostics for Time-Of-Flight and X-ray measurements in laser produced plasmas based on fast diamond detectors", *JINST*, vol. 11, C12048 (2016).

[40] C. Verona *et al.*, "Spectroscopic properties and radiation damage investigation of a diamond based Schottky diode for ion-beam therapy microdosimetry", *J. Appl. Phys.*, vol. 118, 184503 (2015).

[41] P. Bradford *et al.*, "EMP control and characterization on high-power laser systems", *High Power Laser Science and Engineering*, vol. 6, E21 (2018)

[42] M. Salvadori *et al.*, "Accurate spectra for high energy ions by advanced time-of-flight diamond-detector schemes in experiments with high energy and intensity lasers", *arXiv*, 2003.01442 (2020).

[43] J.-E. Ducret *et al.*, "Calibration of the low-energy channel Thomson parabola of the LMJ-PETAL diagnostic SEPAGE with protons and carbon ions", *Rev. Sci. Instrum.*, vol. 89, 023304 (2018).

[44] P. B. Bolton *et al.*, "Instrumentation for diagnostics and control of laser-accelerated proton (ion) beams", *Physica Medica*, vol. 30, 255-270 (2014).

[45] A. Mancic *et al.*, "Isochoric heating of solids by laser-accelerated protons: experimental characterization and self-consistent hydrodynamic modeling", *High Ener. Dens. Phys.*, vol. 6, 21 (2010).

[46] G. Milluzzo *et al.*," A new energy spectrum reconstruction method for time-of- flight diagnostics of high-energy laser-driven protons", *Rev. Sci. Instrum.* vol. 90, 083303 (2019).

[47] C. Verona, M. Marinelli, S. Palomba, G. Verona-Rinati, M. Salvadori, F. Consoli, M. Cipriani, P. Antici , M. Migliorati, F. Bisesto & R. Pompili, "Comparison of single crystal diamond TOF detectors in planar and transverse configuration", *J. of Instrum.*, June 2020.

[48] K. Fehre *et al.*, "Absolute ion detection efficiencies of microchannel plates and funnel microchannel plates for multi-coincidence detection", *Rev. Sci. Instrum.*, vol. 89, 045112 (2018).

[49] R. C. Blase, R. R. Benke, G. P. Miller, K. S. Pickens & J. H. Waite, "Microchannel plate detector detection efficiency to monoenergetic electrons between 3 and 28 keV", *Rev. Sci. Instrum.*, vol. 88, 053302 (2017).

[50] K. Zeil *et al.*, "The scaling of proton energies in ultrashort pulse laser plasma acceleration", *New J. Phys.*, vol. 12, 045015 (2010).

[51] O. Willi *et al.*, "Particle and x-ray generation by irradiation of gaseous and solid targets with a 100 TW laser pulse", *Plas. Phys. Control. Fusion*, vol. 51, 124049 (2009).

[52] O. Lundh, F. Lindau, A. Persson, C.-G. Wahlström, P. McKenna & D. Batani, "Influence of shock waves on laser-driven proton acceleration", *Phys. Rev. E*, vol. 76, 026404 (2007).

[53] A. Pirozhkov *et al.*, "Laser-driven proton acceleration and plasma diagnostics with J-KAREN laser", *Proc. of SPIE*, vol. 7354, 735414-1 (2009).

[54] S. Fourmaux *et al.*, "Investigation of laser-driven proton acceleration using ultra-short, ultra-intense laser pulses", *Phys. Plasmas*, vol. 20, 013110 (2013).

[55] J. Fuchs *et al.*, "Laser-driven proton scaling laws and newpaths towards energy increase", *Nat. Phys.*, vol. 2, 48-54 (2006).

[56] M. Barberio, M. Scisciò, S. Vallières, F. Cardelli, S.N. Chen , G. Famulari, T. Gangolf, G. Revet, A. Schiavi, M. Senzacqua & P. Antici, "Laser-accelerated particle beams for stress testing of materials", *Nat. Comm.*, vol. 9, 372 (2018).

[57] M. Barberio, M. Scisciò, S. Vallières, S. Veltri, A. Morabito & P. Antici, "Laser-Generated Proton Beams for High-Precision Ultra-Fast Crystal Synthesis", *Sci. Rep.*, vol. 7, 12522 (2017).

[58] M. Barberio, S. Vallières, M. Scisciò, G. Kolhatkar, A. Ruediger & P. Antici, "Graphitization of diamond by laser-accelerated proton beams", *Carbon*, vol. 138, 531-537 (2018).

[59] M. Barberio & P. Antici, "Laser-PIXE using laser-accelerated proton beams", *Sci. Rep.*, vol. 9, 6855 (2019).

[60] M. Barberio, S. Veltri, M. Scisciò & P. Antici, "Laser-Accelerated Proton Beams as Diagnostics for Cultural Heritage", *Sci. Rep.*, vol. 7, 40415 (2017).

4.5 Perspectives

The design and implementation of efficient particle diagnostics is essential for any accelerator beamline. In light of the two studies presented in this Chapter, it appears clear that particular requirements are associated with the incorporation of detectors in the environment of laser-driven ion beamlines. As aforementioned in section 4.2, the chosen detectors must face several challenges with regards to their resistance or shielding to optical light, RF pollution, X-rays, high energy electrons and multiple ion species emerging from the laser-matter interaction concomitantly. As such, radiochromic films have the capability to overcome these challenges, although they cannot be implemented as detector dedicated to continuous use, being incompatible with high repetition-rate requirements. Nevertheless, they are particularly useful in the initial stages of a beamline for beam characterization, or for punctual measurements. An important point that is highlighted by the study performed on EBT-XD RCFs is concerning the dose quenching when the particle's Bragg peak is positioned near or within the active layer. A dose error, hence also a particle number misestimation error, ranging between 25%-55% was

noted when comparing the dose depositions of 4 MeV and 10 MeV protons (for the same netOD) from low doses ($\sim$ 10 Gy) to high doses (60 Gy), respectively (*i.e.* the full operational dose range of the film type). This effect even grows larger when the Bragg peak falls inside the active layer (3.2 MeV $< \mathcal{E}_{K,0} <$ 3.6 MeV) due to the broad stopping power distribution, reaching 200% for 3.2 MeV protons. Up to now, RCF stacks have been used widely in the context laser-driven ion acceleration for particle number determination, *i.e.* with broadband energy spectra, based on the assumption that the sampled kinetic energy is the one that has its Bragg peak falling within a corresponding layer depth of the stack. Hence, based on the conclusion of our work that corroborates several other studies [207–213], the conventional absolute particle number determination with RCF stacks in laser-driven ion acceleration is inherently flawed from its first premise. More precisely, the choice of the word 'flawed' here means that the uncertainty associated to a measured value is as high as the measured value itself (*i.e.* $\sigma_x/\overline{x} \sim 100\%$, with x being the estimated value). However, this observation does not mean that RCF stacks are useless from now on in TNSA, on the contrary they are still well adapted for particle energy estimation, beam profiling, divergence measurements and source size retrieval. In other words, they must be used for relative dose measurements and not for absolute dose determination.

Concerning the particular efficiency of the EBT-XD RCF type, their higher density compared to EBT3 ($\rho_{\text{EBT-XD}} = 1.35$ g/cm^3 vs $\rho_{\text{EBT3}} = 1.20$ g/cm^3) makes their minimum detectable proton energy higher ($\mathcal{E}_{\text{K, min}}^{\text{EBT-XD}} = 3.2$ MeV vs $\mathcal{E}_{\text{K, min}}^{\text{EBT3}} = 2.8$ MeV), but also grants them with a larger operational dose range ($D_{\text{max}}^{\text{EBT-XD}} = 60$ Gy vs $D_{\text{max}}^{\text{EBT3}} = 40$ Gy). Therefore, it appears obvious that EBT-XD are better suited for being used in higher energy and higher flux (*i.e.* more intense) ion beamlines compared to their EBT3 homologue. They have to be used in facilities where the mean proton energy of the spectrum is at least greater than 3.2 MeV, in order to measure the energy deposition from the majority of generated protons, which is not exactly the case for the actual ALLS 100 TW ion beamline. More precisely, we have seen from the second study on the ALLS beamline that most protons (>80%) are located within the range of 1-3 MeV, even though the maximum proton energy reaches 9 MeV, as a result of the exponential spectral shape. In the case of the present ALLS 100 TW ion beamline, the HD types (e.g. HD-810 or HD-V2) of RCF are better suited, having lower energy detection thresholds varying around 1 MeV. The EBT-XD will be better used on ALLS 100 TW when higher proton energies will be reached in upcoming experimental campaigns with thinner foils ($\leq$ 1 μm) or with nanowire targets.

The latter are expected to double the maximum proton energy, as shown experimentally in the Lund laser campaign (see section 5.4.4).

Regarding the MCP-TP spectrometer, the choice of a P43 phosphor as well as the Chevron configuration were particularly judicious choices in terms of high gain yield for the present ALLS 100 TW ion beamline. The decay time of P43 phosphors, which are known to be slow but have high photon yield, is of approximately 3.2 ms down to 1% of maximum intensity, much shorter than the time interval between two laser pulses of 400 ms (*i.e.* 2.5 Hz). As the signal decay time of an MCP-phosphor assembly is limited by the phosphor, and not by the electron avalanche within the microchannels, the shot-to-shot dead time in a TNSA experiment with solid targets will not be limited by the detector but rather by the laser's repetition rate, assuming refreshable targets at the same rate. Even though the chosen phosphor is among the slowest available in the market, the P43 is not slow enough to seriously compromise TNSA experiments, while providing among the highest light yield as an output. Similarly, the same MCP-TP spectrometer could be used on a smaller scale laser reaching potentially $1/(2 \times 3.2\ \text{ms}) \approx 150$ Hz, including the necessary gain required for the expected lower particle intensities obtained at lower laser energies. This is justified since the MCP-TP spectrometer on the ALLS 100 TW ion beamline is still far from being used at maximum gain, leaving amplification margin. Besides, the Chevron configuration provides considerable additional gain when compared to other studies [214, 215] with single MCPs. Even though the Chevron configuration lowers the spatial resolution due to larger electron beam divergence, the spatial resolution in the transverse plane of the MCP-phosphor assembly is again limited by the phosphor. Furthermore, in the case of a MCP-TP spectrometer, it was shown that the spatial resolution's bottleneck is limited by the entrance pinhole diameter [104], thus the choice of a single MCP would not have yielded better spatial resolution. Additionally, the combined choices of P43 and Chevron allow to avoid using CCD cameras with expensive cooling systems for shot noise reduction, or amplifying CCDs, such as EMCCDs, which introduce significant electronic noise in the signal. In the case of the present study, the CCD used for imaging in the MCP detection system was operated at minimum gain thereby leaving amplification margin for lower particle yields, for instance if a smaller entrance pinhole is used to increase the spatial resolution of the TPs.

Another point that deserves high importance is the proper Bragg peak modeling to obtain the absolute response of the MCP detection system. It was observed that using the surface stopping power [104] is insufficient for the proper modeling at lower proton energies below 2 MeV,

an energy range that typically has copious amounts of protons for TNSA experiments using TW-scale lasers. Moreover, we strongly recommend to perform the data point measurements on a conventional particle accelerator that includes particle counting devices calibrated in absolute terms, such as Faraday Cups for instance, rather than *in situ* with CR-39 detectors due to the strong user-dependent (*i.e.* subjective) errors that CR-39 introduce in the data collection. In particular, this is even more recommended when the MCP response function is required for energies around the response's peak (typically a few MeVs, 1.4 MeV here), due to the presence of a strong non-linearity in the response function.

As shown in the second study presented in this Chapter, the image intensity signal resulting from impacts of single particles hitting the MCP was done in a Rutherford Backscattering Spectroscopy (RBS) experimental setup. The pixel clusters analysis necessary to analyze particle impacts presents some limitations regarding the retrieval of the mean pixel intensity for a given particle kinetic energy. The manufacturer, *Photonis*, states that the FWHM of Pulse Height Distribution at maximum operating voltage (2000 V) reaches 175% of the mean, leading to an inherently large signal distribution even for monoenergetic particles incident on the detector. Albeit appearing very large, this signal width is very typical for MCPs and is an adverse effect of the electron avalanche amplification. Hence, during the pixel cluster analysis, we did not observe highly peaked signal that would have facilitated the mean pixel intensity retrieval. The pixel intensity distribution was broad, strongly dependent on an empirically defined intensity threshold, and required the calculation of mean statistical values as opposed to a typical Gaussian fit on a peak, for instance. The proper statistical convergence with reasonably low uncertainties was ensured through the collection of tens of images in identical experimental contexts to increase the number of particle events collected. Even considering this non-negligible difficulty, the response function reconstructed from the pixel clusters analysis yielded particle spectra amplitudes well in line with other 100 TW-scale laser facilities, with approximately 10^{12} particles/sr/shot. More precisely, after long and careful analysis to understand the results, along with extensive discussions with my colleague Dr. Sylvain Fourmaux who is an expert in X-ray photon counting for LWFA betatron radiation sources, I estimate that the reconstructed response function is at most a factor of 2 away from the real amplitude in a worse case scenario, otherwise closer. This is most probably due to the use of correct assumptions and proper thresholding. The physical reasons of this correspondence with literature are

not totally well understood, further investigations on the correct pixel clustering methodology to use are recommended. The pixel clustering analysis performed during this doctoral work has already a non-negligible level of complexity, nevertheless better comprehension of the proper cluster shape to use in this context is required. This will allow to further reduce the uncertainties on the sampled points of the response function.

The choice of having a TP-TOF cross-calibrated detection system is particularly useful in a laser-based ion beamline. TNSA ion beams generated with solid targets have become consolidated enough, from past experiments and models, to be easily predictable and can serve as benchmark. Hence, having a set of correlated detectors opens the path for performing applications using so-called 'blind shots', into which the 0° axis of the TP spectrometer is blocked by a secondary target used in a given application context, while the ion beam is still measured indirectly at each shot from TOF lines placed at other angles ($+6^\circ$ and -9° here), allowing to infer the flux and energies obtained on-axis with high certainty. This is a technique that will, in my opinion, democratize TNSA-based accelerators for further developments and commercialization due to its robustness an ease to use. On this matter, a successful attempt of 'blind shots' was performed in an experimental campaign dedicated to test laser-based Particle-Induced X-ray Emission (laser-PIXE), for which the results are currently submitted. The experiment is, to our knowledge, the first successful laser-PIXE experiment performed with a single shot on a commercially available laser. In further developments, a tomographic version of PIXE, as shown in Bazalova-Carter *et al.* (2015) [216], using a laser-based ion source and thin samples is foreseeable. The technique would be similar to X-ray Fluorescence Computed Tomography (XFCT) [217–221], however performed with an intense ion source having nanosecond-scale temporal resolution from a laser-based system. Many of these applications would benefit from an enhanced ion number and higher ion kinetic energy, such as to increase the ion beam intensity incident on a sample for a given application. In order to improve these ion beam characteristics, in the next Chapter 5, this doctoral work focuses on using different nanostructured metallic targets that could contribute to amplify the relativistic laser-matter interactions, ultimately providing higher ion yield.

Chapter 5

Enhanced Relativistic Laser-Matter Interactions Using Nanostructures

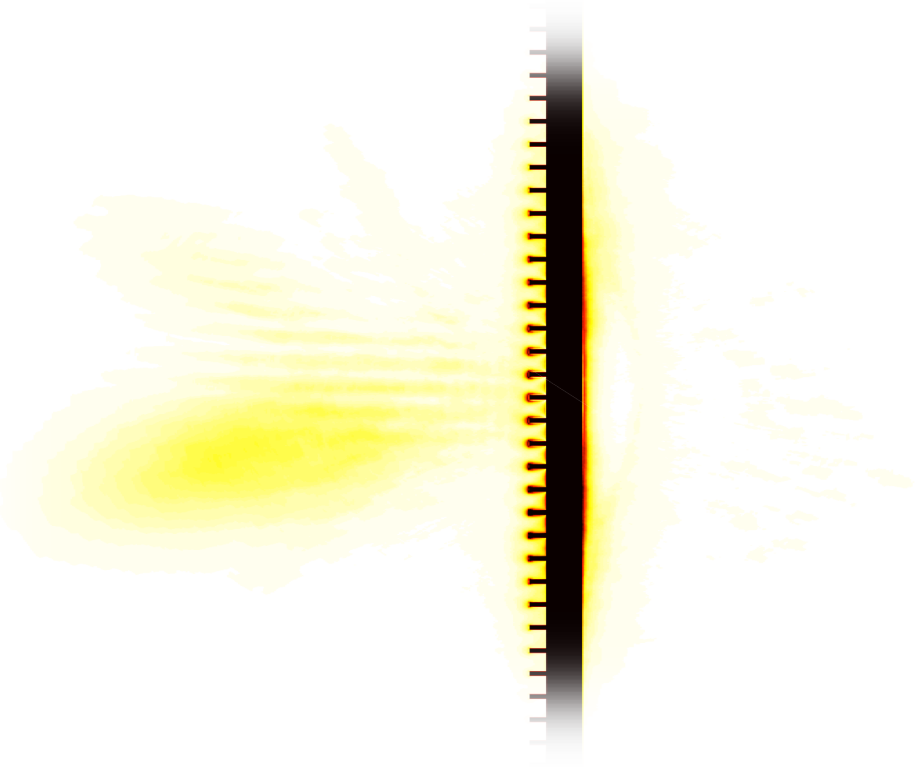

PIC simulation of ALLS 100 TW laser interacting with a nanowire target.

Chapter Content

5.1 Foreword

This Chapter details two studies performed to increase the laser energy absorption from solid targets using surface nanostructuration, in order to enhance laser-driven ion beams. The Chapter starts by overviewing some target nanostructuration techniques used in the laser-based ion

acceleration community, then continues by exposing the work done within this doctoral degree, to finally end with perspectives and recommendations for further developments. I was the project lead for both works and they resulted in the following two publications:

— **S. Vallières**, M. Barberio, M. Scisciò, E. d'Humières & P. Antici, "Enhanced Laser-Driven Proton Acceleration Using Ultrasmall Nanoparticles", *Physical Review Accelerators and Beams*, vol. 22, 091303 (2019).

— **S. Vallières**, M. Salvadori, A. Permogorov, G. Cantono, K. Svendsen, Z. Chen, S. Sun, F. Consoli, E. d'Humières, C.-G. Wahlström & P. Antici, "Enhanced Laser-Driven Proton Acceleration Using Nanowire Targets", *Scientific Reports*, Accepted, December 2020.

5.2 Solid target nanostructuration for enhanced proton acceleration

The most conventional solid targets used in the context of laser-driven ion acceleration in the TNSA regime are typically metallic thin foils (Al, Au, Cu, Ag or Ti) of micrometric thicknesses (0.1 - 20 μm thick). As we can observe with the naked eye, metallic targets are highly reflective as a result of their overdense nature (n_e of several hundreds of n_c in the visible range), their reflection coefficient being around 95% at 800 nm. This occurs when the intensity of the incident light is low ($\ll 10^{12}$ W/cm^2) and does not generate a plasma upon reflection on the target. For further investigations at high-intensities, the correct evaluation of the reflection coefficient, and hence of the laser energy absorption, requires to be evaluated through PIC simulations for a proper description of the relativistic laser-plasma interaction. Albeit reflecting most of the incoming laser energy, conventional metallic foils used for TNSA allow to generate a high number of hot electrons at the rear target surface that form the accelerating sheath. More importantly, foils conserve steep electron density gradients that are essential for establishing a high-amplitude quasi-static longitudinal electric field. The target's flatness, at least on its rear side, is key to provide the strongest accelerating gradients, as well as to induce high beam laminarity. Since the maximum proton kinetic energy approximately scales with the square-root of the laser intensity, moreover that the financial cost per Joule of laser energy grows as a power law, it is indeed becoming increasingly difficult to justify the monetary investments to achieve higher ion energies with laser-based sources. Laser-plasma researchers soon started to investigate alternative target geometries to produce stronger accelerating field, thereby generating higher proton energies with the same laser, but as well to enhance the ion beam quality

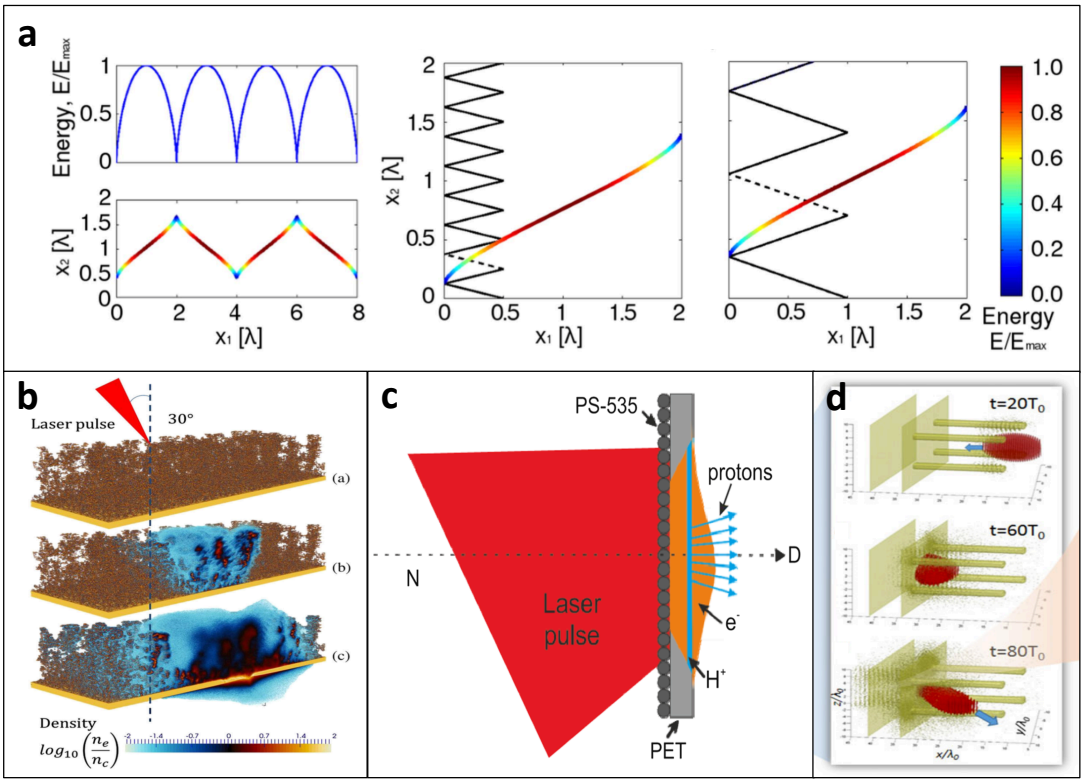

FIGURE 5.1: The most studied solid target nanostructuration schemes in laser-driven ion acceleration. (a) Nanotriangle optimization for enhancing electron heating through Direct Laser Acceleration (DLA) using the equations of movement (2.20), (2.21) and (2.22). This figure is extracted and adapted from [222]. (b) Nanofoams sitting on a flat target substrate to maximize the electric field on the target's rear side. This figure is extracted and adapted from [223]. (c) Use of polystyrene nanospheres of several hundreds of nanometers to increase laser energy absorption. This figure is extracted and adapted from [224]. (d) Investigation of nanowires through PIC simulations to increase the laser energy confinement within the nanostructure, resulting in enhanced ion beams. This figure is extracted and adapted from [225].

with lower divergences. For instance, early studies investigated the use of so-called "flat-top cone targets" which confine the laser light due to their conical geometry, leading to hotter and denser hot electrons clouds that in turn produce higher proton energies [121, 126, 127]. However, the difficult machining (and its related high financial cost) of flat-top cone targets hinders their large-scale production for a widespread use, yet another factor to take into serious consideration. Along the same ideas, front surface nanostructuration of flat targets soon became a subject of general interest, the original idea being to improve the laser energy absorption from the target, in order to produce hotter and denser sheath electron clouds at the rear target surface. Numerous target front side nanostructuration schemes have been and are still investigated in the laser-plasma community. The most popular geometries are presented in Figure 5.1, namely nanotriangles [222], nanofoams [223], nanospheres [224] and nanowires [225]. Of course, there are many other target nanostructuration studies and geometries investigated in

this context, which receive proper referencing in the following sections of this Chapter. The next sections are detailing two studies performed during this doctoral work, in particular with ultrasmall nanospheres and nanowires, for generating enhanced laser-based ion sources yielding increased particle numbers and kinetic energies (*i.e.* more intense ion bunches) in the TNSA regime.

5.3 Enhanced Laser-Driven Proton Acceleration Using Ultrasmall Nanoparticles

5.3.1 Abstract

An efficient way to enhance laser-driven proton acceleration is by increasing the laser-to-target energy transfer, which can be obtained using nanostructured target surfaces. In this paper, we show that inexpensive and easily producible solid target nanostructuration using ultrasmall nanoparticles having 10 nm in diameter exhibits a nearly twofold maximum proton energy and proton number enhancement. Results are confirmed by Particle-In-Cell simulations, for several laser pulse lengths. A parameter scan analyzing the effect of the nanoparticle diameter and space gap between the nanospheres shows that the gap has a stronger influence on the enhancement mechanism than the sphere diameter.

5.3.2 Introduction

Laser-driven proton acceleration, as obtained by the interaction of a high-intensity laser with a target, is a growing field of interest, in particular, for the different potential applications that are consolidating or emerging. These applications include their use in ultrafast radiography[1], novel fusion schemes[2], high-energy density matter[3], laboratory astrophysics[4], medical applications[5-7], novel neutron sources[8], cultural heritage[9,10], using them as injectors for larger accelerators[11,12], and material science[13-16]. Many of these applications build on the routine production of protons, where one of the main challenges is to optimize the proton energy and yield given specific laser parameters. The most common proton acceleration mechanisms that is obtained on typical commercially available multihundred terawatt laser systems is the so-called target-normal sheath acceleration (TNSA)[17], in which protons are accelerated at the rear

target surface of a solid foil (target), typically made of Au, Ag, Al, or CH, that is irradiated by a high-intensity ($I_0 > 10^{18}$ W/cm^2), short pulse ($\tau_L < 1$ ps) laser operating at wavelengths around 800-1057 nm. In this context, the laser-to-target absorption, *i.e.* how much energy is transferred from the laser to the target and from there to the particles, is a crucial parameter, since it allows improving the efficiency of the acceleration mechanism. Currently, this efficiency is at most in the order of a few or tens of percent and depends on the target and its structure.

Several attempts have been made to use different kinds of targets, such as to optimize the mean energy, collimation, and number of energetic ("hot") electrons that drive the proton acceleration mechanisms, since, generated at the target front by the ponderomotive force, they travel through the target bulk and establish at its rear surface the electrostatic field that enables the acceleration process[18,19]. In this scenario, several groups demonstrated, both theoretically[20-22] and then experimentally, that the use of nanostructured targets could enhance the absorption of the laser pulse, e.g., by using elliptical Cu nanoparticles in the tens of nanometers size - but irradiated at lower intensities ($I_0 = 10^{15} - 10^{17}$ W/cm^2)[23] - or using hundreds of nanometer-size Mylar spheres[24,25]. The use of gold nanoparticles in the tens and hundreds of nanometers has also been tested on other (longer pulse) facilities or in an embedded scenario, resulting in increased absorbance even in these conditions[26,27]. Additional effort is put in improving the laser-to-target absorption using various target nanostructuration techniques[24,28-30], such as low-density target foams[31,32], bacteria[33], parabolic structures[34], or nanowires[35]. One of the main disadvantages of the proposed enhancement solutions is that they typically require complex manufacturing or implementation methods, and often their efficiency is strongly dependent on stringent target alignment conditions, making them a less favorable candidate for inexpensive use in high-repetition rate systems.

In this study, we demonstrate that the use of front surface nanostructured targets in the < 100 nm range, irradiated with intensity $I_0 > 10^{17}$ W/cm^2, strongly enhances the laser-to-proton energy transfer and the proton yield. Compared to existing nanostructured targetry, our targets have the advantage of being cheap, easy to manufacture and, thus, easy to implement on higher-repetition rate systems without many constraints. We also show that the gap spacing between the nanostructures is an influential parameter that determines the absorption efficiency in the laser-interaction process. Particle-In-Cell (PIC) simulations confirm our findings.

5.3.3 Experimental Campaigns

The experiments were performed on the TITAN laser of the Jupiter Laser Facility (JLF) in Livermore, USA, and on the ELFIE laser of the Laboratoire pour l'Utilisation des Lasers Intenses (LULI) in Palaiseau, France. The laser parameters were, respectively, for the TITAN laser an energy $\mathcal{E}_L \sim 220$ J, pulse duration $\tau_L = 700$ fs, and central wavelength $\lambda_0 = 1.054$ μm and for the ELFIE laser an energy $\mathcal{E}_L \sim 12$ J, pulse duration $\tau_L = 350$ fs, and central wavelength $\lambda_0 = 1.057$ μm. Both lasers were focused down by an $f/3$ off-axis parabola to about 8-10 μm focal spot diameter (FWHM), yielding an intensity $I_0 \sim 3 \times 10^{19} - 5 \times 10^{20}$ W/cm^2 on target. The laser was irradiating with normal incidence the different targets (for the setup, see Figure 5.2.a). The amplified spontaneous emission (ASE) has been measured to be $< 10^{-6}$ in contrast in both cases. The proton beam spectrum was monitored by placing two Thomson Parabola (TP) spectrometers, respectively, at 0° and 16° for the TITAN laser and 0° and 9° for the ELFIE laser with respect to the normal direction from the proton source. Additional information about the proton beam was retrieved using radiochromic films[36]. The nanostructured targets were produced by spray drying different layers of in-house-produced gold or silver nanoparticles (NPs) with a diameter of 10 nm onto a solid aluminum target with thickness 15 μm[37,38] (for an image of the produced NPs, see Figure 5.2.b). We considered this target material since it is one of the most used and cheapest target materials in laser-driven proton acceleration, was producing the best results compared to other materials and thicknesses when used as a proton source[13,39], and the wetting properties between them and the gold or silver NPs can ensure the realization of a uniform nanostructured film on the surface with limited aggregation of nanoparticles[40]. As shown in Figure 5.2.b, NPs can aggregate locally on the surface, which changes the effective gap parameter of the nanostructuration. The latter is a linear combination of the different gap space that the laser encounters in its focal spot when hitting the target. With this technique, we were able to generate targets that have simultaneously high light absorption, high roughness, and low cost. The low fabrication costs of all nanostructured films result from a simple process combination of laser ablation synthesis in solution for the production of the NPs of different sizes[41] and spray-dry of the solution onto planar surfaces, which increases the surface roughness.

Figures 5.2.c and 5.2.d show the proton spectra obtained for nanostructured aluminum targets as produced on the TITAN and ELFIE lasers, each spectrum representing a five-shot average

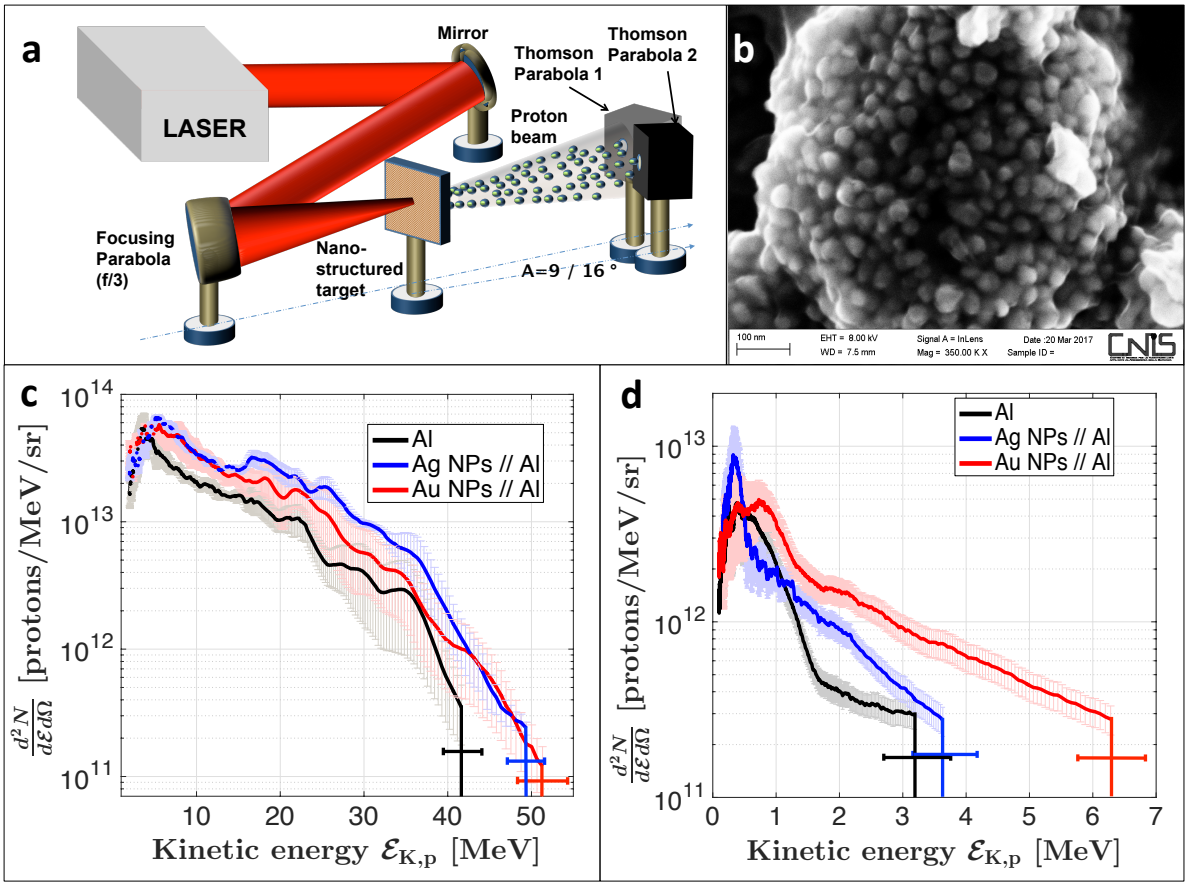

FIGURE 5.2: (a) Experimental setup; (b) Scanning electron microscope (SEM) image of gold NPs deposited onto a planar 15 μm Au foil target; (c) Proton spectra with error bars obtained on the TITAN laser with Ag (blue curve) and Au NPs (red curve) on Al foils compared to a standard 15 μm Al foil (black curve); (d) Proton spectra obtained on the ELFIE laser with Ag (blue curve) and Au NPs (red curve) on Al foils compared to a standard 15 μm Al foil (black curve).

along with its standard error bars. As one can see, all nanostructured targets perform better than the solid targets for both the maximum proton energy and proton number. Regarding the TITAN laser, we find an enhancement of 79% and 51% in the proton yield, as obtained by integrating the number of protons between 1 MeV and the maximum proton energy, and an enhancement of 19% and 23% in the maximum proton energy, for Ag NPs deposited on Al foils (AgNPs//Al) and AuNPs//Al, respectively. Similarly, we obtain for the ELFIE laser a proton yield enhancement of 67% and 190% in the proton yield and a maximum proton energy enhancement of 13% and 97% for AgNPs//Al and AuNPs//Al, respectively. For both lasers, the use of Au nanoparticles seems preferable to the use of Ag particles. The higher atomic number of gold indeed provides greater electron density in the accelerating hot electron sheath, thus giving a higher proton number and energies.

5.3.4 PIC Simulations

We run PIC simulations to shed light onto the underlying acceleration process and confirm the optimized conditions. PIC simulations were performed using the 2D3V PICLS code[42] using a Gaussian p-polarized normally incident laser pulse with a peak intensity of 5×10^{20} W/cm^2 ($a_0 = 15$, the normalized intensity of the vector potential). Two sets of simulations were developed, the first one consisting in varying the pulse length duration $\tau_L = 25$, 100, 200 and 300 fs at Full-Width-Half-Maximum (FWHM) on the target. Given the nanometric matrix of the target, we used highly resolved spatial steps of $dx = dy = 2$ nm, leading to temporal steps of $dt = dx/c = 6.6$ as. Concerning the box size, a plane-wave approximation with periodic boundaries in the transverse direction was used to compensate the strong computing time limitation from the small cell size (for the setup of the simulation box, see Figure 5.4.a). The box size was 24200 $\times$ 420 cells ($30\lambda_0 \times 1\lambda_0$) in the longitudinal and transverse axes, respectively, with 20 macroparticles per cell. The target was made of a layer of gold spheres with diameter d_{NP} of 20 nm placed side by side, on a 500-nm-thick gold foil ($2500n_c$, where n_c is the critical density). At the rear side of the target was placed a 20 nm layer of protons ($15n_c$), representing water and hydrocarbon contaminants on the surface, and simulations were run for 600 fs. The second set of simulations consisted in varying NP diameters in the range of 5-100 nm as well as the space gap g between NPs in the range of 0-400 nm. To achieve a good resolution of NPs smaller in size, we decreased the cell size to 1 nm. To compensate the highly demanding computing power of these simulations, the box size was reduced to 11200 $\times$ 800 pixels ($14\lambda_0 \times 1\lambda_0$) and the simulation time to 200 fs, with a pulse duration of 25 fs. In order to optimize the computational burden, we first verified for a few pulse lengths that the results obtained using the shorter pulse (25 fs) were consistent for those obtained using longer pulses ($\tau_L > 300$ fs), the latter simulations being far more computationally demanding. The results are presented in Figure 5.3. In Figures 5.3.a and 5.3.b, we can note the continuously increasing laser energy absorption and maximum proton kinetic energy in this pulse duration range. Small NPs of 20 nm in diameter do provide a considerable gain for both parameters, reaching an enhancement ratio of roughly 50% even for long pulse durations of hundreds of femtoseconds (see Figure 5.3.c), which is consistent with experimental enhancements observed in Figure 5.2. This particular enhancement seem to flatten off for long pulses, although for a short pulse (25 fs) the maximum energy gain reaches over 250%. Even if small NPs of 20 nm seem to add a negligible

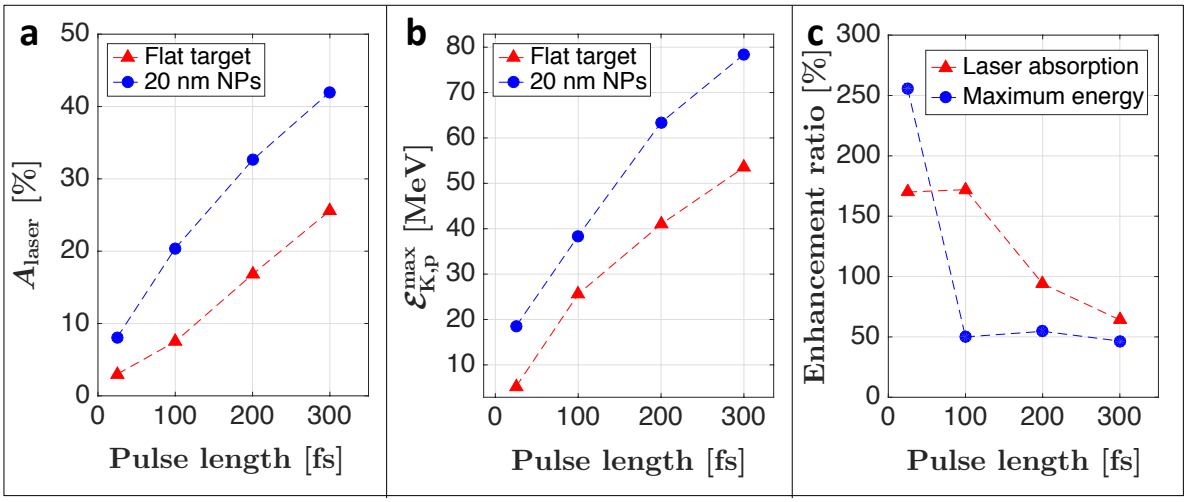

FIGURE 5.3: Pulse length effect on total laser energy absorption A_{laser} from the target (a) and on the maximum kinetic energy gained by protons $\mathcal{E}^{max}_{K,p}$ (b). The enhancement ratio for both parameters is also shown in (c).

thickness over a target with a thickness of 500 nm (which in the PIC simulation was the thickness of the solid target), the simulations still demonstrate a strong enhancement potential for long pulses of a few hundred femtoseconds. Given the many simulations required to do a parameter scanning and the good representation of NP enhancement even with a short pulse, we performed the rest of the simulations using the same on-target intensity but using the shorter laser pulse duration (25 fs) to allow for shorter computation time and knowing that our simulations would only underestimate the phenomena. The short-pulse results are also of interest for the many short-pulse commercial lasers that are currently implementing laser-generated proton acceleration.

At first, we explore the effect of the nanoparticle dimensions on the laser energy absorption 200 fs after the main pulse, which is a sufficiently long time span to allow for saturation of the acceleration process (see Figure 5.4.b). We clearly observe a rapid absorption enhancement for increasing nanoparticle diameters ranging from 5 to 20 nm (the 0 nm size representing the flat target), while after this dimension the absorption only minimally improves, almost coming to saturation. This reflects on the simulated electron spectra taken 20 fs after the interaction (where this time interval has been chosen since at this time span most energy is transferred to the electrons) (see Figure 5.4.c), where we note that the maximum kinetic energy of the electrons more than doubles when using 10-60 nm nanoparticles compared to a flat target. We also observe that the number of electrons increases similarly to the maximum energy. The surface density of the NPs is very likely to play a central role in this enhancement, which is not solely

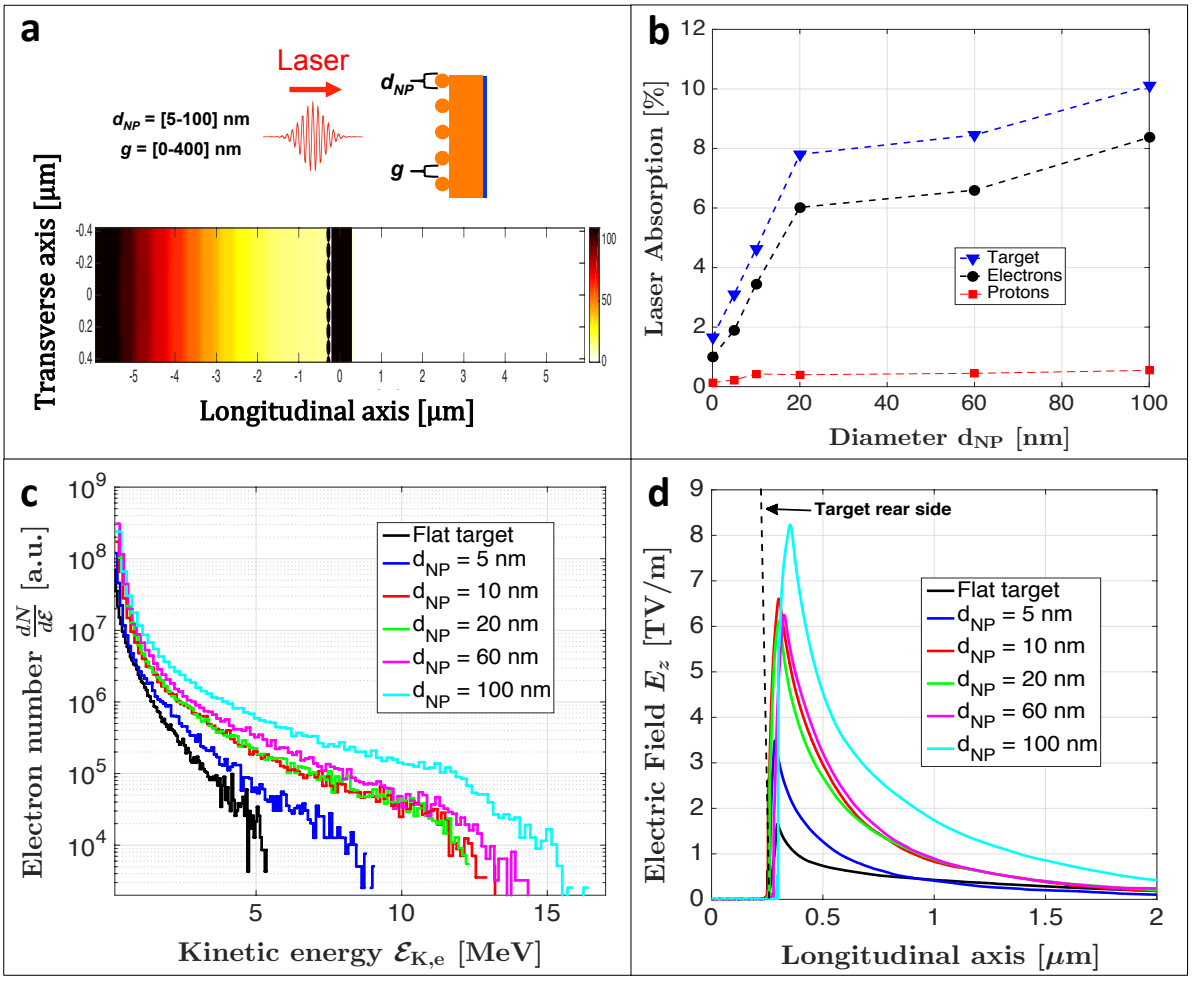

FIGURE 5.4: (a) Schematic geometry of the PIC simulations (b) Laser energy absorption for different nanoparticle diameters, comparing energy absorption from the whole target (blue triangles), from electrons (black circles) and from protons (red squares) (c) Hot electron spectra for different nanoparticle diameters (d) Mean longitudinal electric field at central radial position.

provoked from the NP diameter, suggesting a strong importance of the number and size of gaps between NPs rather than just the NP dimension. Our findings are supported by the analysis of the longitudinal electric field produced at the target rear surface at the time 20 fs after the impact (see Figure 5.4.d). We see that the electric field at the target rear surface increases almost proportionally to the maximum electron energy enhancement up to a nanoparticle size of 10 nm and then stabilizes between 10 and 60 nm. After this particle size, the position of the field shifts away from the rear target surface, thus lowering its effect on the acceleration process, and finally climbs up again for 100 nm particles. The increasing trend of the electrons' maximum energy in Figure 5.4.c follows the same pattern as in Figure 5.4.d, denoting well the electron-dependent behavior of the accelerating field.

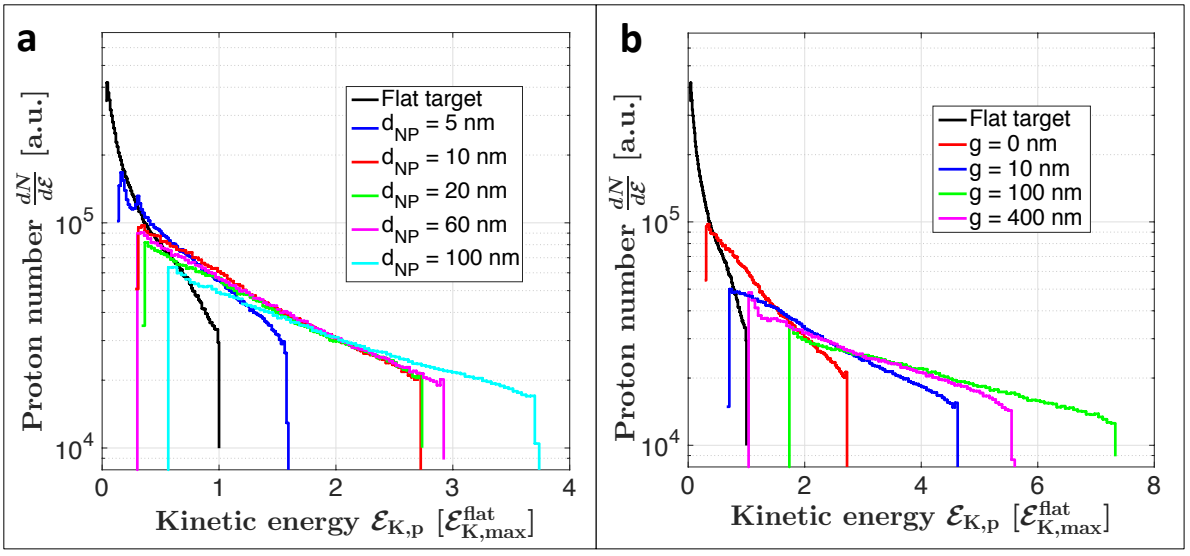

FIGURE 5.5: (a) Proton kinetic energy spectra for different NP diameters d_{NP} - the gap size g between the different nanoparticles is kept at $g = 0$ nm. (b) Influence of the gap size g on the proton spectra - the nanoparticle dimension has been kept fixed at $d_{\mathrm{NP}} = 10$ nm. Since the number of protons in the simulation is fixed and the plane-wave approximation is used, the minimum energy (low energy drop in the spectrum) is shifted with an increasing maximum proton energy. The flat target maximum normalization energy is 4.5 MeV.

In Figure 5.5.a), we show the respective proton spectra for different NP diameters d_{NP}, where the maximum energy axis has been normalized to the maximum proton energy obtained with the flat target. One can see that an increase in the laser energy absorption significantly increases the maximum achievable proton energy, up to a nearly four-fold increase, in line with the experimental results. In order to investigate the importance of the gap g between the nanospheres, we fixed the NP diameter at 10 nm, our experimental working point, and changed the gap in the range of $g = 0 - 400$ nm (see Figure 5.5.b). We can clearly note that the gap opening plays a stronger role than varying the nanoparticle diameter: When separating the nanoparticles by a gap of 10 nm, simulations show that the maximum proton energy enhancement is much more pronounced than when using 100 nm diameter nanoparticles but with gap distance $g = 0$ nm. This is because the ejected electrons from the NPs can accelerate in the laser field while traveling in the gap space before passing through the target bulk, where the electric field is nearly zero for dense plasmas. The gap region allows for greater electron heating and, therefore, stronger laser energy absorption, a consistent conclusion to those presented in the paper of Blanco *et al.* (2017)[22], where a theoretical study with triangular nanostructures shows that this phenomenon is due to the relativistic electron trajectory in the gap space. This is a different but complementary trend when compared to several other

papers using targets nanostructured with nanoparticles, where the nanospheres are always tightly packed (*i.e.* $g = 0$ nm)[23-25]. The aforementioned papers foresee a nearly absent improvement in the acceleration regime for NPs with a diameter of 10 nm. Our results indicate that the gap distance plays a stronger role than the diameter size. This effect is more pronounced for smaller NPs, since they allow for a greater amount of gap spaces. We also see that there is an increasing trend for larger gaps, up to gap sizes of 100 nm, most likely since up to those gap distances this phenomenon is enhanced. For a gap distance of $g = 400$ nm (magenta curve), the enhancement is still present but the trend is reverting. At this larger gap size, the effect of the nanoparticles is reduced, and we are returning back towards the flat target case (*i.e.* $\mathcal{E}_{\mathrm{K,\,max}}^{\mathrm{flat}} < \mathcal{E}_{\mathrm{K,\,max}}^{g=400\,\mathrm{nm}} < \mathcal{E}_{\mathrm{K,\,max}}^{g=100\,\mathrm{nm}}$). The maximum energy enhancement is maximized for a gap of 100 nm, reaching a sevenfold increase, much higher than the fourfold obtained by varying the NP diameter. This suggests that, when using nanoparticle-enhanced targets, it is preferable to have larger gap spaces (about $g = 100$ nm) with many small NPs ($d_{\mathrm{NP}} < 100$ nm) rather than tightly packed ($g = 0$ nm) large NPs ($d_{\mathrm{NP}} > 100$ nm). Indeed, having smaller NPs provides the possibility to have greater NP surface densities and, hence, greater gap densities, rather than solely relying on the NPs diameter. Moreover, in the presented PIC simulations, the NPs are all equally spaced with a single gap value, whereas the experimental targets have a random distribution of gap spaces. Hence, the optimum experimental condition strongly depends on the effect of several gap distances, which explains the strong maximum energy increase seen experimentally. Concerning the thickness of the NP layer, as shown in the paper of Barberio *et al.* (2016)[37] detailing the present nanostructured target fabrication methodology, the NPs are dried on a flat target until the surface roughness saturates, adding at most several tens of nanometers on the initial flat target surface (NPs multilayer), hence making the thickness of the nanostructured layer negligible compared to the total thickness. The substrate thickness (as long as the target remains opaque to the laser, which is the case in our simulations) has an influence on the absolute maximum energy but not on the relative increase when comparing targets with and without nanospheres. The important factor here is the increased transverse density variations (given by the increased surface roughness) rather than the target thickness variation. This enhancement process is dependent on an increased density of hotter electrons at the rear side of the target, as shown in Figure 5.4., which ultimately leads to a stronger TNSA electric field. Having a less dense plasma (produced by higher absorption through an increased surface roughness) at the target front allows one to reduce the reflection coefficient of the target and, thus, increases the energy absorption from the incident wave, compared to

the flat target case. Details about the modifications of the nanospheres when the impinging laser reaches the peak intensity are thus not a necessary requirement for this enhancement mechanism as observed in our simulations. The production of a favorable preplasma up to the peak intensity is key to produce a greater number of hotter electrons, leading to higher kinetic energies of the accelerated protons.

5.3.5 Conclusion

In conclusion, we have shown that nanostructured targets with ultrasmall NPs allow enhancing the laser energy absorption and, thus, increase the maximum proton energy and number. Moreover, we have investigated the effect of the gap parameter g, showing that this parameter has a stronger enhancement effect on the proton maximum energy than the diameter of the NPs, reaching a seven-fold increase with gap variation compared to four-fold in tightly packed geometry ($g = 0$ nm). This conclusion differs from other findings published in the literature using nanoparticles for target nanostructuration, where the use of 10 nm NPs should be of negligible importance. Here, we show that ultrasmall NPs provide significant proton energy enhancement, in particular, due to the strong gap opening effect along with a greater gap density provided by small NPs. Compared to existing nanostructured targets that require the use of complex and expensive manufacturing procedures (e.g., lithographic methods), our targets present the advantage of being both simple and inexpensive to manufacture and do not exhibit the stringent laser-matter alignment conditions as required by microstructured targets. These targets are therefore good candidates for being implemented on high repetition-rate laser-driven proton beam lines, where any efficiency enhancement in the laser-driven acceleration process is of high impact.

5.3.6 Acknowledgements

We acknowledge the expert support of the TITAN and LULI laser teams and the expertise of F. Mura from the CNIS center. We thank S. Veltri, A. Morabito, K. Nelissen, and J. Fuchs for their precious help and for providing equipment. This work is supported by FRQNT (nouveaux chercheurs, Grant No. 174726, Equipe 2016-PR-189974), the National Sciences and Engineering Research Council of Canada (NSERC) (Discovery Grant No. RGPIN-2018-05772 and the Alexander-Graham-Bell Graduate Scholarship for S.V.), Compute Canada (Job: pve-323-ac, P.

A.) as well as the Canada Foundation for Innovation (CFI). The use of the Jupiter Laser Facility was supported by the U.S. Department of Energy, Lawrence Livermore National Laboratory, under Contract No. DE-AC52-07NA27344. Concerning the use of the ELFIE laser facility, we acknowledge support by LASERLAB Europe (Grant Agreement No. 654148 under the European Union's Horizon 2020 research and innovation program). Additional support comes from the EU program HPRI CT 1999-0052, LANL Laboratory Directed Research & Development, corporate support of General Atomics, and UNR Grant No. DE-FC08-01NV14050.

5.3.7 References

[1] L. Romagnani *et al.*, "Dynamics of Electric Fields Driving the Laser Acceleration of Multi-MeV Protons", *Phys. Rev. Lett.*, vol. 95, 195001 (2005).

[2] M. Roth *et al.*, "Fast Ignition by Intense Laser-Accelerated Proton Beams", *Phys. Rev. Lett.*, vol. 86, 436 (2001).

[3] P. K. Patel, A. J. Mackinnon, M. H. Key, T. E. Cowan, M. E. Foord, M. Allen, D. F. Price, H. Ruhl, P. T. Springer & R. Stephens, "Isochoric Heating of Solid-Density Matter with an Ultrafast Proton Beam", *Phys. Rev. Lett.*, vol. 91, 125004 (2003).

[4] B. Albertazzi *et al.*, "Laboratory formation of a scaled protostellar jet by coaligned poloidal magnetic field", *Science*, vol. 346, 325 (2014).

[5] A. Yogo *et al.*, "Measurement of relative biological effectiveness of protons in human cancer cells using a laser-driven quasi-monoenergetic proton beamline", *Appl. Phys. Lett.*, vol. 98, 053701 (2011).

[6] J. Metzkes, T. E. Cowan, L. Karsch, S. D. Kraft, J. Pawelke, C. Richter, T. Richter, K. Zeil & U. Schramm, "Preparation of laser-accelerated proton beams for radio-biological applications", *Nucl. Instrum. Methods Phys. Res.*, Sect. A, vol. 653, 172 (2011).

[7] D. Doria *et al.*, "Biological effectiveness on live cells of laser driven protons at dose rates exceeding 109 Gy/s", *AIP Adv.*, vol. 2, 011209 (2012).

[8] M. Roth *et al.*, "Bright Laser-Driven Neutron Source Based on the Relativistic Transparency of Solids", *Phys. Rev. Lett.*, vol. 110, 044802 (2013).

[9] M. Barberio, S. Veltri, M. Scisciò & P. Antici, "Laser-accelerated proton beams as diagnostics for cultural heritage", *Sci. Rep.*, vol. 7, 40415 (2017).

[10] M. Barberio & P. Antici, "Laser-PIXE using laser-accelerated proton beams", *Sci. Rep.*, vol. 9, 6855 (2019).

[11] P. Antici, M. Fazi, A. Lombardi, M. Migliorati, L. Palumbo, P. Audebert & J. Fuchs, "Numerical study of a linear accelerator using laser-generated proton beams as a source", *J. Appl. Phys.*, vol. 104, 124901 (2008).

[12] P. Antici, M. Migliorati, A. Mostacci, L. Picardi, L. Palumbo & C. Ronsivalle, "A compact post-acceleration scheme for laser-generated protons", *Phys. Plasmas*, vol. 18, 073103 (2011).

[13] M. Barberio, S. Vallières, M. Scisciò, G. Kolhatkar, A. Ruediger & P. Antici, "Graphitization of diamond by laser-accelerated proton beams", *Carbon*, vol. 139, 531 (2018).

[14] M. Barberio, M. Scisciò, S. Vallières, F. Cardelli, G. Famulari, T. Gangolf, G. Revet, M. Senzaqua, S. N. Chen, A. Schiavi & P. Antici, "Laser-accelerated particle beams for stress testing of materials", *Nat. Commun.*, vol. 9, 372 (2018).

[15] M. Barberio, M. Scisciò, S. Vallières, S. Veltri, A. Morabito & P. Antici, "Laser-generated proton beams for high-precision ultra-fast crystal synthesis", *Sci. Rep.*, vol. 7, 12522 (2017).

[16] M. Barberio, S. Veltri, M. Scisciò & P. Antici, "Laser-Accelerated Proton Beams as Diagnostics for Cultural Heritage", *Sci. Rep.*, vol. 7, 40415 (2017).

[17] S. C. Wilks, W. L. Kruer, M. Tabak & A. B. Langdon, "Absorption of Ultra-Intense Laser Pulses", *Phys. Rev. Lett.*, vol. 69, 1383 (1992).

[18] L. Cao, Y. Gu, Z. Zhao, L. Cao, W. Huang, W. Zhou, X. T. He, W. Yu & M. Y. Yu, "Control of the hot electrons produced by laser interaction with nanolayered target", *Phys. Plasmas*, vol. 17, 103106 (2010).

[19] P. Antici, J. Fuchs, M. Borghesi, L. Gremillet, T. Grismayer, Y. Sentoku, E. d'Humières, C. A. Cecchetti, A. Mancic, A. C. Pipahl, T. Toncian, O. Willi, P. Mora & P. Audebert, "Hot and Cold Electron Dynamics Following High-Intensity Laser Matter Interaction", *Phys. Rev. Lett.*, vol. 101, 105004 (2008).

[20] A. Andreev, N. Kumar, K. Platonov & A. Pukhov, "Efficient generation of fast ions from surface modulated nanostructure targets irradiated by high intensity short-pulse lasers", *Phys. Plasmas*, vol. 18, 103103 (2011).

[21] J. Yu, Z. Zhao, X. Jin, F. Wu, Y. Yan, W. Zhou, L. Cao, B. Li & Y. Gu, "Laser-driven proton acceleration using a conical nanobrush target", *Phys. Plasmas*, vol. 19, 053108 (2012).

[22] M. Blanco, M. T. Flores-Arias, C. Ruiz & M. Vranic, "Table-top laser-based proton acceleration in nanostructured targets", *New J. Phys.*, vol. 19, 033004 (2017).

[23] S. Bagchi, P. Prem Kiran, M.K. Bhuyan, S. Bose, P. Ayyub, M. Krishnarmurthy & G.R. Kumar, "Fast ion beams from intense, femtosecond laser irradiated nano-structured surfaces", *Appl. Phys. B*, vol. 88, 167 (2007).

[24] D. Margarone *et al.*, "Laser-Driven Proton Acceleration Enhancement by Nanostructured Foils", *Phys. Rev. Lett.*, vol. 109, 234801 (2012).

[25] O. Klimo, J. Psikal, J. Limpouch, J. Proska, F. Novotny, T. Ceccotti, V. Floquet & S. Kawata, "Short pulse laser interaction with micro-structured targets: simulations of laser absorption and ion acceleration", *New J. Phys.* , vol. 13, 053028 (2011).

[26] L. Torrisi, L. Calcagno, M. Cutroneo, J. Badziak, M. Rosinski, A. Zaras-Szydlowska & A. Torrisi, "Nanostructured targets for TNSA laser ion acceleration", *Nukleonika*, vol. 61, 103 (2016).

[27] L. Torrisi, "Ion acceleration from intense laser-generated plasma: methods, diagnostics and possible applications", *Nukleonika*, vol. 60, 207 (2015).

[28] H. Schwoerer, S. Pfotenhauer, O. Jäckel, K.-U. Amthor, B. Liesfeld, W. Ziegler, R. Sauerbrey, K. W. D. Ledingham & T. Esirkepov, "Laser-plasma acceleration of quasi-monoenergetic protons from microstructured targets", *Nature*, vol. 439, 445 (2006).

[29] M. Cutroneo, L. Torrisi, L. Calcagno & A. Torrisi, "Characterization of thin films for TNSA laser irradiation", *J. Phys. Conf. Ser.*, vol. 508, 012012 (2014).

[30] L. Willingale, S. R. Nagel, A. G. R. Thomas, C. Bellei, R. J. Clarke, A. E. Dangor, R. Heathcote, M. C. Kaluza, C. Kamperidis, S. Kneip, K. Krushelnick, N. Lopes, S. P. D. Mangles, W. Nazarov, P.M. Nilson & Z. Najmudin, "Characterization of High-Intensity Laser Propagation in the Relativistic Transparent Regime through Measurements of Energetic Proton Beams", *Phys. Rev. Lett.*, vol. 102, 125002 (2009).

[31] M. Passoni, A. Sgattoni, I. Prencipe, L. Fedeli, D. Dellasega, L. Cialfi, Il Woo Choi, I. Jong Kim, K. A. Janulewicz, H. W. Lee, J. H. Sung, S. K. Lee & C. H. Nam, "Toward high-energy laser-driven ion beams: Nanostructured double-layer targets", *Phys. Rev. Accel. Beams*, vol. 19, 061301 (2016).

[32] P. Antici, J. Fuchs, E. d'Humières, J. Robiche, E. Brambrink, S. Atzeni, A. Schiavi, Y. Sentoku, P. Audebert & H. Pepin, "Laser acceleration of high-energy protons in variable density plasmas", *New J. Phys.*, vol. 11, 023038 (2009).

[33] M. Dalui, M. Kundu, S. Tata, A. D. Lad, J. Jha, K. Ray & M. Krishnamurthy, "Novel target design for enhanced laser driven proton acceleration", *AIP Adv.*, vol. 7, 095018 (2017).

[34] A. Lübcke, A. A. Andreev, S. Höhm, R. Grunwald, L. Ehrentraut, and M. Schnürer, "Prospects of target nanostructuring for laser proton acceleration", *Sci. Rep.*, vol. 7, 44030 (2017).

[35] M. A. Purvis, V. N. Shlyaptsev, R. Hollinger, C. Bargsten, A. Pukhov, A. Prieto, Y. Wang, B. M. Luther, L. Yin, S. Wang & J. J. Rocca, "Relativistic plasma nanophotonics for ultra-high energy density physics", *Nat. Photonics*, vol. 7, 796 (2013).

[36] S. Vallières, C. Bienvenue, P. Puyuelo-Valdes, M. Salvadori, E. d'Humières, F. Schiettekatte & P. Antici, "Low-energy proton calibration and energy-dependence linearization of EBT-XD radiochromic films", *Rev. Sci. Instrum.*, vol. 90, 083301 (2019).

[37] M. Barberio, M. Scisciò, S. Veltri & P. Antici, "Fabrication of nanostructured targets for improved laser-driven proton acceleration", *Superlattices Microstruct.*, vol. 95, 159 (2016).

[38] S. Vallières, A. Morabito, S. Veltri, M. Scisciò, M. Barberio & P. Antici, "Laser-driven proton acceleration with nanostructured targets", *SPIE Opt. Optoelectron.*, vol. 10240, 1024009 (2017).

[39] M. Gauthier, A. Lévy, E. d'Humières, M. Glesser, B. Albertazzi, C. Beaucourt, J. Breil, S. N. Chen, V. Dervieux, J.L. Feugeas, P. Nicolaï, V. Tikhonchuk, H. Pépin, P. Antici & J. Fuchs, "Investigation of longitudinal proton acceleration in exploded targets irradiated by intense short-pulse laser", *Phys. Plasmas*, vol. 21, 013102 (2014).

[40] M. Barberio, F. Stranges & F. Xu, "Coating geometry of Ag, Ti, Co, Ni, and Al nanoparticles on carbon nanotubes", *Appl. Surf. Sci.*, vol. 334, 174 (2015).

[41] M. Barberio & P. Antici, "In situ study of nucleation and aggregation phases for nanoparticles grown by laser-driven methods", *Sci. Rep.*, vol. 7, 41372 (2017).

[42] Y. Sentoku & A. J. Kemp, "Numerical methods for particle simulations at extreme densities and temperatures: Weighted particles, relativistic collisions and reduced currents", *J. Comput. Phys.*, vol. 227, 6846 (2008).

5.4 Enhanced Laser-Driven Proton Acceleration Using Nanowire Targets

5.4.1 Abstract

Laser-driven proton acceleration is a growing field of interest in the high-power laser community. One of the big challenges related to the most routinely used laser-driven ion acceleration mechanism, Target-Normal Sheath Acceleration (TNSA), is to enhance the laser-to-proton energy transfer such as to maximize the proton kinetic energy and number. A way to achieve this is using nanostructured target surfaces in the laser-matter interaction. In this work, we show that nanowire (NW) structures can increase the maximum proton energy by a factor of two, triple the proton temperature and boost the proton numbers, in a campaign performed on the ultra-high contrast 10 TW laser at the Lund Laser Center (LLC). The optimal nanowire length, generating maximum proton energies around 6 MeV, is around 1-2 μm. This nanowire length is sufficient to form well-defined highly-absorptive NW forests and short enough to minimize the energy loss of hot electrons going through the target bulk. Results are further supported by Particle-In-Cell simulations. Systematically analyzing nanowire length, diameter and gap size, we examine the underlying physical mechanisms that are provoking the enhancement of the longitudinal accelerating electric field. The parameter scan analysis shows that optimizing the spatial gap between the nanowires leads to larger enhancement than by the nanowire diameter and length, through increased electron heating.

5.4.2 Introduction

Laser-driven ion acceleration, as obtained by interaction of a high-intensity short-pulse laser with a target, is a recent field of interest for its many diverse potential applications[1-3]. Besides being a compact source, laser-accelerated protons feature a high brillance, a short bunch duration and a large energy spread. This has catalyzed their utilization in different domains that include ultra-fast radiography[4], novel fusion schemes[5], high energy density matter[6], laboratory astrophysics[7], medical applications[8-10], novel neutron sources[11], cultural heritage[12,13], material science[14-16] and using them as injectors for larger accelerators[17,18]. Most of these applications

have been currently explored with the most consolidated acceleration mechanism that is obtained on typical commercially available TW laser systems, the so-called Target-Normal Sheath Acceleration (TNSA)[19]. In this acceleration scheme, hydrogen containing contaminants are accelerated at the rear surface of a thin solid foil (target), typically made of gold (Au), aluminum (Al) or copper (Cu), that is irradiated by a high-intensity ($I_0 > 10^{18}$ W/cm^2), short pulse (< 1 ps) laser operating in the near-infrared spectral range. Since about two decades, scientists are trying to find ways to increase the proton energy and proton flux, such as to expand the portfolio of viable applications. Besides increasing the laser energy, which results in high proton energies[20], the most straightforward method to do so is by improving the laser energy absorption on the target, a key parameter to transferring energy into the accelerated ions.

In the past, there have been many suggestions on how to improve the target in order to maximize the laser-to-target absorption. Since one of the current trends for utilizing these sources for applications is by increasing the particle flux (for example, by increasing the shot rate), any new target proposal needs to result viable in terms of being easy and cheap to manufacture, and fast and non-stringent to align. Similar to photovoltaic applications, trapping light using micro- and nano-structured surfaces is one of the most established approaches to enhance the laser energy absorption[21-23]. In laser-driven ion acceleration, many studies have proposed nanostructuring the front target surface for this purpose, demonstrating both theoretically[24-31], and experimentally[32-42], an improvement in the absorption mechanisms. The drawback of such structures is that any trapping is limited to a nanometric scale in all three dimensions, which might not be always ideal. Nanometric rods standing up-right on a substrate in a brush-like geometry, also called nanowire (NW) targets, have recently been suggested for TNSA: These targets have the advantage of combining micrometric trapping thickness with nanometric structures. First theoretical and numerical estimations made by Wang *et al.* (2008)[43]have shown that this target type allows for an enhanced laser energy absorption. The same nanowire geometry has been demonstrated experimentally to be very effective for enhanced THz pulse generation[44], and several other works have demonstrated enhanced X-ray emission though greater electron heating with nano-velvets[45] and nanowires[46-48]. The high aspect ratio between length and diameter of NWs favors an increased laser absorption due to a greater effective interaction surface area with the incoming electromagnetic (EM) wave, occurring within a few laser cycles such as to maximize the interaction with the intact NW forest.

This increased interaction ejects electrons from the NW boundaries mainly through Brunel-type and $\boldsymbol{J} \times \boldsymbol{B}$ absorption processes, which are further accelerated in the gaps between the NWs by Direct Laser Acceleration (DLA) before re-collision with the target bulk[49], where the electrons seed a cascade of impact ionization events. This leads to a denser and hotter electron cloud at the rear side of the target and generates a more intense accelerating sheath electric field driving the TNSA mechanism. Only two experimental studies have been performed to demonstrate this effect: Firstly, Khaghani *et al.* (2017)[50] irradiated micro-pillar targets with a 80 J and 500 fs laser. They obtained a maximum energy enhancement ratio of up to 2.4 and 20 times more protons in the spectrum. They show a measured hot electron temperature increase by a factor of 2 at lower laser intensity. Secondly, Dozières *et al.* (2019)[51] used NW targets and obtained a maximum energy enhancement factor in the range 1.5-2. In the same work, an experimental evaluation of the influence of d and g was performed, recommending a thorough evaluation of influence of length l in a subsequent study. In both works, a direct comparison between nanowires and flat targets having the same thickness, within a systematic approach is missing, preventing conclusions to be drawn.

In this work we present a systematic study of enhanced laser-driven proton acceleration using Cu nanowire targets with regards to the geometrical parameters (length, diameter and gap). Our findings are supported and complemented numerically by Particle-In-Cell (PIC) simulations, which enabled a full parametric investigation. The effect of the NW's geometrical parameters are related to theoretical models for plasma expansion in vacuum[52]. The experimental study is complementary to Dozières *et al.* (2019)[51] and focuses on the NW length l as the main investigated parameter. Using experimental NW targets, we find average proton enhancement ratios of 2 and 3 for maximum energy and temperature respectively, as well as multiple-fold proton number enhancement. We relate these improvements to an enhanced TNSA-related electric field produced by a stronger hot electron yield, both in density n_e and temperature T_e. We find that the number of hot electrons generated by the interaction is dominantly influenced by the nanowire diameter, whereas a larger gap opening boosts the electron temperature up to a particular optimized gap size value. Between both parameters, the gap size has stronger influence compared to the nanowire diameter with regards to the laser energy absorption.

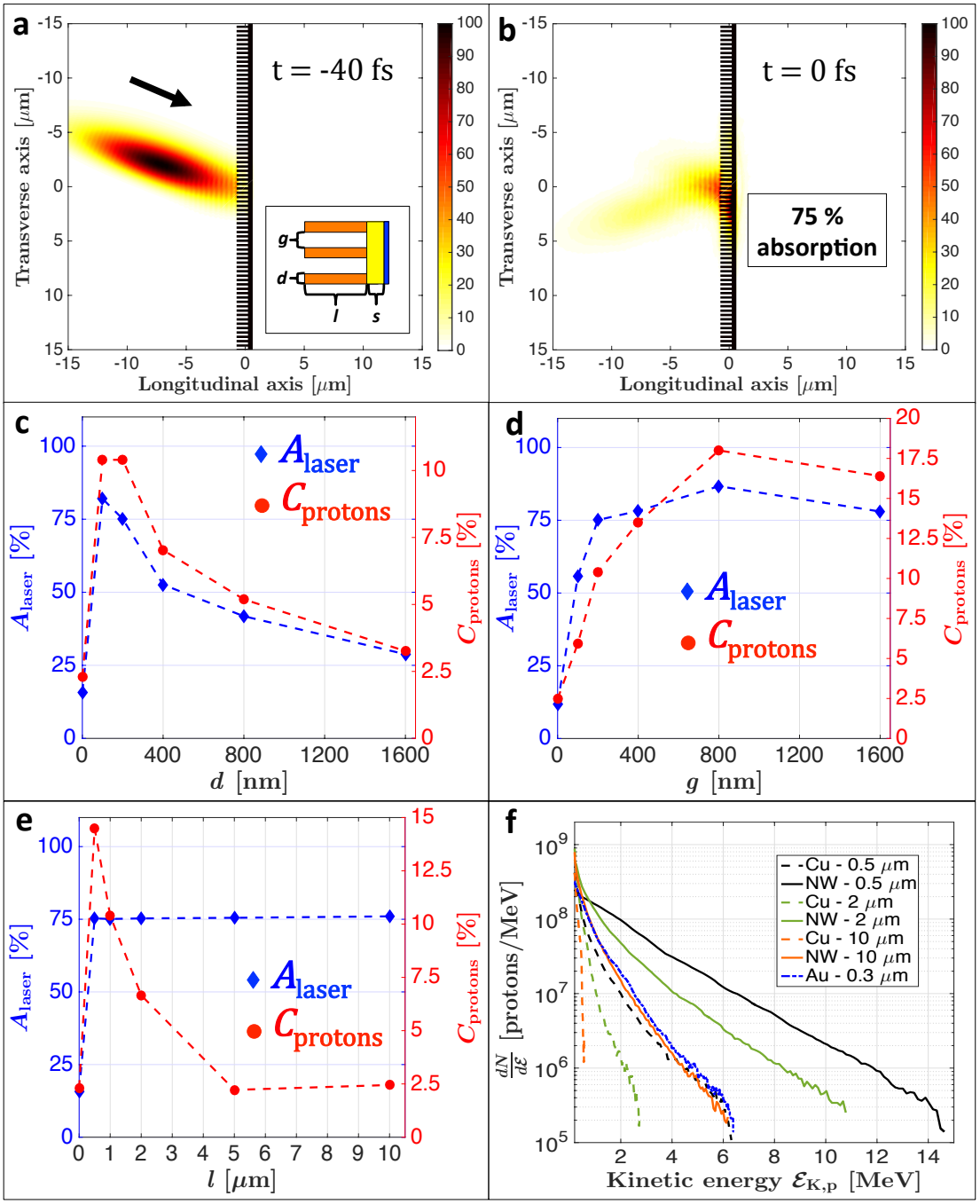

FIGURE 5.6: Numerical optimization of NW geometry through PIC simulations using the 2D3V PICLS code. (a) EM intensity and simulated target shown just before the laser interaction at $t = -40$ fs. Color scale is in percentage of maximum intensity. The inset is a NW scheme defining the geometry parameters d, g and l; target is composed of copper NW (orange), gold substrate (yellow) and a proton layer (blue). (b) EM intensity and simulated target shown during the laser-target interaction at $t = 0$ fs. (c-e) Variation of laser energy absorption (blue diamonds - left scale) and laser-to-proton conversion efficiency (red points - right scale) for different NW (c) diameters d, (d) gaps g and (e) lengths l. (f) Simulated proton spectra for NWs with $d = g = 200$ nm (same values as the experimental working point) and three different NW lengths of 0.5, 2 and 10 μm (solid lines), along with their thickness-equivalent Cu reference foils and the bare Au substrate of 0.3 μm (dotted lines).

5.4.3 NW Geometry Optimization

We performed Particle-In-Cell (PIC) simulations using the 2D3V PICLS code[53] to determine the optimal NW geometry for proton acceleration and thus to orient the NW production process. The 2D PIC simulations allow to investigate the role of NW length and check the optimal parameter range for the specific experimental configuration used in this work. In addition, the extensive parametric investigation considering all three parameter (d, g and l) allows a more comprehensive understanding of how the increased absorption and electron generation result in enhanced proton acceleration. Details about the simulation parameters can be found in *Methods* (see section 5.4.7). The simulation geometry is shown in Figure 5.6.a. We performed different parametric simulations to optimize the diameter d, gap g and length l of the NWs, starting from the best case scenario depicted by Wang *et al.* (2008)[43] (*i.e.* $d = 200$ nm, $g = 200$ nm and $l = 1$ μm at central laser wavelength of $\lambda_0 = 800$ nm) which we define as the nominal parameters. We varied each parameter independently, keeping the other parameters fixed. We can note in Figure 5.6.b where we present a snapshot of the simulation using the nominal parameters, a laser energy absorption of 75% compared to about 5% for a typical flat Cu foil, as is also shown in Figures 5.6.c-e for the best laser absorption cases (blue markers). Figure 5.6.c shows that the laser energy absorption and laser-to-proton conversion efficiency peak for NW diameters of $d = 200$ nm ($\lambda_0/4$). Laser absorption and conversion efficiency both increase for $d < 100$ nm, as consistent with the work of Martinez *et al.* (2018)[54], and then decrease after $d = 200$ nm. This can be justified as follows: for small NW diameters $d < 100$ nm, increasing d leads to higher laser energy absorption through a greater number of electrons interacting with the laser pulse, whereas for values larger than $d = 200$ nm the area irradiated by the laser is closer to a flat surface as it reflects more energy from the NW tip surface. Figure 5.6.d shows the variation of absorption with gap distance g, the laser energy absorption is already near-maximal at $g = 200$ nm ($\lambda_0/4$)[43], whereas the proton conversion efficiency optimum is found at $g = 800$ nm (λ_0). Interestingly, the laser absorption increases only slightly between 200 and 800 nm, while the laser-to-proton conversion efficiency increases significantly (almost doubles, passing from 10 to 18%). This difference among the two absorption mechanisms is due to the ejected electrons that are accelerated within the laser field in the gap region before re-collision with the target bulk: For too small gaps, the electrons reach the next NW with lower kinetic energy (*i.e.* lower electron temperature) than for larger gaps. Therefore, larger

gaps lead to a greater energy transfer to the protons, a phenomenon also observed and explained in the work of Blanco *et al.* (2017)[27] using triangular nanostructures and found also in other works[42,54,56,57]. Concerning the NW length variation exposed in Figure 5.6.e, we see that the laser energy absorption (blue diamonds) improves very strongly from $l = 0$ μm (flat target substrate of thickness s = 300 nm) to $l = 0.5$ μm, whereas for $l > 0.5$ μm it only increases by less than 1%. Concerning the laser-to-proton conversion efficiency (red dots), it is best for the shortest NWs and decreases for longer NW lengths. This is similar to what is observed in the TNSA regime when increasing the thickness of flat targets[55]. More precisely, electrons ejected from longer NWs will go through a larger effective material thickness and thus lose more energy (*i.e.* lower electron temperature) before reaching the rear target surface where they establish the accelerating sheath electric field. Hence, even if longer NWs lead to a greater laser energy absorption and therefore to greater number of ejected electrons, using long lengths also increases the energy loss of electrons during their re-collision with the target (wires and substrate), which ultimately produces lower laser-to-proton conversion efficiency. This effect is exhibited in Figure 5.6.f where we compare the simulated proton spectra for NW lengths of l =0.5, 2 and 10 μm with respect to their thickness-equivalent reference flat Cu foil spectra, along with the bare Au substrate case. All NW targets yield higher energies than their respective reference Cu foils, moreover the least performant NWs (*i.e.* $l = 10$ μm) provide equivalent kinetic energies than the most performant flat foil case, namely the 0.3 μm-thick Au substrate. The estimated maximum energy enhancement ratio is about 3 for $l = 0.5$ μm, 4.4 for $l = 2$ μm and goes up to a factor of 10 for $l = 10$ μm due to the low energies generated for such large thickness. We limited our simulations to 2D PIC simulations presented here, without exploring 3D PIC simulations, since our simulations already give a sufficiently complete idea of the main phenomena with regards to the enhanced acceleration mechanism, as well as offering a comprehensive view of the underlying phenomena occurring within the geometry optimization. However, we expect to observe lower enhancement ratios in the experiment since 2D PIC simulations are known to overestimate the electrons energies by a factor in the range of 1.5-2[58,59] through greater $\boldsymbol{J} \times \boldsymbol{B}$ electron heating, although this effect can be compensated by the shorter travel time of hot electrons in the NW interspace in 2D[60]. This proton energy overestimation is further amplified for NWs due to an overestimated electron confinement, leading to stronger TNSA electric field[60]. In the experiment, described in the following section, we did not use the proton-optimized gap of 800 nm due to limitations in the fabrication methodology and this will be the subject of further investigations. Nevertheless, the experimentally used gap of g

= 200 nm already provides a substantially increased laser-to-proton conversion efficiency by a factor of 5 with respect to the flat target case, moreover being near-optimal for the laser energy absorption as shown in Figure 5.6.d (blue diamonds).

5.4.4 Experimental Campaign

We performed experiments on the high-power Ti:Sapphire laser of the Lund Laser Center (LLC)[61] in Lund (Sweden). The system benefits of a double plasma mirror (DPM) configuration providing an Amplified Spontaneous Emission (ASE) pedestal contrast better than of 10^{-11} at 100 ps and 10^{-9} at 3 ps before the main pulse, with an energy transmission efficiency of 40%. Having an ultra-high contrast is essential for this type of study in order to keep the nanostructures intact when the main pulse arrives. The laser pulses had an energy of $\mathcal{E}_{\mathrm{L}} = 0.35$ J on target, a duration of $\tau_{\mathrm{L}} = 35$ fs yielding a peak power of 10 TW at a central wavelength of $\lambda_0 = 800$ nm, and the beam was focused down using an $f/3$ off-axis parabola to a focal spot diameter of $w_{\mathrm{FWHM}} = 3$ μm, providing an on-target intensity of $I_0 \sim 5 \times 10^{19}$ W/cm^2. The P-polarized pulses were incident on the targets at an angle of 20° with respect to target-normal direction to allow for the measurement of the reflected laser pulse and to avoid sending the reflection back in the laser system as when using 0° incidence, while preserving an efficient TNSA mechanism (reduction of laser-to-proton conversion efficiency from 13% at 0° compared to 10% at 20°, obtained from NW simulations using the nominal parameters). The proton beam spectrum was monitored by a calibrated Thomson Parabola (TP) spectrometer placed at 0°, coupled to a microchannel plate-phosphor assembly for particle detection. In order to monitor particles accelerated in the laser-backward direction, we used a Time-of-Flight (TOF) delay line oriented at 180° with respect to the TP spectrometer. In the TOF detector, the ions were detected using a Chemical Vapor Deposition (CVD) diamond detector[62-64]. The reflectivity of the target was measured using a Spectralon diffuser placed at the specular reflection angle compared to the impinging laser; an image of the scattered light was recorded on a CCD through a window of the chamber. Details of the experimental setup are presented in Figure 5.7. As targets we used Cu NW targets, with an average diameter of $d = 200$ nm, gap of $g = 200$ nm and five different verified lengths of $l = 0.5$, 1, 2, 5 and 10 μm. The used NW geometry provided an areal density of 6.25 NW/μm^2 (*i.e.* reduction of the effective electron density by a factor of 0.4 compared to Cu flat targets) and therefore approximately 44 NWs were located within the focal spot area. This NW density is slightly higher that the reported

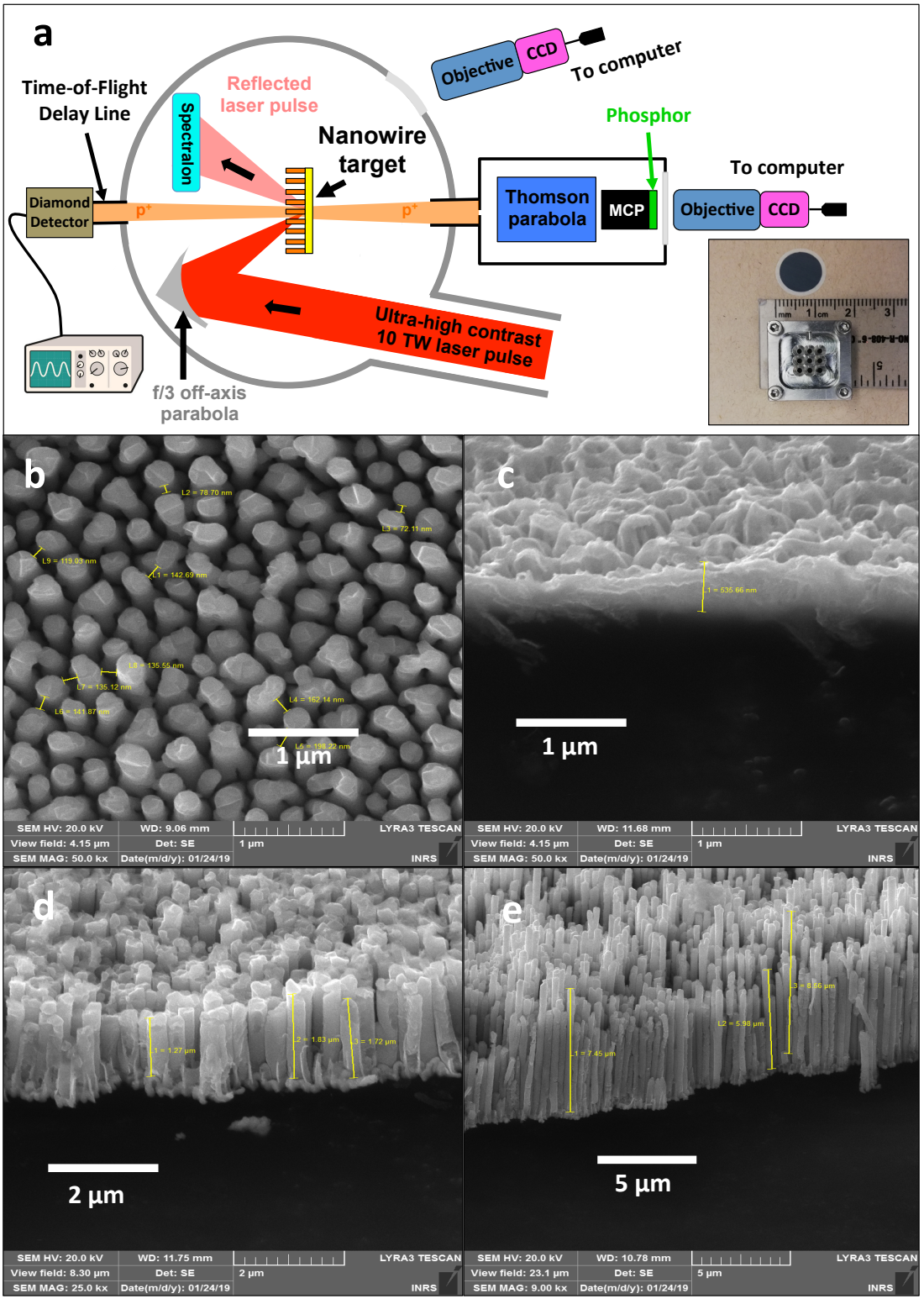

FIGURE 5.7: Experimental setup. (a) Schematic of the experimental setup showing the three main proton monitoring systems: a TP spectrometer at 0°, a TOF line at 180° and a Spectralon diffuser. (inset) Target holder specifically designed for holding the NW discs. (b-e) SEM images showing (b), a top view of the nanowire target. (c-e) different NW targets of different lengths (0.3 μm in (c), 1.5 μm in (d) and 8 μm in (e)).

optimum in the work of Dozières *et al.* (2019)[51] (around 1 NW per focal spot area), nevertheless the numerical optimum of this present study (d_{opt} = 200 nm and g_{opt} = 800 nm) yields 7 NWs per focal spot and thus points toward the same optimum value. We expect that this difference is due to the higher laser intensity (1.5×10^{21} W/cm^2) used in their study, as increasing the intensity would require longer traveling time for attaining maximal heating of the ejected electrons, suggesting the use of larger gap distances (*i.e.* lower number of NW per focal spot). The NWs were grown on a s = 300 nm thick Au substrate (the total thickness of the target being $s + l$) by electrodeposition using Anodic Aluminum Oxide (AAO) templates of 1 cm in diameter (available commercially, WHATMAN Anodisc), following the methodology described in Mondal *et al.* (2017)[44] and adapted from Gao *et al.* (2002)[65]. The NW production methodology is easily implementable in-house and inexpensive, allowing for large amounts of targets to be produced at once. However, the method still presents some limitations to vary the parameters d and g, another reason why we focused our attention on the experimental investigation of the parameter l. A specific target holder was designed for the NW discs allowing for 9 repetitive shots per disc, as shown in the inset of Figure 5.7.a. In order to test the repeatability of the data, and ensure statistically valid information, each target type was irradiated several times (3-18 times, depending on the available targets). Scanning Electron Microscope (SEM) images of the NW targets are shown in Figures 5.7.b-e for three different NW lengths. One can see that for very short NWs (NW length of 0.3 μm as indicated in Figure 5.7.c), the target surface appears to be very irregular and rugged, due to the too short growth time. Longer growth times form the as-expected forests of wires, as visible in Figures 5.7.d (1.5 μm) and 5.7.e (8 μm). The NW lengths l are measured using the postprocessing software of the SEM microscope, so that the NW lengths l are calibrated with the chemical reaction growth time. Reference shots were also taken on five types of Cu foils with thicknesses equivalent to the different NW lengths l (0.5, 1, 2, 5 and 10 μm), along with the NW bare Au substrate.

Figure 5.8.a shows the averaged proton spectra for different target types. Only three NW lengths (l = 0.5, 2 and 10 μm) are shown for better visualization of the data, along with their respective reference Cu foils. Considering the reference Cu foils, one can observe an improvement in the proton yield and maximum proton energy with decreasing foil thickness, the expected behavior for the TNSA mechanism. We find that any NW target we used results in an equivalent or higher proton yield and maximum proton energy than what obtained with the flat targets, including the bare Au substrate, in a very similar situation to what is observed

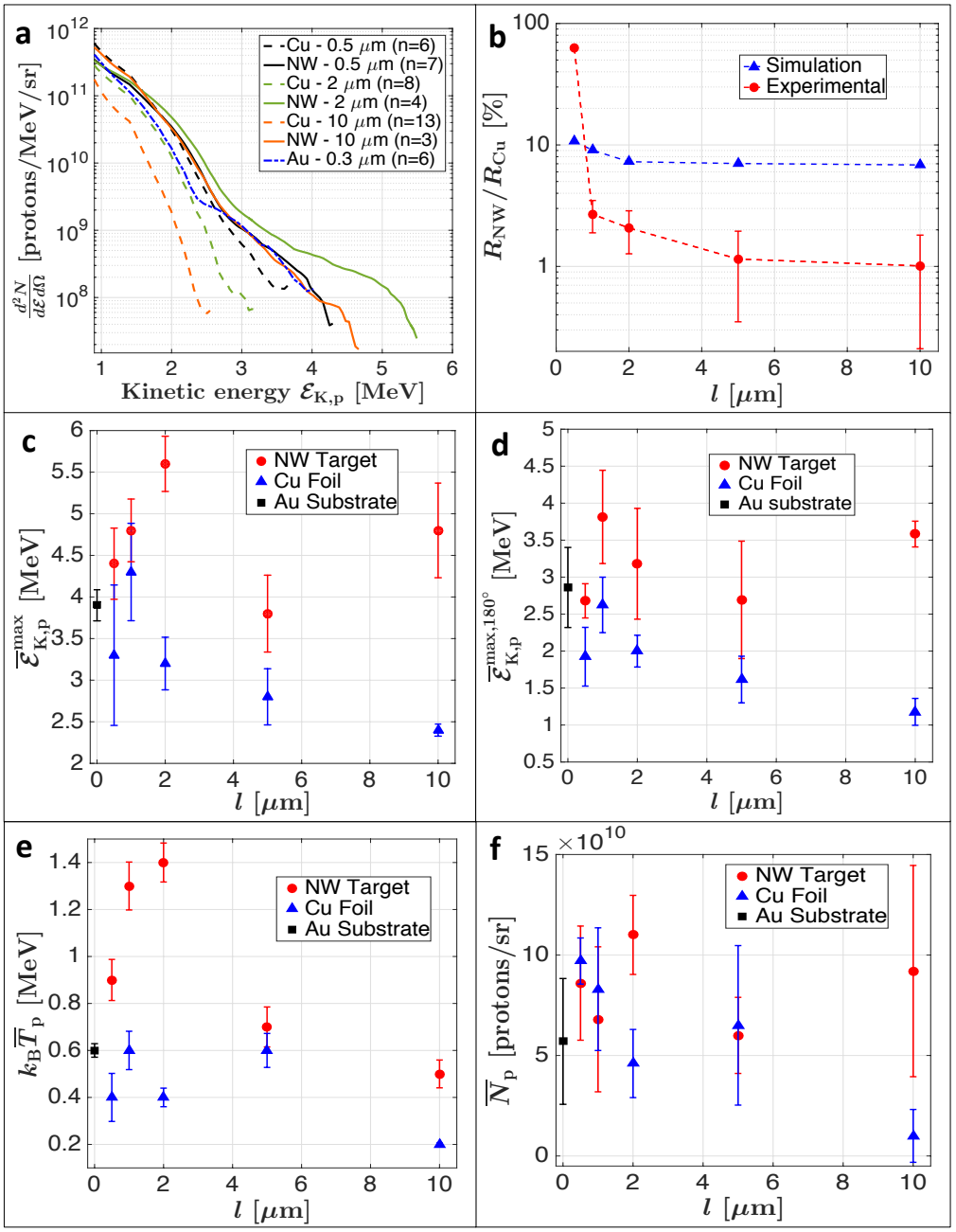

FIGURE 5.8: Experimental results for NW length investigation. ((a) Averaged spectra for NW targets (solid lines) along with their thickness-equivalent Cu reference foils and the bare Au substrate of 0.3 μm (dotted lines). (b) Reflectivity ratios of NW targets and Cu foils as obtained experimentally from the Spectralon diffuser (red points) and through PIC simulations (blue diamonds). Proton spectra characteristics (c-f) shown for NW targets (red circles), Cu reference foils (blue diamonds) and the bare 300 nm-thick Au substrate (black squares). (c) Average maximum proton energy in the forward acceleration direction $\overline{\mathcal{E}}^{max}_{K,p}$. (d) Average maximum proton energy in the backward acceleration direction $\overline{\mathcal{E}}^{max,180^\circ}_{K,p}$. (e) Average proton temperature $k_B\overline{T}_p$ as obtained by a linear fit on the log-plotted spectra in the high energy section. (f) Average integrated proton numbers $\overline{N}_p$ for $\mathcal{E}_{K,p} > 1$ MeV. The cumulated number of shots are of 7, 7, 4, 4 and 3 for NWs of length l = 0.5, 1, 2, 5 and 10 μm respectively. For Cu foils, the cumulated number of shots are of 6, 18, 8, 10 and 13 for thicknesses of 0.5, 1, 2, 5 and 10 μm respectively, as well as 6 shots the Au substrate. The shown uncertainties are the total standard deviations (instrument accuracy and shot-to-shot fluctuation summed in quadrature).

through simulations (see Figure 5.6.f). The NW length that yields the highest proton energies is found to be $l = 2$ μm with maximal proton energy of 5.6 MeV compared to 3.2 MeV for a Cu foil of equivalent thickness, giving a mean enhancement ratio of 1.8. Indeed, for NW lengths below 2 μm, the wires are not yet formed as well-defined cylinders (see Figure 5.7.c). This decreases the laser energy absorption and therefore reduces their performance in enhancing the TNSA acceleration mechanism. Nevertheless, a non-negligible enhancement is observed even for the rough surfaces as for the case of $l = 0.5$ μm, and is likely to be attributed to a different absorption mechanism such as from stochastic incidence angles as shown in Cerchez *et al.* (2018)[66]. As a comparison, the mean enhancement ratio for maximum energy with l = 10 μm is of about 2, however, the absolute maximum energy is slightly lower, 4.8 MeV, as expected for thicker targets. Hence, there is a compromise when choosing the working point: Short NW lengths produce higher proton energies, but are difficult to manufacture in a well-defined NW geometry. Longer NW lengths produce well-defined NW forests yielding high laser energy absorption, but decrease the TNSA mechanism efficiency due to the increased thickness[55]. Indeed, one can also note that if the spectra for the NW targets with length of 0.5 μm (full black curve) would have yielded the highest proton energies, the spectra from Figure 5.8.a would have been sorted in the same order of maximum energies (*i.e.* 10, 2 and 0.5 μm, from lowest to highest maximum energy) as is expected from simulations in Figure 5.6.f. In Figure 5.8.b we show the experimental and simulated laser-energy reflectivity ratios between NW targets and reference Cu foils. We can note that the reflectivity ratio obtained from PIC simulations very slowly increases from 7% for a target thickness of $l = 10$ μm to 10% for a thickness of $l = 0.5$ μm. The experimental reflectivity heavily increases for thicknesses below 2 μm since NWs become too short and form the aforementioned very rough surface (see Figure 5.7.c), which explains the less performant NWs with lengths of $l = 0.5$ and 1 μm. Nevertheless, we observe a good agreement between the simulated and experimental reflectivity ratio in terms of functional trend and amplitude, moreover also exhibiting the inverse trend as observed in Figure 5.6.e for laser energy absorption. The difference is due to the fact that during the experiment only the energy reflected in the specular direction is captured by the CCD looking at the Spectralon. Part of the energy is dispersed also by non-aligned nanowires, which leads to an underestimation of the total reflectivity. Figures 5.8.c-d show the maximum proton energy measured on the TP spectrometer placed at 0° in the forward acceleration direction $\overline{\mathcal{E}}_{\mathrm{K,p}}^{\mathrm{max}}$, in addition to those recorded at 180° in the backward acceleration direction $\overline{\mathcal{E}}_{\mathrm{K,p}}^{\mathrm{max,180^\circ}}$ using the TOF lines equipped with a diamond detector. One can see that all the NW types are univocally

superior in maximum energy compared to their equivalent Cu foils and also with respect to the bare Au substrate. TP measurements depicted in Figure 5.8.c show that the highest maximum energy is achieved for a NW length of 2 μm, before decreasing with shorter NWs of 0.5 and 1 μm. This represents a different but complementary trend than what is shown with simulations on Figure 5.6.e, but is explained by the fact that experimental NWs with thickness below 2 μm do not form a uniform and well-defined NW forest compared to longer lengths. Consequently, this effect decreases the laser energy absorption and thus also the efficiency of the TNSA mechanism. As a results, a decrease in performance is observed compared to a more efficient TNSA mechanism for shorter NWs, hence why the optimum is slightly shifted at $l = 1$ μm in backward direction. This suggests that the experimental optimal length is in the range of $l = 1 - 2$ μm. Some manufacturing problems occured with the $l = 5$ μm target, preventing to obtain perfectly flat NW targets. As a result, the performance of $l = 5$ μm is lower than for $l = 10$ μm. It is likely that this changed the target-normal direction and thus reduced the measured maximum energy. TOF measurements (Figure 5.7.d) show that even in the backward direction the enhancement in the maximum proton energy is significant for long NWs, despite a lower absolute energy value. The correlation between forward and backward direction acceleration mechanism has already been investigated for thin foil targets, and for high contrast lasers the two target sides showed similar maximum energy trends[67-69], with maximum energy slightly in favor of the forward acceleration scheme. The maximum proton energy in the backward direction is increased by a factor of 1.4 for target thicknesses of $l = 0.5$ μm, up to a factor of 2.9 at $l = 10$ μm. This effect is expected as the increase in laser energy absorption from NW geometry produces a larger amount of electrons and with higher temperatures in the plasma located also at the front target surface (the NW side), which expands and induces a charge separation that catalyzes the backward acceleration of ions. Even in the presence of nanostructures, the plasma expansion does uniformize the sheath electric field over time and produces an enhanced proton acceleration in the backward direction. On the temporal scale, the sheath electric field may have a lower peak value and gradient due to the rough NW surface compared to a flat surface, nevertheless the higher number of hotter electrons ultimately leads to a greater energy transfer to the ions also on the front target surface for backward acceleration. This is coherent with what is observed in the works of Dalui *et al.* (2015)[38], Cristoforretti *et al.* (2017)[39] and as well in Bagchi *et al.* (2012)[37] in the sub-relativistic regime where the laser intensity (10^{16} W/cm^2) is sufficient to strongly ionize the target bulk and induces a charge separation that leads to the backward ion acceleration. In Figure 5.8.e we show the extracted

energetic proton temperature $k_B\overline{T}_p$ as obtained by fitting a straight line in the high energy part of the log-spectrum just before the cutoff (*i.e.* Maxwell-Boltzmann distribution). The straight lines for obtaining the proton temperature are not shown in Figure 5.8.e for better visualization, but examples are shown in Figure 5.9. The trend regarding proton temperatures is more clear than for the maximum energies; Since the temperature is an average metric over the hot proton population, it is less dependent on variations of the target-normal direction compared to the measurements of the maximum energy with the TP spectrometer. It is clearly possible to see in Figure 5.8.e, the increasing proton temperature with decreasing NW length, having its optimum at $l = 2$ μm, before decreasing back for $l < 2$ μm due to misformed NWs. The proton temperatures are also all superior compared to their respective reference Cu foils, the enhancement ratio going up to a factor of 3.5 for $l = 2$ μm. In Figure 5.8.f we show the total proton number per unit solid angle $\overline{N}_p$ obtained by integrating the spectra for proton energies > 1 MeV. The trend here is less clear; proton numbers are slightly lower for some NW cases, but this is strongly dependent on the low energy threshold that we fixed when computing the integrated number and on the orientation of target-normal which produces a high statistical fluctuation in the measurement, given the small acceptance angle of the TP diagnostic. Nevertheless, the proton number enhancement is clear for $l = 2$ μm and $l = 10$ μm for enhancement ratios going up to 2.5 and 9, respectively.

As can be seen from these results, in all cases NW configurations improve the acceleration mechanism compared to flat foils of equivalent thickness, even when compared to the very thin Au substrate of 300 nm thick. This demonstrates that the enhancement mostly comes from the laser energy confinement determined by the NW parameters d and g, and is influenced to a lesser extent by the NW length l. The results obtained in this work are in agreement with the work of Khaghani *et al.* (2017)[50] with regards to maximum energy and number enhancement ratios. Moreover, they measured hot electron temperature improvements of a factor of 2 at a lower laser intensity (5×10^{17} W/cm^2), in agreement with our factor of 2, as shown for the electron temperature calculations through simulations presented in the next section. Concerning the work of Dozières *et al.* (2019)[51], the maximum energy enhancement ratios are again in good agreement with those of the present study.

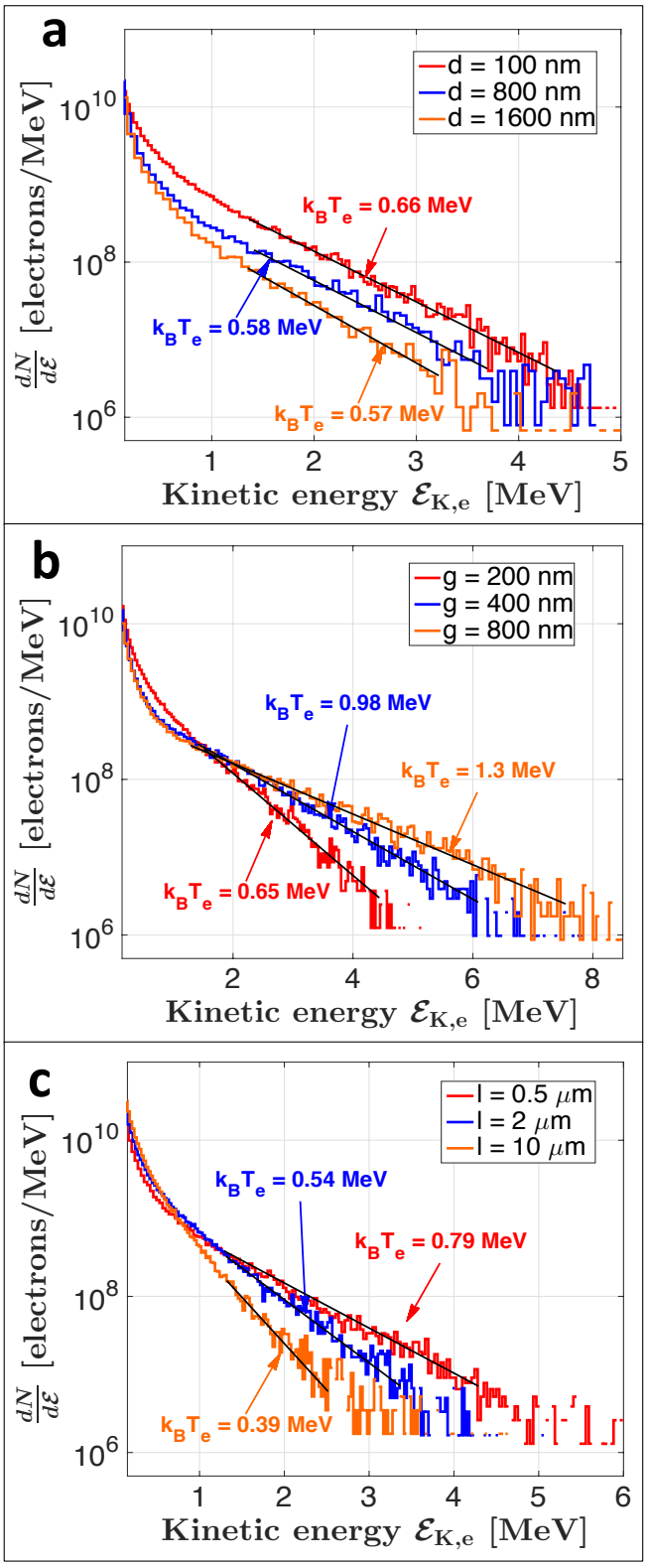

FIGURE 5.9: Simulated electron spectra at t = 40 fs after the interaction with the laser pulse for different NW (a) diameters d, (b) gaps g and (c) lengths l. Values of d, g and l are chosen for better visualization. The black lines correspond to linear fits in the relevant energy range for the retrieval of the hot electron temperature T_e^{hot}.

5.4.5 Underlying physical phenomena & Discussion

In light of the experiments, we analyzed the simulations to highlight the underlying physical mechanisms responsible for the enhanced proton acceleration. In Figure 5.9 we show the electron spectra immediately after the interaction of the laser pulse with the target at t = 40 fs. The hot electron temperature T_e^{hot} was calculated by obtaining the slope of a straight line fit in the high-energy part of the log-spectra, as for a Maxwell-Boltzmann distribution where $dN/d\mathcal{E} \sim e^{-\mathcal{E}_K/k_B T}$. The number of hot electrons N_e^{hot} was then calculated by integrating the spectra for energies above the ponderomotive energy $\mathcal{E}_{pond} = m_e c^2 \left(\sqrt{1+\frac{a_0^2}{2}} - 1\right)$ = 1.47 MeV, where a_0 is the normalized amplitude of the vector potential. On the first hand, we note from Figure 5.9.a that the hot electron temperature does not vary significantly with increasing NW diameter d (*i.e.* the slope does not change), however the number of hot electrons continuously decreases with increasing d (*i.e.* spectra are shifted downwards). Since large NW diameters tend towards the flat target case, this suggests that the NW diameter optimum for protons is due to an increased production of hot electrons, balanced by an increased reflection of the energy from the NW tips. On the other hand, varying the NW gap induces significant changes in the slope at high energies (*i.e.* the hot electron temperature) as we can observe in Figure 5.9.b, which is also observed in the work of Blanco *et al.* (2017)[27] and Vallières *et al.* (2019)[42]. The empty space between the nanostructures allows to eject and heat electrons from the NW boundaries by the laser pulse through Brunel-type and $\boldsymbol{J} \times \boldsymbol{B}$ absorptions. These electrons are then further accelerated by DLA due to a greater time of flight before re-collision with the target bulk, thereby increasing the temperature of the population. Finally in Figure 5.9.c, we note that increasing the NW length produces a reduction of both the hot electron number, since less low energy electrons can cross an increasingly thicker target, and the hot electron temperature. This results in an increased energy loss for thicker targets.

Showing that the behavior of n_e and T_e with nanostructured targets still respects fundamental equations of the TNSA mechanism, as presented by the work Mora (2003)[52], denotes a pure enhancement of the hot electron cloud by the nanostructures. To show that this occurs without any new unexpected effects facilitates the comprehension of the enhancement process. This is very important in order to guide the subsequent advances in enhanced laser-driven proton beams with nanostructures. To do so, we have checked the correspondence of N_e^{hot} and T_e^{hot} with $E_{sheath} = \sqrt{n_e k_B T_e/\varepsilon_0}$ and have first calculated $\overline{E}_{z,theory}^{max} \propto \sqrt{N_e^{hot} k_B T_e^{hot}}$, and further

evaluated the maximum longitudinal electric field from the simulations $\overline{E}^{\max}_{z,\mathrm{sim}}$. More precisely, $\overline{E}^{\max}_{z,\mathrm{sim}}$ is investigated in the simulations as the time-averaged maximum longitudinal electric field defined as follows:

$$\overline{E}^{\max}_{z,\mathrm{sim}} = \frac{1}{\tau_{\mathrm{acc}}} \int_{t_0}^{t_\mathrm{f}} \max_{x,z}\Big[E_z(x,z,t)\Big]\,\mathrm{d}t \tag{5.1}$$

where t_0 is the laser pulse interaction time with the target, t_f is the time where the simulation ends and $\tau_{\mathrm{acc}} = t_\mathrm{f} - t_0$ is the acceleration time. The metric presented in equation (5.1) allows to remove the temporal variation of the electric field, which is disturbed compared to the typical flat target case due to the NW shape, and rather looks at the global effect as is observed with the simulated or measured proton spectra. The variation of $\overline{E}^{\max}_{z,\mathrm{sim}}$ with d, g and l, compared to $\overline{E}^{\max}_{z,\mathrm{theory}}$, is shown in Figure 5.10. As it is possible to observe in Figures 5.10.a-c-e, there is a clear proportionality between $\overline{E}^{\max}_{z,\mathrm{sim}}$ and $\overline{E}^{\max}_{z,\mathrm{theory}}$ as they exhibit the same functional trend. Moreover, all parameters show the same trend and optima (d_{opt} = 100-200 nm, g_{opt} = 800 nm and l_{opt} = 0.5 μm) as for the geometry optimization presented on Figure 5.6. This brings a very comprehensive view of the effect of d, g and l on the TNSA mechanism. In particular, d increases the hot electron density, g is the driver for hot electron temperatures, which combined together produce an enhanced accelerating sheath electric field that ultimately leads to improved proton beam characteristics. This latter parameter g is key to achieve the highest value of temperatures and therefore of the rooted product $\sqrt{N_\mathrm{e}^{\mathrm{hot}} k_\mathrm{B} T_\mathrm{e}^{\mathrm{hot}}}$ for g = 800 nm, in agreement with the proton optimum presented in Figure 5.6.d. We have further verified the correspondence with the theoretical maximum proton energy expected from Mora (2003)[52], *i.e.* $\mathcal{E}^{\max}_{\mathrm{K,p}} = 2k_\mathrm{B}T_\mathrm{e}\left[\ln\left(t_\mathrm{p} + \sqrt{t_\mathrm{p}^2+1}\right)\right]^2$ with $t_\mathrm{p} = \omega_{\mathrm{p,i}} t/\sqrt{2\mathrm{e}}$ being the normalized acceleration time and $\omega_{\mathrm{p,i}} = \sqrt{Ze^2 n_\mathrm{e}/m_\mathrm{i}\varepsilon_0}$ being the ion plasma frequency. Using the maximum proton energies extracted from simulations, as well the extracted hot electrons numbers $N_\mathrm{e}^{\mathrm{hot}}$ and temperatures $k_\mathrm{B}T_\mathrm{e}^{\mathrm{hot}}$, we compare in Figures 5.10.b-d-f the theoretical $\mathcal{E}^{\max}_{\mathrm{K,p,theory}}$ and simulated $\mathcal{E}^{\max}_{\mathrm{K,p,sim}}$ maximum energies using the proportionality presented in the following equation (5.2):

$$\mathcal{E}^{\max}_{\mathrm{K,p,theory}} \propto 2k_\mathrm{B}T_\mathrm{e}^{\mathrm{hot}}\left[\ln\left(\sqrt{N_\mathrm{e}^{\mathrm{hot}}} + \sqrt{N_\mathrm{e}^{\mathrm{hot}}+1}\right)\right]^2 \tag{5.2}$$

As is possible to note from Figures 5.10.b-d-f, the functional behavior is well reproduced from theory (red markers in Figures 5.10.b-d-f) and is furthermore in agreement with the shapes of the laser-to-proton conversion efficiencies C_{proton} shown in Figures 5.6.c-d (red markers). The

linear dependence of $\mathcal{E}_{K,p}^{max}$ on T_e and logarithmic dependence on n_e, combined with the previously demonstrated relationships $T_e(d,g) \simeq T_e(g)$ and $n_e(d,g) \simeq n_e(d)$ (for a fixed optimized length l_{opt}) extracted from Figure 5.9, highlights the predominant importance of the parameter g to achieve the highest proton energies.

Regarding the discrepancy between the experimental and numerical maximum energy enhancement ratios of respectively 2 and 3, this is partially due to the very uniform and quasi-periodic geometry within the simulation box, whereas with the experimental NWs there is a distribution of gap distances within the focal spot area of the laser which lowers its efficiency. Concerning the optimal NW length l, shorter NWs are the most efficient to enhance the proton acceleration as correctly shown by simulations in the present study (Figure 5.6.e-f), down to the theoretical minimum proposed by Wang *et al.* (2008)[43] at 0.5 μm for a 800 nm laser wavelength. However, it is experimentally challenging to manufacture well-defined forests of short NWs using the electrodeposition methodology. This reduces the performance of too short NWs and produces an experimental optimum around $l = 1 - 2$ μm for this present study. On the one hand, even if long NWs are prone to generate more hot electrons due to an increased laser energy absorption (*i.e.* high hot electron density n_e), too long NWs produce an important energy loss of hot electrons going through the target bulk (*i.e.* lower hot electron temperature T_e) which has a greater impact on the maximum energy, as predicted by the Mora model. On the other hand, too short NWs, fabricated using the electrodeposition method used in this study, do not favor a high laser energy absorption due to a misformed NW forest, explaining the presence of an optimum that is clearly visible experimentally on Figure 5.8.e, but is not observable numerically on Figures 5.6.e and 5.10.e-f. Since it is the rooted product of n_e and T_e that is of crucial importance for the TNSA sheath electric field enhancement, a greater number of hot electrons does not necessarily produce a more intense accelerating field if the electron temperature is consequently lower, hence emphasizing the need to find the experimental optimum as in the case of this study. Moreover, regarding the substrate thickness, it is important to note that a too thin substrate may also lead to an over-fragile structure, a substrate thickness of about $s = 1$ μm or of comparable size to the length l is recommended.

This type of analysis is translatable and in agreement with other types of monolayered quasi-periodic nanostructures such as nanospheres in Vallières *et al.* (2019)[42] or nanotriangles in the work of Blanco *et al.* (2017)[27]. The best NW parameters for d and g are a compromise between high laser confinement in the interspace of NWs and reflection of the laser energy

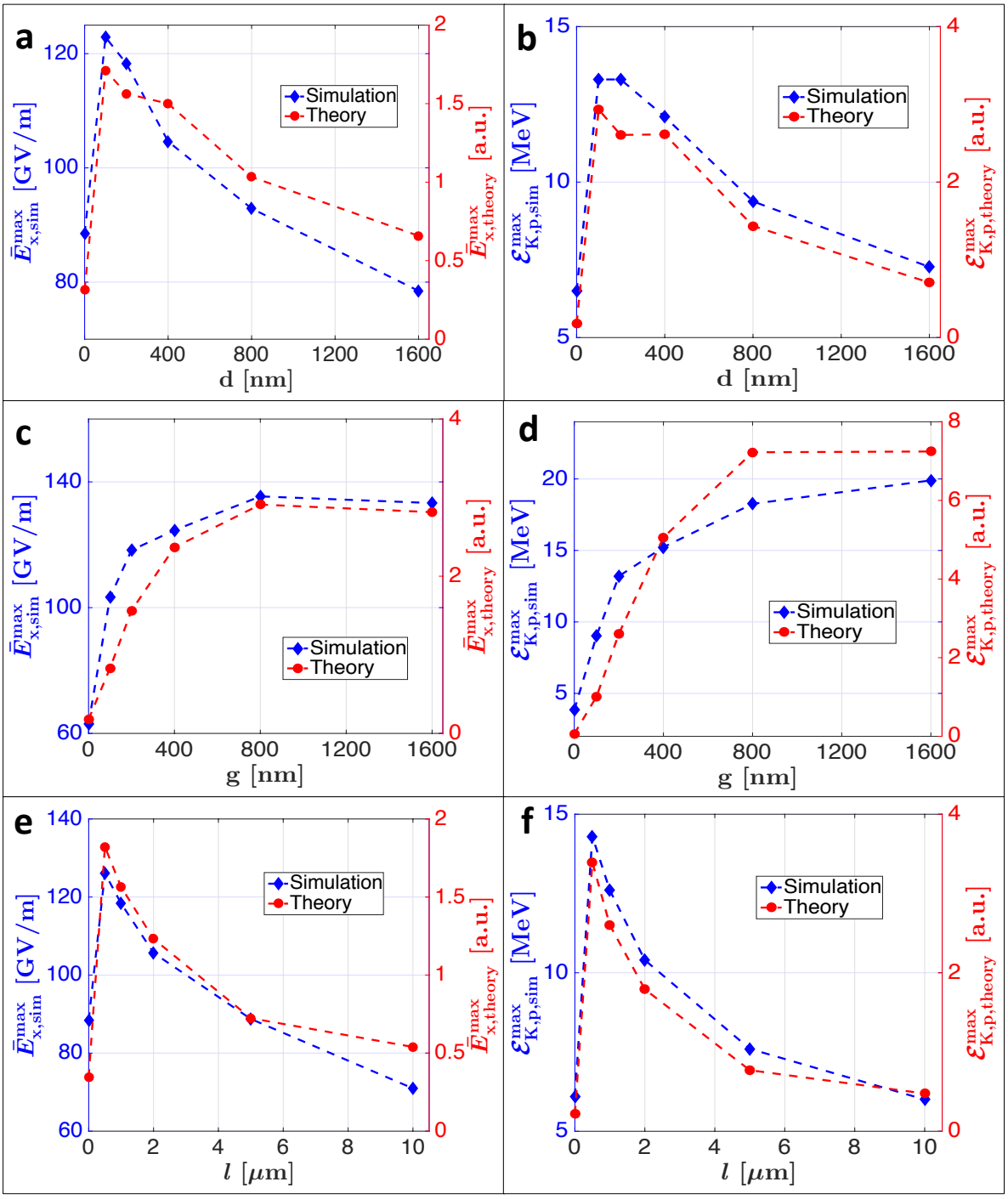

FIGURE 5.10: Time-averaged maximum longitudinal accelerating electric field $\overline{E}^{\max}_{z,\mathrm{sim}}$ (blue diamonds) calculated using (5.1) variation with NW (a) diameter d, (c) gap g and (e) length l, compared to $\overline{E}^{\max}_{z,\mathrm{theory}}$ (red dots). Simulated maximum proton energies $\mathcal{E}^{\max}_{\mathrm{K,p,sim}}$ variation with NW (b) diameter d, (d) gap g and (f) length l, compared to $\mathcal{E}^{\max}_{\mathrm{K,p,theory}}$ (red dots) calculated using (5.2).

from the NW tips. According to our simulations, an optimized NW diameter d favors the generation of higher hot electron densities n_e due to the multiple reflections of the pulse which ejects more electrons, whereas an optimized gap distance g boosts the electron temperature T_e since electrons are accelerated by the EM wave in the nanostructure interspace before re-collision with the substrate, in agreement with previous numerical studies[27,42,54,56,57]. It is the proper combination of these two parameters d and g that enhances the maximal TNSA sheath electric field as described in the formula $E_{sheath} = \sqrt{n_e k_B T_e / \varepsilon_0}$. Regarding the forward-accelerated proton beam enhancement also obtained at a sub-relativistic intensity (2×10^{17} W/cm^2) in Khaghani *et al.* (2017)[50] (backward acceleration enhancement with nanostructures at sub-relativistic intensity was demonstrated in other works[36,37]), we conclude that, if the hot electron production is not hindered by too thick substrate or NW length, then the hot electron cloud reaching the rear-side of the target can be substantially boosted in terms of numbers and temperature due to the strong heating in the wire interspace even if the absorption mechanisms vary. The DLA occurring within one laser cycle during the time of flight in the NW gap space is therefore essential, and reduces the need of very strict relativistic intensities for forward ion acceleration.

5.4.6 Conclusion

In conclusion, this work is the first to present a systematic study of the enhancement provided by nanowire targets for laser-driven proton acceleration in terms of the relevant geometrical parameters d, g and l, but also regarding their influence on the proton spectra characteristics (proton maximum energy, temperature and total number) in the TNSA regime, hence providing a comprehensive understanding of the proton beam enhancement with nanostructured targets. Experimental evidence exhibits high enhancement ratios for the proton spectra characteristics, in agreement with PIC simulations. A geometry optimization was also performed through PIC simulations allowing to define the best parameters for the LLC laser characteristics. A larger gap value of g = 800 nm between the nanowires is expected to provide even higher enhancement ratios according to our simulations. The aforementioned improvements will be the subject of a subsequent study. The easy production method along with the high enhancement ratios provided by NW targets open very promising avenues for laser-driven proton beam generation on ultra-high power laser facilities, where the proton energies would be of strong interest for material science, medical applications and laboratory astrophysics.

5.4.7 Methods

5.4.7.1 Nanowire Production

The Cu nanowire arrays were fabricated by the electrochemical deposition method, based on the methodology of Mondal *et al.* (2017)[44] which is adapted from Gao *et al.* (2002)[65]. The through-hole Anodic Aluminum Oxide (AAO) membrane (pore size: 0.2 μm, membrane thickness: 60 μm, WHATMAN Anodisc) was applied as the template for the electrochemical deposition of Cu NWs. With a layer of gold (300 nm) sputtered on the one side, the AAO membrane served as the working cathode electrode in a conventional three-electrode cell for the electrochemical deposition. The graphite carbon and the saturated calomel electrode (SCE) were applied as the counter and the reference electrode, respectively. The electrolyte was a mixture of 0.2 M $CuSO_4$ and 0.1 M H_3BO_3. Experiments were carried out by using a potentiostat (Autolab) with the constant potential of -1.20 V (vs. SCE) at room temperature. The length of the Cu NWs can be controlled between 0 and 20 μm by adjusting the deposition time during the synthesis. The nanowire diameter and the gap size were dictated by the template itself, which were around 200 nm for both and further confirmed by the Scanning Electron Microscope (SEM) characterization. For the SEM characterization, the as-prepared Cu nanowires embedded in the template were first immersed in a 1 M NaOH solution for 20 min to dissolve the AAO membrane. Then, they were rinsed in distilled water several times and let dry for 24 hours prior to the shots. Special multi-target holders have been developed to perform multiple laser shots on one template. Prior to the laser shots, the AAO templates were dissolved inside the multi-target holder using the aforementioned methodology.

5.4.7.2 PIC Simulations

The PIC simulations involve a Gaussian p-polarized laser pulse incident at 20° with respect to target-normal, at a wavelength of $\lambda_0 = 800$ nm, a pulse duration of $\tau_L = 35$ fs at Full-Width Half-Maximum (FWHM), focused down to a Gaussian focal spot size of $w_{FWHM} = 3$ μm on the target at an intensity of 6×10^{19} W/cm^2, leading to $a_0 = 5.3$ where a_0 is the normalized amplitude of the vector potential. The simulation grid uses $\Delta x = \Delta z = 20$ nm, $\Delta t = \Delta z/c = 66$ as and runs over 800 fs. The box size is of 4080×4000 cells ($102\lambda_0 \times 100\lambda_0$) in the transverse and longitudinal axes respectively. Copper nanowires were placed on a 300 nm thick gold foil,

both with electron densities of $100n_c$, where n_c is the critical density at $\lambda_0 = 800$ nm. A 20 nm proton layer was placed at the back of the target with a density of $15n_c$. Copper and gold ion species were initiated at the 3+ ionization level with field and collisional ionizations enabled. We used 30 macroparticles per cell for electrons and the corresponding numbers for ion species to ensure charge neutrality in each cell at the initial state of the simulation. The investigated geometrical parameters were lengths of l = 0, 0.5, 1, 2, 5 and 10 μm, diameters of d = 0, 100, 200, 400, 800 and 1600 nm, as well as gaps of g = 0, 100, 200, 400, 800 and 1600 nm. Only one NW parameter was varied at a time around the nominal NW parameters of $d = 200$ nm, $g = 200$ nm and $l = 1$ μm. Each simulation runs 16 hours on 600 cores.

5.4.8 Acknowledgements

This work is supported by FRQNT (nouveaux chercheurs, Grant No. 174726, Equipe 2016-PR-189974), the National Sciences and Engineering Research Council of Canada (NSERC) (Discovery Grant RGPIN-2018-05772 and the Alexander-Graham-Bell Graduate Scholarship for S.V.), Compute Canada (Job: pve-323-ac) as well as the Canada Foundation for Innovation (CFI). This study has also received financial support from the French National Research Agency (ANR) in the frame of "the Investments for the future" Programme IdEx Bordeaux - ANR-10-IDEX-03-02, from the Swedish Research Council (VR) and the Knut and Alice Wallenberg Foundation (KAW). Concerning the use of the Lund Laser Center, we acknowledge support by Laserlab Europe (grant agreement 654148 under the European Union's Horizon 2020 research and innovation programme). We would like to thank Tsuneyuki Ozaki for the fruitful discussions, Anders Persson, Riccardo De Angelis and Pierluigi Andreoli for the technical support, and Claudio Verona for lending us some equipment.

5.4.9 References

[1] J. Badziak, "Laser-driven ion acceleration: methods, challenges and prospects", *IOP Conf. Series: J. of Physics: Conf. Series*, vol. 95, 012001 (2018).

[2] A. Macchi, "A Review of Laser-Plasma Ion Acceleration", *arXiv:1712.06443*, (2017).

[3] H. Daido, M. Nishiuchi & A. S. Pirozhkov, "Review of laser-driven ion sources and their applications", *Rep. Prog. Phys.*, vol. 75, 056401 (2012).

[4] L. Romagnani *et al.*, "Dynamics of Electric Fields Driving the Laser Acceleration of Multi-MeV Protons", *Phys. Rev. Lett.*, vol. 95, 195001 (2005).

[5] M. Roth *et al.*, "Fast Ignition by Intense Laser-Accelerated Proton Beams", *Phys. Rev. Lett.*, vol. 86, 436 (2001).

[6] P. K. Patel, A. J. Mackinnon, M. H. Key, T. E. Cowan, M. E. Foord, M. Allen, D. F. Price, H. Ruhl, P. T. Springer & R. Stephens, "Isochoric Heating of Solid-Density Matter with an Ultrafast Proton Beam", *Phys. Rev. Lett.* vol. 91, 125004 (2003).

[7] B. Albertazzi *et al.*, "Laboratory formation of a scaled protostellar jet by coaligned poloidal magnetic field", *Science*, vol. 346, 325 (2014).

[8] A. Yogo *et al.*, "Measurement of relative biological effectiveness of protons in human cancer cells using a laser-driven quasi-monoenergetic proton beamline", *Appl. Phys. Lett.*, vol. 98, 053701 (2011).

[9] J. Metzkes, T. E. Cowan, L. Karsch, S. D. Kraft, J. Pawelke, C. Richter, T. Richter, K. Zeil & U. Schramm, "Preparation of laser-accelerated proton beams for radio-biological applications", *Nucl. Instrum. Methods Phys. Res.*, Sect. A, vol. 653, 172 (2011).

[10] D. Doria *et al.*, "Biological effectiveness on live cells of laser driven protons at dose rates exceeding 109 Gy/s", *AIP Adv.*, vol. 2, 011209 (2012).

[11] M. Roth *et al.*, "Bright Laser-Driven Neutron Source Based on the Relativistic Transparency of Solids", *Phys. Rev. Lett.*, vol. 110, 044802 (2013).

[12] M. Barberio, S. Veltri, M. Scisciò, & P. Antici, "Laser-accelerated proton beams as diagnostics for cultural heritage", *Sci. Rep.*, vol. 7, 40415 (2017).

[13] M. Barberio & P. Antici, "Laser-PIXE using laser-accelerated proton beams", *Sci. Rep.*, vol. 9, 6855 (2019).

[14] M. Barberio, M. Scisciò, S. Vallières, F. Cardelli, S.N. Chen, G. Famulari, T. Gangolf, G. Revet, A. Schiavi, M. Senzacqua & P. Antici, "Laser-accelerated particle beams for stress testing of materials", *Nat. Comm.*, vol. 9, 372 (2018).

[15] M. Barberio, S. Vallières, M. Scisciò, G. Kolhatkar, A. Ruediger & P. Antici, "Graphitization of diamond by laser-accelerated proton beams", *Carbon*, vol. 138, 531-537 (2018).

[16] M. Barberio, M. Scisciò, S. Vallières, S. Veltri, A. Morabito & P. Antici, "Laser-Generated Proton Beams for High-Precision Ultra-Fast Crystal Synthesis", *Sci. Rep.*, vol. 7, 12522 (2017).

[17] P. Antici, M. Fazi, A. Lombardi, M. Migliorati, L. Palumbo, P. Audebert & J. Fuchs, "Numerical study of a linear accelerator using laser-generated proton beams as a source", *J. Appl. Phys.*, vol. 104, 124901 (2008).

[18] P. Antici, M. Migliorati, A. Mostacci, L. Picardi, L. Palumbo & C. Ronsivalle, "A compact post-acceleration scheme for laser-generated protons", *Phys. Plasmas*, vol. 18, 073103 (2011).

[19] S. C. Wilks., W. L. Kruer, M. Tabak & A. B. Langdon, "Absorption of Ultra-Intense Laser Pulses", *Phys. Rev. Lett.*, vol. 69, 1383 (1992).

[20] J. Fuchs *et al.*, "Laser-driven proton scaling laws and newpaths towards energy increase", *Nat. Phys.*, vol. 2, 48-54 (2006).

[21] G. Shi & E. Kioupakis, "Electronic and Optical Properties of Nanoporous Silicon for Solar-Cell Applications", *ACS Photonics*, vol. 2 (2), 208-2015 (2015).

[22] K. Aydin, V. E. Ferry, R. M. Briggs, & H. A. Atwater, "Broadband Polarization-Independent Resonant Light Absorption Using Ultrathin Plasmonic Super Absorbers", *Nat. Commun.*, vol. 2, 517 (2011).

[23] F. Rosei, "Nanostructured Surfaces: Challenges and Frontiers in Nanotechnology", *Condens. Mat.*, vol. 16 (17), S1373 (2004).

[24] A. Andreev *et al.*, "Efficient Generation of Fast Ions from Surface Modulated Nanostructure Targets Irradiated by High Intensity Short-Pulse Lasers", *Phys. Plasmas*, vol. 18, 103103 (2011).

[25] O. Klimo *et al.*, "Short Pulse Laser Interaction with Micro-Structured Targets: Simulations of Laser Absorption and Ion Acceleration", *New J. of Phys.*, vol. 13, 053028 (2011).

[26] J. Yu *et al.*, "Laser-Driven Proton Acceleration Using a Conical Nanobrush Target", *Phys. Plasmas*, vol. 19, 053108 (2012).

[27] M. Blanco *et al.*, "Table-top laser-based proton acceleration in nanostructured targets", *New J. Phys.*, vol. 19, 033004 (2017).

[28] A. Lübcke *et al.*, "Prospects of Target Nanostructuring for Laser Proton Acceleration", *Sci. Rep.*, vol. 7, 44030 (2017).

[29] L. Ji *et al.*, "Exploring Novel Target Structures for Manipulating Relativistic Laser-Plasma Interaction", *High P. Las. Sci. and Eng.*, vol. 5, e14 (2017).

[30] L. Fedeli, A. Formenti, L. Cialfi, A. Pazzaglia, & M. Passoni, "Ultra-intense laser interaction with nanostructured near-critical plasmas", *Sci. Rep.*, vol. 8, 3834 (2018).

[31] M. Passoni *et al.*, "Advanced laser-driven ion sources and their applications in materials and nuclear science", *Plasma Phys. Control. Fusion*, vol. 62, 014022 (2019).

[32] D. Margarone *et al.*, "Laser-Driven Proton Acceleration Enhancement by Nanostructured Foils", *Phys. Rev. Lett.*, vol. 109, 234801 (2012).

[33] L. Giuffrida *et al.*, "Manipulation of Laser-Accelerated Proton Beam Profiles by Nanostructured and Microstructured Targets", *Phys. Rev. Acc. and Beams*, vol. 20, 081301 (2017).

[34] L. Torrisi, L. Calcagno, M. Cutroneo, J. Badziak, M. Rosinski, A. Zaras-Szydlowska & A. Torrisi, "Nanostructured targets for TNSA laser ion acceleration", *Nukleonika*, vol. 61, 103 (2016).

[35] L. Torrisi, "Ion acceleration from intense laser-generated plasma: methods, diagnostics and possible applications", *Nukleonika*, vol. 60, 207 (2015).

[36] S. Bagchi *et al.*, "Fast Ion Beams from Intense, Femtosecond Laser Irradiated Nanostructured Surfaces", *Appl. Phys.*, vol. 88, 167-173 (2007).

[37] S. Bagchi, P. Prem Kiran, W.-M. Wang, Z. M. Sheng, M. K. Bhuyan, M. Krishnamurthy, & G. Ravindra Kumar, "Surface-plasmon-enhanced MeV ions from femtosecond laser irradiated, periodically modulated surfaces", *Phys. Plasmas*, vol. 19, 030703 (2012).

[38] M. Dalui, W.-M. Wang, T. Madhu Trivikram, S. Sarkar, S. Tata, J. Jha, P. Ayyub, Z. M. Sheng & M. Krishnamurthy, "Preferential enhancement of laser-driven carbon ion acceleration from optimized nanostructured surfaces", *Sci. Rep.*, vol. 5, 11930 (2015).

[39] G. Cristoforetti *et al.*, "Transition from Coherent to Stochastic electron heating in ultrashort relativistic laser interaction with structured targets", *Sci. Rep.*, vol. 7, 1479 (2017).

[40] T. Ebert *et al.*, "Laser-Induced Microstructures on Silicon for Laser-Driven Acceleration Experiments", *High P. Las. Sci. and Eng*, vol. 5, e13 (2017).

[41] M. Passoni *et al.*, "Toward High-energy Laser-Driven Ion Beams: Nanostructured Double-Layer Targets", *Phys. Rev. Acc. and Beams*, vol. 19, 061301 (2016).

[42] S. Vallières, M. Barberio, M. Scisciò, E. d'Humières, & P. Antici, "Enhanced laser-driven proton acceleration using ultrasmall nanoparticles", *Phys. Rev. Acc. and Beams*, vol. 22, 091303 (2019).

[43] W.-M. Wang, Z.-M. Sheng, M. Y. Yu & J. Zhang, "A Model for the Efficient Coupling Between Intense Lasers and Subwavelength Grating Targets", *Phys. Plasmas*, vol. 15, 030702 (2008).

[44] S. Mondal *et al.*, "Aligned Copper Nanorod Arrays for Highly Efficient Generation of Intense Ultra-Broadband THz Pulses", *Sci. Rep.*, vol. 7, 40058 (2017).

[45] G. Kulcsár *et al.*, "Intense Picosecond X-Ray Pulses from Laser Plasmas by Use of Nanostructured 'Velvet' Targets", *Phys. Rev. Lett.*, vol. 84 (22), (2000).

[46] M. A. Purvis *et al.*, "Relativistic Plasma Nanophotonics for Ultrahigh Energy Density Physics", *Nat. Phot.*, vol. 7, 796-800 (2013).

[47] C. Bargsten *et al.*, "Energy penetration into arrays of aligned nanowires irradiated with relativistic intensities: Scaling to terabar pressures", *Sci. Adv.*, vol. 3, 1601558 (2017).

[48] R. Hollinger *et al.*, "Efficient picosecond x-ray pulse generation from plasmas in the radiation dominated regime", *Optica*, vol. 4 (11), 111344 (2017).

[49] A. Moreau *et al.*, "Enhanced electron acceleration in aligned nanowire arrays irradiated at highly relativistic intensities", *Plas. Phys. Control. Fusion*, vol. 62, 014013 (2020).

[50] D. Khaghani *et al.*, "Enhancing Laser-Driven Proton Acceleration by Using Micro-Pillar Arrays at High Drive Energy", *Sci. Rep.*, vol. 7, 11366 (2017).

[51] M. Dozières *et al.*, "Optimization of laser-nanowire target interaction to increase the proton acceleration efficiency", *Plas. Phys. Control. Fusion*, vol. 61, 065016 (2019).

[52] P. Mora, "Plasma Expansion into a Vacuum", *Phys. Rev. Lett.*, vol. 90 (18), 185002 (2003).

[53] Y. Sentoku & A. J. Kemp, "Numerical Methods for Particle Simulations at Extreme Densities and Temperatures: Weighted Particles, Relativistic Collisions and Reduced Currents", *Journal of Computational Physics* vol. 227 (14), p. 6846-6861 (2008).

[54] B. Martinez, E. d'Humières & L. Gremillet, "Synchrotron emission from nanowire array targets irradiated by ultraintense laserpulses", *Plasma Phys. Control. Fusion*, vol. 60, 074009 (2018).

[55] Q. L. Dong, Z.-M. Sheng, M. Y. Yu & J. Zhang, "Optimization of Ion Acceleration in the Interaction of Intense Femtosecond Laser Pulses with Ultrathin Foil", *Phys. Rev. E.*, vol. 68, 026408 (2003).

[56] L. Cao *et al.*, "Control of the hot electrons produced by laser interaction with nanolayered target", *Phys. Plasmas*, vol. 17, 103106 (2010).

[57] L. Cao *et al.*, "Enhanced absorption of intense short-pulse laser light by subwavelength nanolayered target", *Phys. Plasmas*, vol. 17, 043103 (2010).

[58] J.-L. Liu, M. Chen, J. Zheng, Z.-M. Sheng & C.-S. Liu, "Three dimensional effects on proton acceleration by intense laser solid target interaction", *Phys. Plasmas*, vol. 20, 063107 (2013).

[59] D. J. Stark, L. Yin, B. J. Albright & F. Guo, "Effects of dimensionality on kinetic simulations of laser-ion acceleration in the transparency regime", *Phys. Plasmas*, vol. 20, 053103 (2017).

[60] S. Jiang, A. G. Krygier, D. W. Schumacher, K. U. Akli & R. R. Freeman, "Effects of front-surface target structures on properties of relativistic laser-plasma electrons", *Phys. Rev. E*, vol. 89, 013106 (2014).

[61] B. Aurand *et al.*, "A Setup for Studies of Laser-Driven Proton Acceleration at the Lund Laser Centre", *Laser and Particle Beams*, vol. 33, 59-64 (2015).

[62] M. Marinelli *et al.*, "Analysis of laser-generated plasma ionizing radiation by synthetic single crystal diamond detectors", *Appl. Surf. Sci.*, vol. 272, 104-108 (2013).

[63] R. De Angelis *et al.*, "High performance diagnostics for Time-Of-Flight and X ray measurements in laser produced plasmas, based on fast diamond detectors", *J. Instrum.*, vol. 11, C12048 (2016).

[64] M. Cipriani *et al.*, "Spectral characterization by CVD diamond detectors of energetic protons from high-repetition rate laser for aneutronic nuclear fusion experiments", *J. Instrum.*, vol. 14, C01027 (2019).

[65] T. Gao, G. Meng, Y. Wang, S. Sun & L. Zhang, "Electrochemical Synthesis of Copper Nanowires", *Journal of Physics: Condensed Matter*, vol. 14, 355363 (2002).

[66] M. Cerchez, M. Swantusch, M. Toncian, X. M. Zhu, R. Prasad, T. Toncian, Ch. Rödel, O. Jäckel, G. G. Paulus, A. A. Andreev & O. Willi, "Enhanced energy absorption of high intensity laser pulses by targets of modulated surface", *Appl. Phys. Lett.*, vol. 112, 221103 (2018).

[67] S. Fourmaux *et al.*, "Investigation of laser-driven proton acceleration using ultra-short, ultra-intense laser pulses", *Phys. Plasmas*, vol. 20, 013110 (2013).

[68] T. Ceccotti *et al.*, "Proton Acceleration with High-Intensity Ultrahigh-Contrast Laser Pulses", *Phys. Rev. Lett.*, vol. 99, 185002 (2007).

[69] A. Levy *et al.*, "Proton Acceleration With High-Intensity Laser Pulses in Ultrahigh Contrast Regime", *IEEE Trans. Plas. Sci.*, vol. 36 (4), 185002 (2008).

5.5 Perspectives

In light of the two studies on solid target nanostructuration for generating enhanced TNSA ion beams, it appears clear that there are common grounds to both works. One of them is the demonstration that surface nanostructuration ultimately leads to a pure electron sheath enhancement, through a hotter and denser electron cloud, and is well described by Mora's model on plasma expansion into vacuum [81]. Indeed this model requires no further validation, and this is not the point here. What is important to notice is that the electron sheath enhancement occurs without any new unexpected effects, such as complex temporal waveforms (*e.g.* several spikes) of the accelerating field resulting from the multiple EM wave reflection within the nanostructure, and therefore greatly simplifies the comprehension of the enhancement process. The correspondence to Mora's model further strengthens the relationship to the fundamental equations and completes the full link between increased laser energy absorption, hotter and denser electron clouds, more intense accelerating electric fields that ultimately lead to enhanced ion energies. The next step is to build prediction models based on the nanostructure's geometrical parameters and the fundamental equations, namely the relativistic electron interaction with an EM wave as well as plasma expansion into vacuum. Within the range of laser intensities explored during this doctoral work ($I_0 \sim 10^{18} - 10^{21}$ W/cm^2), it is now more obvious that surface nanostructuration provides greater effective interaction surface between the incoming EM wave and the target, leading to an increased amount of relativistic laser-matter absorption processes. It has been noted several times in the literature that electrons stemming out of the target's material undergo stronger $\boldsymbol{J} \times \boldsymbol{B}$ absorption, Vacuum Heating and, most importantly, Direct Laser Acceleration. Interestingly, the work performed by Blanco *et al.* (2017) [222] is an excellent starting point for the proper understanding of the enhanced absorption with nanostructures, within the mathematical framework of the relativistic electron motion in vacuum when it interacts with a high-intensity EM wave (equations (2.20), (2.21) and (2.22)).

In the case of quasi-periodic nanostructures, such as nanospheres or nanowires as investigated in this doctoral work, it is relevant to split the geometrical parameters in two subsets: the shape parameters (*i.e.* diameter d_{NP} for nanospheres, diameter d and length l for nanowires) and the gap distance g. As is shown by both studies on nanostructures performed in this doctoral work, the shape parameters drive the hot electron generation leading to increased hot electron

densities n_e^{hot}, whereas the gap boosts the hot electron temperature T_e^{hot}. The former are the key to obtain higher particles numbers in the resulting ion beam, whereas the latter is the key to reach higher kinetic energies. Understanding the distinctive influence of both parameter subsets is essential for further advances in surface nanostructuration, and their proper optimization is necessary for achieving higher ion beam brightnesses (higher particle numbers, higher kinetic energies and lower divergences), without the need for building excessively expensive large-scale high-power laser facilities. Strong enhancement without excessive costs is what will enable improved applications and further commercialization of laser-driven ion sources. One last important point to note is that the reasoning developed here applies to all type of quasi-periodic nanostructures (*i.e.* nanotriangles, nanoellipsoids, nanowires, *etc.*), and hence can receive further generalization.

For the specific situation of laser-driven ion acceleration with nanowire targets, the effect of nanowire length seems to be of secondary importance when compared to the influence of the nanowire diameter and gap, although not to be neglected. As aforementioned in the study on nanowires of this doctoral work, the shortest nanowire length that can experimentally form a well-defined nanowire forest is advisable. The chosen optimized length henceforth determines the proper substrate thickness to use, which should be around the same magnitude as the nanowire length to infer sufficient torque resistance to the target's structure. Using our very thin 300 nm-thick substrate, it was noted that the nanowire drying period induces strong surface tensions and Van der Waals forces from the water molecules trapped within the nanoforest, which substantially deformed and wrinkled the nanowire target's shape. In some extreme cases, this lead to the complete rupture of the structure, thereby generating a lot of problems to obtain reproducible proton beams in the Thomson Parabola spectrometer. A properly chosen substrate thickness that infers enough target stiffness is therefore required for providing high repeatability. In the case of enhanced X-ray generation using nanowire targets, as noted from several other studies in the literature [226–229], it is preferable to have very long wires (tens of microns) such as to maximize the laser energy absorption leading to strong hot electron generation, hence producing more intense X-ray beams. The substrate, or a secondary target placed directly behind, can be sufficiently thick and made with high Z material in order to maximize the energy conversion of the high energy electrons into X-rays, without over attenuating them by a too thick substrate as a compromise. On this particular subject, a recent study used these concepts all together to enhance the production of Bethe-Heitler electron-positron pairs [230].

Moreover, along the same lines, nanowire targets are also excellent candidates for measuring Breit-Wheeler electron-positron pairs by colliding enhanced X-ray beams [231].

Regarding the production methodology used in this doctoral work, one of the limitations for nanowires is the unavailability to vary the gap distance g, as opposed to the possibility to buy templates with different pore sizes leading to different diameters d. At the considered laser intensities, the theoretical optimal configuration is $d_{\text{opt}} = 200$ nm ($\lambda_0/4$) and $g_{\text{opt}} = 800$ nm (λ_0), the latter being unachievable with the current production methodology. For the nanowire length, the optimal value depends on the application, for TNSA being of 1-2 μm with a substrate thickness of the same size, whereas for X-ray generation being most probably in the tens of microns. It is very likely that these optimal values change when using different laser parameters, for instance with larger gap required for higher intensities or with longer NWs required for longer pulse durations. Hence, the full-parametric analysis has to be re-performed when the laser parameters differ significantly from those used in this work. As scan of the parametric optima variations for different laser parameters would make a very useful future investigation to further generalize the concepts found in this work. Concerning nanospheres, the target production methodology is very random which makes it difficult to control the gap distance, even though it is the key for higher energy enhancement. Similarly to nanowires, it is most probable that an optimum is located for $d_{\text{NP, opt}} \approx \lambda_0/4$ and $g_{\text{opt}} \approx \lambda_0$, a working point not investigated in the literature up to now. Another limitation for nanowires made from commercial AAO templates is the small circular 1 cm^2 surface area of the templates, which is fixed by the manufacturer. It would be better to have access to larger surfaces such as squares of 10×10 cm^2 for instance, to facilitate their insertion in a multi-hole target holder encompassing several hundreds to thousands of holes. Achieving this milestone would be a "game changer" for generating high-repetition rate enhanced ion beams using nanowire targets. In general, cutting large thin foils to make independent targets and, for the specific case of nanowires made from AAO templates, having multiple templates placed in a mosaic to form a larger target setup increases the target-to-target variability, leading to greater shot-to-shot fluctuations in the resulting ion beam. The ideal case is to have only one single large NW target placed in a multi-hole target holder, with an available interwire gap distance of 800 nm.

Lastly, one of the great questions that arise with the use of nanostructured targets regards their enhancement properties without the necessity of using an ultra-high contrast of 10^{10} down to

at least -10 ps before the main pulse. This kind of contrast is typically achieved using double plasma mirrors (DPM), which may not be convenient to use. In non-published data, we have noticed in the Lund experimental campaign that bypassing the DPM yielded higher proton kinetic energies since the on-target intensity is more than doubled (transmission factor of DPM around 30-40%). The use of a DPM also generated strong shot-to-shot fluctuations in the resulting ion beam. Hence, one easily wonders if enhanced proton beams with nanostructured targets can be achieved with moderate (10^7) to high (10^9) picosecond contrasts, obtained without the use of plasma mirrors. This would enable an increased shot-to-shot repeatability, faster repetition-rate and higher intensity ion beams at the same time, compared to the cumbersome use of a DPM. The ALLS 100 TW is an excellent candidate to evaluate this avenue, having a contrast $> 10^9$ up to at least -100 ps, reducing to 10^8 at -20 ps, finally reaching 10^6 at -3 ps before a very steep power rise. This is a good intermediate-range contrast obtained from the combination of saturable absorbers and a cross-wave polarizer (XPW) placed in between the two CPA stages. Repeating the nanowire study on ALLS 100 TW to answer the contrast question seems like an obvious next step to take with nanostructured targets. Performing this experiment requires to have a transverse plane imaging system for target alignment (see Figure 3.1), due to the use of a 9-hole target holder specifically developed for NWs, as shown in the second study of this Chapter. This specific target holder prevents to use the already implemented shadowgraphic target alignment system, however a transverse plane imaging system is in commissioning at the moment of writing these lines. Once implemented, a robust alignment system combined with a high number of shots per pumping from a multi-hole target holder will enable to perform a plethora of novel investigations (see Perspectives of Chapter 4) on the ALLS laser-driven ion beamline.

Chapter 6

General Conclusion

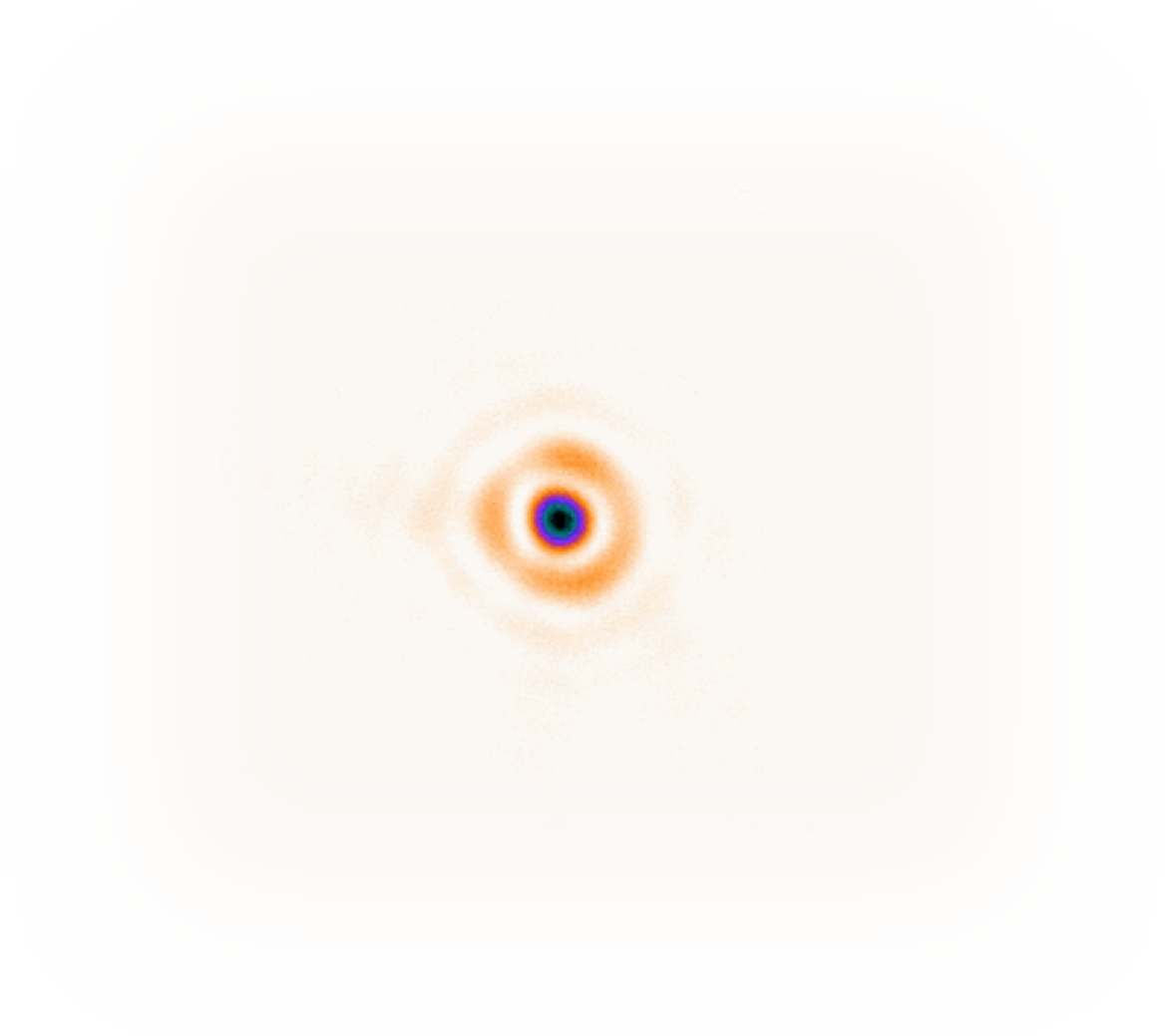

ALLS 100 TW focal spot measured at full laser power.

Chapter Content

6.1 Summary & novelty of work

This doctoral work dealt with the development of laser-driven ion beamlines using solid targets in the TNSA regime. The general effort tackled three different aspects of laser-based ion acceleration, yet equivalently essential, namely precise target positioning, enhanced laser-matter interactions using nanostructures and the development of efficient particle diagnostics. The improvement of these three aspects, for which I hope to have pushed further forward the frontiers of knowledge, lead to greater shot-to-shot ion beam reliability, more intense particle bunches and enables high repetition-rate beamlines, respectively. The work resulted in five first-author articles published or accepted in peer-reviewed scientific journals. The next few sections serve as wrap-up of each independent effort and describes their associated novelties with particular relevance for the laser-plasma community.

Shot-to-shot reliability: Submicrometric target positioning

The repetitive precise positioning of targets is essential, to say the least, to ensure repeatable laser-matter interactions. Obtaining a high-quality focal spot at a particular point in space, here called TCC, already consists in a quite adventurous task from the experimental point of view with high-power lasers. Once this task is achieved, the shot-to-shot precise positioning of targets at TCC, in a high vacuum environment, leading to the minimization of the peak intensity uncertainty at the interaction point, is the subsequent challenge and is explored in Chapter 3. This particular challenge must allow for performing high shot rates as a temporal constraint, otherwise not complying with the high-flux requirements of accelerated ion sources. The study presented in Chapter 3 exposes the development of a Target Positioning Interferometer (TPI) that reaches subwavelength positioning uncertainties of $\Delta z = 350$ nm $\approx \lambda_0/2$, corresponding to an intensity error below 0.2% from target positioning. The TPI's novel design is a modified

Michelson interferometer that incorporates an aspherical converging lens in a fully vacuum-compatible target arm to transform it from a relative to an absolute positioning device having a single unambiguity point in space. Its sensitivity is furthermore boosted by slightly tilting the mirror in the reference arm as to avoid the central lobe of the interferometric pattern. The high positioning accuracy is achieved also through the use of a complex, yet, but efficient numerical fringe analysis algorithm that maximizes the extraction of high SNR signals in an optimized timeframe. Considering the high flux of data incoming from interferometric fringe measurements, the development of a fast numerical algorithm (few hundred milliseconds for a single position measurement) is crucial to make the TPI a viable solution for its implementation in a laser-based ion accelerator. As we could expect, reaching this level of positioning accuracy and sensitivity is a double-edged knife, the TPI being reactive to several environmental factors that generate acousto-mechanical vibrations. In the foreseen context of high repetition-rate ion beamlines achievable in a very near future, it appears clear the place of a device such as the TPI within a beamline must be for a limited temporal use to refine the alignment an entire multi-hole target holder containing hundreds to thousands of holes, and not the individual target holes. Using four sampling points in the transverse plane at the edges of the holder, the TPI would iteratively adjust the target holder's longitudinal position along the focal axis accordingly, beforehand of a raster series of laser shots. Concerning the conventional alignment techniques, shadowgraphic imaging must be set aside if a mutli-hole target holder is used, for the obvious reason that the holder itself blocks the measurement of the thin foil's shadow. In this context, transverse plane imaging is still of high relevance, moreover being more robust and stable than an interferometric technique, at the expense of lower positioning accuracy. This being said, the TPI, when incorporated, should be considered as a higher precision system that refines the alignment and ensures redundancy to the transverse plane imaging method.

High repetition-rate beamlines: Efficient particle diagnostics

Efficient particle diagnostics that incorporate fully-digitized fast readout, resistance to EMP, fine energy resolution and high signal saturation thresholds, essential characteristics that are required on foreseen high repetition-rate ion beamlines. In Chapter 4, two studies on particle diagnostics used for laser-driven ion beams are presented. The first study is related to the absolute number calibration, on a Tandem Van de Graaff accelerator, of the newly released EBT-XD type of RCF. They are found to have larger dose detection range and higher minimum energy

threshold, hence more suitable for intense ion beamlines. A severe response quenching effect was remarked when the Bragg peak of the measured particle falls directly within the active layer of the RCF, causing large dose uncertainties and therefore significant particle number misestimation errors reaching 200%. Based on this fact, it is concluded that the conventional absolute particle number determination using RCF stacks typically performed in laser-based ion acceleration is flawed, and should not be used anymore for absolute dose determination but rather be limited to relative dose measurements. It is also noted that RCFs are not suitable for continuous use in high repetition-rate ion beamlines, nevertheless they still allow to provide very important information on the beam characteristics and should be used in the initial characterization stages of a beamline and for punctual measurements. The second study exposed the performance of a TP-TOF cross-calibrated set of detectors implemented on the ALLS 100 TW ion beamline. The TP spectrometer used includes an MCP detector that was calibrated in intensity from single proton impacts obtained in a RBS experimental setup from a Tandem Van de Graaff accelerator. A unique numerical methodology that uses pixel clusters analysis was developed to analyze the particle impacts and reconstruct the response function of the MCP detection system from them. This detection system shows a high signal amplification gain and exhibits fast temporal response with a dead time in the few milliseconds range, two characteristics very much suitable for being incorporated in a high repetition-rate beamline. Having TOF detection lines oriented slightly off-axis with respect to target-normal proved to be very useful to, firstly, calibrate the field integrals of the TP spectrometer and, secondly, to infer particle numbers and energies on-axis (0°) when performing so-called 'blind shots' for which the TP spectrometer measurement axis is blocked by a secondary target. This type of beamline setup that uses correlated detectors promises to be very efficient to provide particle beam information when high particle fluxes are achieved with a large number of consecutive shots. The 'blind shots' are typically performed in the context of applications of laser-driven ion beams. Their exploitation is, in my opinion, the lever to demonstrate the applicability and commercialization potential of laser-based beamlines, a step enabled by proper constant monitoring of the ion source.

Intense particle bunches: Amplified relativistic laser-matter interactions

Enhanced relativistic laser-matter interactions using target surface nanostructuration allow for the generation of hotter and denser hot electron clouds at the rear side of solid targets used in

laser-based ion acceleration. This ultimately leads to greater ion numbers and higher kinetic energies (*i.e.* more intense ion bunches), compared to the use of the same laser pulse incident on flat target. The multiple-fold enhancements in particle numbers and energies are most welcome in this context considering the ponderomotive scaling ($\mathcal{E}_K^{max} \propto \sqrt{I_0}\lambda$) in the TNSA regime. It was shown numerically and experimentally in Chapter 5 that it is possible to double the maximum kinetic energy of ions using nanostructured targets. Achieving the same enhancement endpoint by tuning the laser pulse would require either to increase the laser energy, reduce the pulse duration or to reduce focal spot area by a factor of four. These achievements for reaching a quadrupled peak intensity involve significant financial costs that are typically much larger than those associated to nanostructured target production, even when considering a combination of these three improvements on the laser pulse. From the theoretical and numerical standpoints, it is shown from the studies exposed in Chapter 5 that the key to reach high kinetic energies when using quasi-periodic nanostructures passes by opening the gap distance between the nanostructure sub-units, in order to properly accelerate the ejected hot electrons during their time-of-flight in the gap space, before their re-collision with the target bulk. This comes out as an elegant correspondence with the proverb "less is more". The gap distance must not be too large, its optimal value being found when $g_{opt} = \lambda_0$. Moreover, both studies also showed that the key to enhance the output particle numbers with nanostructures passes by a careful optimization of what I personally call the shape factors (d_{NP} for nanospheres, d and l for nanowires). The optimal values are found by maximizing the EM wave trapping within the nanostructure, leading to high laser energy absorption, thereby generating copious amounts of hot electrons. For instance, the optimal nanowire diameter, found for $d_{opt} = \lambda_0/4$, is a compromise between larger amounts of hot electrons generated and the laser energy reflection on the nanowire tips. The optimal nanowire length, on its turn, must be the shortest experimentally achievable that produces a well-defined quasi-periodic nanostructure, and was found here to be of $l_{opt} = 1 - 2$ μm. The previous statement is true for lengths at least down to $l = 0.5$ μm, and must be further explored for shorter nanostructures. Incorporating the geometrical parameters in the development of semi-empirical models, based on the equations of motion (2.20), (2.21) and (2.22) as well as the Mora model (see section 2.3.1), is of utmost importance for further pushing the use of nanostructured targets. This will lead to the production of models from fundamental concepts that predict the best geometry to use for generating more intense laser-based ion beams.

6.2 Other contributions

The work performed during this doctoral degree also includes additional contributions to the field of laser-plasma interactions, in particular to applications of laser-driven ion beams. I contributed through the design of experiments (I), support during experimental campaigns (II), numerical modeling (III), data analysis (IV) and manuscript redaction (V). Below are listed the publications into which I am either co-author in articles published in scientific journals or first-author in conference proceedings.

Co-authored publications

1) P. Puyuelo-Valdes, **S. Vallières**, M. Salvadori, S. Payeur, S. Fourmaux, J.-C. Kieffer, F. Hannachi & P. Antici, "Combined Laser-Based X-ray and Proton-Induced Fluorescence: a Versatile, Fast, Multi-Element Analysis Tool for Investigation of Artifacts", *Nature Materials*, submitted, August 2020. **Contribution: I - II - IV - V**

2) M. Barberio, M. Salvadori, **S. Vallières**, M. Patterson, E. Skantzakis, A. Sarkissian & P. Antici, "Nanoparticle Coatings as Fluorescent Sensor Detecting Radiation Pollution in Laser Plasma Experiments", *Scientific Reports*, submitted, August 2020. **Contribution: II**

3) M. Barberio, S. Giusepponi, **S. Vallières**, M. Scisciò, M. Celino & P. Antici, "Ultra-fast High-Precision Metallic Nanoparticle Synthesis using Laser-Accelerated Protons", *Scientific Reports*, vol. 10, 9570 (2020). **Contribution: II - III - IV - V**

4) M. Barberio, **S. Vallières**, M. Scisciò, G. Kolhatkar, A. Ruediger & P. Antici, "Graphitization of Diamond by Laser-Accelerated Proton Beams", *Carbon*, vol. 139, 531-537 (2018). **Contribution: III - IV - V**

5) M. Barberio, M. Scisciò, **S. Vallières**, F. Cardelli, S. N. Chen, G. Famulari, T. Gangolf, G. Revet, A. Schiavi, M. Senzacqua & P. Antici, "Laser-Accelerated Particle Beams for Stress Testing of Materials", *Nature Communications*, vol. 9, 372 (2018). **Contribution: III - IV - V**

6) M. Barberio, M. Scisciò, **S. Vallières**, S. Veltri, A. Morabito & P. Antici, "Laser-Generated Proton Beams for High-Precision Ultra-Fast Crystal Synthesis", *Scientific Reports*, vol. 7, 12522 (2017). **Contribution: III - IV - V**

Conference proceedings

1) **S. Vallières**, P. Puyuelo-Valdes, M. Salvadori, C. Bienvenue, S. Payeur, E. d'Humières & P. Antici, "The Laser-Driven Ion Acceleration Beamline on ALLS 200 TW for Testing Nanowire Targets", *Proceeding SPIE 11037*, 11037-03 (2019).

2) **S. Vallières**, M. Scisciò, S. Veltri, M. Barberio, E. d'Humières & P. Antici, "Enhancement of Laser-Driven Proton Beams Using Nanostructured Solid Foils", *OSA Proceeding*, HM3A.6 (2018).

3) **S. Vallières**, A. Morabito, S. Veltri, M. Scisciò, M. Barberio & P. Antici, "Laser-Driven Proton Acceleration with Nanostructured Targets", *Proceeding SPIE 10240*, 10240-09 (2017).

6.3 Outlook

Some technical prowesses on ALLS 100 TW

In an attempt to further open the discussion, I find it necessary to mention some very important aspects, embedded within this doctoral work, that did not make the subject of publications. It is well-known in the high-power laser community that ramping up the pulse energy of a laser produces distortions in the resulting laser beam due to non-linear effects and heating occurring in the amplifying crystal and other related optics. Moreover the focal spot optimization, performed by adjusting the degrees of freedom of an off-axis parabolic mirror, is typically done at low laser energy in the few milliJoule range as to avoid damaging the focal spot imaging optics and camera. Further ramping up the laser energy in the Joule range makes the task of measuring the focal spot very difficult since the high peak power generates beam distortions caused from non-linear effects in the attenuators themselves, moreover can damage the CCD camera in one single laser shot. For these reasons, in most high-power laser facilities, the focal spot optimization and its imaging are performed at low laser energy, and then the energy is ramped up for performing the high-intensity shots, without knowing the state of the high-intensity focal spot at the shot. Following the clever advices of my colleagues Stéphane Payeur and Sylvain Fourmaux, a focal spot imaging system that allows to measure the focal spot at full laser power (2 J in 20 fs, see Chapter's symbolic image) was successfully developed and implemented on the laser-driven ion beamline. This achievement provides the opportunity to

optimize the focal spot in vacuum at full laser energy, using fully-motorized degrees of freedom on the off-axis parabola, as well as partially compensating the global distortions in the laser beam resulting from the strong amplification. I have to admit that observing with my own (protected) eyes the vivid flashes of white light emitted from the fluorescence of the focal spot imaging optics, used at full laser energy, is one of the most impressive effects I have seen. More precisely, even though the laser's central wavelength is in the near-infrared ($\lambda_0 = 800$ nm) and therefore not being visible to the human eye, the enormous quantities of multiphoton absorptions, harmonic generation and four-wave mixing occurring in the imaging optics at high power make them intensely fluoresce over the entire visible spectrum, yielding observable white light flashes running at the repetition rate of the laser. This high-power focal spot imaging system, used in combination with concomitant high-power wavefront optimization using a deformable mirror, produces a measurable high-quality focal spot even at relativistic intensities thus being, in my humble opinion, one of the keys to reach unprecedented peak intensities. Having this combined system, along with low shot-to-shot pulse energy fluctuations (2.5% RMS here), must be a gauge of laser quality to further increase the reliability of laser-driven ion sources of the next generation.

The next generation of laser-driven ion beamlines

At the present time, reaching several hundreds of MeV proton beams generated with the current high-power laser technologies appears extremely challenging. Nevertheless, a myriad of proton beam applications lie in the 1-100 MeV range, and as such more effort should be put, from the laser-based ion acceleration community, towards the consolidation of the known concepts all together. The next lift-off of the field will occur when the production of compact, cost-effective, reliable, intense and high repetition-rate ion sources will be a reality, all these characteristics being true at the same time. I am personally convinced we are truly on the verge of unlocking this possibility. What do we need to achieve it? Please let me delineate how I think will resemble the next generation of laser-driven ion sources:

- A few Joule-level high-power laser in the hundreds of TW scale, operating at a repetition-rate of several Hz. The environmental characteristics and laser beamline control must be high enough to yield laser energy shot-to-shot fluctuations in the few percent RMS range at most.

- A moderate to high laser contrast better than 10^9 at -100 ps, reaching the critical 10^6 end-point only a few ps before the main pulse, followed by a very abrupt power rise to ensure the generation of steep hot electron density gradients.
- A focal spot imaging system and wavefront sensor-deformable mirror optimization loop operating a full laser power, leading to a high-quality focal spot at relativistic intensity.
- An iterative, automated focal spot optimization loop to fine tune the focused intensity. This technique would iterate the movements of motors on the off-axis parabola using the sampled image of the focal spot obtained at full power. A numerical algorithm that uses Maximum-Likelihood Expectation-Maximization (MLEM) or even Machine Learning is foreseeable.
- A mutli-hole target holder containing roughly a thousand holes placed in a 10×10 cm^2 cartesian grid. The holder should be installed on two long-range (10-20 cm) translation stages for moving the holder in the transverse xy-plane. Their movements should be coordinated electronically with a software such as to provide an automated and fast movement along the cartesian grid of holes. The transverse movements along the holes from center-to-center should be coordinated at the same rate as the laser's repetition-rate. A short-ranged picomotor with very fine step size can be used along the longitudinal axis z.
- Large area metallic nanowire targets such as to fit a single one into the 10×10 cm^2 grid. The nanowires should have a diameter of $d = 200$ nm, a gap of $g = 800$ nm, a length of $l = 1$ μm, and sitting on a substrate of $s = 1$ μm.
- A transverse plane imaging system used on the rear target surface for rough target alignment. A TPI to refine the target holder alignment to a submicrometric position by iteratively adjusting the longitudinal positions using a few judiciously selected points in the transverse plane. These operations are optimized to be performed in real time such as to avoid slowing down the beamline.
- An MCP-TP spectrometer on the 0° axis with respect to target-normal for efficient and fast ion beam characterization. At least two TOF lines using diamond detectors should be placed on both sides of the target-normal (negative and positive orientations). Both TOF lines should be carefully cross-calibrated in particle numbers and energies with the MCP-TP spectrometer. All detectors should be properly triggered to operate at the repetition-rate of the laser.

- A fully-digitized online beam profiler using scintillators and an associated imaging system than can be easily placed "in" or "out" of the entire ion beam path. This detector needs to be properly calibrated and characterized for absolute dose measurements, ideally on a conventional particle accelerator using Faraday Cups, therefore allowing for precise estimations of particle number distribution within the conical ion beam.
- The use of Insertion Devices (ID) for enhanced applications of laser-driven ion beams. More precisely, Energy Selectors are of strong interest, for example to perform laser-PIXE in a layer-by-layer configuration in a material by benefiting of the Bragg peak energy deposition profile. Another set of IDs of interest would be beam shaping devices, such as solenoids, electromagnetic lenses or quadrupoles used for beam focusing.

Although combining all the above points together seems like a colossal task, I am persuaded it is possible to achieve such a task in the near future, seeing no fundamental obstacle in the path. This will enable the production of laser-based ion sources that are reliable (maximum 10% shot-to-shot particle number and maximum energy fluctuations in the resulting ion beam), intense (>10^{12} particles/sr/shot with kinetic energies of several tens of MeV), moreover operating high repetition-rate (several Hz). The construction of a beamline of this kind will certainly attract a lot of attention in the community, and will permit the next sequence of rigorous application testings using laser-based ion beams. I have the conviction that the testing of applications is what will cause a paradigm shift for laser-driven ion beams, showcasing their versatility and a set of beam characteristics unmatched all together by conventional sources. It is always impressive to see how large particle accelerators can be nowadays, nevertheless the exact opposite (*i.e.* compact ion sources) is the key to democratize these technologies. I truly hope that one day particle accelerators will not be regarded solely as very complex scientific tools, but will be part of the global society's day-to-day life.

Appendix A

Useful mathematical derivations

A.1 Laser intensity in focal spot

First, the laser intensity distribution within the first lobe in the focal plane (focal spot) can be approximated by Gaussian distributions in time and radially, assuming azimuthal symmetry:

$$I(r,t) = \; I_0 \, e^{-(r/w_0)^2} \, e^{-(t/\tau)^2} \tag{A.1}$$

Hence, the energy contained within the focal spot is evaluated as:

$$\mathcal{E}_{\text{spot}} = \int_{-\infty}^{\infty} \int_{0}^{2\pi} \int_{0}^{\infty} I(r,t) \; r \, \mathrm{d}r \mathrm{d}\phi \mathrm{d}t = 2\pi I_0 \int_{-\infty}^{\infty} \int_{0}^{\infty} e^{-(r/w_0)^2} \, e^{-(t/\tau)^2} \; r \, \mathrm{d}r \mathrm{d}t$$

Using the following change of variable:

$$u = r^2/w_0^2 \qquad \Longrightarrow \qquad \mathrm{d}u = 2r\mathrm{d}r/w_0^2 \qquad \therefore \qquad r \, \mathrm{d}r = \frac{w_0^2}{2} \mathrm{d}u$$

We get:

$$\mathcal{E}_{\text{spot}} = \pi I_0 w_0^2 \int_{-\infty}^{\infty} \int_{0}^{\infty} e^{-u} \, e^{-(t/\tau)^2} \, \mathrm{d}u \mathrm{d}t = \pi I_0 w_0^2 \int_{-\infty}^{\infty} e^{-(t/\tau)^2} \, \mathrm{d}t = \pi \sqrt{\pi} I_0 \tau w_0^2$$

where we have used the Gauss integral identity for the last integration over time. It is now convenient to change the standard deviations w_0 and τ with their corresponding values at

Full-Width at Half-Maximum (FWHM) by:

$$\tau = \frac{\tau_{\text{FWHM}}}{2\sqrt{\ln(2)}} \qquad\qquad w_0 = \frac{w_{\text{FWHM}}}{2\sqrt{\ln(2)}}$$

Hence, we obtain:

$$\mathcal{E}_{\text{spot}} = \frac{\pi\sqrt{\pi}}{\left[2\sqrt{\ln(2)}\right]^3} I_0 \, \tau_{\text{FWHM}} \, w_{\text{FWHM}}^2 = \mathcal{E}_{\text{L}} \, f$$

where we define E_{L} as the laser pulse energy and f is the fraction of the energy contained within the central lobe. We can then isolate I_0 which gives:

$$I_0 = \frac{\left[2\sqrt{\ln(2)}\right]^3}{\pi\sqrt{\pi}} \frac{\mathcal{E}_{\text{L}} \, f}{\tau_{\text{FWHM}} \, w_{\text{FWHM}}^2}$$

Typically $f = 0.3$ - 0.6 for used beam profiles and numerical apertures of high-power focusing systems, and $\left[2\sqrt{\ln(2)}\right]^3 / \pi\sqrt{\pi} \approx= 0.83$. If we group together the constant through $f' = f\left[2\sqrt{\ln(2)}\right]^3 / \pi\sqrt{\pi}$, we finally find:

$$I_0 = \frac{\mathcal{E}_{\text{L}} \, f'}{\tau_{\text{FWHM}} \, w_{\text{FWHM}}^2} \tag{A.2}$$

$f' \approx 0.5$ in the best cases, which can be used as a rule of thumb for intensity estimation. For instance, using the ALLS 100 TW laser parameters ($\mathcal{E}_{\text{L}} = 2$ J, $\tau_{\text{FWHM}} = 20$ fs, $w_{\text{FWHM}} = 5$ μm and $f = 0.4$) yields $I_0 \approx 1.3 \times 10^{20}$ W/cm^2. In the general case, f' needs to be evaluated experimentally as the fraction of energy contained within the first lobe:

$$f' = \frac{\int_{-\infty}^{\infty} \int_{0}^{2\pi} \int_{0}^{r_{\text{1st lobe}}} I(r,t) \, r \, \mathrm{d}r\mathrm{d}\phi\mathrm{d}t}{\int_{-\infty}^{\infty} \int_{0}^{2\pi} \int_{0}^{\infty} I(r,t) \, r \, \mathrm{d}r\mathrm{d}\phi\mathrm{d}t} \tag{A.3}$$

□

A.2 Thomson parabola kinematics

The geometrical definitions related to the derivations are shown on Figure A.1. We set the following initial conditions for the incident particle and static electric and magnetic field distributions:

$$\boldsymbol{r}(t=0) = \langle x(0), y(0), z(0)\rangle = \langle 0,0,0\rangle$$

$$\boldsymbol{v}(t=0) = \langle v_x(0), v_y(0), v_z(0)\rangle = \langle 0,0,v_0\rangle$$

$$\boldsymbol{E} = \langle E_x, E_y, E_z\rangle = \langle 0, E_y(z), 0\rangle$$

$$\boldsymbol{B} = \langle B_x, B_y, B_z\rangle = \langle 0, B_y(z), 0\rangle$$

We assume a top-hat distributions for the fields along the y-axis:

$$E_y(z) = E_0 \cdot \text{rect}\left(\frac{z - L_E/2}{L_E}\right) \tag{A.4}$$

$$B_y(z) = B_0 \cdot \text{rect}\left(\frac{z - L_B/2}{L_B}\right) \tag{A.5}$$

where L_E and L_B are the electric and magnetic field lengths, respectively. We first need to solve the equations of movement for the particle passing through the fields using the Lorentz force:

$$\boldsymbol{F} = \frac{d\boldsymbol{p}}{dt} = q(\boldsymbol{E} + \boldsymbol{v} \times \boldsymbol{B}) \tag{A.6}$$

$$\therefore \quad \frac{d\boldsymbol{v}}{dt} = \frac{q}{m}\langle 0, E_y, 0\rangle + \frac{q}{m}\begin{vmatrix} \hat{\imath} & \hat{\jmath} & \hat{k} \\ v_x & v_y & v_z \\ 0 & B_y & 0 \end{vmatrix} = \frac{q}{m}\langle -v_z B_y, E_y, v_x B_y\rangle \tag{A.7}$$

This leads to the following three equations of movement to solve:

$$\frac{dv_x}{dt} = -\frac{q}{m} v_z B_y \tag{A.8}$$

$$\frac{dv_y}{dt} = \frac{q}{m} E_y \tag{A.9}$$

$$\frac{dv_z}{dt} = \frac{q}{m} v_x B_y \tag{A.10}$$

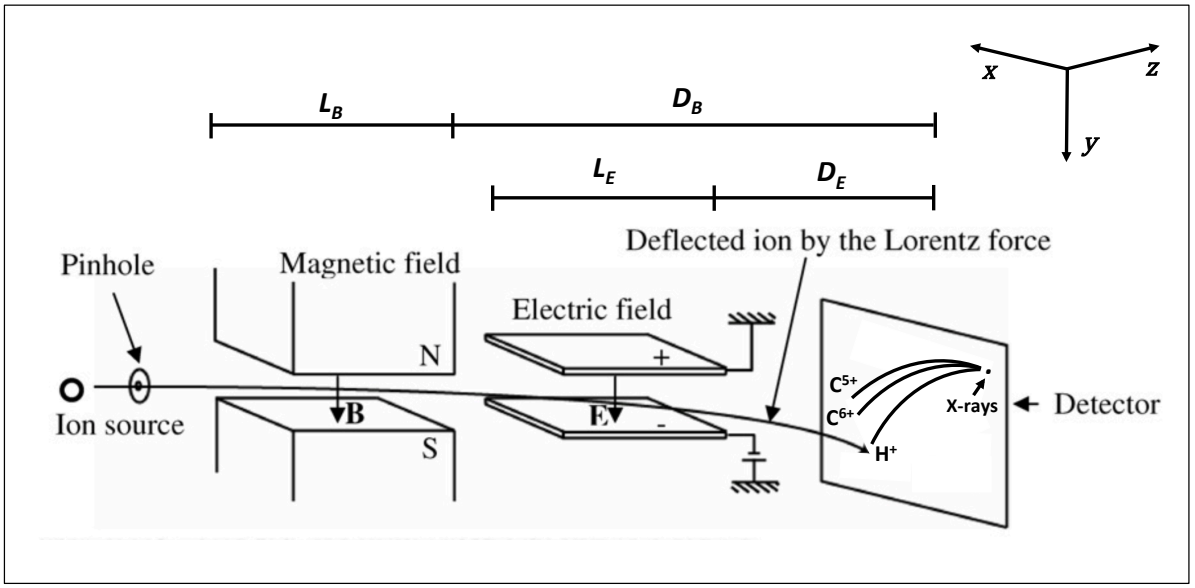

FIGURE A.1: Thomson parabola spectrometer geometry. This figure is extracted and adapted from [65].

The next section will be treating equation (A.9) for the electric deflection separately, then followed in another section by the treatment of equations (A.8) and (A.10) together.

A.2.1 Electric deflection

As the electric force is only oriented along the y, we thus need to solve the equation of movement along y (A.9):

$$\frac{dv_y}{dt} = \frac{dv_y}{dz}\frac{dz}{dt} = v_0\frac{dv_y}{dz} = \frac{q}{m}E_0 \cdot \text{rect}\left(\frac{z - L_E/2}{L_E}\right)$$

Using the non-relativistic kinetic energy $\mathcal{E}_\text{K} = \frac{1}{2}mv_0^2$, we have:

$$\frac{dv_y}{dz} = \frac{qE_0}{\sqrt{2m\mathcal{E}_\text{K}}} \cdot \text{rect}\left(\frac{z - L_E/2}{L_E}\right)$$

Hence we find:

$$v_y(z) = \frac{qE_0}{\sqrt{2m\mathcal{E}_\text{K}}}\int_0^z \text{rect}\left(\frac{z' - L_E/2}{L_E}\right)\,\text{d}z' = \frac{qE_0 z}{\sqrt{2m\mathcal{E}_\text{K}}} \quad , \quad \forall z \in [0, L_E]$$

We then use again the chain rule to find $y(z)$:

$$v_y(z) = \frac{dy}{dt} = \frac{dy}{dz}\frac{dz}{dt} = v_0\frac{dy}{dz} = \sqrt{\frac{2\mathcal{E}_\mathrm{K}}{m}}\frac{dy}{dz}$$

Which leads to the solution:

$$y(z) = \int_0^z \frac{qE_0 z'}{2\mathcal{E}_\mathrm{K}}\,\mathrm{d}z' = \frac{qE_0 z^2}{4\mathcal{E}_\mathrm{K}} \quad , \quad \forall z \in [0, L_E]$$

We now have the following position and velocity after the field $\boldsymbol{E}$ at $z = L_E$:

$$y(L_E) = \frac{qE_0 L_E^2}{4\mathcal{E}_\mathrm{K}} \qquad\qquad v_y(L_E) = \frac{qE_0 L_E}{\sqrt{2m\mathcal{E}_\mathrm{K}}}$$

We then propagate the linear motion using similar triangles for an electric drift distance D_E:

$$\tan\theta = \frac{\Delta y}{D_E} = \frac{v_y(L_E)}{v_z(L_E)}$$

$$\therefore \quad \Delta y = D_E\frac{v_y(L_E)}{v_z(L_E)} = D_E\frac{qE_0 L_E}{\sqrt{2m\mathcal{E}_\mathrm{K}}}\frac{1}{v_0} = D_E\frac{qE_0 L_E}{\sqrt{2m\mathcal{E}_\mathrm{K}}}\sqrt{\frac{m}{2\mathcal{E}_\mathrm{K}}} = \frac{qE_0 L_E D_E}{2\mathcal{E}_\mathrm{K}}$$

Hence, the final position of the particle on the detector along the y-axis is:

$$y(L_E + D_E) = y(L_E) + \Delta y = \frac{qE_0 L_E^2}{4\mathcal{E}_\mathrm{K}} + \frac{qE_0 L_E D_E}{2\mathcal{E}_\mathrm{K}} = \frac{qE_0 L_E}{2\mathcal{E}_\mathrm{K}}\left(\frac{L_E}{2} + D_E\right) \tag{A.11}$$

□

A.2.2 Magnetic deflection

Here, we need to solve the following set of equations (A.8) and (A.10) together:

$$\frac{dv_x}{dt} = -\frac{q}{m}v_z B_y \qquad\qquad \frac{dv_z}{dt} = \frac{q}{m}v_x B_y$$

By taking the time derivative for both equations (A.8) and (A.10), we get:

$$\frac{d^2 v_x}{dt^2} = -\frac{q}{m}B_y\frac{dv_z}{dt} = -\frac{q}{m}B_y\left(\frac{q}{m}v_x B_y\right) = -\omega_L^2 v_x \tag{A.12}$$

$$\frac{d^2v_z}{dt^2} = \frac{q}{m}B_y\frac{dv_x}{dt} = \frac{q}{m}B_y\left(-\frac{q}{m}v_zB_y\right) = -\omega_L^2 v_z \tag{A.13}$$

with $\omega_L = qB_y/m$ is the Larmor precession frequency. Now these 2$^{\text{nd}}$ order differential equations have oscillating solutions of the form:

$$v_x = A\cdot\sin(\omega_L t) + B\cdot\cos(\omega_L t)$$

$$v_z = C\cdot\sin(\omega_L t) + D\cdot\cos(\omega_L t)$$

We will first completely solve for $z(t)$ and then find $x(t)$ through equation (A.10). Applying the initial conditions $v_z(0) = 0$ leads to $D = v_0$. We can now find $z(t)$ by integrating the velocity over time:

$$z(t) = \int v_z(t')\mathrm{d}t' = -\frac{C}{\omega_L}\cdot\cos(\omega_L t) + \frac{v_0}{\omega_L}\cdot\sin(\omega_L t)$$

Applying the initial conditions $z(0) = 0$ gives:

$$z(t) = -\frac{C}{\omega_L} = 0 \qquad \therefore \qquad C = 0$$

Hence, the solutions along the z-axis are:

$$v_z(t) = v_0\cos(\omega_L t) \tag{A.14}$$

$$z(t) = \frac{v_0}{\omega_L}\cdot\sin(\omega_L t) \tag{A.15}$$

Using equation (A.10), we can now find $v_x(t)$ and $x(t)$:

$$v_x(t) = \frac{1}{\omega_L}\frac{dv_z}{dt} = -\frac{1}{\omega_L}v_0\omega_L\sin(\omega_L t) = -v_0\sin(\omega_L t) \tag{A.16}$$

$$x(t) = \int v_x(t')\,\mathrm{d}t' = \frac{v_0}{\omega_L}\cos(\omega_L t) + A'$$

where A' is an integration constant. Applying the initial conditions $x(0) = 0$ leads to $A' = -v_0/\omega_L$. Hence, the final solution for $x(t)$ is:

$$x(t) = \frac{v_0}{\omega_L}\left[\cos(\omega_L t) - 1\right] \tag{A.17}$$

For further use, it is now convenient to find the time t_{L_B} for which $z = L_B$:

$$z(t_{L_B}) = \frac{v_0}{\omega_L}\sin(\omega_L t_{L_B}) = L_B \qquad \therefore \qquad t_{L_B} = \frac{1}{\omega_L}\arcsin\left(\frac{\omega_L L_B}{v_0}\right)$$

We now would like to find the position on the detector after a linear motion for a magnetic drift distance D_B. Again we use similar triangles:

$$\tan\theta = \frac{\Delta x}{D_B} = \frac{v_x(t_{L_B})}{v_z(t_{L_B})}$$

$$\implies \qquad \Delta x = D_B\frac{-v_0\sin(\omega_L t_{L_B})}{v_0\cos(\omega_L t_{L_B})} = -D_B\tan(\omega_L t_{L_B}) = -D_B\tan\left[\arcsin\left(\frac{\omega_L L_B}{v_0}\right)\right]$$

Hence, the final position of the particle on the detector along the x-axis is:

$$x(L_B + D_B) = x(L_B) + \Delta x = \frac{v_0}{\omega_L}\left\{\cos\left[\arcsin\left(\frac{\omega_L L_B}{v_0}\right)\right] - 1\right\} - D_B\tan\left[\arcsin\left(\frac{\omega_L L_B}{v_0}\right)\right]$$

Re-writing everything in terms of the particle's kinetic energy $\mathcal{E}_\mathrm{K}$ and field B_0 gives:

$$v_0/\omega_L = \frac{\sqrt{2\mathcal{E}_\mathrm{K}/m}}{qB_0/m} = \frac{\sqrt{2\mathcal{E}_\mathrm{K}m}}{qB_0}$$

$$x(L_B + D_B) = \frac{\sqrt{2\mathcal{E}_\mathrm{K}m}}{qB_0}\left\{\cos\left[\arcsin\left(\frac{qB_0 L_B}{\sqrt{2\mathcal{E}_\mathrm{K}m}}\right)\right] - 1\right\} - D_B\tan\left[\arcsin\left(\frac{qB_0 L_B}{\sqrt{2\mathcal{E}_\mathrm{K}m}}\right)\right] \quad \text{(A.18)}$$

□

A.3 Time-of-Flight calculations

A typical TOF signal as obtained on an oscilloscope is shown on Figure A.2. First, the total relativistic energy of a particle is written as:

$$\mathcal{E} = \gamma\mathcal{E}_0 = \mathcal{E}_0 + \mathcal{E}_\mathrm{K} \quad \text{(A.19)}$$

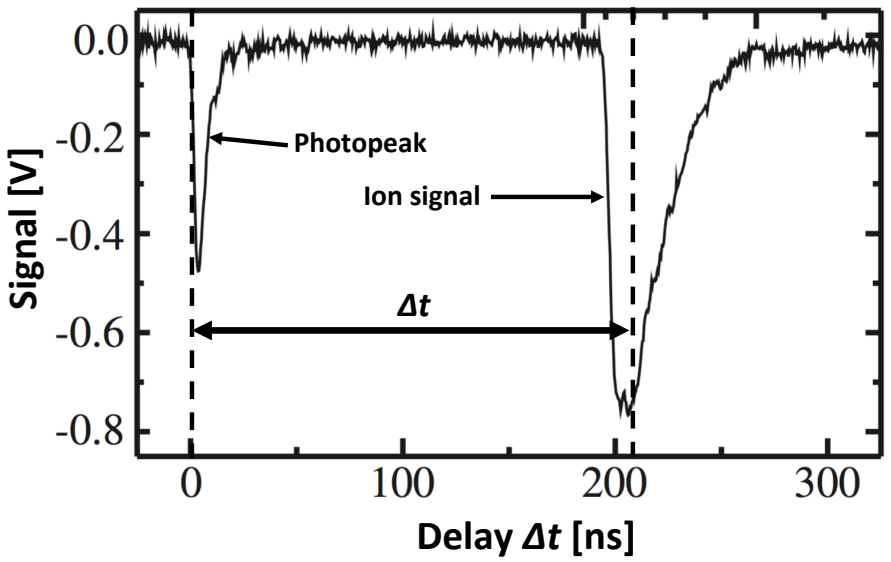

FIGURE A.2: Typical Time-of-Flight signal as obtained on an oscilloscope. This figure is extracted and adapted from [202].

where $\mathcal{E}_K$ is the kinetic energy, $\mathcal{E}_0 = m_0c^2$ is the rest mass energy and $\gamma = \left(1-\beta^2\right)^{-1/2}$ is the Lorentz factor with $\beta = v/c$. Hence, we can write:

$$\gamma^2 = \left(1+\frac{\mathcal{E}_K}{\mathcal{E}_0}\right)^2 = \frac{1}{1-\beta^2}$$

$$\beta^2 = 1-\left(1+\frac{\mathcal{E}_K}{\mathcal{E}_0}\right)^{-2}$$

$$\therefore \quad v = c\sqrt{1-\left(1+\frac{\mathcal{E}_K}{\mathcal{E}_0}\right)^{-2}} \tag{A.20}$$

Assuming that the acceleration time due to the laser-matter interaction is much faster than the travel time along the delay line of length d, we can write:

$$\mathrm{TOF}(\mathcal{E}_K) = d/v = \frac{d}{c}\left[1-\left(1+\frac{\mathcal{E}_K}{\mathcal{E}_0}\right)^{-2}\right]^{-1/2} = t_{\mathrm{ph}} + \Delta t(\mathcal{E}_K) \tag{A.21}$$

where $t_{\mathrm{ph}} = c/d$ is the time travelled by X-ray photons generated from the laser-matter interaction to reach the detector (also called the "photopeak" as observed on an oscilloscope), and $\Delta t(\mathcal{E}_K)$ is the time delay between the beginning of the photopeak and any subsequently sampled particle signal arriving after. Hence, is practice one measures directly $\Delta t(\mathcal{E}_K)$ on a oscilloscope and, using a precise value of d through obtained through a calibration, adds t_{ph}

to find the TOF and finally retrieve the kinetic energy $\mathcal{E}_K$ of the particle. The retrieval of $\mathcal{E}_K$ requires the assumption of the right particle m and hence of the correct ion species to be detected. To evaluate the uncertainty on the determination $\mathcal{E}_K$, one can first re-write equation (A.21) using $\gamma = (1 + \mathcal{E}_K/\mathcal{E}_0)$:

$$\mathrm{TOF}(\gamma) = \frac{d}{c}\left[1-\gamma^{-2}\right]^{-1/2}$$

and then take the derivative with respect to $\mathcal{E}_K$ using the chain rule:

$$\frac{d(\mathrm{TOF})}{d\mathcal{E}_K} = \frac{d(\mathrm{TOF})}{d\gamma}\cdot\frac{d\gamma}{d\mathcal{E}_K}$$

$$= \frac{d}{c}\cdot -\frac{1}{2}\cdot\left[1-\gamma^{-2}\right]^{-3/2}\cdot -1\cdot -2\cdot\gamma^{-3}\cdot\frac{1}{\mathcal{E}_0}$$

$$= -\frac{d}{c\mathcal{E}_0}\left[1-\gamma^{-2}\right]^{-3/2}\gamma^{-3} = -\frac{d}{c\mathcal{E}_0}\left[\gamma^2-1\right]^{-3/2}$$

The measurement uncertainty on the kinetic energy $\sigma_{\mathcal{E}_K}$ can be written as:

$$\sigma_{\mathcal{E}_K} = \left|\frac{d\mathcal{E}_K}{d(\mathrm{TOF})}\right|\cdot\sigma_{\mathrm{TOF}} = \left|\frac{d(\mathrm{TOF})}{d\mathcal{E}_K}\right|^{-1}\cdot\sigma_{\mathrm{TOF}}$$

where σ_{TOF} is the uncertainty on time determination which is given by sampling time step used on the oscilloscope. Therefore, we finally find:

$$\sigma_{\mathcal{E}_K} = \frac{c\mathcal{E}_0}{d}\left[\left(1+\frac{\mathcal{E}_K}{\mathcal{E}_0}\right)^2-1\right]^{3/2}\sigma_{\mathrm{TOF}} \tag{A.22}$$

□

A.4 Energy deposition in matter by charged particles

The macroscopic dose deposition from charged particles in matter, expressed in J/kg or Gy, is defined as:

$$D = \frac{\mathcal{E}_{\text{dep}}}{m} = \frac{S_{\text{col}}}{\rho}(\mathcal{E}_{\text{K},0}, x, z, Z) \cdot \phi \tag{A.23}$$

where ρ is the material density, $\mathcal{E}_{\text{K},0}$ is the initial kinetic energy of the particle, x the penetration depth, z the charge state of the incident particle, Z the atomic number of the material, ϕ the particle fluence and S_{col} is the particle's collisional stopping power as governed by the well-known corrected Bethe-Bloch equation:

$$S_{\text{col}} = -\frac{d\mathcal{E}_{\text{K}}}{dx} = 4\pi\frac{N_{\text{A}}}{M}\left(\frac{e^2}{4\pi\varepsilon_0}\right)^2 \frac{z^2 Z}{m_{\text{e}}c^2\beta^2}\left\{\ln\left[\frac{2m_{\text{e}}c^2\beta^2}{I(1-\beta^2)}\right] - \beta^2 - \frac{C}{Z} - \delta\right\} \tag{A.24}$$

Assuming a uniform deposited energy distribution in matter through the equipartition theorem, it possible to relate equation (A.23) to a local increase in temperature through the following relationship:

$$D = c_p \cdot \Delta T \qquad \therefore \qquad \Delta T = -\frac{d\mathcal{E}_{\text{K}}}{dx}\frac{\phi}{\rho c_p} \tag{A.25}$$

Equation (A.25) allows to model the proton beam energy deposition in matter through the propagation of its stopping power with depth, resulting in temperature rise, with the assumption of fast isochoric heating. An *Energy Deposition Code* (EDC) was developed in Matlab® to simulate the energy deposition process from a beam of charged particles and estimate the temperature reached by fast proton heating. The modeling approximates that the thermalization process is much slower than the proton bunch length (few nanoseconds), which is a valid approximation for short distances between the proton source and the secondary target in the range of 1-10 cm. The code takes as input the experimental beam parameters presented in Figure A.3, which include the proton spectrum $\frac{d^2N_{\text{p}}}{d\mathcal{E}d\Omega}(\mathcal{E}_{\text{K}})$, the cone beam half-angle divergence $\sigma_\theta(\mathcal{E}_{\text{K}})$ and the virtual point source position $d_{\text{virtual}}(\mathcal{E}_{\text{K}})$, all three varying with proton kinetic energy $\mathcal{E}_{\text{K}}$. The model considers a Gaussian transverse fluence profile with azimuthal symmetry, and the conical energy deposition is calculated using beamlets superposition in cylindrical coordinates for a specific cone beam geometry, with the stopping power tables available from the NIST-PSTAR [233] database. All beam characteristics (spectrum, half-angle and virtual

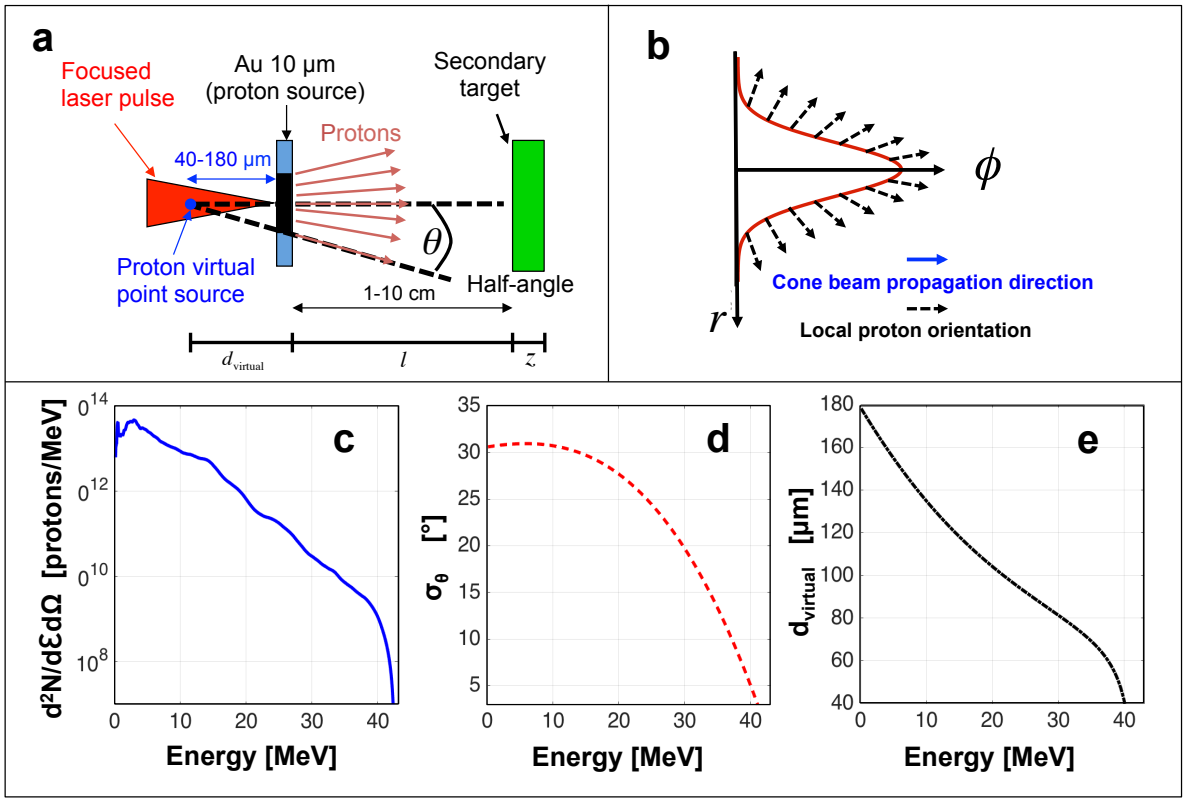

FIGURE A.3: Geometry and laser-driven proton beam characteristics obtained on TITAN laser using the EDC. (a) EDC geometry used for calculations (b) Gaussian transverse fluence profile with azimuthal symmetry (c) Proton spectrum $\frac{d\phi}{d\mathcal{E}}(\mathcal{E}_K, r, z)$ acquired on TITAN laser using a TP spectrometer. (d) Cone half-angle beam divergence $\sigma_\theta(\mathcal{E}_K)$ obtained with RCF measurements. (e) Virtual point source position $d_{\text{virtual}}(\mathcal{E}_K)$ inferred from RCF measurements. This figure is extracted and adapted from [232].

point source position) are obtained experimentally using Thomson Parabola (TP) spectrometers and radiochromic films (RCF) for determining the half-angle and virtual source position for each proton energy. More precisely, the proton fluence per unit proton energy $\frac{d\phi}{d\mathcal{E}}(\mathcal{E}_K, r, z)$ is defined as:

$$\frac{d\phi}{d\mathcal{E}}(\mathcal{E}_K, r, z) = \frac{d^2N_p}{dSd\mathcal{E}}(\mathcal{E}_K, r, z) = \frac{dN_p}{d\mathcal{E}} \frac{e^{-\frac{r^2}{\sigma_r^2}}}{\pi\sigma_r^2} \tag{A.26}$$

In equation (A.26), the number of protons per unit energy $\frac{dN_p}{d\mathcal{E}}$ and beam radius σ_r are further found using:

$$\frac{dN_p}{d\mathcal{E}_K}(\mathcal{E}_K) = \frac{d^2N_p}{d\mathcal{E}d\Omega}\,\Omega_{\text{cone}} = \frac{d^2N_p}{d\mathcal{E}d\Omega}\,2\pi\,(1-\cos\sigma_\theta) \tag{A.27}$$

$$\sigma_r(\mathcal{E}_K, z) = (d_{\text{virtual}} + l + z)\tan\sigma_\theta \tag{A.28}$$

For each proton kinetic energy bin, the EDC then calculates the conical energy deposition

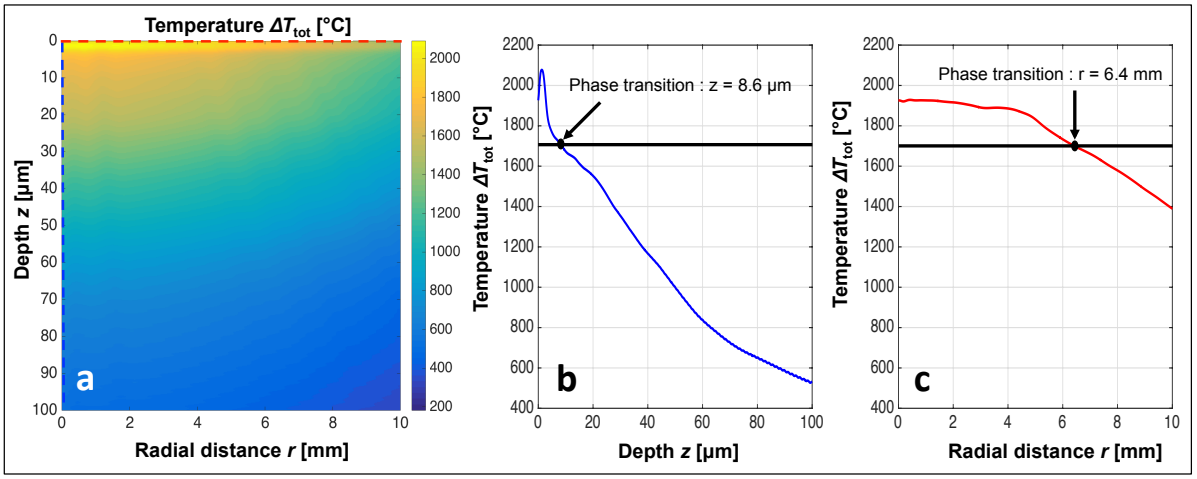

FIGURE A.4: Energy deposition of laser-driven protons in diamond as calculated from the EDC. (a) Temperature map expressed in cylindrical coordinates (r,z). (b) Central depth profile retrieved from the temperature map for $r = 0$. (c) Surface radial profile retrieved from the temperature map for $z = 0$. This figure is extracted and adapted from [232].

by decomposing the proton beam in N_θ beamlets, each of them oriented at an angle θ_i with i denoting the i^{th} beamlet. The temperature increase per unit proton energy $\frac{dT}{d\mathcal{E}}(\mathcal{E}_\text{K}, r, z)$ is thus calculated using the following decomposition:

$$\frac{dT}{d\mathcal{E}}(\mathcal{E}_\text{K}, r, z) = \frac{1}{\rho c_p} \cdot \frac{1}{N_\theta} \sum_{i=1}^{i=N_\theta} \left[-\frac{d\mathcal{E}_\text{K}}{dx}(\mathcal{E}_\text{K}, x) \frac{d\phi}{d\mathcal{E}}(\mathcal{E}_\text{K}, r, z) \right]_{\hat{\theta}_i} \tag{A.29}$$

with:

$$x = \sqrt{(d_\text{virtual} + l + z)^2 + r'^2} - \sqrt{(d_\text{virtual} + l)^2 + r'^2} \tag{A.30}$$

and:

$$\text{and} \qquad r'(\theta_i, z) = (d_\text{virtual} + l + z) \tan\theta_i \tag{A.31}$$

The variable x in equation (A.30) is the proton penetration depth along the unit direction vector $\hat{\theta}_i$, and r' is the radial distance from the z-axis along the line delimited by $\hat{\theta}_i$. The total temperature increase for the entire proton beam is finally found by summing the energy deposition patterns for each energy $\mathcal{E}_\text{K}$ for an associated binwidth $\Delta\mathcal{E}$:

$$\Delta T_\text{tot}(r, z) = \sum_0^{\mathcal{E}_\text{K}^\text{max}} \frac{dT}{d\mathcal{E}}(\mathcal{E}_\text{K}, r, z) \Delta\mathcal{E} \tag{A.32}$$

The dose deposition maps calculated from the EDC were further benchmarked against the Monte Carlo code Geant4 [234]. The results of this benchmarking can be found in the *Supplementary Materials* of Barberio *et al.* (2018) [235]. The development and very practical use of the EDC has contributed to the publication of four articles into which I am co-author [232, 235–237]. An example of the calculated energy deposition maps is shown in Figure A.4, in a study concerning the graphitization of diamond using the laser-driven proton beam obtained on the TITAN laser facility.

Bibliography

[1] R. J. Van de Graaff, "A 1,500,000 volt electrostatic generator", *Phys. Rev.*, vol. 38, 1 919 A (1931).

[2] J. D. Cockcroft & E. T. S. Walton, "Disintegration of Lithium by Swift Protons", *Nature*, vol. 129, p. 649 (1932).

[3] R. J. Van de Graaff, K. T. Compton & L. C. Van Atta, "The Electrostatic Production of High Voltage for Nuclear Investigations", *Phys. Rev.*, vol. 43 (3), 1 919 A (1933).

[4] R. Wideröe, "Über ein neues Prinzip zur Herstellung hoher Spannungen", *Archiv f. Elektrotechnik*, vol. 21, 387-406 (1928).

[5] L. W. Alvarez, H. Bradner, J. Franck, H. Gordon, J. D. Gow, L. C. Marshall, F. F. Oppenheimer, W. K. H. Panofsky, C. Richman & J. R. Woodyard, "Berkeley Proton Linear Accelerator", *United States*, Technical Report (1953). DOI:10.2172/4375045

[6] J.-B. Lallemant & V. Dimov, "LINACS", Lecture, *Joint Universities Accelerator School*, (2018).

[7] E. O. Lawrence & M. S. Livingston, "The Production of High Speed Light Ions Without the Use of High Voltages", *Phys. Rev.*, vol. 40 (19), (1932).

[8] B. Jacquot & F. Chautard, "Beam dynamics for cyclotrons", Lecture, *Joint Universities Accelerator School*, (2018).

[9] P. Lebrun, "Accelerator Discoveries", Lecture, Joint Universities Accelerator School (2018).

[10] G. Aad *et al.*, "Observation of a new particle in the search for the Standard Model Higgs boson with the ATLAS detector at the LHC", *Phys. Lett. B*, vol. 716 (1), 1-29 (2012).

[11] S. Chatrchyan *et al.*, "Observation of a new boson at a mass of 125 GeV with the CMS experiment at the LHC", *Phys. Lett. B*, vol. 716 (1), 30-61 (2012).

[12] J. D. Jackson, "Classical Electrodynamics", 3rd edition, *John Wiley & sons.*, (1999).

[13] E. B. Podgoršak, "Radiation Physics for Medical Physicists", 2nd edition, *Springer*, (2010).

[14] R. Bartolini, "Synchrotron radiation", Lecture, *Joint Universities Accelerator School*, (2018).

[15] A. L. Schawlow & C. H. Townes, "Infrared and Optical Masers", *Phys. Rev.*, vol. 112 (6), 1940-1948 (1958).

[16] T. H. Maiman, "Stimulated Optical Radiation in Ruby", *Nature*, vol. 187, 493-494 (1960).

[17] T. Tajima & J. M. Dawson, "Laser Electron Accelerator", *Phys. Rev. Lett.*, vol. 43 (4), 267-270 (1979).

[18] D. Strickland & G. Mourou, "Compression of Amplified Chirped Optical Pulses", *Opt. Comm.*, vol. 56 (3), 219-221 (1985).

[19] P. Moulton, "Spectroscopic and laser characteristics of Ti:Al_2O_3", *J. Opt. Soc. Am. B*, vol. 3 (1), 125-133 (1986).

[20] M. C. Asplund, J. A. Johnson & J. E. Patterson, "The 2018 Nobel Prize in Physics: optical tweezers and chirped pulse amplification", *Anal. Bioanal. Chem.*, vol. 411 (3), 5001-5005 (2019).

[21] V. Malka, J. Faure, Y. A. Gauduel, E. Lefebvre, A. Rousse & K. Ta Phuoc, "Principles and applications of compact laser-plasma accelerators", *Nat. Phys.*, vol. 4, 447-453 (2008).

[22] V. Malka, "Review of Laser WakeField Accelerators", *Proc. IPAC 2013*, MOYBB101, 11-15 (2013).

[23] E. Esarey, C. B. Schroeder & W. P. Leemans, "Physics of laser-driven plasma-based electron accelerators", *Rev. Mod. Phys.*, vol. 81 (3), 1229-1285 (2009).

[24] T. Tajima, "Laser acceleration and its future", *Proc. Jpn. Acad. Ser. B*, vol. 86 (3), 147-157 (2010).

[25] A. Cakir & A. O. Guzel, "A Brief Review of Plasma Wakefield Acceleration", *arXiv*, 1908.07207 (2019).

[26] Y. Kitagawa *et al.*, "Beat-wave excitation of plasma wave and observation of accelerated electrons", *Phys. Rev. Lett.*, vol. 68, 48-51 (1992).

[27] C. E. Clayton *et al.*, "Ultrahigh-gradient acceleration of injected electrons by laser-excited relativistic electron plasma waves", *Phys. Rev. Lett.*, vol. 70 (1), 37 (1993).

[28] M. J. Everett *et al.*, "Trapped electron acceleration by a laser-driven relativistic plasma wave", *Nature*, vol. 368, 527 (1994).

[29] A. Modena *et al.*, "Electron acceleration from the breaking of relativistic plasma waves", *Nature*, vol. 377, 606 (1995).

[30] K. Nakajima *et al.*, "Observation of Ultrahigh Gradient Electron Acceleration by a Self-Modulated Intense Short Laser Pulse", *Phys. Rev. Lett.*, vol. 74 (22), 4428 (1995).

[31] D. Umstadter, S.-Y. Chen, A. Maksimchuk, G. Mourou & R. Wagner, "Nonlinear optics in relativistic plasmas and laser wake field acceleration of electrons", *Science*, vol. 273, 472-475 (1996).

[32] A. Ting, K. Krushelnick, C. I. Moore, H. R. Burris, E. Esarey, J. Krall & P. Sprangle, "Temporal Evolution of Self-Modulated Laser Wakefields Measured by Coherent Thomson Scattering", *Phys. Rev. Lett.*, vol. 77 (27), 5377 (1997).

[33] C. I. Moore *et al.*, "Electron trapping in self-modulated laser wakefields by Raman backscattering, *Phys. Rev. Lett.*, vol. 79, 3909-3912 (1997).

[34] F. Amiranoff *et al.*, "Observation of laser wakefield acceleration of electrons", *Phys. Rev. Lett.*, vol. 81 (5), 995 (1998).

[35] C. Gahn *et al.*, Multi-MeV electron beam generation by direct laser acceleration in high-density plasma channels", *Phys. Rev. Lett.*, vol. 83, 4772-4775 (1999).

[36] V. Malka *et al.*, "Characterization of electron beams produced by ultrashort (30 fs) laser pulses", *Phys. Plasmas*, vol. 8, 2605-2608 (2001).

[37] V. Malka *et al.*, "Electron Acceleration by a Wake Field Forced by an Intense Ultrashort Laser Pulse", *Science*, vol. 298, 1596-1600s (2002).

[38] S. Mangles *et al.*, "Monoenergetic beams of relativistic electrons from intense laser-plasma interactions", *Nature*, vol. 431, 535 (2004).

[39] C. G. R. Geddes *et al.*, "High-quality electron beams from a laser wakefield accelerator using plasma-channel guiding", *Nature*, vol. 431, 538 (2004).

[40] J. Faure *et al.*, "A laser-plasma accelerator producing monoenergetic electron beams", *Nature*, vol. 431, 541 (2004).

[41] W. P. Leemans, B. Nagler, A. J. Gonsalves, C. Tóth, K. Nakamura, C. G. R. Geddes, E.

Esarey, C. B. Schroeder & S. M. Hooker, "GeV electron beams from a centimetre-scale accelerator", *Nature Phys.*, vol. 2, 696-699 (2006).

[42] J. Faure, C. Rechatin, A. Norlin, A. Lifschitz, Y. Glinec & V. Malka, "Controlled injection and acceleration of electrons in plasma wakefields by colliding laser pulses", *Nature*, vol. 444 (7120), 737-739 (2006).

[43] S. Karsch *et al.*, "GeV-scale electron acceleration in a gas-filled capillary discharge waveguide", *New J. of Phys.*, vol. 9, 415 (2007).

[44] N. A. M. Hafz *et al.*, "Stable generation of GeV-class electron beams from self-guided laser-plasma channels", *Nat. Phot.*, vol. 2, 571 (2008).

[45] C. G. R. Geddes, K. Nakamura, G. R. Plateau, C. Tóth, E. Cormier-Michel, E. Esarey, C. B. Schroeder, J. R. Cary & W. P. Leemans, "Plasma-Density-Gradient Injection of Low Absolute-Momentum-Spread Electron Bunches", *Phys. Rev. Lett.*, vol. 100 (21), 215004 (2008).

[46] D. H. Froula *et al.*, "Measurements of the Critical Power for Self-Injection of Electrons in a Laser Wakefield Accelerator", *Phys. Rev. Lett.*, vol. 103, 215006 (2009).

[47] C. E. Clayton *et al.*, "Self-Guided Laser Wakefield Acceleration beyond 1 GeV Using Ionization-Induced Injection", *Phys. Rev. Lett.*, vol. 105, 105003 (2010).

[48] H. Lu *et al.*, "Laser wakefield acceleration of electron beams beyond 1 GeV from an ablative capillary discharge waveguide", *Appl. Phys. Lett.*, vol. 99, 091502 (2011).

[49] H. T. Kim, K. H. Pae, H. J. Cha, I. J. Kim, T. J. Yu, J. H. Sung, S. K. Lee, T. M. Jeong & J. Lee, "Enhancement of Electron Energy to the Multi-GeV Regime by a Dual-Stage Laser-Wakefield Accelerator Pumped by Petawatt Laser Pulses", *Phys. Rev. Lett.*, vol. 111, 165002 (2013).

[50] W. P. Leemans *et al.*, "Multi-GeV Electron Beams from Capillary-Discharge-Guided Subpetawatt Laser Pulses in the Self-Trapping Regime", *Phys. Rev. Lett.*, vol. 113, 245002 (2014).

[51] H. T. Kim *et al.*, "Stable multi-GeV electron accelerator driven by waveform-controlled PW laser pulses", *Sci. Rep.*, vol. 7, 10203 (2017).

[52] A. J. Gonsalves *et al.*, "Petawatt Laser Guiding and Electron Beam Acceleration to 8 GeV in a Laser-Heated Capillary Discharge Waveguide", *Phys. Rev. Lett.*, vol. 122, 084801

(2019).

[53] E. Esarey, B. A. Shadwick, P. Catravas & W. P. Leemans, "Synchrotron radiation from electron beams in plasma-focusing channels", *Phys. Rev. E*, vol. 65, 056505 (2002).

[54] I. Kostyukov *et al.*, "X-ray generation in an ion channel", *Phys. Plasmas*, vol. 10, 4818-4828 (2003).

[55] A. Rousse *et al.*, "Production of a keV X-ray beam from synchrotron radiation in relativistic laser-plasma interaction", *Phys. Rev. Lett.*, vol. 93, 135005 (2004).

[56] F. Albert *et al.*, "Laser wakefield accelerator based light sources: potential applications and requirements", *Plasmas Phys. Cont. Fus.*, vol. 56, 084015 (2014).

[57] F. Albert & A. G. R. Thomas, "Applications of laser wakefield accelerator-based light sources", *Plasma Phys. Control. Fusion*, vol. 58, 103001 (2016).

[58] S. Fourmaux, S. Corde, K. Ta Phuoc, P. Lassonde, G. Lebrun, S. Payeur, F. Martin, S. Sebban, V. Malka, A. Rousse & J.-C. Kieffer , "X-ray phase contrast imaging of spherical capsules", *Opt. Lett.*, vol. 36 (13), 2426-2428 (2011).

[59] S. Fourmaux, J.-C. Kieffer & E. Hallin, "Laser wakefield driven X-ray sources in Canada: a brilliant future for agriculture and global food security", *Proc. of SPIE*, vol. 10760, 107600E (2018).

[60] S. Fourmaux, E. Hallin, A. Krol, J. L. Bourgade & J.-C. Kieffer, "X-ray phase contrast imaging of spherical capsules", *Opt. Express*, vol. 28 (9), 13978-13990 (2020).

[61] A. E. Hussein *et al.*, "Laser-wakefield accelerators for high-resolution X-ray imaging of complex microstructures", *Sci. Rep.*, vol. 9, 3249 (2019).

[62] J. Badziak, "Laser-driven ion acceleration: methods, challenges and prospects", *IOP Conf. Series: Journal of Physics: Conf. Series*, vol. 95, 012001 (2018).

[63] A. Macchi, "A Review of Laser-Plasma Ion Acceleration", *arXiv*, 1712.06443, (2017).

[64] A. Macchi, M. Borghesi & M. Passoni, "Ion acceleration by superintense laser-plasma interaction", *Rev. Mod. Phys.*, vol. 85 (2), 751 (2013).

[65] H. Daido, M. Nishiuchi & A. S. Pirozhkov, "Review of laser-driven ion sources and their applications", *Rep. Prog. Phys.*, vol. 75, 056401 (2012).

[66] M. Borghesi, J. Fuchs, S. V. Bulanov, A. J. MacKinnon, P. K. Patel & M. Roth, "Fast Ion

Generation by High-Intensity Laser Irradiation of Solid Targets and Applications", *Fusion Sci. Technol.*, vol. 49, 412-439 (2006).

[67] M. Roth & M. Schollmeier, "Ion Acceleration - Target Normal Sheath Acceleration", *Proceedings of the CAS-CERN Accelerator School: Plasma Wake Acceleration*, Geneva, Switzerland, 23-29 November 2014, vol. 1, pp. 231-270 (2016).

[68] V. Veksler, "The principle of coherent acceleration of charged particles", *Soviet J. At. Energy*, vol. 2, 525-528 (1957).

[69] R. F. Benjamin, G. H. McCall & A. W. Ehler, "Measurement of return current in a laser-produced plasma", *Phys. Rev. Lett.*, vol. 42 (14), 890 (1979).

[70] S. J. Gitomer, R. D. Jones, F. Begay, A. W. Ehler, J. F. Kephart & R. Kristal, "Fast ions and hot electrons in the laser-plasma interaction", *Phys. of Fluids*, vol. 29, 2679 (1986).

[71] A. P. Fews, P. A. Norreys, F. N. Beg, A. R. Bell, A. E. Dangor, C. N. Danson, P. Lee & S. J. Rose, "Plasma Ion Emission from High Intensity Picosecond Laser Pulse Interactions with Solid Targets", *Phys. Rev. Lett.*, vol. 73 (13), 1801 (1994).

[72] F. N. Beg, A. R. Bell, A. E. Dangor, C. N. Danson, A. P. Fews, M. E. Glinsky, B. A. Hammel, P. Lee, P. A. Norreys & M. Tatarakis, "A study of picosecond laser-solid interactions up to 10^{19} Wcm^{-2}", *Phys. Plasmas*, vol. 4 (2), 447 (1997).

[73] T. Ditmire, J. W. G. Tisch, E. Springate, M. B. Mason, N. Hay, R. A. Smith, J. Marangos & M. H. R. Hutchinson, "High-energy ions produced in explosions of superheated atomic clusters", *Nature*, vol. 386, 54-56 (1997).

[74] K. Krushelnick, E. L. Clark, Z. Najmudin, M. Salvati, M. I. K. Santala, M. Tatarakis, A. E. Dangor, V. Malka, D. Neely, R. Allott & C. Danson, "Multi-MeV Ion Production from High-Intensity Laser Interactions with Underdense Plasmas", *Phys. Rev. Lett.*, vol. 83 (4), 737 (1999).

[75] G. S. Sarkisov, V. Yu. Bychenkov, V. N. Novikov, V. T. Tikhonchuk, A. Maksimchuk, S.-Y. Chen, R. Wagner, G. Mourou & D. Umstadter, "Self-focusing, channel formation, and high-energy ion generation in interaction of an intense short laser pulse with a He jet", *Phys. Rev. E*, vol. 59 (6), 7042 (1999).

[76] E. L. Clark, K. Krushelnick, J. R. Davies, M. Zepf, M. Tatarakis, F. N. Beg, A. Machacek,

P. A. Norreys, M. I. K. Santala, I. Watts & A. E. Dangor, "Measurements of Energetic Proton Transport through Magnetized Plasma from Intense Laser Interactions with Solids", *Phys. Rev. Lett.*, vol. 84 (4), 670 (2000).

[77] R. A. Snavely *et al.*, "Intense High-Energy Proton Beams from Petawatt-Laser Irradiation of Solids", *Phys. Rev. Lett.*, vol. 85 (14), 2945 (2000).

[78] A. Maksimchuk, S. Gu, K. Flippo, D. Umstadter & V. Y. Bychenkov, "Forward Ion Acceleration in Thin Films Driven by a High-Intensity Laser", *Phys. Rev. Lett.*, vol. 84 (18), 4108 (2000).

[79] S. P. Hatchett *et al.*, "Electron, photon, and ion beams from the relativistic interaction of Petawatt laser pulses with solid targets", *Phys. Plasmas*, vol. 7 (5), 2076 (2000).

[80] S. C. Wilks, A. B. Langdon, T. E. Cowan, M. Roth, M. Singh, S. Hatchett, M. H. Key, D. Pennington, A. MacKinnon & R. A. Snavely , "Energetic proton generation in ultra-intense laser-solid interactions", *Phys. Plasmas*, vol. 8 (2), 542 (2001).

[81] P. Mora, "Plasma Expansion into a Vacuum", *Phys. Rev. Lett.*, vol. 90 (18), 185002 (2003).

[82] T. E. Cowan *et al.*, "Ultralow emittance, multi-MeV proton beams from a laser virtual-cathode plasma accelerator", *Phys. Rev. Lett.*, vol. 92, 204801 (2004).

[83] M. Borghesi, A. Bigongiari, S. Kar, A. Macchi, L. Romagnani, P. Audebert, J. Fuchs, T. Toncian, O. Willi, S. V. Bulanov, A. J. Mackinnon & J. C. Gauthier, "Laser-driven proton acceleration: source optimization and radiographic applications", *Plasma Phys. Control. Fusion*, vol. 50, 124040 (2008).

[84] M. Borghesi *et al.*, "Multi-MeV Proton Source Investigations in Ultraintense Laser-Foil Interactions", *Phys. Rev. Lett.*, vol. 92, 055003 (2004).

[85] F. Nürnberg *et al.*, "Radiochromic film imaging spectroscopy of laser-accelerated proton beams", *Rev. Sci. Instrum.*, vol. 80, 033301 (2009).

[86] H. Schwoerer *et al.*, "Laser-Plasma Acceleration of Quasi-Monoenergetic Protons from Microstructured Targets", *Nature*, vol. 439, 445-448 (2006).

[87] M. Roth *et al.*, "Fast Ignition by Intense Laser-Accelerated Proton Beams", *Phys. Rev. Lett.*, vol. 86 (3), 436 (2001).

[88] H. Ruhl, S. V. Bulanov, T. E. Cowan, T. V. Liseikina, P. Nickles, F. Pegoraro, M. Roth & W. Sandner. "Computer simulation of the three-dimensional regime of proton acceleration

in the interaction of laser radiation with a thin spherical target", *Plasma Phys. Rep.*, vol. 27 (5), 363-371 (2001).

[89] S. Atzeni, M. Temporal & J. Honrubia, "A first analysis of fast ignition of precompressed ICF fuel by laser-accelerated protons", *Nucl. Fusion*, vol. 42, L1-L4 (2002).

[90] S. V. Bulanov & V. Khoroshkov, "Feasibility of using laser ion accelerators in proton therapy", *Plasma Phys. Rep.*, vol. 28, 453-456 (2002).

[91] S. V. Bulanov, T. Z. Esirkepov, V. S. Khoroshkov, A. V. Kuznetsov & F. Pegoraro, "Oncological hadrontherapy with laser ion accelerators", *Phys. Lett. A*, vol. 299, 240-247 (2002).

[92] E. Fourkal, J. S. Li, W. Xiong, A. Nahum & C. Ma, "Intensity modulated radiation therapy using laser-accelerated protons: a Monte Carlo dosimetric study", *Phys. Med. Biol.*, vol. 48, 3977 (2003).

[93] V. Malka, S. Fritzler, E. Lefebvre, E. d'Humières, R. Ferrand, G. Grillon, C. Albaret, S. Meyroneinc, J.-P. Chambaret, A. Antonetti & D. Hulin, "Practicability of protontherapy using compact laser systems", *Med. Phys.*, vol. 31, 1587-1592 (2004).

[94] K. Nemoto, A. Maksimchuk, S. Banerjee, K. Flippo, G. Mourou, D. Umstadter & V. Y. Bychenkov, "Laser-triggered ion acceleration and table top isotope production", *Appl. Phys. Lett.*, vol. 78, 595 (2001).

[95] I. Spencer *et al.*, "Laser generation of proton beams for the production of short-lived positron emitting radioisotopes", *Nucl. Inst. Meth. Phys. Res. B*, vol. 183, 449-458 (2001).

[96] M. I. K. Santala *et al.*, "Production of radioactive nuclides by energetic protons generated from intense laser-plasma interactions", *Appl. Phys. Lett.*, vol. 78, 19-21 (2001).

[97] S. Fritzler, V. Malka, G. Grillon, J. P. Rousseau, F. Burgy, E. Lefebvre, E. d'Humières, P. McKenna & K. W. D. Ledingham, "Proton beams generated with high-intensity lasers: Applications to medical isotope production", *Appl. Phys. Lett.*, vol. 83, 3039-3041 (2003).

[98] K. W. D. Ledingham, P. McKenna & R. P. Singhal, "Applications for nuclear phenomena generated by ultra-intense lasers", *Science*, vol. 300, 1107-1111 (2003).

[99] M. Roth *et al.*, "Energetic ions generated by laser pulses: A detailed study on target properties", *Phys. Rev. ST Accel. Beams*, vol. 5, 061301 (2002).

[100] J. A. Cobble, R. P. Johnson, T. E. Cowan, N. R.-L. Galloudec & M. Allen, "High resolution laser-driven proton radiography", *J. Appl. Phys.*, vol. 92, 1775-1779 (2002).

[101] M. Borghesi *et al.*, "Electric field detection in laser-plasma interaction experiments via the proton imaging technique", *Phys. Plasmas*, vol. 9, 2214-2220 (2002).

[102] A. J. Mackinnon *et al.*, "Proton radiography as an electromagnetic field and density perturbation diagnostic (invited)", *Rev. Sci. Instrum.*, vol. 75, 3531-3536 (2004).

[103] L. Romagnani *et al.*, "Dynamics of Electric Fields Driving the Laser Acceleration of Multi-MeV Protons", *Phys. Rev. Lett.*, vol. 95, 195001 (2005).

[104] K. Harres *et al.*, "Development and calibration of a Thomson parabola with microchannel plate for the detection of laser-accelerated MeV ions", *Rev. Sci. Instrum.*, vol. 79, 093306 (2008).

[105] A. J. Mackinnon, Y. Sentoku, P. K. Patel, D. W. Price, S. Hatchett, M. H. Key, C. Andersen, R. Snavely & R. R. Freeman, "Enhancement of proton acceleration by hot-electron recirculation in thin foils irradiated by ultraintense laser pulses", *Phys. Rev. Lett.* vol. 88, 215006 (2002).

[106] P. K. Patel, A. J. Mackinnon, M. H. Key, T. E. Cowan, M. E. Foord, M. Allen, D. F. Price, H. Ruhl, P. T. Springer & R. Stephens, "Isochoric heating of solid-density matter with an ultrafast proton beam", *Phys. Rev. Lett.*, vol. 91, 125004 (2003).

[107] I. Spencer *et al.*, "Experimental study of proton emission from 60-fs, 200-mJ high-repetition-rate tabletop-laser pulses interacting with solid targets", *Phys. Rev. E*, vol. 67 046402 (2003).

[108] P. McKenna *et al.*, "Characterization of proton and heavier ion acceleration in ultrahigh-intensity laser interactions with heated target foils", *Phys. Rev. E*, vol. 70, 036405 (2004).

[109] M. Kaluza, J. Schreiber, M. I. K. Santala, G. D. Tsakiris, K. Eidmann, J. Meyer-ter-Vehn & K. J. Witte, "Influence of the laser prepulse on proton acceleration in thin-foil experiments", *Phys. Rev. Lett.*, vol. 93, 045003 (2004)

[110] Y. Oishi *et al.*, "Dependence on laser intensity and pulse duration in proton acceleration by irradiation of ultrashort laser pulses on a Cu foil target", *Phys. Plasmas*, vol. 12, 073102 (2005).

[111] J. Fuchs *et al.*, "Comparison of Laser Ion Acceleration from the Front and Rear Surfaces of Thin Foils", *Phys. Rev. Lett.*, vol. 94 (4), 045004 (2005)

[112] J. Fuchs *et al.*, "Laser-driven proton scaling laws and new paths towards energy increase", *Nature Phys.*, vol. 2, 48-54 (2006).

[113] D. Neely, P. Foster, A. Robinson, F. Lindau, O. Lundh, A. Persson, C.-G. Wahlström & P. McKenna, "Enhanced proton beams from ultrathin targets driven by high contrast laser pulses", *Appl. Phys. Lett.*, vol. 89, 021502 (2006).

[114] L. Willingale *et al.*, "Collimated multi-MeV ion beams from high-intensity laser interactions with underdense plasma", *Phys. Rev. Lett.*, vol. 96, 245002 (2006).

[115] T. Ceccotti, A. Levy, H. Popescu, F. Reau, P. D'Oliveira, P. Monot, J. P. Geindre, E. Lefebvre & P. Martin, "Proton acceleration with high-intensity ultrahigh-contrast laser pulses", *Phys. Rev. Lett.*, vol. 99, 185002 (2007).

[116] L. Robson *et al.*, "Scaling of proton acceleration driven by petawatt-laser-plasma interactions", *Nature Phys.*, vol. 3, 58-62 (2007).

[117] P. Antici *et al.*, "Energetic protons generated by ultrahigh contrast laser pulses interacting with ultrathin targets", *Phys. Plasmas*, vol. 14, 030701 (2007).

[118] A. Yogo *et al.*, "Laser prepulse dependency of proton-energy distributions in ultraintense laser-foil interactions with an online time-of-flight technique", *Phys. Plasmas*, vol. 14, 043104 (2007).

[119] A. Yogo *et al.*, "Laser ion acceleration via control of the near-critical density target", *Phys. Rev. E*, vol. 77, 016401 (2008).

[120] M. Nishiuchi *et al.*, "Efficient production of a collimated MeV proton beam from a polyimide target driven by an intense femtosecond laser pulse", *Phys. Plasmas*, vol. 15, 053104 (2008).

[121] K. Flippo *et al.*, "Increased efficiency of short-pulse laser-generated proton beams from novel flat-top cone targets", *Phys. Plasmas*, vol. 15, 056709 (2008).

[122] K. V. Safronov, D. A. Vikhlyaev, A. G. Vladimirov, D. S. Gavrilov, S. A. Gorokhov, A. G. Kakshin, E. A. Loboda, V. A. Lykov, E. S. Mokicheva & A. V. Potapov, "Experimental study of the acceleration of protons emitted from thin foils irradiated by ultrahigh-contrast laser pulses", *JETP Lett.*, vol. 88, 716-719 (2008).

[123] A. Henig *et al.*, "Laser-driven shock acceleration of ion beams from spherical mass-limited targets", *Phys. Rev. Lett.*, vol. 102, 095002 (2009).

[124] Y. Fukuda *et al.*, "Energy increase in multi-MeV ion acceleration in the interaction of a short pulse laser with a cluster-gas target", *Phys. Rev. Lett.*, vol. 103, 165002 (2009).

[125] K. Zeil, S. D. Kraft, S. Bock, M. Bussmann, T. E. Cowan, T. Kluge, J. Metzkes, T. Richter, R. Sauerbrey & U. Schramm, "The scaling of proton energies in ultrashort pulse laser plasma acceleration", *New J. Phys.*, vol. 12, 045015 (2010).

[126] S. A. Gaillard, T. Kluge, K. A. Flippo, M. Bussmann, B. Gall, T. Lockard, M. Geissel, D. T. Offermann, M. Schollmeier, Y. Sentoku & T. E. Cowan, "Increased laser-accelerated proton energies via direct laser-light-pressure acceleration of electrons in microcone targets", *Phys. Plasmas*, vol. 18 (5), 056710 (2011).

[127] P. Antici *et al.*, "Optimization of flat-cone targets for enhanced laser-acceleration of protons", *Nucl. Instrum. Methods Phys. Res. A*, vol. 620, 14-17 (2010).

[128] F. Wagner, O. Deppert, C. Brabetz, P. Fiala, A. Kleinschmidt, P. Poth, V. A. Schanz, A. Tebartz, B. Zielbauer, M. Roth, T. Stöhlker & V. Bagnoud, "Maximum proton energy above 85 MeV from the relativistic interaction of laser pulses with micrometer thick CH2 targets", *Phys. Rev. Lett.*, vol. 116, 205002 (2016).

[129] A. Higginson *et al.*, "Near-100 MeV protons via a laser-driven transparency-enhanced hybrid acceleration scheme", *Nat. Commun.*, vol. 9, 724 (2018).

[130] Q. L. Dong, Z.-M. Sheng, M. Y. Yu & J. Zhang, "Optimization of Ion Acceleration in the Interaction of Intense Femtosecond Laser Pulses with Ultrathin Foil", *Phys. Rev. E.*, vol. 68, 026408 (2003).

[131] T. Esirkepov, M. Yamagiwa & T. Tajima, "Laser ion-acceleration scaling laws seen in multiparametric particle-in-cell simulations", *Phys. Rev. Lett.*, vol. 96 (10), 105001 (2006).

[132] L. Silva, M. Marti, J. R. Davies & R. A. Fonseca, "Proton shock acceleration in laser-plasma interactions", *Phys. Rev. Lett.*, vol. 92, 015002 (2004).

[133] E. d'Humières, J. L. Feugeas, P. Nicolaï, S. Gaillard, T. Cowan, Y. Sentoku & V. Tikhonchuk, "Investigation of high intensity laser proton acceleration with underdense targets", *J. Phys.: Conf. Ser.*, vol. 244, 042023 (2010).

[134] C. Palmer, N. P. Dover, I. Pogorelsky, M. Babzien, G. I. Dudnikova, M. Ispiriyan, M. N. Polyanskiy, J. Schreiber, P. Shkolnikov, V. Yakimenko & Z. Najmudin, "Monoenergetic proton beams accelerated by a radiation pressure driven shock", *Phys. Rev. Lett.*, vol. 106,

014801 (2011).

[135] D. Harberberger, S. Tochitsky, F. Fiuza, C. Gong, R. A. Fonseca, L. O. Silva, W. B. Mori & C. Joshi, "Collisionless shocks in laser-produced plasma generate monoenergetic high-energy proton beams", *Nat. Phys.*, vol. 8, 95-99 (2012).

[136] F. Sylla, A. Flacco, S. Kahaly, M. Veltcheva, A. Lifschitz, V. Malka, E. d'Humières, I. Andriyash & V. Tikhonchuk, "Short intense laser pulse collapse in near-critical plasma", *Phys. Rev. Lett.*, vol. 110, 085001 (2013).

[137] M. H. Helle, D. F. Gordon, D. Kaganovich, Y. Chen, J. P. Palastro & A. Ting, "Laser-accelerated ions from a shock-compressed gas foil", *Phys. Rev. Lett.*, vol. 117, 165001 (2016).

[138] S. N. Chen *et al.*, "Collimated protons accelerated from an overdense gas jet irradiated by a 1 mm wavelength high-intensity short-pulse laser", *Sci. Rep.*, vol. 7, 13505 (2017).

[139] J. L. Henares, T. Tarisien, P. Puyuelo, J.-R. Marquès, T. Nguyen-Bui, F. Gobet, X. Raymond, M. Versteegen & F. Hannachi, "Optimization of critical-density gas jet targets for laser ion acceleration in the collisionless shockwave acceleration regime", *J. Phys.: Conf. Ser.*, vol. 1079, 012004 (2018).

[140] J. L. Henares, P. Puyuelo-Valdes, F. Hannachi, T. Ceccotti, M. Ehret, F. Gobet, L. Lancia, J.-R. Marquès, J. J. Santos, M. Versteegen & M. Tarisien, "Development of critical-density gas jet targets for laser-driven ion acceleration", *Rev. Sci. Instrum.*, vol. 90, 063302 (2019).

[141] P. Puyuelo-Valdes, J. L. Henares, F. Hannachi, T. Ceccotti, J. Domange, M. Ehret, E. d'Humières, L. Lancia, J. R. Marquès, J. Santos & M. Tarisien, "Laser-driven ion acceleration in high-density gas jets", *Proc. SPIE*, vol. 11037, Laser Acceleration of Electrons, Protons, and Ions V, 110370B (2019).

[142] P. Puyuelo-Valdes, J. L. Henares, F. Hannachi, T. Ceccotti, J. Domange, M. Ehret, E. d'Humières, L. Lancia, J.-R. Marquès, X. Ribeyre, J. J. Santos, V. Tikhonchuk & M. Tarisien, "Proton acceleration by collisionless shocks using a supersonic H_2 gas-jet target and high-power infrared laser pulses", *Phys. Plasma*, vol. 26, 123109 (2019).

[143] A. Macchi, "A Superintense Laser-Plasma Interaction Theory Primer", *SpringerBriefs in Physics*, Heidelberg (2013).

[144] L. V. Keldysh, "Ionization in the field of a strong electromagnetic wave", *Sov. Phys. - JETP*, vol. 20 (5), 1307-1314 (1965).

[145] K. Amini *et al.*, "Symphony on strong field approximation", *Rep. Prog. Phys.*, vol. 82, 116001 (2019).

[146] M. V. Ammosov, N. B. Delone & V. P. Krainov, "Tunnel ionization of complex atoms and of atomic ions in an alternating electromagnetic field", *Sov. Phys. JETP*, vol. 64 (6), 1191 (1986).

[147] A. I. Akhiezer & R. V. Polovin, "Theory of Wave Motion of an Electron Plasma", *Sov. Phys. JETP*, vol. 3 (5), 696 (1956).

[148] P. Kaw & J. Dawson, "Relativistic Nonlinear Propagation of Laser Beams in Cold Overdense Plasmas", *Phys. of Fluids*, vol. 13 (2), 472 (1970).

[149] A. Vlasov, "On the kinetic theory of an assembly of particles with collective interaction", *Russ. Phys. J.*, vol. 9, 25-40 (1945).

[150] J. W. Eastwood, "The virtual particle electromagnetic particle-mesh method", *Comp. Phys. Commun.*, vol. 64 (2), 252-266 (1991).

[151] K. Noguchi, "Formulation of the relativistic moment implicit particle-in-cell method", *Phys. Plasmas*, vol. 14, 042308 (2007).

[152] Y. Sentoku & A. J. Kemp, "Numerical Methods for Particle Simulations at Extreme Densities and Temperatures: Weighted Particles, Relativistic Collisions and Reduced Currents", *J. Comp. Phys.*, vol. 227 (14), p. 6846-6861 (2008).

[153] E. d'Humières & Y. Sentoku, *PICLS Handbook*, private documentation, 29 p. (2009).

[154] J. W. Yoon, C. Jeon, J. Shin, S. K. Lee, H. W. Lee, I. W. Choi, H. T. Kim, J. H. Sung & C. H. Nam, "Achieving the laser intensity of 5.5×10^{22} W/cm^2 with a wavefront-corrected multi-PW laser", *Opt. Express*, vol. 27, 20412-20420 (2019).

[155] T. Ma, T. Döppner, R. W. Falcone, L. Fletcher, C. Fortmann, D. O. Gericke, O. L. Landen, H. J. Lee, A. Pak, J. Vorberger, K. Wünsch & S. H. Glenzer, "X-Ray Scattering Measurements of Strong Ion-Ion Correlations in Shock-Compressed Aluminum", *Phys. Rev. Lett.*, vol. 110, 065001 (2013).

[156] T. Ma *et al.*, "Observations of strong ion-ion correlations in dense plasmas", *Phys. Plasmas*, vol. 21, 056302 (2014).

[157] W. L. Kruer, "The physics of laser plasma interactions", *Frontiers in Physics*, New York: Addison-Wesley, (1988).

[158] T.-Y. B. Yang, W. L. Kruer, R. M. More & A. B. Langdon, "Absorption of laser light in overdense plasmas by sheath inverse bremsstrahlung ", *Phys. Plasmas*, vol. 2 (8), 3146 (1995).

[159] E. S. Weibel, "Anomalous Skin Effect in a Plasma", *Phys. Fluids*, vol. 10 (4), 741-748 (1967).

[160] P. J. Catto & R. M. More. "Sheath inverse bremsstrahlung in laser produced plasmas", *Phys. Fluids*, vol. 20 (4), 704-705 (1977).

[161] P. Gibbon, "Short Pulse Laser Interaction with Matter: An Introduction", *Imperial College Press*, 328 p. (2005).

[162] D. W. Forslund, J. M. Kindel & K. Lee., "Theory of Hot-Electron Spectra at High Laser Intensity", *Phys. Rev. Lett.*, vol. 39, 284-288 (1977).

[163] K. Estabrook & W. L. Kruer, "Properties of Resonantly Heated Electron Distributions", *Phys. Rev. Lett.*, vol. 40, 42-45 (1978).

[164] F. Brunel, "Not-so-resonant, resonant absorption", *Phys. Rev. Lett.*, vol. 59, 52-55 (1987).

[165] P. Gibbon & A. R. Bell, "Collisionless absorption in sharp-edged plasmas", *Phys. Rev. Lett.*, vol. 68 (10), 1535 (1992).

[166] W. L. Kruer & K. Estabrook, "$\boldsymbol{J} \times \boldsymbol{B}$ heating by very intense laser light", *Phys. Fluids*, vol. 28, 430 (1985).

[167] S. C. Wilks, W. L. Kruer, M. Tabak & A. B. Langdon, "Absorption of Ultra-Intense Laser Pulses", *Phys. Rev. Lett.*, vol. 69, 1383 (1992).

[168] H. Alfvén, "On the Motion of Cosmic Rays in Interstellar Space", *Phys. Rev.*, vol. 55 (5), 425 (1939).

[169] J. E. Crow, P. L. Auer & J. E. Allen, "The expansion of a plasma into a vacuum", *J. Plasma Phys.*, vol. 14 (1), 65-76 (1975).

[170] H. Ruhl, T. Cowan & J. Fuchs, "The generation of micro-fiducials in laser-accelerated proton flows, their imaging property of surface structures and application for the characterization of the flow, *Phys. Plasmas*, vol. 11 (5), L17-L20 (2004).

[171] J. Schreiber *et al.*, "Source-size measurements and charge distributions of ions accelerated

from thin foils irradiated by high-intensity laser pulses", *Appl. Phys. B*, vol. 79, 1041-1045 (2004).

[172] M. Roth *et al.*, "Laser accelerated ions in ICF research prospects and experiments", *Plasma Phys. Control. Fusion*, vol. 47, B841-B850 (2005).

[173] M. Roth *et al.*, "Laser accelerated heavy particles - tailoring of ion beams on a nano-scale", *Opt. Commun.*, vol. 264, 519-524 (2006).

[174] M. Nishiuchi *et al.*, "Repetitive highly collimated intense proton beam with sub-MeV energy range driven by a compact few terawatt femto-second laser", *Appl. Phys. B*, vol. 87, 615-621 (2007).

[175] P. Monot *et al.*, "High-order harmonic generation by nonlinear reflection of an intense high-contrast laser pulse on a plasma", *Opt. Lett.*, vol. 29 (8), 893 (2004).

[176] A. Lévy, T. Ceccotti, P. D'Oliveira, F. Réau, M. Perdrix, F. Quéré, P. Monot, M. Bougeard, H. Lagadec, P. Martin, J.-P. Geindre & Patrick Audebert, "Double plasma mirror for ultrahigh temporal contrast ultraintense laser pulses", *Opt. Lett.*, vol. 32, 310-312 (2007).

[177] P. McKenna, F. Lindau, O. Lundh, D. Neely, A. Persson & C.-G. Wahlström, "High-intensity laser-driven proton acceleration: influence of pulse contrast", *Phil. Trans. R. Soc. A*, vol. 364, 711-723 (2006).

[178] I. J. Kim, I. W. Choi, S. K. Lee, K. A. Janulewicz, J. H. Sung, T. J. Yu, H. T. Kim, H. Yun, T. M. Jeong & J. Lee, "Spatio-temporal characterization of double plasma mirror for ultrahigh contrast and stable laser pulse", *Appl. Phys. B*, vol. 104, 81-86 (2011).

[179] T. Wittmann, J. P. Geindre, P. Audebert, R. S. Marjoribanks, J. P. Rousseau, F. Burgy, D. Douillet, T. Lefrou, K. Ta Phuoc & J. P. Chambaret, "Towards ultrahigh-contrast ultraintense laser pulses?complete characterization of a double plasma-mirror pulse cleaner", *Rev. Sci. Instrum.*, vol. 77, 083109 (2006).

[180] P. McKenna *et al.*, "Effects of front surface plasma expansion on proton acceleration in ultraintense laser irradiation of foil targets", *Laser Part. Beams*, vol. 26 (4), 591-596 (2008).

[181] J. S. Green *et al.*, "Enhanced proton beam collimation in the ultra-intense short pulse regime", *Plasma Phys. Control. Fusion*, vol. 56, 084001 (2014).

[182] T. Z. Esirkepov, M. Borghesi, S. V. Bulanov, G. Mourou & T. Tajima, "Highly efficient relativistic-ion generation in the laser-piston regime", *Phys. Rev. Lett.*, vol. 92, 175003

(2004).

[183] A. P. L. Robinson, M. Zepf, S. Kar, R. G. Evans & C. Bellei, "Radiation pressure acceleration of thin foils with circularly polarized laser pulses", *New J. Phys.*, vol. 10, 013021 (2008).

[184] A. P. L. Robinson, P. Gibbon, M. Zepf, S. Kar, R. G. Evans & C. Bellei, "Relativistically correct hole-boring and ion acceleration by circularly polarized laser pulses", *Plasma Phys. Control. Fusion*, vol. 51 (2), 024004 (2009).

[185] T. Schlegel, N. Naumova, V. T. Tikhonchuk, C. Labaune, I. V. Sokolov & G. Mourou, "Relativistic laser piston model: Ponderomotive ion acceleration in dense plasmas using ultraintense laser pulses", *Phys. Plasmas*, vol. 16, 083103 (2009).

[186] A. Macchi & C. Benedetti, "Ion acceleration by radiation pressure in thin and thick targets", *Nucl. Inst. Meth. Phys. Res. A*, vol. 620, 41-45 (2010).

[187] A. P. L. Robinson, "Production of high energy protons with hole-boring radiation pressure acceleration", *Phys. Plasmas*, vol. 18, 056701 (2011).

[188] A. P. L. Robinson, R. M. G. M. Trines, N. P. Dover & Z. Najmudin, "Hole-boring radiation pressure acceleration as a basis for producing high-energy proton bunches", *Plasma Phys. Control. Fusion*, vol. 54, 115001 (2012).

[189] B. Qiao, M. Zepf, M. Borghesi & M. Geissler, "Stable GeV ion-beam acceleration from thin foils by circularly polarized laser pulses", *Phys. Rev. Lett.*, vol. 102, 145002 (2009).

[190] A. Macchi, S. Veghini & F. Pegoraro, "'Light sail' acceleration reexamined", *Phys. Rev. Lett.*, vol. 103, 085003 (2009a).

[191] V. A. Vshivkov, N. M. Naumova, F. Pegoraro & S. V. Bulanov, "Nonlinear electrodynamics of the interaction of ultra-intense laser pulses with a thin foil", *Phys. Plasmas*, vol. 5, 2727-2741 (1998).

[192] L. Yin, B. J. Albright, B. M. Hegelich & J. C. Fernández, "GeV laser ion acceleration from ultrathin targets: The laser break-out afterburner", *Laser Part. Beams*, vol. 24, 291-298 (2006).

[193] L. Yin, B. J. Albright, B. M. Hegelich, K. J. Bowers, K. A. Flippo, T. J. T. Kwan & J. C. Fernández, "Monoenergetic and GeV ion acceleration from the laser breakout afterburner using ultrathin targets", *Phys. Plasmas*, vol. 14, 056706 (2007).

[194] J. Denavit, "Absorption of high-intensity subpicosecond lasers on solid density targets", *Phys. Rev. Lett.*, vol. 69, 3052 (1992).

[195] L. Ji, B. Shen, X. Zhang, F. Wang, Z. Jin, X. Li, M. Wen & J. R. Cary, "Generating monoenergetic heavy-ion bunches with laser-induced electrostatic shocks", *Phys. Rev. Lett.*, vol. 101, 164802 (2008).

[196] M. Gauthier *et al.*, "Investigation of longitudinal proton acceleration in exploded targets irradiated by intense short-pulse laser", *Phys. Plasmas*, vol. 21, 013102 (2014)

[197] P. Antici *et al.*, "Acceleration of collimated 45 MeV protons by collisionless shocks driven in low-density, large-scale gradient plasmas by a 10^{20} W/cm^2, 1 μm laser", *Sci. Rep.*, vol. 7, 16463 (2017).

[198] A. Pak *et al.*, "Collisionless shock acceleration of narrow energy spread ion beams from mixed species plasmas using 1 μm lasers", *Phys. Rev. Accel. Beams*, vol. 21 (10), 103401 (2018).

[199] M. C. Downer, R. Zgadzaj, A. Debus, U. Schramm & M. C. Kaluza, "Diagnostics for plasma-based electron accelerators", *Rev. Mod. Phys.*, vol. 90, 035002 (2018).

[200] P. B. Bolton *et al.*, "Instrumentation for diagnostics and control of laser-accelerated proton (ion) beams", *Physica Medica*, vol. 30, 255-270 (2014).

[201] Hamamatsu, *MCP & MCP assembly selection guide*, Hamamatsu Photonics KK, https://www.hamamatsu.com/resources/pdf/etd/MCP_TMCP0002E.pdf.

[202] S. Nakamura *et al.*, "Real-Time Optimization of Proton Production by Intense Short-Pulse Laser with Time-of-Flight Measurement", *Jap. J. of App. Phys.*, vol. 45 (34), pp. L913-L916 (2006).

[203] M. Seimetz *et al.*, "Spectral characterization of laser-accelerated protons with CR-39 nucleartrack detector", *Rev. Sci. Instrum.*, vol. 89, 023302 (2018).

[204] J. Metzkes, L. Karsch, S. D. Kraft, J. Pawelke, C. Richter, M. Schörer, M. Sobiella, N. Stiller, K. Zeil & U. Schramm, "A scintillator-based online detector for the angularly resolved measurement of laser-accelerated proton spectra", *Rev. Sci. Instrum.*, vol. 83, 123301 (2012).

[205] A. Mančić, J. Fuchs, P. Antici, S. A. Gaillard & P. Audebert, "Absolute calibration of photostimulable image plate detectors used as (0.5 ? 20 MeV) high-energy proton detectors",

Rev. Sci. Instrum., vol. 79, 073301 (2008).

[206] A. P. L. Robinson *et al.*, "Spectral modification of laser-accelerated proton beams by self-generated magnetic fields", *New J. Phys.*, vol. 11, 083018 (2009).

[207] D. Kirby, S. Green, H. Palmans, R. Hugtenburg, C. Wojnecki & D. Parker, "LET dependence of GafChromic films and an ion chamber in low-energy proton dosimetry", *Phys. Med. Biol.*, vol. 55, 417-433 (2010).

[208] M. C. Battaglia, D. Schardt, J. M. Espino, M. I. Gallardo, M. A. Cortés-Giraldo, J. M. Quesada, A. M. Lallena, H. Miras & D. Guirado, "Dosimetric response of radiochromic films to protons of low energies in the Bragg peak region", *Phys. Rev. Accel. Beams.*, vol. 19, 064701 (2016).

[209] M. C. Battaglia, J. M. Espino, M. I. Gallardo, A. M. Lallena, B. Fernandez, M. A. Cortés-Giraldo, J. M. Quesada & D. Schardt, "EBT3 film calibration in the Bragg peak region for proton beams below 5 MeV", *Nuclear Inst. and Methods in Physics Research B*, vol. 444, 117-124 (2019).

[210] S. Reinhardt, M. Wurl, C. Greubel, N. Humble, J. J. Wilkens, M. Hillbrand, A. Mairani, W. Assmann & K. Parodi, "Investigation of EBT2 and EBT3 films for proton dosimetry in the 4-20 MeV energy range", *Radiat. Environ. Biophys.*, vol. 54, 71-79 (2015).

[211] M. Martisikova & O. Jakel, "Dosimetric properties of Gafchromic EBT films in monoenergetic medical ion beams", *Phys. Med. Biol.*, vol. 55, 3741-3751 (2010).

[212] L. Zhao & I. J. Das, "Gafchromic EBT film dosimetry in proton beams", *Phys. Med. Biol.*, vol. 55, N291-N301 (2010).

[213] G. Angellier, M. Gautier & J. Hérault, "Radiochromic EBT2 film dosimetry for low-energy protontherapy", *Med. Phys.*, vol. 38 (11), 6171-6177 (2011).

[214] R. Prasad *et al.*, "Calibration of Thomson parabola-MCP assembly for multi-MeV ion spectroscopy", *Nucl. Instrum. and Meth. in Phys. Res. A*, vol. 623, 712-715 (2010).

[215] T. W. Jeong, P. K. Singh, C. Scullion, H. Ahmed, K. F. Kakolee, P. Hadjisolomou, A. Alejo, S. Kar, M. Borghesi & S. Ter-Avetisyan, "Experimental evaluation of the response of micro-channel plate detector to ions with 10s of MeV energies", *Rev. Sci. Instrum.*, vol. 87, 083301 (2016).

[216] M. Bazalova-Carter, M. Ahmad, T. Matsuura, S. Takao, Y. Matsuo, R. Fahrig, H. Shirato,

K. Umegaki & L. Xing, "Proton-induced x-ray fluorescence CT imaging", *Med. Phys.*, vol. 42 (2), 900-907 (2015).

[217] M. Bazalova, Y. Kuang, G. Pratx & L. Xing, "Investigation of X-ray fluorescence computed tomography (XFCT) and K-edge imaging", *IEEE Trans. Med. Imaging*, vol. 31 (8), 1620-1627 (2012).

[218] M. Bazalova, M. Ahmad, G. Pratx & L. Xing, "L-shell x-ray fluorescence computed tomography (XFCT) imaging of Cisplatin", *Phys. Med. Biol.*, vol. 59, 219-232 (2014).

[219] M. Bazalova-Carter, M. Ahmad, L. Xing & R. Fahrig, "Experimental validation of L-shell x-ray fluorescence computed tomography imaging: phantom study", *J. of Med. Imaging*, vol. 2 (4), 043501 (2015).

[220] M. Bazalova-Carter, "The potential of L-shell X-ray fluorescence CT (XFCT) for molecular imaging", *Br. J. Radiol.*, vol. 88, 20140308 (2015).

[221] C. A. S. Dunning & M. Bazalova-Carter, "X-Ray Fluorescence Computed TomographyInduced by Photon, Electron, and Proton Beams", *IEEE Trans. Med. Imaging*, vol. 38 (12), 2735 (2019).

[222] M. Blanco, M. T. Flores-Arias, C. Ruiz & M. Vranic, "Table-top laser-based proton acceleration in nanostructured targets", *New J. Phys.*, vol. 19, 033004 (2017).

[223] M. Passoni *et al.*, "Toward High-energy Laser-Driven Ion Beams: Nanostructured Double-Layer Targets", *Phys. Rev. Acc. and Beams*, vol. 19, (2016).

[224] D. Margarone *et al.*, "Laser-Driven Proton Acceleration Enhancement by Nanostructured Foils", *Phys. Rev. Lett.*, vol. 109, 234801 (2012).

[225] L. Ji, S. Jiang, A. Pukhov, R. Freeman & K. Akli, "Exploring Novel Target Structures for Manipulating Relativistic Laser-Plasma Interaction", *High P. Las. Sci. and Eng.*, vol. 5, e14 (2017).

[226] M. A. Purvis *et al.*, "Relativistic Plasma Nanophotonics for Ultrahigh Energy Density Physics", *Nat. Phot.*, vol. 7, 796-800 (2013).

[227] C. Bargsten *et al.*, "Energy penetration into arrays of aligned nanowires irradiated with relativistic intensities: Scaling to terabar pressures", *Sci. Adv.*, vol. 3, 1601558 (2017).

[228] R. Hollinger *et al.*, "Efficient picosecond x-ray pulse generation from plasmas in the radiation dominated regime", *Optica*, vol. 4 (11), 111344 (2017).

[229] A. Moreau *et al.*, "Enhanced electron acceleration in aligned nanowire arrays irradiated at highly relativistic intensities", *Plas. Phys. Control. Fusion*, vol. 62s, 014013 (2020).

[230] Y.-C. Wang, Y. Yin, W.-Q. Wang, D.-B. Zou, W.-X. Miao, T.-P. Yu & F.-Q. Shao, "Copious positron production by femto-second laser via absorption enhancement in a microstructured surface target", *Sci. Rep.*, vol. 10, 5861 (2020).

[231] X. Ribeyre, E. d'Humières, O. Jansen, S Jequier & V. T. Tikhonchuk, "Electron-positron pairs beaming in the Breit-Wheeler process", *Plasma Phys. Control. Fusion*, vol. 59, 014024 (2017).

[232] M. Barberio, S. Vallières, M. Scisciò, G. Kolhatkar, A. Ruediger & P. Antici, "Graphitization of Diamond by Laser-Accelerated Proton Beams", *Carbon*, vol. 139, 531-537 (2018).

[233] Stopping Power and Range Tables for Protons (PSTAR), National Institute of Standards and Technology, https://physics.nist.gov/PhysRefData/Star/Text/PSTAR.html.

[234] S. Agostinelli *et al.*, "Geant4 - a simulation toolkit", *Nucl. Inst. & Meth. in Phys. Res. A*, vol. 506 (3), 250-303 (2003).

[235] M. Barberio, M. Scisciò, S. Vallières, F. Cardelli, S. N. Chen, G. Famulari, T. Gangolf, G. Revet, A. Schiavi, M. Senzacqua & P. Antici, "Laser-Accelerated Particle Beams for Stress Testing of Materials", *Nature Commun.*, vol. 9, 372 (2018).

[236] M. Barberio, M. Scisciò, S. Vallières, S. Veltri, A. Morabito & P. Antici, "Laser-Generated Proton Beams for High-Precision Ultra-Fast Crystal Synthesis", *Sci. Rep.*, vol. 7, 12522 (2017).

[237] M. Barberio, S. Giusepponi, S. Vallières, M. Scisciò, M. Celino & P. Antici, "Ultra-fast High-Precision Metallic Nanoparticle Synthesis using Laser-Accelerated Protons", *Sci. Rep.*, vol. 10, 9570 (2020).